



Daphne Schneider Cukierman

Physico-chemical optimization and Structure-Activity Relationship studies of aldehyde-derived *N*-acylhydrazones: towards the improvement of moderate metal chelators as a strategy against metal-enhanced aggregopathies

Tese de Doutorado

Thesis presented to the Programa de Pós-Graduação em Química of PUC-Rio in partial fulfillment of the requirements for the degree of Doutor em Química.

Advisor: Prof. Dr. Nicolás A. Rey

Rio de Janeiro
February 2021



Daphne Schneider Cukierman

Physico-chemical optimization and Structure-Activity Relationship studies of aldehyde-derived *N*-acylhydrazones: towards the improvement of moderate metal chelators as a strategy against metal-enhanced aggregopathies

Thesis presented to the Programa de Pós-Graduação em Química of PUC-Rio in partial fulfillment of the requirements for the degree of Doutor em Química. Approved by the Examination Committee:

Prof. Dr. Nicolás Adrián Rey

Advisor

Departamento de Química – PUC-Rio

Prof. Dr. Tiago Fleming Outeiro

UMG (Germany)

Prof. Dr. Ana Maria da Costa Ferreira

USP

Prof. Dr. Maria Domingues Vargas

UFF

Prof. Dr. Yraima Moura Lopes Cordeiro

UFRJ

Prof. Dr. Lidia Moreira Lima

UFRJ

Prof. Dr. Jones Limberger

Departamento de Química – PUC-Rio

Rio de Janeiro, February 25th, 2021

All rights reserved

Daphne Schneider Cukierman

Graduated in Chemistry at the Pontifical Catholic University of Rio de Janeiro (PUC-Rio) in 2016. In view of her academic performance, the author was allowed to enter the Ph.D. Program without having a Master's degree.

Bibliographic data

Cukierman, Daphne Schneider

Physico-chemical optimization and structure-activity relationship studies of aldehyde-derived *N*-acylhydrazones : towards the improvement of moderate metal chelators as a strategy against metal-enhanced aggregopathies / Daphne Schneider Cukierman ; advisor: Prof. Dr. Nicolás A. Rey. – 2021.

244 f. : il. color. ; 30 cm

Tese (doutorado) – Pontifícia Universidade Católica do Rio de Janeiro, Departamento de Química, 2021.

Inclui bibliografia

1. Química - Teses. 2. Doença de Parkinson. 3. Agregopatias. 4. Biometais. 5. Cobre. 6. N-acilidrazonas. I. Rey, Nicolás Adrián. II. Pontifícia Universidade Católica do Rio de Janeiro. Departamento de Química. III. Título.

CDD: 540

This thesis is dedicated to my greatest mentor, everyday teacher and supporter.
You have always known my path and my passion, even before I did.

Acknowledgements

I would like to thank PUC-Rio and the Department of Chemistry, for making a home out of a university.

I thank *Coordenação de Aperfeiçoamento de Pessoal de Nível Superior - Brasil* (CAPES) for the scholarship 88882.146163/2017-01 (03/2017 – 08/2018), as well as *Programa de Doutorado Sanduíche no Exterior* (PDSE), from the same institution, grant number 88881.188436/2018-01 (09/2018 – 02/2019), which funded 6 of the 10 months spent in Germany. I also appreciate *Conselho Nacional de Desenvolvimento Científico e Tecnológico* (CNPq) for the scholarship, grant number 142322/2019-9 (07/2019 – 02/2021).

To the members of this thesis committee: thank you for accepting the invitation to read and collaborate with this work. It is an honor to have each and every one of you, important Professors, evaluating my work and journey.

To all collaborators (professors, students, postdocs and technicians) of this work: Álvaro for the help with NMR analyses; Prof. Dr. Ricardo Aucélio and Ana Paula Diniz for the CHN analyses; Prof. Dr. Renata Diniz and Dr. Chris H. J. Franco for the X-ray assays; Prof. Dr. Jones Limberger and his student Carlos Castanho Neto for one of the aldehyde precursors; Dr. Claudio Fernández and his student Pamela Sacco for the protein NMR studies; Prof. Dr. Csilla Kállay and her student Nikollet Bodnár for the collaboration in the PrP project.

To Dídimo, Marlene and Fátima for the endless help and patience.

To Prof. Dr. Nicolás A. Rey, the best mentor and advisor a student could ask for. It has been a long way since I first joined the group, in 2013. I have grown so much, overcame many adversities, and grew stronger every day, thanks to you. My scientific journey began the moment I stepped into your classroom. Thank you for all the discussions, scientific or not, and for all the advices. It has been a privilege to work under your supervision. Words can never be enough to describe my gratitude to you for the opportunities and the investment you have given me.

To Prof. Dr. Tiago F. Outeiro, my co-advisor in Germany: thank you for the hospitality, the opportunity and for believing in me. It has been an honor to be part of your group, to learn so much and to see and go further than my comfort zone.

I would like to appreciate all the help from the people at the Experimental Neurodegeneration group. It was a challenge and an adventure to adapt to a new culture, learn new protocols in such a short time, and to share a new way of thinking. You have all been very patient to me during those amazing 10 months. A special mention to M. Sc. Daniela Dias, who helped me even before I got there, especially with the “living things”; And to my “almost-Portuguese-speaking” friends: Dr. Diana F. Lázaro, M. Sc. Renato G. Domingues, Dr. Antonio M. Dominguez, M. Sc. Patrícia Santos and my “brazuca” Dr. Ricardo Sant’Anna.

Special thanks to the dearest Diana F. Lázaro: you have been a good friend, a mother and a sister to me during my little German adventure. You have not only taught me everything I know about cell biology, but so much about myself. I would have never imagined I could find someone so similar to me, with whom I could share my life experiences and genuine thoughts. I could never thank you enough for all the knowledge, help and fun that we still share every day.

To my dear pupil Beatriz Nico: never stop questioning the world. A wise, inspiring woman once said: “Nothing in life is to be feared, it is only to be understood. Now is the time to understand more, so that we may fear less.” (Marie Curie, 1867-1934). Thank you for the help and the fun we had while doing the experiments. Teaching you has also been an exercise for me, from which I learned so much.

To Myriam Rodrigues, for the different teaching and learning experience of being the mentor of a “senior” trainee (“*Programa de Iniciação Científica e Tecnológica Sênior, PICT Sênior*”), and for all the help with syntheses and characterization.

To all the new students from LABSO-Bio: thank you for the laughs, for making the lab environment so great to work in, and for supporting me many times I needed. Patrícia, Eduarda, Milena, Bárbara, Carol, Isabela, Roberta Lamosa and Ygor: I already miss all the fun we have every day. You guys made me feel close to you even when we were apart due to the pandemic quarantine.

To Patrícia Ferreira specifically, for the endless Job Plot replicates and for enduring the cold while doing the measurements in the Spectroscopy lab. You are the sweetest!

To Roberta Lamosa in particular, for the artwork done, not only in this thesis but also in our lab's Instagram page, @labsobio. You are the most patient and creative person I know! Thank you for all the fun we had suffering together with our OCDs!

To M. Sc. Alessandra Carvalho and M. Sc. Fagner Moura: after 7 and a half years in LABSO-Bio, I hope I can now leave an organized and happy environment for your future work. And I fully trust you to keep both the productivity and uplifting spirit of this place that was, and always will be, my second home.

To Dr. Anna De Falco, for the endless help with software, data treatment, statistics, "MacGyvering" lab equipment, borrowing stuff, coordinating the humidity clearance in the Spectroscopy lab for me during quarantine, and specially, for trying to keep me sane on a daily basis through every panic and anxiety attack. Thank you for sharing so much with me. I am so happy that we finally reached this level of friendship and understanding of each other's emotions. I am happy that we went through so much together and only grew out stronger, better people.

To my husband: you are my greatest inspiration. Like I once said, I married the smartest person I know. As well as the most kind and comprehensive human being on Earth. Loving you has been a constant exercise of loving myself and the people we are becoming together. Thank you for your presence and endless support throughout this whole process.

My parents, Rogério and Thais Cukierman: you have taught me to question everything and to chase my dreams no matter what. Thank you for giving me the ideal tools needed for pursuing a scientific career. Thank you for giving me strength and support. "I love you more than my own life."

To my big brother, Yannick Cukierman. Over the years you have become a little less annoying, so I acknowledge that. Trying to overcome your geniality is what started this whole process... I think I have won. Love you!

To my grandfather Samuel: thank you for all the help and opportunities. From the very beginning, if it hadn't been for you, I would have never even began studying

at PUC-Rio. I am grateful for our recent approximation and almost daily conversations.

Yes, I will also thank my dog Dexter, my best friend, and my beautiful blond hamster Claudio (*in memoriam*).

This thesis represents not only an academic achievement but also the growth of a young woman, who learned how to deal with a lot of adversities and uncertainties, and came out stronger, more resilient, and even more in love with Science. Thank you all who have been with me during this evolution path, which has not always been smooth. As a proud fighter of obsessive-compulsive disorder, I have imagined many different scenarios for the end of my Ph.D. None of them included a pandemic that would cost me my whole last year of experiments and suffocating anxiety. However, resilience is doing the best you can in an adverse situation and this is what represents me the best right now. I thank again my advisor whom was very understanding and helpful during this especially difficult moment.

This study was financed in part by the *Coordenação de Aperfeiçoamento de Pessoal de Nível Superior - Brasil* (CAPES) - Finance Code 001.

Abstract

Cukierman, Daphne Schneider; Rey, Nicolás Adrián (Advisor). **Physico-chemical optimization and Structure-Activity Relationship studies of aldehyde-derived *N*-acylhydrazones: towards the improvement of moderate metal chelators as a strategy against metal-enhanced aggregopathies.** Rio de Janeiro, 2021. 244p. Tese de Doutorado - Departamento de Química, Pontifícia Universidade Católica do Rio de Janeiro.

Although normal aging results in an accumulation of copper, iron and zinc in the brain, this becomes more relevant in neurodegeneration. Protein misfolding has long been linked with the development of some degenerative diseases, called aggregopathies. Metal binding is generally a factor for promoting the aggregation of such proteins, as well as generalized oxidative stress when redox-active metals are involved. In this sense, the use of therapies that target metal dyshomeostasis has been the subject of intense research in recent years. Our research group has already established that *N*-acylhydrazones compose a set of truly encouraging agents for the bioinorganic management of metal-enhanced aggregopathies. Our lead compound, INHHQ, however, does not present ideal pharmacokinetic parameters, which might constitute an obstacle in its path towards becoming a commercial drug. The present work consists of the study of fifty-five *N*-acylhydrazones of related structure (INHHQ + fifty-four analogues) and in the selection of the best candidates as moderate chelators, Metal-Protein Attenuating Compounds (MPACs), in the context of important human aggregopathies. The ligands were designed through rationally thought changes in INHHQ's structure. Initially, *in silico* analyses were conducted. Blood-brain barrier crossing reference values, together with water solubility, were limiting features to select compounds for the next step. The hydrazones with the best theoretical pharmacological prospect (9 compounds + INHHQ) were synthesized and thoroughly characterized, both in solution and in the solid state. Moreover, their hydrolysis resistance profiles were determined and, when possible, also their experimental octanol/water partition coefficient. A total of eight hydrazones were selected for the next phases, in which their effect on the survival of H4 cells and their ability of inhibiting protein aggregation in a cellular model of synucleinopathy were evaluated. 1-methylimidazole-containing *N*-

acylhydrazone **1d** excelled the expectations, being not only the most stable and least toxic analogue, but the one which interfered the most with protein inclusion patterns in the evaluated model, making them less compact. Furthermore, this compound binds selectively to aggregated forms of the α -Syn protein, as proven through STD experiments. A series of additional *in vitro* biophysical characterizations by NMR were carried out with the purpose of evaluating the ability of **1d** to compete with monomers of α -Syn for the binding of copper(I) and copper(II) ions, which are central to Parkinson's disease pathology. A desired preference for copper(I) was observed. The apparent affinity constant of this *N*-acylhydrazone for copper(II) was determined through calculations based on the Job method and is in the order of 5.66. A qualitative structure-activity relationship was established for the synthesized compounds. We believe that the present work may constitute a significant contribution to the field of study in question, opening new perspectives for the development of MPACs for the therapy of metal-enhanced aggregopathies.

Keywords

Parkinson's disease; aggregopathies; biometals; copper; *N*-acylhydrazones.

Resumo Expandido em Português

Cukierman, Daphne Schneider; Rey, Nicolás Adrián. **Otimização físico-química e estudos de Relação Estrutura-Atividade de *N*-acilidrazonas derivadas de aldeídos: aperfeiçoamento de quelantes moderados como uma estratégia contra agregopatias exacerbadas por metais.** Rio de Janeiro, 2021. 244p. Tese de Doutorado - Departamento de Química, Pontifícia Universidade Católica do Rio de Janeiro.

Embora o envelhecimento normal tenha como consequência o acúmulo de cobre, ferro e zinco no cérebro, isso se torna mais relevante na neurodegeneração. Há muito tempo que o dobramento defeituoso de proteínas tem sido associado ao desenvolvimento de algumas doenças degenerativas, chamadas de agregopatias. A ligação a metais geralmente é um fator promotor da agregação de tais proteínas, bem como do estresse oxidativo generalizado quando metais redox-ativos estão envolvidos.

Neste sentido, o uso de terapias que têm como alvo a desomeostase metálica tem sido motivo de intensa pesquisa nos últimos anos. Os compostos atenuadores da interação metal-proteína (MPACs, *Metal-Protein Attenuating Compounds*) são quelantes moderados que visam interromper interações metal-proteína anormais específicas. Nosso grupo de pesquisa já estabeleceu que a classe química das *N*-acilidrazonas compõe um conjunto de MPACs verdadeiramente promissores para o manejo bioinorgânico de agregopatias exacerbadas por metais. Nosso composto-líder, INHHQ, entretanto, não apresenta parâmetros farmacocinéticos ideais, o que pode constituir um obstáculo em seu caminho para se tornar um fármaco comercial.

O presente trabalho consiste no estudo de cinquenta e cinco *N*-acilidrazonas de estrutura relacionada (INHHQ + cinquenta e quatro análogos) e na seleção dos melhores candidatos como quelantes moderados, chamados MPACs, no contexto de agregopatias humanas importantes. Os compostos foram projetados por meio de mudanças racionalmente efetuadas na estrutura do INHHQ, que podem reduzir sua taxa de hidrólise, melhorar sua solubilidade em meio aquoso e ajustar sua afinidade de coordenação por cobre. Inicialmente, foram realizadas análises farmacológicas *in silico* para determinar algumas características dos compostos que são relevantes no desenvolvimento de um novo fármaco. Os valores de referência para permeação

da barreira hematoencefálica, em conjunto com a solubilidade em água, foram limitantes para selecionar compostos para a próxima etapa. As hidrazonas com melhor perspectiva farmacológica teórica foram sintetizadas (9 compostos + INHHQ) e caracterizadas minuciosamente, tanto em solução quanto no estado sólido. Além disso, seus perfis de resistência à hidrólise foram determinados e, quando possível, também seus coeficientes de partição experimental octanol/água. Um total de oito hidrazonas foram selecionadas para as etapas seguintes.

Estes compostos foram então novamente avaliados *in silico*, desta vez com relação ao seu potencial tóxico teórico, o que demonstrou que a presença da porção *orto*-piridina derivada do aldeído leva a uma moderada toxicidade. Isso foi provado experimentalmente por meio de ensaios de sobrevivência em células H4 de neuroglioma humano. Ademais, a inibição de agregação proteica em um modelo celular de sinucleinopatia foi avaliada para todas os oito compostos selecionados.

A *N*-acilidrazona **1d**, contendo o grupamento 1-metilimidazol, superou as expectativas, sendo não só o análogo mais estável e menos tóxico, mas também o que mais interferiu no padrão de inclusões de proteína no modelo celular avaliado, tornando-as menos compactas e, portanto, mais acessíveis para serem clivadas por proteinase-K. Além disso, este composto se liga seletivamente a formas agregadas da proteína α -Syn, conforme comprovado por meio de experimentos de RMN-STD.

Uma série de caracterizações biofísicas *in vitro* adicionais por RMN foram realizadas com o propósito de avaliar a capacidade de **1d** de competir com monômeros de proteína (α -sinucleína) pela ligação de íons cobre(I) e cobre(II), que são centrais na patologia da doença de Parkinson. Uma desejada preferência por cobre(I) foi observada. A constante de afinidade aparente desta *N*-acilidrazona por cobre(II) foi determinada através de cálculos baseados no método de Job e encontra-se na ordem de 5,66.

Devido aos promissores resultados apresentados pelo grupo de hidrazonas derivadas do 1-metilimidazol-2-carboxaldeído, quatro compostos da classe foram parte de um pedido de patente depositado junto ao Instituto Nacional da Propriedade Industrial (INPI), que inclui uma estrutura Markush mais genérica.

Além disto, os compostos foram avaliados qualitativamente frente a um modelo de formação de grânulos de estresse (SGs, *Stress Granules*), para se obter

uma perspectiva do efeito dessas *N*-acilidrazonas sobre essas importantes inclusões. Nesse âmbito, três dos quatro ligantes contendo 1-metilimidazol em sua estrutura apresentaram, mais uma vez, resultados encorajadores, evitando completamente a formação de SGs a uma concentração de 100 $\mu\text{mol L}^{-1}$.

Finalmente, embora as agregopatias exacerbadas por metais apresentem certas características em comum, como por exemplo proteínas que são propensas a se agregar após a interação com íons metálicos, essas doenças são multifatoriais, e pode-se esperar que *N*-acilidrazonas estruturalmente diferentes tenham atividades distintas em modelos experimentais de diversas patologias. Neste sentido, embora hidrazonas derivadas de piridina-2-carboxaldeído não tenham mostrado resultados significativos na agregação da proteína α -sinucleína, elas atuam como agentes protetores de peptídeos com relação aos efeitos deletérios da oxidação catalisada por cobre em um fragmento mutante da proteína priônica humana.

Através da coleta de todos esses dados teóricos, químicos, espectroscópicos e biológicos, foi estabelecida uma relação qualitativa entre estrutura e atividade, a fim de determinar a influência de cada característica estrutural no desempenho de uma hidrazona como MPAC. Acredita-se que o presente trabalho possa constituir uma contribuição significativa para o campo de estudo em questão, abrindo novas perspectivas para o desenvolvimento de compostos atenuadores da interação metal-proteína para a terapia de agregopatias exacerbadas por metais.

Palavras-chave

doença de Parkinson; agregopatias; biometais; cobre; *N*-acilidrazonas.

Table of contents

List of Acronyms and Abbreviations	1
List of Figures.....	5
List of Tables	11
List of Appendix Figures	13
1. Introduction.....	16
1.1. Protein aggregation and disease	16
1.2. Alzheimer's disease	20
1.3. Parkinson's disease	23
1.4. Prion diseases	27
1.5. Metals and aggregopathies	29
1.6. Metal-Protein Attenuating Compounds (MPACs)	32
2. Work proposal and justification	38
3. Objectives	48
3.1. General objective	48
3.2. Specific objectives	48
4. Methodology	50
4.1. <i>In silico</i> pharmacological analyses	50
4.2. Organic syntheses	50
4.3. Characterization	52
4.3.1. Infrared Vibrational Spectroscopy	52
4.3.2. Nuclear Magnetic Resonance (NMR).....	52
4.3.3. X-ray diffraction (XRD).....	52
4.3.4. Thermogravimetry (TG)	53
4.3.5. Melting Point (MP).....	53
4.3.6. Elemental Analysis (CHN)	53
4.4. Molecular Absorption Spectroscopy.....	53
4.5. Experimental Log P	54
4.6. Method of Continuous Variations (Job Plot)	54
4.7. Disruption of metal-protein interactions.....	55
4.8. Compound-protein interactions (STD-NMR).....	56
4.9. <i>In cell</i> assays	57
4.9.1. Cell culture	57
4.9.2. Cellular viability in H4 cells (MTT cytotoxicity assay)	58
4.9.3. Intracellular α -Syn aggregation: Syn-T + Sph1 model.....	58

4.9.3.1. Immunocytochemistry (ICC)	59
4.9.3.2. Cell lysates and Western Blot.....	60
4.9.3.3. Triton-X100 solubility of α -Syn inclusions.....	61
4.9.3.4. Proteinase-K digestion of α -Syn inclusions	62
4.9.4. Stress Granules	62
4.10. Copper-catalyzed oxidation of the M112A PrP ₁₀₃₋₁₁₂ mutant fragment.....	62
5. Results and discussion: Part I – Design, syntheses, characterization and pharmacological parameters	66
5.1. <i>In silico</i> pharmacological descriptors.....	66
5.2. Syntheses and chemical characterization	72
5.2.1. Compound 1a:.....	72
3,4-dihydroxybenzaldehyde isonicotinoyl hydrazone	72
5.2.2. Compound 1c:.....	74
2-(1H-pyrazol-1-yl)benzaldehyde isonicotinoyl hydrazone (1c).....	74
5.2.3. Compounds 1d, 2d, 3d and 4d:.....	83
1-methyl-1H-imidazole-2-carboxaldehyde <i>N</i> -acylhydrazones	83
5.2.4. Compound 1e:.....	98
2-hydroxy-3-methoxy-benzaldehyde isonicotinoyl hydrazone	98
5.2.5. Compounds 1f and 3f:	99
pyridine-2-carboxaldehyde <i>N</i> -acylhydrazone	99
5.2.6. Compound 1h (lead compound):.....	104
8-hydroxyquinoline-2-carboxaldehyde isonicotinoyl hydrazone..	104
5.2.7. Compound 1i:.....	104
4-chloro-3-formylcoumarin isonicotinoyl hydrazone.....	104
5.2.8. 4-methylpiperazine-derived hydrazones (series 5)	105
5.3. Nuclear Magnetic Resonance	106
5.4. Electronic spectroscopy and hydrolytic stability	107
5.5. Experimental log P.....	121
5.6. Is it possible to correlate spectroscopic trends with calculated physicochemical properties for <i>N</i> -acylhydrazones? ...	122
5.7. <i>In silico</i> prediction of the toxic potential of <i>N</i> -acylhydrazones	125
6. Results and discussion: Part II – Effects of the selected <i>N</i>-acylhydrazones on synucleinopathies-related models	134
6.1. <i>In cell</i> assays.....	134

6.1.1.	Cellular viability in H4 cells (MTT)	134
6.1.2.	Intracellular α -syn aggregation: SynT + Sph1 model	135
6.1.2.1.	Immunocytochemistry (ICC)	136
6.1.2.2.	Western Blot.....	141
6.1.2.3.	Triton-X100 solubility.....	143
6.1.2.4.	Proteinase-K (PK) digestion.....	145
6.2.	Biophysical characterizations	147
6.2.1.	Interaction between 1d and aggregated forms of α -Syn ..	147
6.2.2.	Interactions of <i>N</i> -acylhydrazones with copper in the absence and presence of monomeric, <i>N</i> -acetylated α -Syn.....	148
7.	Results and discussion: Part III – Effects of the selected <i>N</i> - acylhydrazones on models for other aggregopathies	158
7.1.	Impact of pyridine-2-carboxaldehyde-derived aroylhydrazones on the copper-catalyzed oxidation of M112A PrP ₁₀₃₋₁₁₂ fragment.....	158
7.2.	Prospective effect of <i>N</i> -acylhydrazones in Stress Granules 172	
8.	Conclusions	179
9.	Bibliography.....	184
10.	Appendix	210
11.	Scientific Production.....	220

List of Acronyms and Abbreviations

8-H₂QS, 2-[(8-hydroxyquinolinyl)methylene]hydrazinecarboxamide

8-HQ-2-CA, 8-hydroxyquinoline-2-carboxaldehyde

AD, Alzheimer's disease

ADME, Absorption, Distribution, Metabolism, Excretion

AhR, aryl hydrocarbon receptor

ALS, Amyotrophic Lateral Sclerosis

APP, Amyloid Precursor Protein

APS, ammonium persulfate

AR, androgen receptor

A β , amyloid-beta peptide

A β O, amyloid-beta peptide oligomers

BBB, Blood-Brain Barrier

BES, N,N-bis(2-hydroxyethyl)-2-aminoethanesulfonic acid

BSA, Bovine Serum Albumin

CNS, Central Nervous System

COSY, Correlation Spectroscopy

CSF, cerebrospinal fluid

CTR1, copper uptake protein 1

CYP1A2, cytochrome P450 1A2

CYP2C9, cytochrome P450 2C9

CYP2D6, cytochrome P450 2D6

CYP3A4, cytochrome P450 3A4

DAPI, 4',6-diamidino-2-phenylindole

DMEM, Dulbecco's Modified Eagle's Medium

dMKHA, mutant fragment of human PrP (Ac-SKPKTNMKHA-NH₂)

DMSO, dimethylsulfoxide

DMSO-*d*₆, deuterated dimethylsulfoxide

DPBS, Dulbecco's Phosphate-Buffered Saline

EDTA, ethylenediamine tetraacetic acid

EGFP, enhanced green fluorescent protein

ENS, Enteric Nervous System

ER α , estrogen- α receptor

ER β , estrogen- β receptor

ESI-MS, electrospray ionization mass spectrometry

FBS, Fetal Bovine Serum

FDA, Food and Drug Administration

GAPDH, glyceraldehyde 3-phosphate dehydrogenase

GR, Glucocorticoid Receptor

GSH, reduced glutathione

HATR, Horizontal Attenuated Total Reflectance

HBA, Hydrogen Bond Acceptors

HBD, Hydrogen Bond Donors

HEPES, 4-(2-hydroxyethyl)-1-piperazineethanesulfonic acid

hERG, human Ether-à-go-go-Related Gene

HMBC, Heteronuclear Multiple Bond Coherence

HPCFur, piridine-2-carboxaldehyde 2-furoyl hydrazone

HPCIH, piridine-2-carboxaldehyde isonicotinoyl hydrazone

HPLC, High Performance Liquid Chromatography

HSQC, Heteronuclear Single Quantum Coherence

i.c.v., intracerebroventricular

IAPP, islet amyloid polypeptide

IC₅₀, half maximal inhibitory concentration

ICC, Immunocytochemistry

INH HQ, 8-hydroxyquinoline-2-carboxaldehyde isonicotinoyl hydrazone

IR, Infrared Vibrational Spectroscopy

ITC, Isothermal Titration Calorimetry

K_{app}, apparent affinity constant

K_d, dissociation constant

LDH, lactate dehydrogenase

L-dopa, Levodopa

LLPS, liquid-liquid phase separation

Log P, logarithm of the partition coefficient in 1-octanol/water

Log S, logarithm of solubility in water

LXR, liver X receptor

MP, melting point

MPAC, Metal-Protein Attenuating Compound

mQSAR, Multidimensional Quantitative Structure-Activity Relationship

MR, mineralocorticoid receptor

MSA, Multiple System Atrophy

MTT, 3-(4,5-dimethylthiazol-2-yl)-2,5-diphenyltetrazolium bromide
tetrazolium

MW, molecular weight

NMDA, N-methyl-D-Aspartate

NMR, Nuclear Magnetic Resonance

OptiMEM, Optimized Reduced Serum Medium

PBS, Phosphate-Buffered Saline

PBT2, 5,7-dichloro-2-[(dimethylamino)methyl]quinolin-8-ol

PD, Parkinson's disease

PFA, paraformaldehyde

PK, proteinase-K

PMCA, Protein Misfolding Cyclic Amplification

Ponceau-S, 3-hydroxy-4-[2-sulfo-4-(4-sulfophenylazo)phenylazo]-2,7-naphthalenedisulfonic acid sodium salt

PPAR γ , peroxisome proliferator-activated receptor gamma

PR, progesterone receptor

PrP, prion protein

PrP^C, cellular prion protein

PrP^{Sc}, scrapie prion protein

PSA, Polar Surface Area

PTMs, Post-Translational Modifications

PVDF, polyvinylidene difluoride
RBP, RNA binding protein
RNS, Reactive Nitrogen Species
ROS, Reactive Oxygen Species
RP- HPLC, Reversed Phase High Performance Liquid Chromatography
SDS, sodium dodecyl sulphate
SDS-PAGE, sodium dodecyl sulphate–polyacrylamide gel electrophoresis
SG, Stress Granule
SOD1, superoxide dismutase 1
Sph1, synphilin-1
STD, Saturation-Transfer Difference
SynT, construction of α -syn linked with a truncated fragment of EGFP
T2DM, type 2 diabetes *mellitus*
TBS, Tris-Buffered Saline
TBS-t, Tris-Buffered Saline with Tween 20
TEMED, tetramethylethylenediamine
TFA, trifluoroacetic acid
TG, Thermogravimetry
TIA1, cytotoxic granule-associated RNA binding protein
TP, toxic potential
Tris, tris(hydroxymethyl)aminomethane
TR α , thyroid hormone receptor- α
TR β , thyroid hormone receptor- β
TSP-d₄, deuterated 3-(trimethylsilyl)propionic-2,2,3,3 acid sodium salt
UV-Vis, Ultraviolet-Visible
WT, wild-type
XRD, X-Ray Diffraction
 α -Syn, alpha-synuclein protein

List of Figures

Figure 1. The aggregation process of proteins. Adapted from (Theillet <i>et al.</i> , 2014).....	18
Figure 2. Schematic differences between a healthy neuron (left) and a neuron from an AD patient (right). Extracellular amyloid plaques and intracellular neurofibrillary tangles can be observed. Adapted from (De Falco <i>et al.</i> , 2016) and reproduced with the author's approval.....	21
Figure 3. Lewy body inclusion in neuronal cells. Obtained from http://whatislyme.com/lewy-body-dementia-putting-the-puzzle-pieces-together/ , accessed on 08/11/2017.	25
Figure 4. Structures of some 8-hydroxyquinoline-derived compounds that have been studied in the context of neurodegenerative diseases.	35
Figure 5. General scheme of <i>N</i> -acylhydrazones' synthesis.....	39
Figure 6. Structures of the 55 proposed carbonylhydrazones. Lead compound INHHQ (1h) is highlighted in red color.....	40
Figure 7. Structures of L-dopa, dopamine and the compounds of row a ..	41
Figure 8. Mechanism of hydrolysis of hydrazones. The catalyst is shown in blue.	43
Figure 9. cLog S of the 55 hydrazones. The lead compound (1h) is shown in red and the hydrazones selected for synthesis are shown in light gray. The (*) symbol highlights the compound with undesired positive cLog S. 71	71
Figure 10. ¹ H NMR spectrum of 1a (400 MHz) in DMSO- <i>d</i> ₆ at room temperature.....	74
Figure 11. Molecular structure representations of (A) compound 1c and (B) compound 1c' . The ellipsoids were drawn at the 50% probability level....	75
Figure 12. Intermolecular interactions in (A) compound 1c' , where each color represents a dimeric unit linked in a one-dimensional network along the crystallographic axis a and (B) compound 1c . The intricate tridimensional network can be observed along axis b (left) and c (right). Extracted from (Cukierman <i>et al.</i> , 2021).....	77
Figure 13. ¹ H NMR spectrum of 1c (400 MHz) in DMSO- <i>d</i> ₆ at room temperature.....	81
Figure 14. ¹ H NMR spectrum of 1c' (400 MHz) in DMSO- <i>d</i> ₆ at room temperature.....	81
Figure 15. Study of the complexation potential of compound 1c towards copper(II): Absorption UV-Vis spectra of compound 1c in methanol, in the absence (dark blue) and presence (gray) of CuCl ₂ , and after 3h30 kept under constant stirring (light blue). Absorptions of methanol (green) and CuCl ₂ methanolic solution (yellow) are shown for control purposes.	83
Figure 16. Structure of the 1-methyl-1H-imidazole-2-carboxaldehyde-derived <i>N</i> -acylhydrazones (i.e. compounds 1d , 2d , 3d and 4d).....	83
Figure 17. ORTEP representation of the crystal structures of (A) 1d' , (B) 2d , (C) 3d and (D) 4d . The ellipsoids were drawn with 50% probability level.	86

Figure 18. Hydrogen bond interactions in the crystal networks of compounds (A) 1d' , (B) 2d , (C) 3d and (D) 4d .	89
Figure 19. π - π stacking interactions in the structures of compounds 2d , 3d and 4d .	91
Figure 20. (A) ^1H NMR spectrum of compound 1d (400 MHz) in DMSO- d_6 at room temperature. (B) Comparison between the ^1H NMR spectra (400 MHz) of 1d and its hydrochloride 1d' in DMSO- d_6 at room temperature.	95
Figure 21. ^1H NMR spectrum of 2d (400 MHz) in DMSO- d_6 at room temperature.	96
Figure 22. ^1H NMR spectrum of 3d (400 MHz) in DMSO- d_6 at room temperature.	96
Figure 23. ^1H NMR spectrum of 4d (400 MHz) in DMSO- d_6 at room temperature.	97
Figure 24. Electronic molecular absorption spectra of compound 1e in 10% DMSO taken at regular intervals for 30 hours. The spectrum of the precursor 2-hydroxy-3-methoxy-benzaldehyde, in the same solvent, is shown in black. Blue arrows indicate the temporal changes that occur. Reproduced with the author's approval (De Falco, 2017).	99
Figure 25. ^1H NMR spectrum of 1f (400 MHz) in DMSO- d_6 at room temperature.	102
Figure 26. ^1H NMR spectrum of 3f (400 MHz) in DMSO- d_6 at room temperature.	102
Figure 27. ^1H NMR spectrum of 1i (400 MHz) in DMSO- d_6 at room temperature.	105
Figure 28. Scheme of the possible species of <i>N</i> -acylhydrazones present in solution. Both substituents, R and R', must be aromatic but may be different from each other.	106
Figure 29. Photos at different timepoints of the stock solutions (25 mmol L ⁻¹) in 100% DMSO, used for dilution to 1% DMSO/ultra-pure water stability assays. All vials were kept at 4 °C, mimicking the conditions of storage that would be employed for the cellular assays. (A) Solutions immediately after preparation. (B) Solutions after 4 days and (C) after 14 days. Compound 1i is highlighted in red circle due to its evident change of color over time. Additionally, compound 1e was also excluded and not evaluated at 1% DMSO solution due to its known low stability under these conditions, as demonstrated in Section 5.2.4.	108
Figure 30. Structures of the 8 <i>N</i> -acylhydrazones (7 + INHHQ, which is highlighted in red) selected for the next steps of the present work.	109
Figure 31. Absorption UV-Vis spectra of 1a in 1% DMSO/H ₂ O. (A) Deconvolution of the bands in the spectrum at t_0 . Fitting was performed using the software Origin. (B) Spectra taken at regular intervals of 1 hour during the first 12 hours and then after 4 days, at room temperature.	110
Figure 32. Absorption UV-Vis spectra of 1h in 1% DMSO/H ₂ O. (A) Deconvolution of the bands in the spectrum at t_0 . Fitting was performed using the software Origin. (B) Spectra taken at regular intervals of 1 hour during the first 12 hours and then after 4 days, at room temperature.	112

- Figure 33.** Absorption UV-Vis spectra of **1f** in 1% DMSO/H₂O. **(A)** Deconvolution of the bands in the spectrum at t_0 . Fitting was performed using the software Origin. **(B)** Spectra taken at regular intervals of 1 hour during the first 12 hours and then after 4 days, at room temperature..... 113
- Figure 34.** Absorption UV-Vis spectra of **3f** in 1% DMSO/H₂O. **(A)** Deconvolution of the bands in the spectrum at t_0 . Fitting was performed using the software Origin. **(B)** Spectra taken at regular intervals of 1 hour during the first 12 hours and then after 4 days, at room temperature..... 114
- Figure 35.** Absorption UV-Vis spectra of **2d** in 1% DMSO/H₂O. **(A)** Deconvolution of the bands in the spectrum at t_0 . Fitting was performed using the software Origin. **(B)** Spectra taken at regular intervals of 1 hour during the first 12 hours and then after 4 days, at room temperature..... 116
- Figure 36.** Absorption UV-Vis spectra of **4d** in 1% DMSO/H₂O. **(A)** Deconvolution of the bands in the spectrum at t_0 . Fitting was performed using the software Origin. **(B)** Spectra taken at regular intervals of 1 hour during the first 12 hours and then after 4 days, at room temperature..... 117
- Figure 37.** Absorption UV-Vis spectra of **3d** in 1% DMSO/H₂O. **(A)** Deconvolution of the bands in the spectrum at t_0 . Fitting was performed using the software Origin. **(B)** Spectra taken at regular intervals of 1 hour during the first 12 hours and then after 4 days, at room temperature..... 118
- Figure 38.** Absorption UV-Vis spectra of **1d** in 1% DMSO/H₂O. **(A)** Deconvolution of the bands in the spectrum at t_0 . Fitting was performed using the software Origin. **(B)** Spectra taken at regular intervals of 1 hour during the first 12 hours and then after 4 days, at room temperature..... 120
- Figure 39.** Chemical shift of azomethine's hydrogen versus calculated solubility of 1-methylimidazole-containing *N*-acylhydrazones. In order to compare compounds of the same type, data regarding the protonated form of **1d**, i.e., **1d'**, were employed. 123
- Figure 40.** Wavenumber of carbonyl's stretching vibration versus calculated solubility of pyridine-containing *N*-acylhydrazones. In order to compare compounds of the same type, data regarding the protonated form of **1d**, i.e., **1d'**, were employed. 124
- Figure 41.** Hydrogen bond interactions between androgen receptor and compound **1a**..... 128
- Figure 42.** Hydrogen bond interactions between androgen receptor and lead compound **1h**..... 129
- Figure 43.** Hydrogen bond interactions between aryl hydrocarbon receptor and compound **3f**. 130
- Figure 44.** Cytotoxicity of *N*-acylhydrazones in human neuroglioma (H4) cells, at different concentrations. Dashed line represents the threshold for cell death caused by the presence of 1% DMSO. Significant differences (2-way ANOVA) are shown with (*) for $p < 0.05$ with respect to the 1% DMSO control. 135
- Figure 45.** Representative images of the inclusion pattern in transfected cells: effect of 1% DMSO control and different concentrations of hydrazones **1a**, **1d**, **1f** and **1h** in SynT inclusions. α -Syn localization is highlighted in green, while the cell nuclei are colored in blue. 137

- Figure 46.** Representative images of the inclusion pattern in transfected cells: effect of different concentrations of hydrazones **2d**, **3d**, **3f** and **4d** in SynT inclusions. α -Syn localization is highlighted in green, while the cell nuclei are colored in blue. 138
- Figure 47.** Quantification of effect of the treatments in SynT inclusions in the transfected cells, divided into the defined categories. 139
- Figure 48.** Statistical *t* test analyses, with significance level of $p < 0.05$, of the number of inclusions in each group (GraphPad Prism software). **(A)** Cells without inclusions, **(B)** cells with 1-4 inclusions, **(C)** cells with 5-9 inclusions and **(D)** cells with more than 10 inclusions. 140
- Figure 49.** Levels of Syn-T after **1d** and **1h** treatments. **(A)** Representative immunoblot showing the expression levels of SynT and GAPDH after treatment with **1d**. **(B)** Representative immunoblot showing the expression levels of SynT and GAPDH after treatment with lead compound INHHQ (**1h**). **(C)** Expression levels of Syn-T normalized to GAPDH for the treatment with both compounds. 142
- Figure 50.** Levels of Syn-T partition in Triton-X100 soluble/insoluble fractions after **1d** and **1h** treatments. **(A)** Representative immunoblot after treatment with compound **1d** showing Ponceau S staining for control purposes. **(B)** Representative immunoblot showing the levels of Syn-T in Triton-X100 soluble and insoluble fractions after treatment with **1d**. **(C)** Representative immunoblot after treatment with compound **1h** showing Ponceau S staining for control purposes. **(D)** Representative immunoblot showing the levels of Syn-T in Triton-X100 soluble and insoluble fractions after treatment with **1h**. **(E)** Triton-X100 soluble and insoluble fractions normalized to total amount of Syn-T after treatment with both compounds **1d** and **1h**. 144
- Figure 51.** Effect of the compounds' treatments on α -Syn inclusion digestion by Proteinase-K. **(A)** Representative immunoblot after treatment with compound **1d** showing Ponceau S staining for control purposes. **(B)** Representative immunoblot stained for α -Syn after 1, 3 and 5 minutes of PK digestion for each treatment with compound **1d**. **(C)** Syn-T levels normalized to samples without Proteinase K for the treatment with **1d**. **(D)** Representative immunoblot after treatment with compound **1h** showing Ponceau S staining for control purposes. **(E)** Representative immunoblot stained for α -Syn after 1, 3 and 5 minutes of PK digestion for each treatment with lead compound **1h**. **(F)** Syn-T levels normalized to samples without Proteinase K for the treatment with **1h**. 146
- Figure 52.** STD-NMR experiment. Green: ^1H spectrum of the mixture containing **1d** and aggregates of α -Syn without specific irradiation. The signals of the compound are highlighted with the (*) symbol. Blue: STD spectrum of the compound in the presence of monomers of the protein, irradiated at 0.85 ppm. Red: STD spectrum of **1d** and aggregated α -Syn, irradiated at 0.85 ppm. 148
- Figure 53.** Method of Continuous Variations for the binding of **1d** to copper(II). **(A)** Job Plot: absorbance versus molar fraction. **(B)** Selected UV-Vis spectra of molar fractions from 0.5 to 1.0 of **1d** : $\text{CuCl}_2 \cdot 2\text{H}_2\text{O}$ in 1%

- DMSO/H₂O, at room temperature. Reference: (Cukierman *et al.*, 2020).
..... 151
- Figure 54.** ¹H (400 MHz) spectra of **1d** in DMSO-d₆ in the absence (blue) and presence of 0.05 eq. (red), 0.10 eq. (green) and 0.20 eq. (purple) of copper(II) chloride dihydrate, at room temperature. Adapted from (Cukierman *et al.*, 2020).
..... 152
- Figure 55. (A)** Effect of **1d** on α-Syn-Cu²⁺ complexes. I/I₀ intensity profiles for the backbone amide resonances of 50 μmol L⁻¹ α-Syn in the presence of 1 equivalent of Cu²⁺ (blue), followed by the addition of 1 (red), 3 (purple) and 5 (green) equivalents of compound **1d**. **(B)** Effect of **1d** on the high-affinity α-Syn-Cu⁺ complex. Differences in the mean weighted chemical shift displacements (MW ¹H-¹⁵NΔCS) between free and Cu⁺-complexed α-Syn at a molar ratio of 1:1 (black), followed by the addition of 1 (red), 2 (green), 3 (purple) and 5 (blue) equivalents of compound **1d**. Insets show the chemical shift changes on the resonances of Asp2 and Phe4 residues from the metal-complexed state (black) induced by increasing levels of **1d**: 1 (red), 3 (green) and 5 (blue) equivalents. Cross-peaks colored in brown correspond to metal-free α-Syn. Extracted from (Cukierman *et al.*, 2020).
..... 155
- Figure 56.** Chemical structures of the *N*-acylhydrazones **(A)** compound **1f** (pyridine-2-carboxaldehyde isonicotinoyl hydrazone inhere called **HPCIH**) and **(B)** compound **3f** (pyridine-2-carboxaldehyde 2-furoyl hydrazone inhere called **HPCFur**). Extracted from (Cukierman *et al.*, 2019).
..... 159
- Figure 57.** Structure of the mutant human prion protein PrP₁₀₃₋₁₁₂ fragment Ac-SKPKTNMKHA-NH₂ (dMKHA). Extracted from (Cukierman *et al.*, 2019).
..... 159
- Figure 58.** NMR study of the coordination of copper(II) by dMKHA. ¹H-¹³C HSQC contour plots and ¹H NMR spectra of **(A)** dMKHA apo-form, **(B)** dMKHA + 0.1 eq copper(II) and **(C)** dMKHA + 1.0 eq copper(II). pH 7.4 at 25 °C. Extracted from (Cukierman *et al.*, 2019).
..... 161
- Figure 59.** Proposed structures for the main species present in equilibrium at pH 7.4 in the dMKHA–copper(II) system. The peptide’s main-chain is highlighted in bold grey, while the main amino acid residues involved in coordination are labelled. Reference: (Cukierman *et al.*, 2019).
..... 163
- Figure 60.** HPLC study of the oxidation of dMKHA in the presence of copper(II) and H₂O₂. **(A)** Representative chromatograms of the different studied systems after 30 min of reaction. **(B)** Ratio of products at the end of this timepoint. Extracted from (Cukierman *et al.*, 2019).
..... 165
- Figure 61.** MS/MS spectrum of **(A)** the methionine oxidized dM(O)KHA species and of **(B)** the doubly oxidized dM(O)KH(O)A product. Extracted from (Cukierman *et al.*, 2019).
..... 166
- Figure 62.** NMR study of the oxidation of dMKHA in the presence of copper(II) and H₂O₂. **(A)** A series of ¹H NMR acquired at regular intervals for 45 min, at 25 °C and pH 7.4. Inset: Peak intensities of the ε methyl hydrogens’ signal from methionine at 2.02 ppm (black) and the oxidized product formed (methionine sulfoxide) at 2.65 ppm (red). **(B)** Normalized

- intensity of the ϵ methyl hydrogens' signal from methionine at 2.02 ppm (black), in the presence of 0.1 eq (red) and 0.5 eq (blue) HPCFur (**3f**). Inset: Magnification of the methionine ϵ methyl signal intensity versus reaction time curves. Extracted from (Cukierman *et al.*, 2019). 168
- Figure 63.** Suggested interactions in the ternary system dMKHA–copper(II)–HPCFur (**3f**). **(A)** ^1H NMR titration performed for the dMKHA (5 mmol L⁻¹) : Cu²⁺ (0.5 mmol L⁻¹) : HPCFur (0.5-2.5 mmol L⁻¹) system, at 5 °C and pH 7.4. Insets: Zooms of the H $_{\epsilon 1}$ signal from H111 (left) and H $_{\epsilon}$ from M109 (right). **(B)** Proposed schematic structure for the ternary complex [Cu(H $_{-1}$ dMKHA)(HPCFur)]⁴⁺. Extracted from (Cukierman *et al.*, 2019). . 170
- Figure 64.** ESI-MS(+) spectrum of a mixture of dMKHA (5 mmol L⁻¹), Cu²⁺ (0.5 mmol L⁻¹) and HPCFur (**3f**) (2.5 mmol L⁻¹), at pH 7.4. The ternary species [Cu(H $_{-1}$ dMKHA)(HPCFur)Cl]³⁺ is observed at m/z 499.32. Extracted from (Cukierman *et al.*, 2019). 171
- Figure 65.** Representative images of the stress granules pattern in HEK cells: effect of positive and negative controls. TIA1 is shown in red, while the cell nuclei are colored in blue. 173
- Figure 66.** Representative images of the stress granules pattern in HEK cells: effect of different concentrations of compound **1a**. TIA1 is shown in red, while the cell nuclei are colored in blue. 174
- Figure 67.** Representative images of the stress granules pattern in HEK cells: effect of different concentrations of lead compound **1h** (INHHQ). TIA1 is shown in red, while the cell nuclei are colored in blue. 175
- Figure 68.** Representative images of the stress granules pattern in HEK cells: effect of different concentrations of pyridine-2-carboxaldehyde-derived compounds **1f** and **3f**. TIA1 is shown in red, while the cell nuclei are colored in blue. 175
- Figure 69.** Representative images of the stress granules pattern in HEK cells: effect of different concentrations 1-methylimidazole-containing compounds **1d**, **2d**, **3d** and **4d**. TIA1 is shown in red, while the cell nuclei are colored in blue. 176

List of Tables

Table 1. Synthetic conditions, yields and melting points for the synthesized <i>N</i> -acylhydrazones.....	51
Table 2. Amount of reagent per well for each type of plate used in the transfection assays.....	59
Table 3. Calculated descriptors of pharmacological relevance for the 55 <i>N</i> -acylhydrazones studied. Red color indicates results that do not fit into the reference values for BBB crossing. Lead compound 1h is highlighted in blue color, while the compounds that presented no violations of the reference values are shown in gray.....	67
Table 4. (Continuation of Table 3). Calculated descriptors of pharmacological relevance for the 55 <i>N</i> -acylhydrazones studied. Red color indicates results that do not fit into the reference values for BBB crossing. Lead compound 1h is highlighted in blue color, while the compounds that presented no violations of the reference values are shown in gray.....	68
Table 5. Reference values for the pharmacological descriptors.....	69
Table 6. Crystal data and refinement parameters for compounds 1c and 1c'	76
Table 7. Selected bond distances and angles for compounds 1c and 1c'	78
Table 8. ¹ H (400 MHz) data for compounds 1c and 1c' in DMSO- <i>d</i> ₆ at room temperature.....	82
Table 9. Crystal, data collection and refinement parameters for compounds 1d' , 2d , 3d and 4d	87
Table 10. Selected geometric parameters for compounds 1d' , 2d , 3d and 4d	88
Table 11. Hydrogen bond geometric parameters for compounds 1d' , 2d , 3d and 4d	90
Table 12. π - π stacking geometric parameters for compounds 2d , 3d and 4d	91
Table 13. Calculated and experimental elemental analyses of the 1-methylimidazole-derived compounds 1d , 1d' , 2d , 3d and 4d	92
Table 14. Selected infrared frequencies of compounds 1d , 1d' , 2d , 3d and 4d , along with their assignments. Samples were prepared as KBr pellets.....	93
Table 15. Comparative ¹ H (400 MHz) signal attribution for the 1-methyl-1H-imidazole-2-carboxaldehyde-derived compounds (i.e. compounds 1d , 1d' , 2d , 3d and 4d), in DMSO- <i>d</i> ₆ solution at room temperature.....	98
Table 16. Selected infrared frequencies of compounds 1f and 3f , along with their assignments. Samples were prepared as KBr pellets.....	100
Table 17. Comparative ¹ H (400 MHz) signal attribution for compounds 1f and 3f in DMSO- <i>d</i> ₆ , at room temperature.....	103
Table 18. Comparative ¹ H (400 MHz) hydrazonic azomethine and -NH attribution for all the synthesized compounds, in DMSO- <i>d</i> ₆ solution at room temperature.....	107

Table 19. Comparison between experimental and calculated partition coefficient values (log P and cLogP) for the studied *N*-acylhydrazones. 122

Table 20. Toxic Potential (TP) classification over the binding affinity of the tested compound for 16 selected proteins. Extracted from the OpenVirtualToxLab™ User and Reference Manual – Version 5.8, freely available at <http://www.biograf.ch/downloads/VirtualToxLab.pdf>..... 125

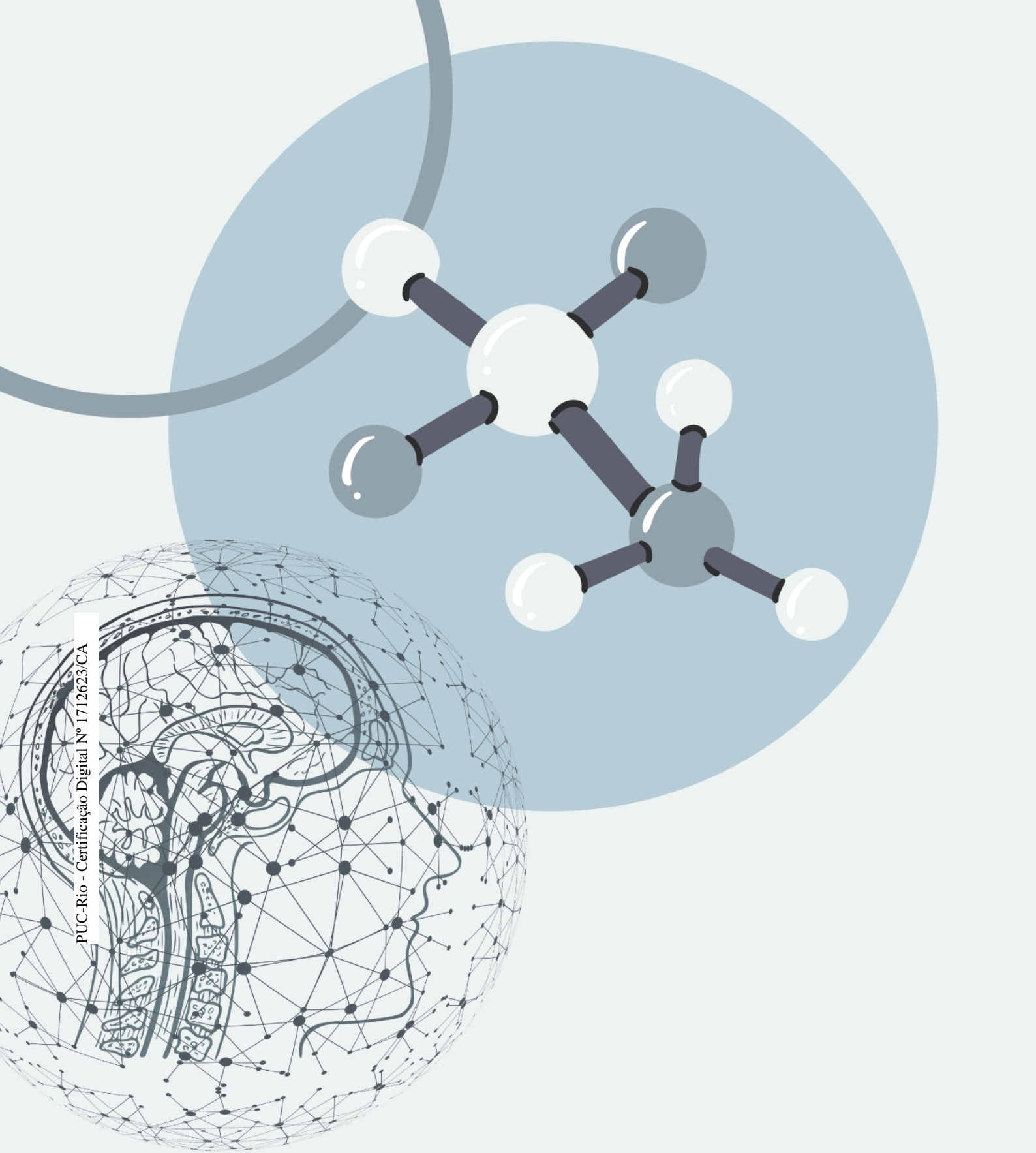
Table 21. Affinity constant (K_d) values, in $\mu\text{mol L}^{-1}$, calculated for the binding of the 8 *N*-acylhydrazones to each of the 16 proteins – OpenVirtualToxLab™. Red color indicates elevated predicted toxicity, which was only observed for compound **1a**..... 131

List of Appendix Figures

Appendix Figure 1. TG and dTG curves of polycrystalline solid 1a	210
Appendix Figure 2. Mid-infrared spectrum of compound 1a	210
Appendix Figure 3. Mid-infrared spectrum of compound 1c	211
Appendix Figure 4. Mid-infrared spectrum of compound 1c'	211
Appendix Figure 5. TG and dTG curves of polycrystalline solid 1d	212
Appendix Figure 6. TG and dTG curves of single crystals of compound 1d'	212
Appendix Figure 7. TG and dTG curves of single crystals of compound 2d	213
Appendix Figure 8. TG and dTG curves of single crystals of compound 3d	213
Appendix Figure 9. TG and dTG curves of single crystals of compound 4d	214
Appendix Figure 10. Mid-infrared spectrum of compound 1d	214
Appendix Figure 11. Mid-infrared spectrum of compound 1d'	215
Appendix Figure 12. Mid-infrared spectrum of compound 2d	215
Appendix Figure 13. Mid-infrared spectrum of compound 3d	216
Appendix Figure 14. Mid-infrared spectrum of compound 4d	216
Appendix Figure 15. TG and dTG curves of compound 1f	217
Appendix Figure 16. TG and dTG curves of compound 3f	217
Appendix Figure 17. Mid-infrared spectrum of compound 1f	218
Appendix Figure 18. Mid-infrared spectrum of compound 3f	218

“I believe things cannot make themselves impossible.”

Stephen Hawking (1942-2018)



PUC-Rio - Certificação Digital Nº 1712623/CA

INTRODUCTION

1. Introduction

1.1. Protein aggregation and disease

Proteins are one of the most important class of biomolecules, constituted by chains of amino acid residues, performing different, life-essential functions in the organisms. Structural, catalytic, metabolic and transportation roles are within these vital tasks. The primary (amino acid sequence and eventual disulfide bridges), secondary (local organization), tertiary (spatial long-range conformation), and quaternary (when more than one subunit is present) structures of a protein are fundamental for its correct activity (Nelson, 2005).

Conformational instability in a protein's structure can result in its partial unfolding and aggregation due to hydrophobic interactions and inter- amino acid hydrogen bonds characteristic of the β -sheet conformation (Kopito and Ron, 2000). Usually, chaperones are able to prevent misfolding of proteins through the shielding of the hydrophobic amino acid residues that may be exposed during natural folding and are likely to aggregate. Protein aggregation is one of the most biologically relevant processes that lead to protein instability, which, in turn, is associated to a variety of diseases.

When proteins aggregate through the adoption of non-native conformations, many copies of the protein are joined together forming large fibrils, often losing their usual role and exerting a pathological function in the body, affecting nearby organs and tissues. Intracellular aggregates of proteins in wrong, non-native forms are frequently called inclusion bodies. These inclusions are often characterized as amyloids, when presented as elongated, β -sheet-rich fibers. This name comes from an old mistake of identification, based on the iodine staining technique, of a substance as starch (*amylum* in Latin), by Rudolph Virchow. It is now known, through Congo red staining, that amyloids look pink under normal light and present green birefringence under polarized light, which separates them from other types of protein aggregates (Kyle, 2001). Other techniques can be employed to identify amyloid through the analysis of the secondary structure of proteins, such as circular dichroism, infrared and Raman vibrational spectroscopies. The classical histopathological definition of an amyloid is an extracellular β -sheet protein

deposit, aligned in an antiparallel way. Together, these sheets can form rigid, non-branching mature fibrils that usually cannot be broken down through proteolysis and cause oxidative stress in the affected organs (Merlini and Bellotti, 2003). It has, however, already been recognized that amyloids can also occur intracellularly (Fändrich, 2007). Furthermore, the Amyloidosis Nomenclature Committee of the International Society of Amyloidosis (Benson *et al.*, 2018) agreed on a more general definition of the word “amyloid”, to avoid its usage for describing only pathological deposits of specific fibrillary protein aggregates. Nowadays, the term “amyloid fibril” is employed for any cross β -sheet fibril, and a new term, “functional amyloid”, has been introduced, since these β -sheet structures have been assigned to many other purposes as well (Benson *et al.*, 2020).

Protein misfolding is a thermodynamically favored process, driven by the reduction in the free energy of the organized system, due to the lessening of the contact between the hydrophobic residues and the solvent. Although there is still great divergence in the literature regarding the native conformations, rates and ideal concentrations and conditions, the main features of the amyloidogenic aggregation are quite similar between the various proteins. The process is described as a nucleation-elongation polymerization, and is highly dependent on the initial protein concentration, pH, temperature, presence of metal ions and of pre-aggregated proteins that can act as seeds (Nielsen *et al.*, 2001; Sabaté *et al.*, 2003; Chiti and Dobson, 2006). Most of the mechanisms start with chemical or physical perturbations in the native conformation of the protein that produce partially folded intermediates, which present great propensity towards aggregation. These intermediates promote the aggregation of the monomers into dimers and soluble oligomers in the so-called nucleation phase, through intermolecular associations. The oligomeric species are usually rich in β -sheet structures that rapidly convert them into high molecular weight structures, the protofibrils, during the exponential growth stage. Protofibrils eventually become elongated structures, sometimes characterized as mature amyloids, in the stationary phase (Theillet *et al.*, 2014). The determining step in most of these processes is the early formation of oligomeric species, which act as promoters of aggregation, from which the fibrils and protofibrils grow in a nucleation-dependent way. Figure 1 summarizes the described aggregation process.

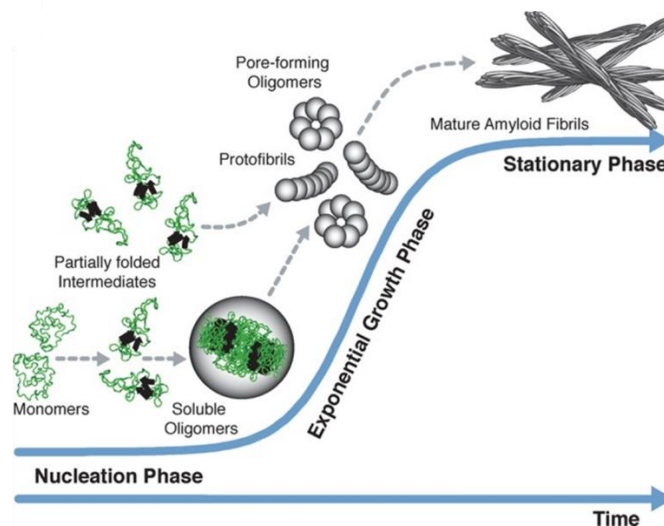


Figure 1. The aggregation process of proteins. Adapted from (Theillet *et al.*, 2014).

Several amyloid-forming proteins and polypeptides are known and are currently associated with a number of human diseases, known as amyloidoses, having a key role, mainly, in neurodegenerative disorders. However, the terminology amyloidosis is nowadays only used for a limited number of localized deposits. Other diseases, which have been described as presenting amyloid or other amyloid protein aggregates (such as cytotoxic oligomers and protofibrils) are not yet included in such terminology. Known example of such pathologies are Alzheimer's and Parkinson's diseases (AD and PD, respectively), as well as type 2 diabetes. Although there is strong evidence that specific proteins may be involved in their pathogenesis, these diseases are rarely called localized amyloidoses because the central role of the proteinaceous components in the development of the disease has not yet been fully proven. Another important factor is that the oligomeric aggregates, rather than mature fibrils themselves, may be the central species in pathogenesis (Benson *et al.*, 2020).

Some proteins also aggregate in a non-amyloid, but still pathological way, which is the case for γ D-crystallin protein in cataracts disease. Amorphous aggregates are usually seen as granular structures, being composed by disordered protein chains, even though some regions are β -sheet rich (Morell *et al.*, 2008). The different types of inclusions cannot be distinguished through regular light microscopy, being necessary, therefore, a clinical pathological analysis in order to

identify the type of protein involved, since the current treatment of the various diseases differ widely depending on the protein and region implicated.

Although some diseases may have certain cellular and molecular mechanisms in common, including protein aggregation and the formation of inclusion bodies, there are particularities and unique features of each pathology, such as the areas affected, or the proteins involved in the aggregation process.

Neurodegenerative diseases are the group of pathologies characterized by the progressive dysfunction and death of neurons (Dugger and Dickson, 2017). Until a few years ago, they were classified according to their clinical presentation, separating: 1) diseases in which dementia is the main clinical manifestation (such as Alzheimer's disease); 2) diseases that, although they may present dementia, are characterized by a predominant clinical feature involving movement disorders (such as Parkinson's and Huntington's diseases and progressive supranuclear palsy); and 3) diseases that present exclusively movement disorders (such as spinocerebellar ataxias). From a neuropathological point of view, these diseases have in common the selective and progressive loss of neurons in one or more anatomical regions of the central nervous system (CNS), bilaterally and symmetrically, being nowadays classified according to the most affected region: cerebral cortex, basal ganglia, spinocerebellar system and motor neurons. The existence of combined forms is very usual (Przedborski *et al.*, 2003). A common feature of all neurodegenerative disorders is that only a few areas, considered vulnerable, are affected by neurodegeneration, but not the brain as a whole. It is, up until now, recognized that a definitive diagnosis can only be obtained through an autopsy, although many efforts have been recently made to determine a biomarker for such diseases (Bachli *et al.*, 2020).

It is important to highlight the increasing pathological evidence that neurodegenerative diseases could actually be copathologies, characterized as mixed aggregopathies (Nguyen *et al.*, 2021).

Aggregopathies, however, include other degenerative diseases that do not specifically affect the brain, such as the non-amyloid aggregation of γ D-crystallin in cataracts disease and the amyloidosis type 2 diabetes *mellitus* (T2DM). The latter is characterized by the aggregation of the hormone amylin, or islet amyloid

polypeptide (IAPP), which is secreted by the β -cells in the pancreas (Marzban *et al.*, 2006; Westermarck *et al.*, 2011). Although our research group has started new projects on these non-neurodegenerative aggregopathies as well, the focus of our research lies in the most common neurodegenerative disorders Alzheimer's and Parkinson's diseases. Some work on prion diseases is also underway.

1.2. Alzheimer's disease

Alzheimer's disease (AD) is a neurodegenerative condition that currently represents the most common form of dementia in the elderly. The German psychiatrist and neuropathologist Alois Alzheimer published the first study describing this disease more than a century ago, reporting symptoms of memory loss, paranoia, behavioral and language problems, as well as atrophied brain and signs of anomalous protein deposition in this organ (*post mortem* observations), which were later called senile plaques and neurofibrillary tangles (Alzheimer, 1907).

Briefly, AD is characterized by the impairment of the patients' cognitive functions, which becomes more severe with age and disease progression. AD is commonly known to cause the loss of the patient's recent memory, which is usually the first affected function. However, disease progression can also affect other everyday cognitive abilities, such as the capacity to perform calculations and to operate simple objects and tools (Small *et al.*, 1997).

The neuropathology of AD is characterized by neurovascular degeneration, diffuse cortical atrophy, neuronal and synaptic losses involving various neurotransmission systems, the presence of extracellular senile plaques composed of filaments of the β -amyloid protein (A β) and intracellular neurofibrillary tangles, mainly formed by the hyperphosphorylated tau protein (Serrano-Pozo *et al.*, 2011). Some of these brain alterations can also be observed in healthy elderly brains, but at much lower intensity (Smith, 1999). From a biochemical point of view, AD is characterized by generalized oxidative stress in the brain, neuroinflammation, calcium dysregulation, synaptic toxicity, A β peptide oligomerization and metal disbalance.

Since the original description of AD, the development of intraneuronal and extracellular filamentous lesions, known as dystrophic neurites, has been recognized. Neurofibrillary tangles are abnormal aggregates of cytoplasmic fibers that occur in neuronal cell bodies. Another important histopathological characteristic of AD is the widespread presence of plaques and aggregates, mainly formed by the A β peptide, in the extracellular portion of the brain tissue (Jenkins *et al.*, 1988; Selkoe, 1996; Nie *et al.*, 2011). Figure 2 shows a scheme that differentiates a healthy neuron from a characteristic neuron of the pathology and such inclusions can be visualized. The A β peptide is commonly considered essential in the development of AD and is at the center of the amyloid cascade hypothesis, which postulates that the A β peptide and/or the cleavage products of its precursor protein, the amyloid precursor protein (APP), are neurotoxic and can lead to the formation of senile plaques, causing cell death (Hardy and Higgins, 1992).

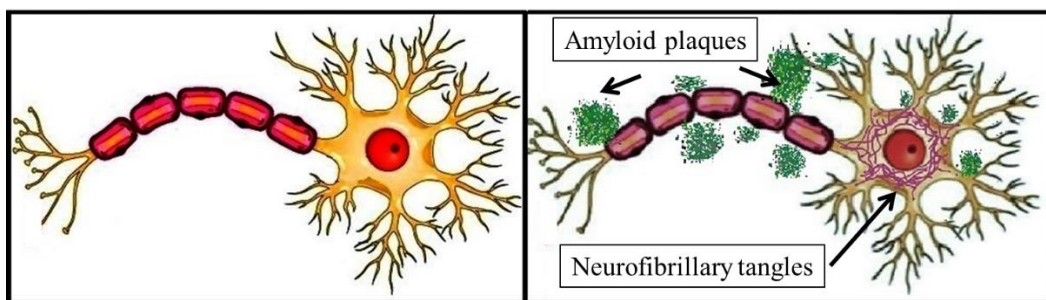


Figure 2. Schematic differences between a healthy neuron (left) and a neuron from an AD patient (right). Extracellular amyloid plaques and intracellular neurofibrillary tangles can be observed. Adapted from (De Falco *et al.*, 2016) and reproduced with the author's approval.

APP can be cleaved at different sites, yielding fragments of diverse sizes, the most important ones with 40 and 42 amino acid residues, A β ₁₋₄₀ and A β ₁₋₄₂. Although the former is the most common, the latter is more hydrophobic and has greater amyloidogenic potential. Both are capable of aggregating and originating oligomers, protofibrils, fibrils and insoluble plaques (Soreghan *et al.*, 1994).

The A β peptide is found in different forms in the brains of patients with AD, each with their own specific properties (Citron *et al.*, 1992; Nitsch *et al.*, 1993; Saido *et al.*, 1995; Selkoe, 1996; Mattson, 1997; He and Barrow, 1999). Soluble A β seems to be the first form of peptide accumulation (Tabaton *et al.*, 1994), being

found as monomers and also as oligomers (composed of dimers, trimers and so on). The structure of A β may adopt different conformations, giving rise to a large amount of oligomeric species (Moore *et al.*, 2011). The peptide can also form protofibrils, structures of intermediate order between oligomers and mature fibrils, present in the senile plaques (Gandy, 2005). Once the extracellular aggregates are formed, an inflammatory response is induced and there is damage to the cells of the cholinergic system, related to the learning and memory processes (Deutsch, 1971).

The oligomeric hypothesis of AD is based on the amyloid cascade hypothesis, specifying that soluble A β oligomers are the most toxic form of aggregates (Klein *et al.*, 2001; Kaye *et al.*, 2004). In its reactive oligomeric form, A β immediately damages the neuronal synapses, leading to cell death. The same does not occur with A β fibrils (Lambert *et al.*, 1998).

Regarding the intracellular neurofibrillary tangles, these are formed by another protein, called tau, associated with microtubules' stabilization (Lee, 1995). This protein undergoes hyperphosphorylation in the AD scenario, becoming insoluble and aggregating into fibrils and tangles that may eventually lead to the death of neurons (Selkoe, 1996; Iqbal *et al.*, 2005; Craddock *et al.*, 2012; Hong-Qi *et al.*, 2012; Selkoe *et al.*, 2012). Several studies point to a relationship between A β accumulation and hyperphosphorylation of the tau protein (Busciglio *et al.*, 1995; Selkoe, 1996; Zheng *et al.*, 2002; Lloret *et al.*, 2011; Hu *et al.*, 2014; Stancu *et al.*, 2014; Annamalai *et al.*, 2015). However, the mechanisms behind this association are still poorly understood.

Based on the different molecular hypotheses of AD, the treatment approaches for this disease are remarkably diverse. Several clinical studies have been conducted over the years to find a treatment for the pathology, but currently there is neither a cure, nor a truly effective treatment for AD. However, there are medications that can partially control some of its symptoms. For example, memantine, the last small molecule-based drug approved by the Food and Drug Administration of the United States (FDA), is used to treat symptoms of AD in moderate to severe stages by regulating glutamate activity, an important neurotransmitter involved in learning and memory whose receptor, NMDA (*N*-methyl-D-Aspartate), is damaged in AD (Molino *et al.*, 2013). On the other hand,

acetylcholinesterase inhibitory drugs, which retard the metabolic degradation of acetylcholine, can help delay the progression of cognitive dysfunction and may be effective for some patients in the initial and intermediate stages of the disease (Anand and Singh, 2013). Examples of approved drugs from this class are rivastigmine and donepezil. In addition to the currently available medications that treat the symptoms of AD, there is also a common prescription of drugs for the control of depression (Lyketsos *et al.*, 2000) and vitamin E, a natural antioxidant that can protect brain cells and other body tissues from oxidative damage (Barnes and Yaffe, 2005).

Furthermore, researchers are also trying to limit the accumulation of A β in tissues by reducing its production, but this approach has proved difficult in practice. Nevertheless, recently Wang and collaborators (Zhao *et al.*, 2020) described a small molecule capable of inhibiting the γ -secretase cleavage of APP, decreasing the production of A β ₁₋₄₀ and A β ₁₋₄₂ in a dose dependent way.

1.3. Parkinson's disease

Parkinson's disease (PD) is a chronic and progressive neurological condition that affects an increasing number of people around the world and is currently the second most frequent neurodegenerative disease, after AD. Approximately 60,000 people are diagnosed every year in the United States (Parkinson's-Disease-Foundation, 2016). This age-related neurodegenerative disorder is characterized by motor and non-motor manifestations and is commonly associated with tremor. However, apart from the resting tremor, PD is also characterized by rigidity, bradykinesia or movement slowness, gait disturbance, postural instability, sleep disorder, loss of smell and constipation. In fact, bradykinesia is the main manifestation of PD, which can exist without the well-known tremor. There are also some other neurodegenerative disorders related to PD, such as Lewy body dementia, corticobasal degeneration and multiple-system atrophy, which are called parkinsonian syndromes.

From a pathological point of view, degeneration of dopaminergic neurons in the *substantia nigra pars compacta* is observed, coupled with cytoplasmic inclusions known as Lewy bodies and Lewy neurites containing the presynaptic

protein α -synuclein (α -Syn) (Spillantini *et al.*, 1997; Olanow and Tatton, 1999). In addition to the cardinal motor features, cognitive impairment and dementia have been reported, as a result of a multisystem/multineurotransmitter dysfunction that involves deficits in the cholinergic, noradrenergic and serotonergic systems, along with the well-known disturbance in the motor-related dopaminergic system (Aarsland *et al.*, 2005). Currently, the clinical diagnosis is related to the observation of a good response to the use of dopaminergic drugs. Neuropathological diagnosis requires the detection of marked neuronal loss in the *substantia nigra pars compacta*, as well as the presence of Lewy bodies, observed as eosinophilic inclusions, consisting of a dense nucleus surrounded by a pale halo of radial filaments, as can be seen in Figure 3 (Alexander, 2004).

The loss of these dopaminergic neurons has been observed early in the disease's timeline progression, which suggests that degeneration starts before the manifestations of the motor symptoms. Apart from the CNS, inclusion bodies have also been found in the neurons of the enteric nervous system (ENS), which is a division of the nervous system that controls the function of the gastrointestinal tract. The idea that PD could start in the gut before spreading to the brain has gotten new supporting evidence. A recent study showed lower rates of incidence of the disease in patients who had undergone a truncal vagotomy, which is an operation that removes sections of the nerve that links the digestive tract with the brain (Liu *et al.*, 2017). These preliminary evidences are in accordance with the fact that the vast majority of PD patients present gastrointestinal symptoms, such as constipation, that usually start decades before the motor manifestations of the disease.

Although the role of Lewy bodies in the pathogenesis of PD remains inconclusive, the discovery of denatured α -Syn as an important component of these inclusions has led to the proposition that this protein plays a relevant role in the processes that lead to neuronal loss. Besides protein misfolding, oxidative stress may also contribute to the observed neuronal degeneration (Blesa *et al.*, 2015).

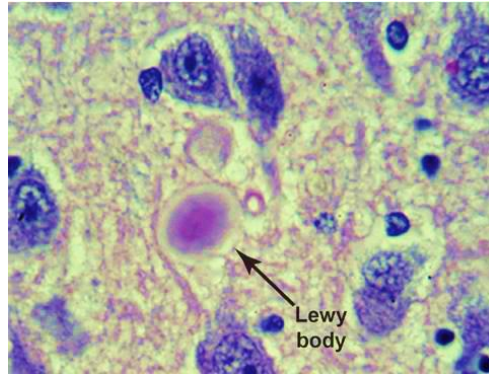


Figure 3. Lewy body inclusion in neuronal cells. Obtained from <http://whatislyme.com/lewy-body-dementia-putting-the-puzzle-pieces-together/>, accessed on 08/11/2017.

α -Syn is a highly soluble, intrinsically disordered protein, with 140 amino acid residues, abundant in the CNS and widely expressed in presynaptic terminals in the proximity of synaptic vesicles (Cheng *et al.*, 2011), which suggests a physiological role in the regulation of synaptic transmission, although it is still not known if this mechanism occurs through monomers or oligomers of the protein. It has been demonstrated that α -Syn exists predominantly as unfolded monomers in the CNS (Fauvet *et al.*, 2012), and that it undergoes post-translational *N*-terminal acetylation, adopting a compact α -helical conformation, in which the regions that are critical for the spontaneous assembly into oligomers are not exposed (Theillet *et al.*, 2016). On the other hand, different sizes of α -Syn oligomers have been observed in PD patients' brains, in much higher levels when compared to healthy individuals (Ingelsson, 2016). In addition to that, elevated amounts of oligomeric α -Syn have been described in the cerebrospinal fluid (CSF) of PD patients (Park *et al.*, 2011).

Post-translational modifications (PTMs) are related to the diversity of chemical alterations that occur in a protein's structure during or after its biosynthesis (translation of mRNAs). This phenomenon is important because it gives rise to a bigger protein catalogue than that which can be obtained with the 21 encoded amino acid combination. This is achieved through the cleavage, modification, or the covalent addition of specific functional groups in the protein's structure. Some sites are more prone to suffer PTMs due to the presence of nucleophiles such as the hydroxyl, amine and thiolate groups, as well as carboxylates and the *N*- and *C*-termini (Uversky *et al.*, 2013).

Apart from *N*-terminal acetylation, another PTM that occurs to α -Syn and that is directly related to its oligomerization is protein glycation, an unavoidable age-associated alteration. Since neurons need a lot of sugar to function, it is inevitable that these substances react with α -Syn's lysines in the *N*-terminal region. Glycation has proved to promote α -Syn oligomerization and leads to increased cell loss (Vicente Miranda *et al.*, 2017). It is important to note that glycation does not cause PD, but it constitutes a risk factor for some people with higher glucose levels.

Although the mechanism by which α -Syn initiates neuronal death is still elusive, it is certain that the amyloidogenic aggregation of this protein is critical to the pathological effects associated with PD.

In 1957, Dr. Arvid Carlsson proposed the use of levodopa (L-dopa), a precursor of dopamine, for the treatment of the symptoms of PD. In 2000, he was awarded a Nobel Prize for the first description of levodopa therapy in PD. L-dopa is converted to dopamine by dopa decarboxylation in the brain, restoring dopamine levels. This process can also occur outside the blood-brain barrier (BBB), inducing side-effects such as nausea and postural hypotension. The addition of peripheral decarboxylase inhibitor that does not cross the BBB, such as carbidopa, avoids the unwanted effects. Patients with typical Parkinson's disease usually respond to L-dopa treatment immediately. On the other hand, there is usually a long-term effect for patients who present resistance to the drug, which is usually related to the wearing-off phenomenon, delayed response, early morning akinesia, pain, depression, nightmares and hallucination.

Another class of drugs are also used in PD therapy, which are the inhibitors of monoamine oxidase B (MAO-B). These drugs hinder the activity of this enzyme, which is to degrade monoamines such as noradrenaline, serotonin and dopamine as well, and are also employed for depression treatment. MAO-B inhibitors, when used as a monotherapy, usually delay the need for L-dopa treatment. When combined, it reduces the off-time of levodopa, showing improvement in motor-related symptoms (Dezsi and Vecsei, 2017). However, MAO-B inhibitors present a vast list of drug and food interactions, which normally hold back their prescription.

Both L-dopa and MAO-B inhibitors consist of treatments to relieve the symptoms and are not a cure for the disease, though they have substantially improved the quality of the patients' lives and led to a reduction in mortality (Chaudhuri *et al.*, 2011).

1.4. Prion diseases

Prion diseases constitute a group of disorders caused by the so-called prions which, in turn, mean proteinaceous infectious particles. These are crumbs of misfolded protein that are known as infectious due to their ability to cause other proteins to misfold and spread. In humans, the most common prion diseases are the fatal neurodegenerative conditions Creutzfeldt-Jakob disease, fatal familial insomnia, Gertsmann-Straussler-Scheinker syndrome and kuru (Prusiner, 1982; Geschwind, 2015). These are all caused by slightly different forms of the same protein, known as prion protein (PrP).

The physiological, cellular prion protein, usually denoted PrP^C, is a cell surface glycoprotein highly expressed in the central and peripheral nervous system. PrP^C is composed of 209 amino acids, presenting the residues 23-231 from the original translation product that contains 253 amino acids. The peptide 1-22 is cleaved during trafficking and residues 232-253 are replaced by a saccharide moiety (Riesner, 2003). PrP^C is divided in two regions of different structural properties. In mammals, the *N*-terminus (until residue 120) consists of unstructured octapeptide PHGGSWGQ repeats that can bind divalent metal ions such as copper(II) (Viles *et al.*, 1999). The *C*-terminus (residues 121-231), on the other hand, is composed of three α -helixes and a double-stranded antiparallel β -sheet (Riek *et al.*, 1996). The physiological role of PrP^C is still unclear, although it is proposed that it is involved in several functions in the central and peripheral nervous systems. Evidences point to its interaction with a variety of binding partners, which suggests that PrP^C can modulate some processes such as memory and inflammatory reactions, cellular functions like proliferation and differentiation, as well as controlling a number of transduction signaling pathways (Linden *et al.*, 2008). PrP^C has also been implicated in cellular copper homeostasis or copper-dependent enzymatic functions (Brown, 2001), although the physiological relevance of PrP binding to this metal

remains mostly speculative. On the other hand, the confirmation of such a large number of functions, as described in the literature, seems improbable, highlighting the need for rigorous assessments (Wulf *et al.*, 2017).

In pathology, PrP^C misfolds into the insoluble scrapie prion protein (PrP^{Sc}), presenting β -sheet rich content and proteinase resistance (Pan *et al.*, 1993; Prusiner, 1998). The hypothesis that the infectious feature of such diseases depends solely on this conversion is called “protein-only hypothesis” or, more recently, prion hypothesis (Prusiner, 1998).

Although rare, prion diseases cause a rapid cognitive decline through the death of specific neurons, being mostly deadly within months from the first symptoms’ manifestation (Cdc, 2018). Due to the infectious nature of prions, prion diseases can be acquired. This means that a person can be infected through the exposure to contaminated material such as surgical instruments, transplants of dura matter and contaminated tissue. This last was the case for the famous epidemic of kuru in Papua New Guinea, in which the disease was passed from person to person through their ritual cannibalistic culture. It was also the issue in the mad cow disease outbreak in the 1990s UK, in which the disease was passed from cow (bovine spongiform encephalopathy) to humans (Creutzfeldt-Jakob disease) through contaminated flesh (Who, 2004).

However, acquiring prions is the least common form of developing prion diseases, accounting for less than 1% of the cases. In this sense, genetic mutations are estimated to be responsible for around 15% of the reports, while the sporadic form, far more common, adds up to almost 85% (Cjd-Foundation, 2021).

Prion diseases can be quite different from each other, affecting several areas of the brain, thus causing distinct cognitive, behavioral and motor symptoms, as well as striking people at various age ranges. As for other neurodegenerative disorders, there is no cure for prion diseases. Available treatments are focused on providing supportive care in the form of assistance to daily activities, controlling hydration and nutrients, and medicating for pain relief, depression and muscle spasms (Cdc, 2019).

1.5. Metals and aggregopathies

The importance of metal ions to vital functions of living organisms has been already recognized for several years, fueling the research in the field of bioinorganic chemistry. Metals in biological systems can exert several roles such as structural functions, electron and oxygen transportation and reaction catalysis. For example, the transport of oxygen in our body is only possible because this molecule binds to the hemoglobin iron, forming a coordination complex known as oxyhemoglobin. Other metals, such as copper and zinc, are also essential for life as they play key roles in enzyme systems. Around one third of the enzymes in the human body have at least one metal ion in their structure. More specifically in the brain, transition metals play fundamental roles in neurotransmission and synaptic signaling.

An essential element is one that is fundamental for the living being's normal metabolism, and it cannot be substituted efficiently for another element. The essential element exists in an optimal range of concentration in the organism, and an excess or a deficiency can lead to harmful effects and dysfunction, respectively. A deficiency of copper in our body, for example, can lead to impaired production of energy, abnormal metabolism of glucose and cholesterol, and iron accumulation in tissues, among other effects. On the other hand, an excess of this metal is associated with oxidative stress and can be toxic to cells and tissues (Harris, 2003). Thus, it is important to maintain each metal ion's normal concentrations and distribution throughout the body, in order to have a healthy, functional organism.

The brain is an organ that concentrates metal ions whose levels increase as a consequence of healthy aging (Gaggelli *et al.*, 2006; Kozłowski *et al.*, 2006). Several studies indicate that metal dyshomeostasis may play an important role in a variety of age-related neurodegenerative disorders (Gaeta and Hider, 2005; Bolognin *et al.*, 2009). This has led to the proposition that abnormal metal interactions with different specific proteins in various neurodegenerative disorders may be one of the main elements contributing to their etiologies, a postulate currently known as the metal hypothesis.

Quite a few studies have already highlighted the role of endogenous metal ions in AD. It is suggested that such ions, particularly copper(II) and zinc(II), may contribute to A β aggregation, affecting either the kinetic of the process, or the morphology of the aggregates (Deibel *et al.*, 1996; Huang *et al.*, 2004; Tōgu *et al.*,

2008; Azimi and Rauk, 2011; Craddock *et al.*, 2012; Hane *et al.*, 2013; Hane and Leonenko, 2014). Both ions have been shown to increase the rate of aggregation of the synthetic A β peptide through the binding of histidine residues (Bush *et al.*, 1994; Huang *et al.*, 1997; Miura *et al.*, 2000; Yang *et al.*, 2000). In addition, it is important to note that copper(II) and zinc(II) are poorly distributed in the CNS of patients with AD (Smith *et al.*, 1998; Faller and Hureau, 2012).

The aggregation of A β monomers can occur through the dimerization of the peptide, which can be mediated by the presence of these biometals, forming small A β -Cu or A β -Zn oligomers that may eventually form larger aggregates. Because they exhibit a coordination chemistry with certain similarities, zinc and copper compete for the same A β residues. The first metal is more relevant regarding the speed of aggregation, whereas the latter mainly induces the production of reactive oxygen species (ROS) (Hoernke *et al.*, 2010; Marino *et al.*, 2010).

Regarding PD's physiopathology, the role of metal ions in α -Syn's aggregation process has also become a pertinent enquiry (Dexter *et al.*, 1991; Tabner *et al.*, 2005; Barnham and Bush, 2008). PD patients exhibit elevated amounts of copper both in their cerebral spinal fluid (CSF) and in blood serum, while this metal's levels are reduced in the *substantia nigra*, which constitutes an example of the dyshomeostasis mentioned above (Pall *et al.*, 1987; Davies *et al.*, 2014). The high copper concentrations in CSF are positively correlated with increased oxidative stress and protein conformational changes, as well as with disease severity. The deficiency of copper in the *substantia nigra*, on the other hand, is associated to an impaired expression of CTR1, leading to compromised copper transport in disease, which, in turn, affects SOD1 activity in regulating the removal of ROS. Regarding iron, analyses show elevated amounts in the *substantia nigra pars compacta*, the most affected region of the brain with respect to neuronal loss, providing an environment susceptible to oxidative damage (Zecca *et al.*, 2004). Moreover, both copper and iron promote *in vitro* misfolding and pathological intracellular α -Syn aggregation, a recognized PD histological hallmark (Paik *et al.*, 1999; Rasia *et al.*, 2005).

An analysis of the parkinsonian *substantia nigra* has also revealed elevated amounts of zinc (Dexter *et al.*, 1991) which is able to bind to α -Syn (Moons *et al.*, 2020). However, although this metal ion is able to accelerate *in vitro* fibrillation of the protein, it presented lower affinity for α -Syn when compared to other

amyloidogenic proteins such as the A β peptide and IAPP, which puts in check the actual biological relevance of zinc in the pathogenesis of PD (Valiente-Gabioud *et al.*, 2012). Copper, on the other hand, presents high affinity binding to α -Syn, leading to highly efficient aggregation and selective fibrillation (Paik *et al.*, 1999; Wright *et al.*, 2009).

Since copper is predominantly present in its reduced form, Cu(I), inside the cells, both copper(II) and copper(I) interactions with α -Syn have been intensely characterized (Moriarty *et al.*, 2014; Miotto *et al.*, 2015). *N*-terminal acetylation of α -Syn abolishes Cu(II) binding at the high-affinity Met1 site present in the nonacetylated protein and maintains Cu(II) interactions around His50/Asp121 (Moriarty *et al.*, 2014). Cu(I) binding occurs at three independent, non-interacting sites: Met1/Met5, His50 and Met116/Met127 residues.

Copper and iron, having an available redox chemistry, actively participate in electron transfer reactions in biological systems (Kozlowski *et al.*, 2006). However, although redox cycling is an important feature for the regular activity of some metalloenzymes, it is also involved in the generation of ROS (Jomova *et al.*, 2012). Since metal ions are implicated both in the production and in the regulation of ROS, maintenance of their normal distribution is fundamental for healthy aging. In fact, neurodegenerative diseases that have been associated with poor metal homeostasis usually present widespread ROS-mediated oxidation positively correlated with misfolding and aggregation of proteins (Sayre *et al.*, 1999; Bush, 2000; Rotilio *et al.*, 2000). Although, as mentioned before, normal aging presents an accumulation of copper, iron and zinc in the brain, this becomes more relevant in neurodegeneration and in pathologies such as AD and PD (Rivera-Mancía *et al.*, 2010).

With respect to prion diseases, the use of prion fragments has shed some light into another relevant process related to copper coordination by proteins: the metal-catalyzed oxidation of specific amino acid residues, which may lead to loss or gain of function and can be linked to pathology. Requena *et al.* showed that the syrian hamster recombinant SHa₂₉₋₂₃₁ protein presented aggregation and precipitation concomitant with copper-mediated oxidation (Requena *et al.*, 2001). Since residues of the amino acids histidine and methionine are prone to be oxidized in the presence of copper, the wild-type fragment Ac-SKPKTNMKHM-NH₂ and its mutants (Csire *et al.*, 2017) also constitute a simplified model to study post-

translational structural modifications that could be related to the conversion of PrP^C into PrP^{Sc}. It has been shown that the mutant peptide which does not contain any methionine did not undergo oxidation, but fragmentation of the main-chain. However, in the case of methionine-containing peptides, the main-chain was not cleaved, and the oxidation of this residue to methionine sulfoxide occurred. These results reveal that methionine residues of prion protein may play a role as reactive oxygen species (ROS) scavengers and that their presence protects peptides from fragmentation. In all of these cases, Cu²⁺ ions catalyze the oxidation of methionine to methionine sulfoxide (Csire *et al.*, 2017). On the other hand, oxidation of methionine is also not a favorable process, since evidences suggest that it might be a trigger for conformational changes in PrP's structure (Elmallah *et al.*, 2013; Wang *et al.*, 2016), which, in turn, can lead to protein misfolding. This reaction can occur *in vivo*, either because of physiological (normal) aging or at the site of inflammation, where large amounts of oxidants are present (Swaim and Pizzo, 1988).

Since many of these protein aggregation-related diseases have several common structural and pathogenic features and mechanisms, in which metal ions are implicated, the use of an unified therapy has been proposed, based on a mechanism of action through the specific and selective sequestration of metal ions bound to the proteins. Such strategy should not exhibit the deleterious effects of a traditional chelation therapy, since these metal ions should not be eliminated from the organism, but redistributed in the patients' brains, as these elements are not in excess and are of physiological importance.

1.6. Metal-Protein Attenuating Compounds (MPACs)

To avoid the accumulation of oligomers in tissues, one proposition is to evaluate the possibility of using metal chelating agents. This approach is based on one of the most current hypotheses regarding aggregopathies, the metal hypothesis, in which the importance of physiological metals in the pathologies is investigated. The aim is to remove the metal ions bound to the peptide or protein in order to reduce A β and α -Syn oligomers' toxicity (Smoliga *et al.*, 2011; Lu *et al.*, 2013). The results, however, showed serious adverse effects due to the prolonged use of these chelators. In addition to the fact that most chelating agents do not have the

necessary properties to cross the BBB (Pardridge, 2009), they usually present high interaction constants, not being specific for the metal ions complexed to A β , α -Syn or PrP. This leads to non-specific elimination of essential physiological metals (Dedeoglu *et al.*, 2004; Pardridge, 2009).

An emerging class of therapeutic agents that may delay or even prevent the progression of AD and PD are the so-called Metal-Protein Attenuating Compounds (MPACs), which are chelators that present a moderate affinity and specificity for certain metal ions (Prashant, 2008). Thus, instead of binding and systematically removing any metals from tissues, MPACs restore physiological metal homeostasis through the specific binding of copper and/or zinc, attenuating their abnormal interactions with the proteins in local excess, thus preventing oligomerization (Scott and Orvig, 2009). The goal is also to reduce oxidative stress by inhibiting the production of ROS mediated by protein-bound metal ions through Fenton-like and Haber-Weiss reactions (Cherny *et al.*, 2001; Barnham *et al.*, 2004; Sampson *et al.*, 2012; Huang *et al.*, 2014).

In this context, clioquinol, a small lipophilic chelator, was proposed as a drug candidate for AD therapy due to its affinity for Zn²⁺ and Cu²⁺ (Regland *et al.*, 2001; Melov, 2002; Doraiswamy and Finefrock, 2004; Bareggi and Cornelli, 2012). This compound presented positive results in a study that used a transgenic model of the disease, reducing the formation of amyloid plaques in the brain (Mancino *et al.*, 2009). Its mechanism of action was attributed to the removal of biometals present in plaques. However, severe side effects were observed, which stimulated the search for analogues in order to progress in the investigations (Doraiswamy and Finefrock, 2004; Adlard *et al.*, 2008; Levine *et al.*, 2009; Budimir, 2011). The PBT2 ligand, part of a new generation of clioquinol-derived compounds, reduced aggregation of the A β peptide, limited the toxicity of the oligomers and redistributed physiological metal ions into the brains of disease model rats (Adlard *et al.*, 2008; Faux *et al.*, 2010; Crouch *et al.*, 2011; Crouch and Barnham, 2012). This ligand shows greater penetration to the blood-brain barrier than clioquinol and was tolerated by humans at daily oral doses of 50 mg to 250 mg in a study that lasted 12 weeks. Despite the encouraging initial results, the company that owns the rights to the compound reported discontinuation of the tests and its development as an anti-Alzheimer's drug, stating that PBT2 did not achieve its primary goal of

significantly reducing amyloid plaques in the brains of patients with prodromal or mild AD. The secondary objective of PBT2 to improve brain metabolic activity and cognition has also not been met. Currently, the company evaluates the performance of PBT2 against Huntington's disease. Another compound designed by the same company, PBT434, is currently under pre-clinical characterization with implications on the treatment of PD and Multiple System Atrophy (MSA), which is a rare neurodegenerative disease that bears some similarities to PD like α -Syn aggregation. This compound is the first of a new generation of molecules from the quinazolinone group intended to block the accumulation and aggregation of α -Syn (Finkelstein *et al.*, 2017). In practice, PBT434 reduced this protein's aggregation, as well as glial cell inclusions. The compound also prevented neuron death at the *substantia nigra* and improved motor function in an animal model of MSA (Finkelstein *et al.*, 2019).

Other analogues, derivatives of the 8-hydroxyquinoline-2-carboxaldehyde (8-HQ-2-CA) pharmacophore, have been studied for their ability to act as MPACs. The semicarbazone 8-H₂QS showed to be quite active in this sense, presenting the ability to cross the BBB, to bind copper under physiological conditions and to reduce aggregation of A β in the presence of Cu²⁺, as well as to exhibit antioxidant activity similar to that of vitamin E (Gomes *et al.*, 2014).

Our group has been developing and testing MPACs since 2012, having by now pioneered that the chemical class of *N*-acylhydrazones compose a set of promising agents for the tentative management of metal-enhanced aggregopathies (Cukierman *et al.*, 2018). In the past years, we have worked with a hybrid 8-hydroxyquinoline isonicotinoyl hydrazone ligand (De Freitas *et al.*, 2013), INHHQ, showing its potential in competing with both A β (Hauser-Davis *et al.*, 2015) and α -Syn (Cukierman *et al.*, 2017) for the binding of metal ions. This aroylhydrazone has been the subject of recently granted patents in the United States (US 10.189.811 B2 and US 10.316.019 B2). Pharmacological *in silico* analyses have demonstrated that the compound is neutral at physiological pH and is able to cross the blood-brain barrier, which has been recently proven by HPLC detection in the brains of rats intraperitoneally injected with INHHQ (Cukierman *et al.*, 2017). The DrugScore parameter, which estimates the likelihood of a compound becoming a commercial drug, was estimated at about 70%. Acute toxicity tests were also performed in

healthy Wistar rats, as well as the study of a biomarker of oxidative stress (GSH) and concentrations of biometals in the animals exposed to this hydrazone. The results showed that the compound does not act as an unspecific chelating agent in rats with basal levels of metals (Cukierman *et al.*, 2017). This, together with the fact that INHHQ is able to completely remove metal ions bound to A β and α -Syn, strongly suggests that the compound is a promising MPAC in the context of the treatment of Alzheimer's and Parkinson's diseases.

The structures of the forementioned 8-HQ-containing compounds are shown in Figure 4.

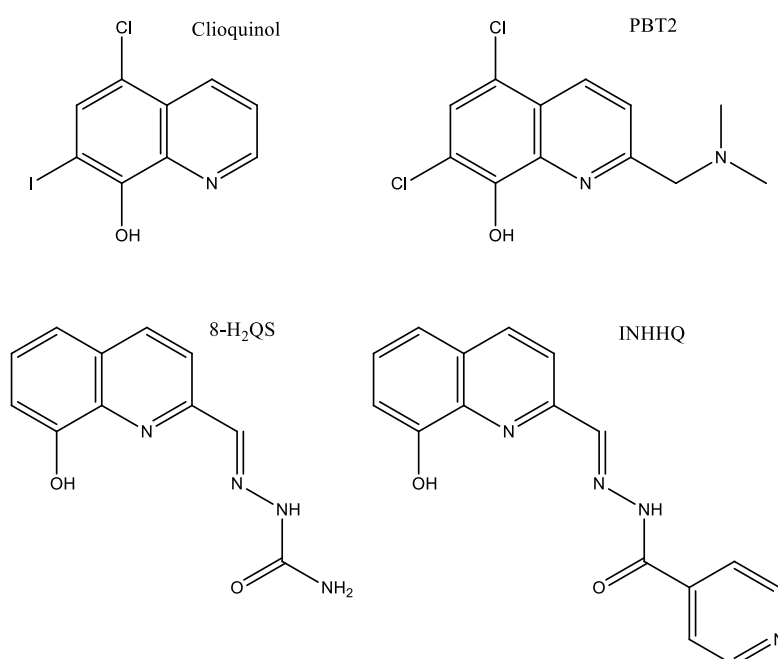


Figure 4. Structures of some 8-hydroxyquinoline-derived compounds that have been studied in the context of neurodegenerative diseases.

Very recently, our research group definitely proved the efficacy of INHHQ as a protective agent in an animal model of sporadic AD (De Falco *et al.*, 2020). The *N*-acylhydrazone prevented both short- and long-term memory impairments induced by the intracerebroventricular (i.c.v.) infusion of A β oligomers (A β O) in mice in the very small dose of 1 mg kg⁻¹. This A β O infusion leads to memory loss, as evidenced by the Novel Object Recognition test. However, mice that were intraperitoneally injected with INHHQ one hour before the i.c.v. infusion of the oligomers showed the same performance as control individuals (that did not receive A β O). Elevated Plus Maze and Open Field evaluations also showed that the

compound does not alter the fear and anxiety-related defensive responses of healthy mice. Moreover, INHHQ diminishes ROS production by Cu-A β ₁₋₁₆ complex, even in the presence of zinc, which is a potential competitor for the binding of copper by the compound (De Falco *et al.*, 2020) and is present at high concentrations in the synaptic cleft (Atrián-Blasco *et al.*, 2017). Despite the presence of the 8-hydroxyquinoline group in INHHQ, we have demonstrated, through the use of a structure-related compound (pyridine-2-carboxaldehyde isonicotinoyl hydrazone, namely HPCIH), that INHHQ's coordination of copper and zinc occurs through the aroylhydrazone system, since both ligands presented very similar results *in vitro*. This constitutes an innovation that opened new perspectives in the development of promising MPACs (Cukierman, 2016; Cukierman *et al.*, 2018).

The first step towards the development of new drugs is the identification of a drug target, which, in the context of the present work, is the protein/peptide aggregates and, in particular, their metal complexes relevant in the context of aggregopathies. Then, a lead compound is usually identified and intensively studied, presenting the desired activity towards its target. A lead compound is one that presents a structure related to a property that is considered therapeutically useful. In this case, INHHQ is the lead compound of our research, and that structure is the *N*-acylhydrazonic moiety. The next step headed for drug discovery is the design, synthesis and testing of structure-related analogues of the lead compound. This allows the identification of the structural features that are important for activity. These features are then taken into account during the design of new analogues with improved pharmacodynamic and pharmacokinetic properties. The present project lies on these steps of the rational drug development process. The search for new analogues is important in order to seek better activity and fewer adverse effects (i.e. better pharmacokinetic profiles). The following phase is when the compound is patented and pre-clinical trials are carried out to assess the properties and safety of the new drug candidate. If these prove to be satisfactory, clinical trials are carried out. Moreover, the development of a large-scale synthesis proceeds in parallel to the biological testing and the regulatory authorities, responsible for approving drugs for clinical trials and the market, must also be contacted.



PUC-Rio - Certificação Digital Nº 1712623/CA

WORK PROPOSAL AND JUSTIFICATION

2. Work proposal and justification

The present work comprises the evaluation and funneling-selection of structure-related *N*-acylhydrazones in the search for the compound or compounds with better pharmacological parameters, *in vitro* reactivity against metal-protein systems, lower toxicity and improved activity in a cellular model of synucleinopathy. Furthermore, correlations between some spectroscopic and/or structural parameters with physico-chemical properties and the presented biological performance are proposed.

The carbonylhydrazonic moiety ($R_1\text{-HC=N-NH-CO-R}_2$) was maintained fixed due to its moderate coordination potential towards copper and zinc, which, together with a third donor atom derived from the aromatic aldehyde moiety, has proven effective in competing with both A β and α -Syn (Hauser-Davis *et al.*, 2015; Cukierman *et al.*, 2017). Carbonylated hydrazones have been the focus of several studies in many research areas due to their performance as bidentate ligands, coordinating the metals through the nitrogen of the azomethine and the carbonyl oxygen. This chelating power is exploited in a wide spectrum of pharmacological applications. Hydrazones are commonly associated with a number of biological uses (Thota *et al.*, 2018), such as analgesics (Lima *et al.*, 2000), antihypertensives, anticonvulsants, anti-inflammatories (Kajal *et al.*, 2014), anti-tuberculosis agents, antitumor agents (El-Hawash *et al.*, 2006; Vicini *et al.*, 2006; Rada *et al.*, 2019; Rada *et al.*, 2020), antiretrovirals (Savini *et al.*, 2004; Vicini *et al.*, 2009), antimalarials, antidepressants and vasodilators (Silva *et al.*, 2005).

From a bioinorganic point of view, this class of compounds have also been investigated as iron chelators for the control of neurodegenerative disorders such as Friedreich's ataxia and other diseases related to the excess of this metal. In this scenario, the *ortho*-pyridine isonicotinoyl hydrazones are interesting because they are able to bind efficiently to the mitochondrial iron through the tridentate chelating system N_{py}, N, O (Richardson, 2003).

Hydrazones are also more stable towards hydrolysis than imines, since the azomethine C=N double bond is conjugated to the electron pair in the neighboring nitrogen, which, through resonance, lowers the electronic deficiency of the carbon atom, reducing its electrophilicity (Kalia and Raines, 2008).

As stated above, INHHQ, which was vastly studied in the last years, is the lead compound of the present work. Despite the encouraging results obtained for INHHQ, recent data (not published) indicate that mainly its poor water solubility, but also its relatively low resistance against hydrolysis, might be obstacles in its path towards becoming a commercial drug. Herein, INHHQ's analogues were designed through rationally thought changes in its structure that may reduce its hydrolysis rate, improve its solubility in aqueous medium and its coordination affinity towards biometals, that is, not too high, so it does not remove these essential metals from the body, but also high enough that it can still compete with proteins such as α -Syn for their binding.

Hydrazones are usually prepared through the condensation reaction between hydrazides and carbonyl compounds, such as aldehydes, as shown in Figure 5.

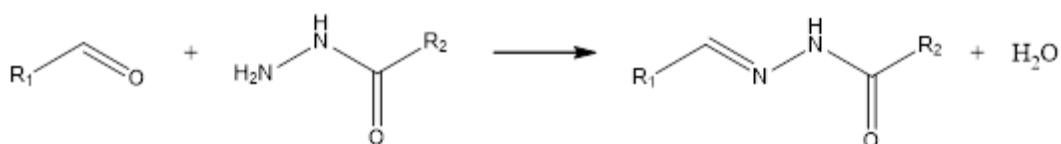


Figure 5. General scheme of *N*-acylhydrazones' synthesis.

Figure 6 shows the compounds proposed in the context of the present work. Going down the rows, the precursor aldehyde is modified, while going sideways among the columns, the hydrazide is the one altered. Changes in the aldehydes are intended to variate the ligands' solubility in water and their coordination strength, while changes in the hydrazides are meant to modulate the ligands' resistance towards hydrolysis and their solubility in aqueous media as well. Some of the aldehydes and hydrazides were selected also based on the experience of our research group in working with them, as well as their commercial availability.

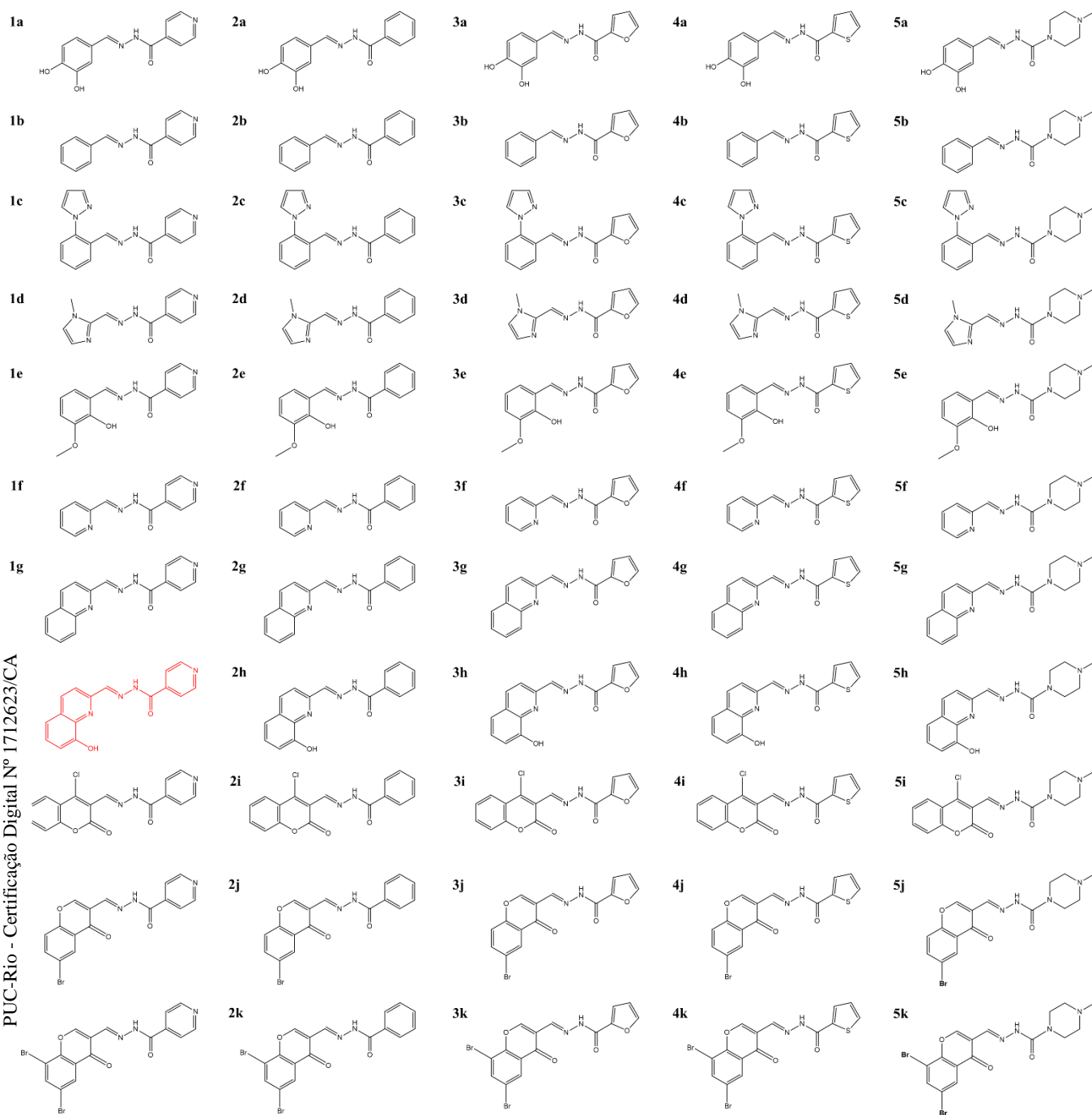


Figure 6. Structures of the 55 proposed carbonylhydrazones. Lead compound INHHQ (**1h**) is highlighted in red color.

The first three rows represent bidentate ligands. The first one, i.e. row **a**, was designed specifically to contain the catechol moiety, in order to obtain similar structures to that of levodopa, the medication currently used for the treatment of Parkinson's disease, which is enzymatically converted into dopamine once it crosses the BBB (Figure 7). Row **b** represents a set of very simple bidentate *N*-acylhydrazones derived from benzaldehyde, containing an “innocent”, non-coordinating aromatic moiety, which can be used, for example, to assess the significance of having donor atoms in this segment of the molecule. On the other hand, row **c** introduces an *ortho*-pyrazole ring in the structures of row **b**, in order to increase their solubility.

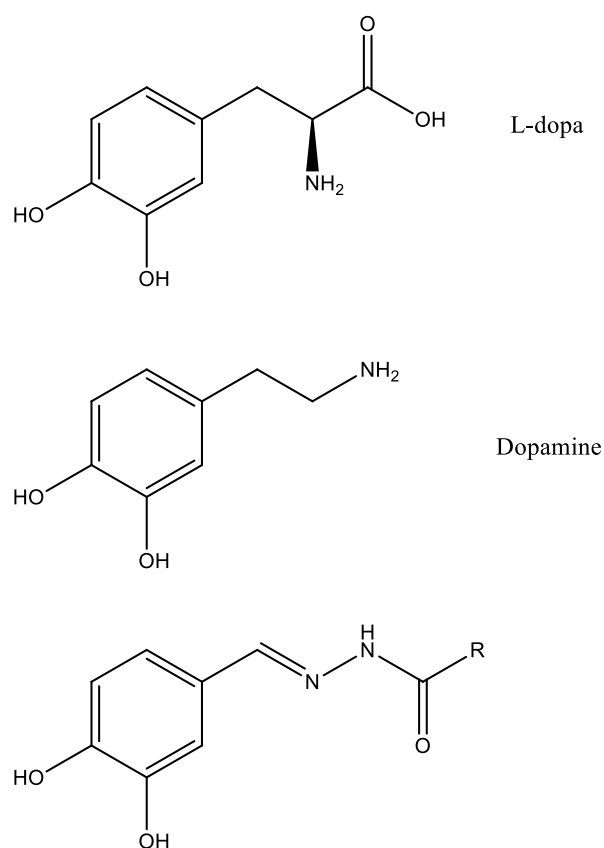


Figure 7. Structures of L-dopa, dopamine and the compounds of row **a**.

Row **d** introduces a third donor atom, an imidazole-derived nitrogen, turning the hydrazone moiety into a tridentate chelating site. This 5-membered ring is present in a variety of important biological molecules, such as the amino acid

histidine. Imidazoles also compose the structures of many antifungal, antiprotozoal and antihypertensive medications (Narasimhan *et al.*, 2011). This chemical group should increase substantially the solubility of the hydrazones and make them more biocompatible, since it is considered a bioisostere of pyridine. The methylation at one of the imidazole nitrogen atoms has as its main objective the simplification of the synthetic procedures, because tautomerism and protonation of the imidazole ring could complicate the isolation of the products.

The next row, **e**, comprises compounds derived from *ortho*-vanillin, which possesses some antifungal and antibacterial properties and is present in the extracts and essential oils of many plants. Compound **1e** has already been studied by our research group and both ligand and its oxidovanadium(V) complex were evaluated against chronic myelogenous leukemia K562 cells, presenting IC₅₀ values in the order of ~30 µmol L⁻¹ (González-Baró *et al.*, 2012; González-Baró *et al.*, 2017).

Row **f** represents some analogues of HPCIH (compound **1f**), which was vastly studied by the group of Richardson and collaborators and by our research group (Becker and Richardson, 1999; Cukierman, 2016). HPCIH is also a promising MPAC but its resistance against hydrolysis is similar to that of INHHQ's. On the other hand, its solubility is greater. This compound was essential to utterly demonstrate the intrinsic activity of *N*-acylhydrazones as moderate chelators for the prospective management of neurodegenerative diseases (Cukierman *et al.*, 2018). This was established in the literature by our research group. This row aims to maintain the good solubility observed for compound **1f** but improve its stability in water. Figure 8 shows the mechanism concerning the acid-catalyzed hydrolysis of a hydrazone, in which the first step is the protonation of the azomethine nitrogen.

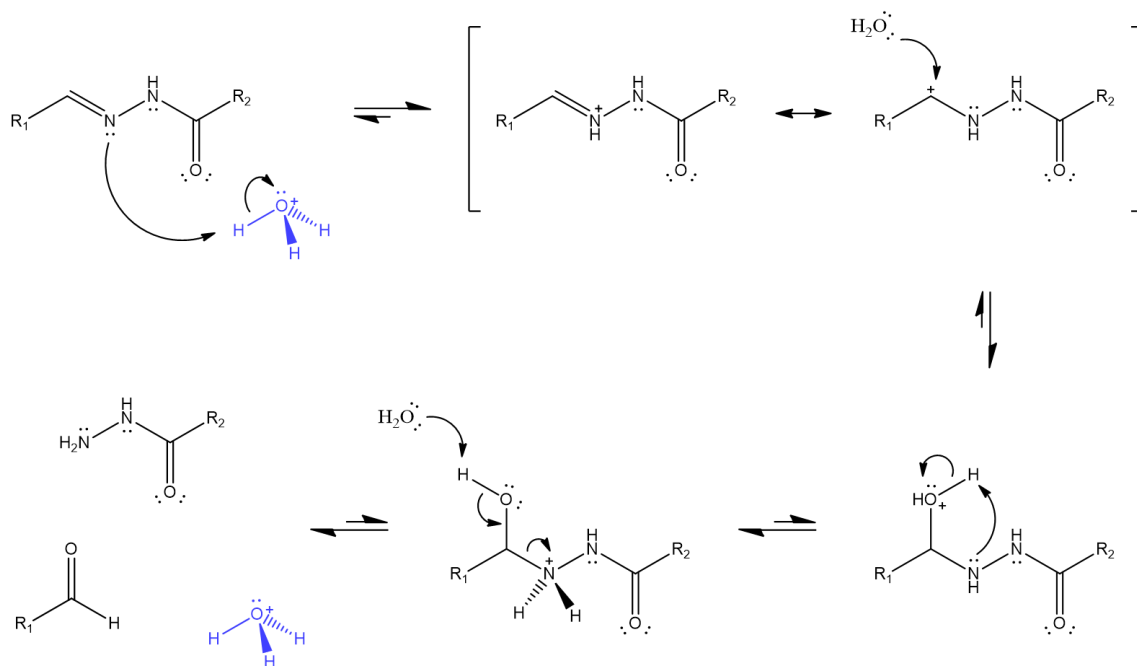


Figure 8. Mechanism of hydrolysis of hydrazones. The catalyst is shown in blue.

Row **g** contains structures that are very closely related to the lead compound's row, being the difference the lack of the phenol OH. This row is also similar to the previous one, except for the presence of a new condensed aromatic ring, resulting in the quinoline moiety. Additionally, compounds of row **g** resemble the structure of the forementioned compound that inhibits APP cleavage (Zhao *et al.*, 2020). Row **h** contains INHHQ, our lead compound (**1h**), and includes four other 8-hydroxyquinoline-derived carbonylhydrazones. The 8-hydroxyquinoline moiety has been the main chemical prototype for the development of MPACs in the last years. Considering that the pharmacophore of this study comprises the hydrazone moiety, and that metal ions do not bind through the phenol group of 8-hydroxyquinoline, compounds of the rows **f**, **g** and **h** should present similar activity, but might differ in their solubility and stability.

On the other hand, compounds in rows **i**, **j** and **k** were proposed based on known fluorophores, in order to have compounds that could be followed through fluorescence microscopy *in vitro*, maintaining a structure similar to that of the lead compound. These compounds are derived from flavones and coumarins.

Regarding the columns in Figure 6, the first series, i.e. series **1**, comprises isoniazid-derived hydrazones. Isoniazid, also known as isonicotinoylhydrazide, is

an approved antibiotic used in the treatment of tuberculosis. This is the first series proposed since it is present in the lead compound's structure. The pyridine ring is a more electron-deficient aromatic group when compared to benzene, and its nitrogen is electron-attracting. Its presence in a hydrazone decreases the electron density of the imine carbon atom, resulting in a higher hydrolysis rate (Scior and Garcés-Eisele, 2006). In this sense, series **2** (derived from benzoylhydrazide) might present higher stability than **1**, but, on the other hand, might decrease the hydrazones' solubility in aqueous media.

Series **3** and **4** represent the heterocyclic furoic- and thiophene- derived hydrazones, respectively. Although the presence of these hydrazides might decrease the hydrazones' solubility, this might not be an undesired effect when these hydrazides are combined with aldehydes that increase substantially the hydrophilicity, since it is necessary to have a balance between this and the lipophilicity for a compound to cross the body's membranes (in accordance to the partition coefficient, log P). Both hydrazides also present a five-membered ring, which makes the compounds smaller and, in some extent, more biocompatible. In addition, our research group has long experience working with furoic- and thiophene-derived hydrazones, having already observed interesting changes with the substitution of a single atom (oxygen / sulfur) in the aromatic ring.

These first four series of aromatic substituents (pyridine, benzene, furan and thiophene) are considered bioisosteres, being equivalent and thus composing a rational synthetic strategy widely employed in medicinal chemistry in the search for safer analogues, with better physico-chemical properties, which will eventually lead to improved pharmacokinetics and effectiveness.

When uncomplexed (metal free), the lead compound (**1h**) azomethine nitrogen can be easily protonated, starting the mechanism of hydrolysis shown in Figure 8. In order to try to avoid this in the new, proposed compounds, we suggested the series number **5**, derived from 4-methyl-1-piperazinecarboxylic acid hydrazide. This group introduces a new, alternative site for protonation, which would not cause any harm to the molecule's integrity. With this series, we should not only obtain hydrazones that are more stable in aqueous solution, but also with a higher solubility in water.

Initially, *in silico* pharmacological analyses were conducted with all 55 structures to determine some characteristics of the compounds that are relevant in the development of a new drug. The most important molecular descriptors are log P and log S. Log P is the partition coefficient, which represents the hydrophilic-lipophilic balance of the molecule, i.e. the ratio of the concentration of the substance in the organic and in the aqueous phases. Log S refers to the solubility of the compound in aqueous solution. These parameters are important since, in order to be absorbed, a drug must be soluble in the body fluids, but, nonetheless, it must present adequate lipophilicity to be permeable to cell membranes.

The Lipinski Rule of 5 was used as a parameter to rule out the structures that do not have the desired pharmacological properties. This rule states that a good candidate for drug development has a limit of multiples of 5 as values for some parameters: log P less than or equal to 5, molecular weight (MW) less than or equal to 500, hydrogen-bond acceptors (HBA) less than or equal to 10 and hydrogen-bond donors (HBD) less than or equal to 5 (Lipinski *et al.*, 2001). The compound in question may present only one violation of these parameters to be considered a promising drug candidate (Thais *et al.*, 2016). These rules allow, therefore, a good theoretical prediction of the oral bioavailability profile and permeability of new molecules. The calculated parameters were also compared to reference values regarding blood-brain barrier crossing and cell permeability (Van De Waterbeemd, Han *et al.*, 1998; Kelder *et al.*, 1999), since these *N*-acylhydrazones were designed as CNS-targeted drug candidates.

Special attention was given to the log S, which is INHHQ's main issue. After this initial step, the compounds with the best theoretical pharmacological prospects were synthesized and fully characterized. Their solubility, log P and hydrolysis profile were also analyzed. Tests were discontinued to those compounds that do not present the desired performance in each step. An *in silico* analysis of the toxic potential of the selected compounds was then performed before toxicity and other biochemical assays were carried out on cellular models of aggregopathies with the most promising compounds. The best candidates were also evaluated *in vitro* concerning their ability to disrupt specific metal-protein interactions. The affinity constant of the most promising ligands with biometals were also determined through calculations based on the Job method.

Through the collection of all these chemical and biological data, different correlations between structural properties and activity were proposed, in order to evaluate the influence of each structural feature to the activity of hydrazones as MPACs. The main goal was to determine the structural patterns that can provide the best pharmacological profile for promising hydrazonic drug candidates as a strategy against metal-enhanced aggregopathies.



PUC-Rio - Certificação Digital Nº 1712623/CA

OBJECTIVES

3. Objectives

3.1. General objective

The general objective of this project was to evaluate the potential of a great number of hydrazone compounds that could act as MPACs and, consequently, be effective in the management of metal-enhanced aggregopathies. Following a preliminary *in silico* round of analyses, the best drug candidates were synthesized and characterized, and their physicochemical properties and *in vitro* activities in a series of models of such disorders were analyzed. The final goal of the project was to find qualitative structure-activity correlations in order to determine which chemical patterns are fundamental for the good performance of a hydrazone MPAC and, thus, to establish a structural criterion to guide future efforts in the area.

3.2. Specific objectives

- 3.2.1. To rationally propose molecules with related structure to that of the lead compound.
- 3.2.2. To carry out a wide-ranging *in silico* pharmacological study of some pharmacokinetic parameters of the proposed compounds.
- 3.2.3. To synthesize and structurally characterize the most promising hydrazones.
- 3.2.4. To evaluate the stability against hydrolysis of the hydrazones, as well as to characterize them in solution.
- 3.2.5. To determine the experimental partition coefficient (log P) of the most stable hydrazones.
- 3.2.6. To assess, *in silico*, the theoretical toxic potential of the compounds.
- 3.2.7. To perform cellular toxicity and aggregation inhibition assays on a synucleinopathy model with the most promising compounds.
- 3.2.8. To describe the interactions of selected *N*-acylhydrazones with Cu²⁺ ions in solution and calculate their apparent affinity constants through calculations based on the Job method.
- 3.2.9. To evaluate the *in vitro* ability of the most promising compounds of disrupting specific interactions between Cu⁺ or Cu²⁺ ions with α -Syn through ¹H x ¹⁵N HSQC experiments.
- 3.2.10. To evaluate and correlate chemical and biological results in order to create qualitative structure-activity criteria for the *N*-acylhydrazones as MPACs in the context of metal-enhanced aggregopathies.



PUC-Rio - Certificação Digital Nº 1712623/CA

METHODOLOGY

4. Methodology

All reagents and solvents used in this work were purchased from commercial sources in the highest purity available and employed without further purification unless when specifically mentioned bellow. All water used was either ultra-pure or bi-distilled.

4.1. *In silico* pharmacological analyses

The descriptor parameters Molecular Weight, cLog P, cLog S, HBA, HBD, PSA and Druglikeness were calculated using the program Osiris Property Explorer: DataWarrior™, software freely available for download at <http://www.organic-chemistry.org/prog/peo/>, accessed on 15/11/2017.

Toxicity of selected compounds was estimated using the OpenVirtualToxLab™ software (Vedani and Smiesko, 2009; Vedani *et al.*, 2012; Vedani *et al.*, 2015), freely available upon license request at <http://www.biograf.ch/>, accessed on 08/11/2020.

4.2. Organic syntheses

Ligands were synthesized through Schiff base condensation reactions between an aldehyde and an *N*-acylhydrazide. Compounds already described in the literature were synthesized accordingly. Novel ligands were synthesized in a similar way. Briefly, the respective aldehyde was weighed in a round-bottom reaction flask and dissolved or diluted (if liquid) in alcohol (ethanol or methanol) or H₂O/alcohol mixture. The hydrazide was weighed in order to attain a 1:1 molar ratio and dissolved in the same solvent. Syntheses were performed in the 0.5 to 3.0 mmol range, using the least volume of solvent necessary for dissolution of each reactant. The hydrazide was dropwise added onto the aldehyde under stirring and gentle heating (up to 50 °C). The need to use acid as a catalyst (conc. HCl or acetic acid), as well as reflux and reaction time varied from one synthesis to another. The precipitates were filtered, washed with cold solvent and dried at room temperature. Table 1 summarizes the synthetic conditions for each synthesized hydrazone.

Table 1. Synthetic conditions, yields and melting points for the synthesized *N*-acylhydrazones.

Compound	Solvent	Acid Catalyst	Reaction	Solid formation	Yield	Melting Point
1a	EtOH	HCl conc. (1 drop)	4h at reflux	Upon addition of acid	60%	274** ± 2
1c	EtOH	HCl conc. (1 drop)	3h at r.t.	After cooling	51%	155 ± 1
1d	EtOH/H ₂ O (50% v/v)	-	6h at r.t.	After cooling	84%	214 ± 2
1f*	EtOH/H ₂ O (50% v/v)	-	30 min at reflux	After cooling	59%	172 ± 1
1h	EtOH	-	3h at reflux	After 1h	56%	246-249 (De Freitas <i>et al.</i> , 2013)
1i	EtOH	-	1h at r.t.	After 15 min	59%	215** ± 2
2d	EtOH	HCl conc. (1 drop)	4h at reflux	After cooling	72%	128 ± 1
3d	EtOH	HCl conc. (1 drop)	8h at r.t.	After cooling	83%	153 ± 2
3f*	EtOH	Acetic Acid (2 drops)	3h at reflux	After cooling	48%	164 ± 1
4d	EtOH	HCl conc. (1 drop)	4h at reflux	After cooling	48%	215 ± 2

* Pyridine-2-carboxaldehyde is a colorless liquid and must be distilled immediately before use.

** Degradation occurs at this temperature, so the actual melting point cannot be observed.

4.3. Characterization

Ligands were characterized by medium infrared vibrational spectroscopy (IR), nuclear magnetic resonance (NMR), as well as by thermogravimetry and melting point determinations. In specific cases, elemental analysis (CHN) was used to fully identify certain compounds. Single crystals suitable for structure determination were studied through X-ray diffraction crystallography in collaboration with Dr. Chris H. J. Franco, from the Federal University of Juiz de Fora (UFJF), Juiz de Fora, Brazil, and with Prof. Dr. Renata Diniz at the Chemistry Department of the Federal University of Minas Gerais (UFMG), Belo Horizonte, Brazil.

4.3.1. Infrared Vibrational Spectroscopy

The analyses were performed in an absorption spectrophotometer in the medium infrared region, either in the 100 FT-IR or in the 400 FT-IR models, Perkin-Elmer, and the data collected in the region of 4000-400 cm^{-1} . Pellets of the samples were prepared in potassium bromide. Alternatively, an HATR accessory was employed.

4.3.2. Nuclear Magnetic Resonance (NMR)

Nuclear magnetic resonance spectra of hydrogen, and, when applied, carbon and contour maps COSY, HSQC and HMBC, were obtained in a Bruker Avance III HD-400 spectrophotometer (operating at 400 MHz for ^1H and 100 MHz for ^{13}C) at 298 K. Samples were solubilized in 0.6 mL of deuterated dimethylsulfoxide (DMSO- d_6) and the spectra, calibrated based on the residual solvent signal (quintet at 2.50 ppm for the H core and septet at 39.52 for the C core). These analyses were performed at the Analytical Facilities “Pe. Leopoldo Hainberger” of the Chemistry Department of PUC-Rio.

4.3.3. X-ray diffraction (XRD)

The single crystal X-ray diffraction data were collected either in an Agilent-Rigaku Supernova (Federal University of Juiz de Fora) or in an Oxford-Rigaku Gemini A Ultra (Federal University of Minas Gerais) diffractometer, using MoK α ($\lambda = 0.71073 \text{ \AA}$) radiation at room temperature. Data collection, reduction and cell refinement were performed using the CRYCALISPRO software (Rigaku, 2015). The structures were resolved by direct methods using SIR (Burla *et al.*, 2015)

program and refined by SHELXL-2018/3 (Sheldrick, 2015) using the WinGX system (Farrugia, 2012). All non-hydrogen atoms were refined with anisotropic thermal parameters. H atoms connected to carbon were placed in idealized positions and treated by rigid model, with $U_{iso}(H) = 1.2U_{eq}$ ($X = C$ or N) for aromatic rings, CH groups and NH of imine group, and $U_{iso}(H) = 1.5U_{eq}$ (C) for the methyl group. Figures were drawn using ORTEP-3 for Windows (Barnes, 1997), Pov-Ray (Vision and Ltd., 1991-2013) and Mercury (Macrae *et al.*, 2008).

4.3.4. Thermogravimetry (TG)

These studies were conducted in a Perkin-Elmer analyzer, model Pyris 1 TGA, under nitrogen atmosphere, in the range of 25-900 °C of temperature, using a heating rate of 10 °C min⁻¹.

4.3.5. Melting Point (MP)

The determinations of the melting points of the organic ligands were performed in a Fisatom model 431 apparatus, in triplicate.

4.3.6. Elemental Analysis (CHN)

Carbon, hydrogen and nitrogen were simultaneously analyzed through gas chromatography, using an analytical curve, in the “*Laboratório de Espectroanalítica e Eletroanalítica Aplicada*”, from the Chemistry Department of PUC-Rio, in collaboration with Prof. Dr. Ricardo Q. Aucélio. Calibration was performed using dried standard reactants of the highest purity available. Between 2 and 3 mg of sample were weighted in a tin capsule and the analyses were done in an Thermo Electron elemental analyzer (CHN), model EA112, in duplicate.

4.4. Molecular Absorption Spectroscopy

The compounds were prepared in 100% DMSO and then diluted to an aqueous solution containing 1% DMSO at low concentrations ($\sim 5.0 \times 10^{-5}$ mol L⁻¹). For stability assays, spectra were acquired between the wavelengths of 200 to 800 nm in a Perkin-Elmer Lambda 35 spectrophotometer at regular intervals over 12 hours. A final measurement was taken after a few days. The room was kept at 17 °C throughout the experiment. The absorbance intensity variation was used to calculate the percentage decrease in the concentration of the initially dissolved compound. A

gaussian fitting was performed in the first (t_0) and last spectra (t_f) using the Origin software.

4.5. Experimental Log P

The distribution coefficient (P) in the 1-octanol/water system was calculated using the shake flask method (Bravo-Gómez *et al.*, 2009). A 10^{-2} mol L⁻¹ Tris buffer pH 7.4 was employed as the aqueous phase. Both phases, organic and aqueous, were separately prepared with the hydrazone at low concentrations (5×10^{-5} mol L⁻¹) from diluting stock solutions (either 1×10^{-3} or 2×10^{-4} mol L⁻¹). Then, the UV-Vis spectrum (Perkin-Elmer Lambda 35 spectrophotometer) was recorded for each phase before mixing them together. The vial containing the mixture was shaken vigorously at 37.0 °C, protected from light, for 3 hours (ThermoShaker, KASVI). At the end of the incubation, the mixture was centrifuged for 10 min at 3000 rpm, and the layers were separated with a Pasteur pipette. Concentrations in both phases were measured in the wavelength of higher absorption for each hydrazone, through a calibration curve. Each compound was analyzed in triplicate and P was calculated as the average concentration ratio C_o/C_w , where C_o is the final concentration in the organic phase and C_w is the final concentration in the aqueous phase. Log P was calculated and compared with the values obtained from *in silico* analyses.

4.6. Method of Continuous Variations (Job Plot)

Firstly, the molar absorptivity of the organic compound was determined, using different concentrations of the ligand in 1% DMSO/H₂O. For the apparent affinity constants' calculations, mixtures with different molar fractions of the ligand and the metal salt (CuCl₂ · H₂O) were prepared in 1% DMSO, from stock solutions, with identical final concentrations of 5×10^{-5} mol L⁻¹. Samples were always kept at 25 °C (ThermoShaker, KASVI). The absorbance scan profiles of the mixtures were obtained in a Perkin-Elmer Lambda 35 spectrophotometer, at room temperature. Using the ligands' ϵ values, the Lambert-Beer law and a plot of absorbance of the complex *versus* the molar fraction (Job plot), the stoichiometry of the complex and the apparent affinity constants were calculated.

4.7. Disruption of metal-protein interactions

These studies involving *in vitro* α -Syn were carried out in collaboration with the research group of Prof. Dr. Claudio O. Fernández (IBR-CONICET), Max Planck Laboratory, Rosario, Argentina. All NMR spectra were obtained on a Bruker Avance III 600 MHz spectrometer using a cryogenically cooled triple resonance $^1\text{H}(^{13}\text{C}/^{15}\text{N})$ TCI probe. Acquisition, processing, and visualization of the NMR spectra were performed using TOPSPIN 3.2 (Bruker) and CCP-NMR.

Unlabeled and ^{15}N isotopically enriched *N*-terminally acetylated α -Syn was obtained by co-transfecting *Escherichia coli* BL21 cells with the plasmid harboring the wild type α -Syn gene and a second one that encodes for the components of yeast NatB acetylase complex (Johnson *et al.*, 2013). Both plasmids carried different antibiotic resistance, namely Ampicillin and Chloramphenicol, to select the doubly transformed *E. coli* colonies. Purification was carried out as previously reported (Hoyer *et al.*, 2004) with the exception that both antibiotics were included in the growth flasks to avoid plasmid purge during growth and expression. The final purity of the α -Syn samples was determined by SDS-PAGE. Copper(II) sulfate, L-ascorbic acid, MES buffer and D_2O were purchased from Merck or Sigma; ^{15}N NH_4Cl was purchased from Cambridge Isotope Laboratories. Purified protein samples were dissolved in 20 mmol L^{-1} MES buffer containing 100 mmol L^{-1} NaCl at pH 6.5 (hereafter named Buffer A). Protein concentrations were determined spectrophotometrically by measuring absorption at 274 nm and using a molar absorptivity of $5600 \text{ L mol}^{-1} \text{ cm}^{-1}$.

To obtain the copper(I) complexes of α -Syn ($50 \text{ } \mu\text{mol L}^{-1}$), the copper(II) complexes were first prepared and then reduced with 7.5 mmol L^{-1} of ascorbic acid, which was added from a 0.5 mol L^{-1} stock solution. After pH adjustment, samples were purged with an N_2 flow for 5 min. NMR tubes sealed under N_2 atmosphere were used in all cases. Reduction of copper(II)-protein complexes with ascorbic acid was followed by the decrease of the characteristic *d-d* transition band in the UV-Vis spectrum, as previously described (Binolfi *et al.*, 2011).

NMR spectra were acquired on a Bruker Avance III 600 MHz spectrometer using a cryogenically cooled triple resonance $^1\text{H}(^{13}\text{C}/^{15}\text{N})$ TCI probe. 2D ^1H - ^{15}N HSQC experiments were performed on $50 \text{ } \mu\text{mol L}^{-1}$ ^{15}N -labeled α -Syn protein samples

dissolved in Buffer A, at 15 °C. 1D ^1H NMR assays were acquired on 50 $\mu\text{mol L}^{-1}$ unlabeled α -Syn protein samples, also dissolved in Buffer A. Aggregation did not occur under these low temperature conditions and absence of stirring. For the mapping experiments, ^1H - ^{15}N amide cross-peaks affected during compound titration in the presence of copper(II) were identified by comparing their intensities (I) with those of the same cross-peaks in the data set of samples lacking the divalent metal ion (I_0). The I/I_0 ratios of non-overlapping cross-peaks were plotted as a function of the protein sequence to obtain the intensity profiles. On the other hand, ^1H - ^{15}N amide cross-peaks affected during compound titration in the presence of copper(I) were identified by comparing their chemical shifts with those of the same crosspeaks in the data set of samples lacking the metal ion. Mean weighted chemical shifts displacements ($\text{MW}\Delta\text{CS}$) were calculated as $[(\Delta\delta^1\text{H})^2 + (\Delta\delta^{15}\text{N}/10)^2]^{1/2}$ for ^1H - ^{15}N . Acquisition, processing, and visualization of the NMR spectra were performed using TOPSPIN 7.0 (Bruker) and CCP-NMR.

4.8. Compound-protein interactions (STD-NMR)

STD-NMR experiments were executed by Prof. Dr. Nicolás A. Rey, with the help of the author of this thesis, at the NMR-based Structural Biology Department, in the Max Planck Institute for Biophysical Chemistry, Göttingen, Germany. For the protein solutions, 70 μL of WT- α -Syn 300 $\mu\text{mol L}^{-1}$ were added to 210 μL of phosphate buffer 20 mmol L^{-1} , pH 7.4, containing 133 mmol L^{-1} NaCl, and 20 μL of D_2O , in order to attain a final protein concentration of 70 $\mu\text{mol L}^{-1}$ in 300 μL . For the assays involving monomeric α -Syn, this solution was employed freshly prepared. For aggregated protein, samples were sonicated in cycles of 30 seconds (40% amplitude) every 30 minutes, at 37 °C, for 48 hours. This is called the Protein Misfolding Cyclic Amplification (PMCA) method. Aggregation was confirmed through fluorescence assays with Thioflavin-T. *N*-acylhydrazone solution was prepared by adding 2.0 μL from DMSO- d_6 stock solution (15 mmol L^{-1}) to 179 μL of phosphate buffer 20 mmol L^{-1} , pH 7.4, containing 100 mmol L^{-1} NaCl, and 13 μL of D_2O . For the interaction assays, to this compound solution, 6.0 μL of diluted protein (concentration 70 $\mu\text{mol L}^{-1}$) was added, either monomeric or aggregated. This constitutes a 75x excess of compound with respect to the protein. NMR measurements were performed in an 800 MHz Bruker Avance III spectrometer with a 3 mm CP TCI 800S7 H-C/N-D-03 Z cryoprobe. All the experiments were done at

5 °C, to decrease the HN exchange rate with the solvent. Samples were irradiated with pulses of 100 Hz at 2.18, 1.50, 0.85.0.30 and -0.5 ppm. Saturation time: 3 s.

4.9. In cell assays

These studies were performed in collaboration with the research group of Prof. Dr. Tiago F. Outeiro, at the Department of Neurodegeneration and Restorative Research, University Medical Center Göttingen (Georg-August Universität), Göttingen, Germany. The author spent 10 months of her Ph.D. studies in Prof. Outeiro's lab, from 09/2018 to 06/2019, enrolled in the PDSE program of "sandwich doctorate" (Programa de Doutorado Sanduíche no Exterior), partially funded by CAPES (6 months). The student was granted a non-funded extension of 4 months in order to complete the cellular studies.

4.9.1. Cell culture

Human neuroglioma (H4) cells were employed for the studies of synuclein inclusions. These are flat, adherent, non-neuronal and non-differentiated cells found in the central nervous system, which can be transfected to constitute a robust model for α -Syn aggregation in the context of Parkinson's disease research.

The other cell line employed was HEK293, or simply HEK, (human embryonic kidney), which are also flat and adherent cells. These cells were used in the assays involving stress granules.

H4 cells were maintained in OPTI-MEM and HEK were kept in DMEM, both media supplemented with 10% Fetal Bovine Serum (FBS) and 1% Penicillin/Streptomycin. The cells were grown at 37°C in an atmosphere of 5% CO₂. Cells were plated 24 hours prior to each experiment, so that 60-80% confluency could be reached. Then, treatment with each compound at different concentrations was kept for another 24 hours before analyses. The dilutions of the compounds in culture media were freshly prepared at each experiment from stock solutions in DMSO, maintaining the final DMSO content at 1% (v/v).

All procedures involving cell cultures were performed under sterile conditions (laminar flow hood).

4.9.2. Cellular viability in H4 cells (MTT cytotoxicity assay)

For the cytotoxicity assays, two control groups were used: a negative control, in which cells were treated only with the culture medium, and a DMSO control, in which cells were treated with medium containing 1% DMSO, which is the total amount of the solvent present in the treatment with the compounds. All the data were normalized regarding the negative control and statistically compared to the 1% DMSO. All the experiments were performed in triplicates. Results are given as mean and standard deviation. The mean values were used after the exclusion of outliers. Parametric data were analyzed through Analysis of Variance (ANOVA) tests with significance level of $p < 0.05$, using GraphPad Prism software. A symbol (*) indicates significant differences between the groups.

MTT [3-(4,5-dimethylthiazol-2-yl)-2,5-diphenyltetrazolium bromide tetrazolium] reduction colorimetric assays were employed in order to evaluate the cytotoxicity of the compounds through the cellular metabolic activity. The MTT assay determines the amount of active cells in proliferation based on the mitochondrial cleavage of the yellow tetrazolium salt, MTT, to form a soluble blue formazan product.

Cells were plated in 96-well plates at 2.5×10^4 cells mL^{-1} density, in 200 μL of culture medium. 24 hours after plating the cells, the medium was replaced with medium containing 1% DMSO, or with the different concentrations of the compounds. Each treatment was performed in 4 biological replicates to allow for better statistical results. After 24 hours of treatment, the medium was removed and a total of 100 μL of MTT solution prepared in DPBS (5 mg mL^{-1}) was added to the wells. The plates were incubated for 3 hours before MTT removal and addition of 100 μL of DMSO. Absorbances were measured in an automated plate reader (TECAN™ Infinity M200, Magellan™ software) at 570 nm and subtracted from reference at 600 nm.

4.9.3. Intracellular α -Syn aggregation: Syn-T + Sph1 model

To generate this model, H4 cells were co-transfected with plasmids overexpressing α -Syn tagged with a truncated fragment of EGFP (SynT) and synphilin-1 (Sph), which, together, promote α -Syn aggregation and the formation of inclusion bodies,

which can be seen by fluorescence microscopy after immunocytochemistry (ICC) and characterized biochemically (Lázaro *et al.*, 2014).

Transfection was performed through the calcium phosphate method, in which a calcium phosphate-DNA precipitate is formed, facilitating the binding of the DNA to the cell surface. The DNA is then incorporated through endocytosis. 12-well plates (70,000 cells/well) were employed for the ICC assays, while 6-well plates (180,000 cells/well) were used for the studies involving cell lysates and Western Blot. First, each DNA were diluted together in water. Then, CaCl₂ was added to the previous mixture. The DNA-CaCl₂ was then dropwise added to BES buffer, which was previously pipetted to a FACS tube, under vortex. The reaction was kept in the dark for 20 minutes. The reaction mixture was dropwise added to the cells containing fresh culture medium. After 16 hours of incubation, medium was removed and cells were washed three times with 1x TBS (Tris-Buffered Saline, diluted according to manufacturer). The *N*-acylhydrazones or their vehicle solution (1% DMSO) was added to the cells and the plate was incubated for 24 hours.

Table 2 summarizes the amount per well of each reagent needed for the transfection for each type of plate.

Table 2. Amount of reagent per well for each type of plate used in the transfection assays.

	DNA*	H ₂ O	CaCl ₂ (2.5 mol L ⁻¹)	BES**
12-well plate	3.75 µg	45 µL	5 µL	50 µL
6-well plate	7.5 µg	90 µL	10 µL	100 µL

* The values of DNA inhere described represents the total amount of DNA per well. In the case of co-transfection with two DNAs, half of this amount of each DNA is added.

** BES buffer pH 6.90 – 7.20: 50 mmol L⁻¹ BES [N,N-bis(2-hydroxyethyl)-2-aminoethanoesulfonic acid], 280 mmol L⁻¹ NaCl, 1.5 mmol L⁻¹ Na₂HPO₄ · 2H₂O.

4.9.3.1. Immunocytochemistry (ICC)

At the end of the treatments, cells were fixed in 4% paraformaldehyde (PFA) in PBS for 10 minutes, washed three times with 1x PBS before membrane permeabilization with 0.1% Triton-X (in PBS) for 20 minutes. The blocking

solution [1.5% (% m/v) BSA in PBS] was kept for at least 1 hour. Primary antibody (mouse anti- α -synuclein, Syn1 BD™ Transduction Laboratory, 250 $\mu\text{g mL}^{-1}$) was added to the cells in a dilution of 1:2000 (in the blocking solution) and incubated at 4 °C overnight or at room temperature for 3 hours. Then, cells were washed three times with 1x PBS, followed by incubation with secondary antibody (donkey anti-mouse IgG Alexa™ 488, 2 mg mL^{-1}), in a dilution of 1:1000 (in the blocking solution). Secondary antibody was kept for 2 hours under constant stirring and protected from light. After washing the cells as before, the cells were stained with DAPI (Molecular Probes) diluted to 1:5000 in PBS. Plates were kept at 4 °C until the imaging.

A Leica Inverted Microscope DMI 6000 B (Leica, Wetzlar, Germany), was employed. Images of transfected cells were taken using a 40x objective (HCX Pl Fluotar). For each condition, at least 50 transfected cells were quantified. Cells were classified into four categories: cells with no inclusions, from 1 to 4 inclusions, between 5 to 9 inclusions and more than 10 inclusions. Three independent experiments were performed for the control and each of the tested compounds. Results are displayed as a percentage of transfected cells in each group. The data were analyzed through *t* tests with significance level of $p < 0.05$, using GraphPad Prism software.

4.9.3.2. Cell lysates and Western Blot

For the biochemical characterization of α -Syn inclusions, plating (6-well plates), transfection and treatment with the compounds were done as described above. Two wells containing the same treatment were collected together by trypsinization. Briefly, cell were washed with DPBS and 150 μL of trypsin was added to each well. The cells were suspended in medium and added into 2 mL centrifuge tubes. These were then centrifuged for 5 minutes at 4 °C and 300 g. The supernatant was discarded, and the pellet was re-suspended in DPBS, which was again centrifuged in the same conditions. Supernatant was removed and the cell pellet was re-suspended in 100 μL of lysis buffer (50 mL PBS, 1 tablet Phosphatase cocktail, 1 tablet Protease inhibitor cocktail). At this point, the samples could be frozen until further analyses.

Lysates were sonicated for 10 seconds at 10% power and the total amount of protein was quantified by the Bradford method (BioRad Laboratories, Hercules, CA, USA). In summary, 50 μL of the analytical curve of standard BSA or 49 μL of water + 1 μL of sample were added, in triplicate, into 96-well plates. Then, 150 μL of the Bradford reagent was added to each well, and a colorimetric reaction could be observed. Samples were quantified at 595 nm.

40 μg of protein from each sample were loaded into 12% acrylamide gels after denaturation in sample buffer (125 mmol L^{-1} from a 1 mol L^{-1} stock Tris HCl pH 6.8, 4% SDS, 0.5% Bromophenol blue, 4 mmol L^{-1} EDTA, 20% Glycerol, 10% β -Mercaptoethanol) at 95 $^{\circ}\text{C}$ for 5 minutes. The proteins were transferred to PVDF membranes through semi-wet transfers using either the Transblot or the iBlot systems and membranes were fixed with PFA 0.4%. Then, blocking was done with BSA 3% in TBS-t (1x TBS, 50% tween) for at least 1 hour, and the membranes were incubated with primary antibody (mouse anti- α -synuclein Syn1 BD™ Transduction Laboratory, 250 $\mu\text{g mL}^{-1}$ and rabbit anti-GAPDH, Cell Signaling Technology) 1:1000 or 1:2000, overnight at 4 $^{\circ}\text{C}$. After washing with TBS-t, secondary antibody (anti-mouse and anti-rabbit IgG, horseradish peroxidase labeled, GE Healthcare, Bucks, UK, dilution 1:10000) was incubated for 3 hours. Proteins were visualized using chemiluminescence, detected using Immobilon Western Chemiluminescent HRP Substrate (Millipore Corp.) and Fusion FX (Vilber Lourmat). ImageJ software was used to quantify the bands signal.

4.9.3.3. Triton-X100 solubility of α -Syn inclusions

For the Triton-X100 solubility assay, cells were lysed as described above, with the exception that 4 wells of each condition were used, and the final pellet was re-suspended in 80 μL of lysis buffer, in order to have a more concentrated sample. In addition, instead of 10 seconds, samples were sonicated 3 times for 30 seconds, with 1-minute interval between each sonication. After Bradford protein quantification, 150 μg of protein were diluted in lysis buffer so that all samples presented the same final volume. Samples were kept on ice during all the procedure. Triton-X100 was added to the samples to attain a 1% v/v final proportion, followed by incubation on ice for 30 minutes. The samples were centrifuged at 15000 g, 4 $^{\circ}\text{C}$ for 1 hour. The supernatant (soluble fraction) was collected, while the pellet

(insoluble fraction) was resuspended in lysis buffer containing 2% SDS and sonicated twice for 30 seconds with 1-minute interval between each sonication. The samples were denatured and run on SDS-PAGE as described above.

4.9.3.4. Proteinase-K digestion of α -Syn inclusions

Samples were collected as defined above, and incubated with Proteinase K (Roth, Carlsbad, Germany, $2.5 \mu\text{g mL}^{-1}$), a broad-spectrum serine protease, for 1, 3, and 5 minutes at 37°C . The reaction was stopped with the addition of protein sample buffer, and the samples were added into 12% acrylamide gels. Transfer of proteins and treatment of the membranes were done as previously described.

4.9.4. Stress Granules

For these assays, HEK cells were employed since the formation of stress granules is better characterized in this cell line. Cells were plated at 100,000 cells/well in 12-well plates 24 hours prior to treatment with different concentrations of the compounds (diluted in DMEM, containing 1% DMSO v/v) for another 24 hours. Then, medium was removed and fresh medium containing $150 \mu\text{mol L}^{-1}$ of sodium(meta)arsenite was added. For this, a fresh solution of NaAsO_2 was prepared in water (10% w/v), and diluted to 150mmol L^{-1} , from which $1 \mu\text{L}$ was added to a total of 1 mL of whole medium. A control of cells treated with 1 mL of whole medium and $1 \mu\text{L}$ of water was also employed. Cells were incubated for 2 hours, then ICC was performed similarly to the procedure described in item 4.9.3.1, being the primary antibody TIA1 at 1:1000 dilution (rabbit anti-TIA1 Sigma Aldrich), and secondary antibody donkey anti-rabbit (IgG Alexa TM 555, 2mg mL^{-1}) at 1:1000 dilution.

4.10. Copper-catalyzed oxidation of the M112A PrP103-112 mutant fragment

Synthesis of the peptide, RP-HPLC and MS/MS experiments were performed by the research group of Prof. Dr. Csilla Kállay, from the Department of Inorganic and Analytical Chemistry of the University of Debrecen, in Hungary. The NMR experiments were executed by Prof. Dr. Nicolás A. Rey, with the help of the author of this thesis, at the NMR-based Structural Biology Department, in the Max Planck

Institute for Biophysical Chemistry, Göttingen, Germany. ESI-MS measurements were done in the same facility, by technician Kerstin Overkamp.

NMR measurements regarding the peptide's signal assignment were performed in an 800 MHz Bruker Avance III spectrometer with a 3 mm CP TCI 800S7 H-C/N-D-03 Z cryoprobe. All the experiments were done at 5 °C, to decrease the HN exchange rate with the solvent. Peptide's interaction with copper(II) ions, as well as its oxidation by the Cu²⁺/H₂O₂ system, was followed by NMR, at 25 °C, in a Bruker UltraShield 400 MHz magnet connected to a Bruker Avance III HD console, using 3 mm NMR tubes from Hilgenberg and a QXI 400S1 H/P-C/N-D-05 Z probehead. The latter configuration was also employed to characterize and assign the *N*-acylhydrazone **3f**, using 5 mm NMR tubes instead. For the measurements, dMKHA·4TFA (MM = 1638.47 g mol⁻¹) was dissolved in 500 µL of HEPES buffer (50 mmol L⁻¹, 100 mmol L⁻¹ NaCl, pH 7.4). 40 µL of D₂O and 10 µL of the reference compound 3-(trimethylsilyl)-2,2,3,3-tetradeuteriopropionic acid (TSP-*d*₄) solution (6.0 mmol L⁻¹) were then added, attaining a final dMKHA concentration equal to 5.0 mmol L⁻¹. The buffer HEPES was chosen to maintain the pH at a physiological value since its interaction with metal ions can be considered very weak, being a suitable choice for complexation studies (Ferreira *et al.*, 2015). From this initial solution, aliquots of 180 µL were transferred to the 3 mm NMR tubes. Small volumes of stock solutions (0.055 or 0.55 mol L⁻¹) of copper(II) chloride in D₂O were added for the interaction studies. For the oxidation evaluation, only the 0.055 mol L⁻¹ stock solution was employed, since higher copper(II) concentrations prevented the observation of the signals of interest due to its strong paramagnetic effect. The reaction started with the addition of 6% (w/w) hydrogen peroxide. Stock solution of compound **3f** (50 mmol L⁻¹) was prepared in methanol instead of acetonitrile due to the overlapping of this latter solvent's residual signal with that of ϵ methyl hydrogens from the methionine residue. Water suppression was achieved through the WATERGATE pulse sequence. 2D TOCSY experiments were carried out using a MLEV17-based sequence with a mixing time of 80 ms. 2D NOESY experiments were done employing a mixing time of 600 ms. Chemical shifts were calibrated by the signal of the internal reference TSP [-0.083 ppm for hydrogen (Hoffman, 2006) and -0.12 ppm for carbon (Wishart *et al.*, 1995), respectively]. For the chemical characterization of the hydrazone ligand, **3f** was

dissolved in DMSO-*d*₆ and the spectra were calibrated through the residual peaks of this solvent at 2.50 (¹H) and 39.52 ppm (¹³C). Additional NMR experiments demonstrated that this hydrazone is stable under the conditions used in the peptide's oxidation studies. Sample acquisition and processing were performed using the TopSpin 3.5p17 software (Bruker Biospin). Electrospray ionization mass spectrometry (ESI-MS) analysis on the ternary system constituted by dMKHA, copper(II), and **3f** was carried out in a Waters ZQ 4000 Single Quadrupole mass spectrometer. Standard configuration parameters for the positive mode were used.



PUC-Rio - Certificação Digital Nº 1712623/CA

RESULTS AND DISCUSSION I

5. Results and discussion: Part I – Design, syntheses, characterization and pharmacological parameters

5.1. *In silico* pharmacological descriptors

The physico-chemical *in silico* calculations were performed in the Osiris Property Explorer: DataWarrior™ software for INHHQ and the 54 proposed compounds in order to obtain some parameters relevant in drug development.

The first one is the molecular weight (MW), related to the ease with which a drug can permeate the cell membrane. The smaller the molecular weight, the more easily the molecule crosses membranes, and may even pass through cellular pores. The second and third analyzed properties are log P and log S. Log P is the partition coefficient, which represents the hydrophilic-lipophilic balance of the molecule, while log S refers to the solubility of the compound in aqueous solution. These parameters combined are of extreme importance in the context of cellular permeability and a compromise between them must be reached, since it is necessary that the drug does not present elevated lipophilicity, which would cause its retention in the highly lipophilic cellular space, nor a very high hydrophilicity, which would result in great difficulty for the drug to cross the lipid bilayer of the membranes.

HBA and HBD parameters (H-bond acceptors and donors) are important because they evaluate the possibility of hydrogen bond formation, aiming at the interaction with biological targets. Finally, PSA is the polar surface area, which evaluates the degree of polarity of the molecule, that is, the higher the concentration of partial charges in some region of the species, the greater its hydrophilic character becomes, which, in turn, would hamper the lipid penetration capacity.

Another parameter that can be taken into account in an analysis of a drug candidate is called druglikeness. This is a value determined from the comparison of compound fragments with a database of commercially available drugs and with a database of non-drug compounds. The molecule in question is compared with 3,300 commercial drugs and 15,000 chemical substances. The calculated parameters for the 55 *N*-acylhydrazones considered are displayed in Table 3 and Table 4,

Table 3. Calculated descriptors of pharmacological relevance for the 55 *N*-acylhydrazones studied.

Red color indicates results that do not fit into the reference values for BBB crossing. Lead compound **1h** is highlighted in blue color, while the compounds that presented no violations of the reference values are shown in gray.

	MW	cLogP	cLogS	HBA	HBD	PSA	Druglikeness
1a	257.248	1.5093	-2.334	6	3	94.81	4.4204
1b	225.250	2.2007	-2.926	4	1	54.35	4.4687
1c	291.313	1.3695	-2.661	6	1	72.17	5.4850
1d	229.242	0.3832	-0.688	6	1	72.17	5.8453
1e	292.301	1.0691	-2.674	7	1	85.06	0.8272
1f	226.238	1.2538	-2.155	5	1	67.24	4.4687
1g	276.298	2.5707	-3.656	5	1	67.24	4.4687
1h	292.297	2.2250	-3.360	6	2	87.47	4.4204
1i	327.726	2.0135	-2.337	6	1	80.65	4.7270
1j	372.177	2.0433	-4.310	6	1	80.65	3.1317
1k	451.073	2.7685	-5.144	6	1	80.65	3.1317
2a	256.260	2.5102	-3.129	5	3	81.92	4.4204
2b	224.262	3.2016	-3.721	3	1	41.46	4.4687
2c	290.325	2.3704	-3.456	5	1	59.28	5.4850
2d	228.254	1.3841	-1.483	5	1	59.28	5.8453
2e	291.313	2.0700	-3.469	6	1	72.17	0.8272
2f	225.250	2.2547	-2.950	4	1	54.35	4.4687
2g	275.310	3.5716	-4.451	4	1	54.35	4.4687
2h	291.309	3.2259	-4.155	5	2	74.58	4.4204
2i	326.738	3.0144	-3.132	5	1	67.76	4.7270
2j	371.189	3.0442	-5.105	5	1	67.76	3.1317
2k	450.085	3.7694	-5.939	5	1	67.76	3.1317
3a	246.221	1.6989	-2.811	6	3	95.06	4.3877
3b	214.223	2.3903	-3.403	4	1	54.60	4.3733
3c	280.286	1.5591	-3.138	6	1	72.42	5.3274
3d	218.215	0.5728	-1.165	6	1	72.42	5.7735
3e	281.274	1.2587	-3.151	7	1	85.31	0.6269
3f	215.211	1.4434	-2.632	5	1	67.49	4.3733
3g	265.271	2.7603	-4.133	5	1	67.49	4.3733

Table 4. (Continuation of Table 3). Calculated descriptors of pharmacological relevance for the 55 *N*-acylhydrazones studied. Red color indicates results that do not fit into the reference values for BBB crossing. Lead compound **1h** is highlighted in blue color, while the compounds that presented no violations of the reference values are shown in gray.

	MW	cLogP	cLogS	HBA	HBD	PSA	Druglikeness
3h	281.270	2.4146	-3.837	6	2	87.72	4.3877
3i	316.699	2.2031	-2.814	6	1	80.90	4.7437
3j	361.150	2.2329	-4.787	6	1	80.90	3.2760
3k	440.047	2.9581	-5.621	6	1	80.90	3.2760
4a	262.288	2.3768	-3.139	5	3	110.16	6.1683
4b	230.290	3.0682	-3.731	3	1	69.70	6.1817
4c	296.353	2.2370	-3.466	5	1	87.52	7.0679
4d	234.282	1.2507	-1.493	5	1	87.52	7.4251
4e	297.341	1.9366	-3.479	6	1	100.41	2.3654
4f	231.278	2.1213	-2.960	4	1	82.59	6.1817
4g	281.338	3.4382	-4.461	4	1	82.59	6.1817
4h	297.337	3.0925	-4.165	5	2	102.82	6.1683
4i	332.766	2.8810	-3.142	5	1	96.00	6.3882
4j	377.217	2.9108	-5.115	5	1	96.00	4.7323
4k	456.114	3.6360	-5.949	5	1	96.00	4.7323
5a	278.311	1.1403	-1.345	7	3	88.40	10.0340
5b	246.313	1.8317	-1.937	5	1	47.94	10.0810
5c	312.376	1.0005	-1.672	7	1	65.76	10.5840
5d	250.305	0.0142	0.301	7	1	65.76	10.4810
5e	313.364	0.7001	-1.685	8	1	78.65	6.0842
5f	247.301	0.8848	-1.166	6	1	60.83	10.0810
5g	297.361	2.2017	-2.667	6	1	60.83	10.0810
5h	313.360	1.8560	-2.371	7	2	81.06	10.0340
5i	348.789	1.6445	-1.348	7	1	74.24	10.0670
5j	393.240	1.6743	-3.321	7	1	74.24	8.5092
5k	472.136	2.3995	-4.155	7	1	74.24	8.5092

The reference values for these descriptors regarding BBB-crossing and cell permeability are shown in Table 5 (Van De Waterbeemd, H. *et al.*, 1998; Kelder *et al.*, 1999).

Table 5. Reference values for the pharmacological descriptors.

	MW	LogP	LogS	HBA	HBD	PSA	Druglikeness
Cell permeability	≤ 500	-1 a 5	≥ -4	≤ 10	≤ 5	≤ 140	> 0
BBB-crossing	≤ 400	-1 a 5	≥ -4	≤ 7	≤ 3	≤ 90	> 0

The results marked in red are those that do not fit into the reference values for BBB crossing, which are more restrictive, and these *N*-acylhydrazones were not synthesized. The lead compound INHHQ, or **1h**, fulfills all the requirements imposed by these pharmacological guidelines, yet its solubility remains an impasse in its preclinical evaluation. Indeed, poor aqueous solubility has been described as one of the major causes of failure in drug development (Danishuddin and Khan, 2016). For this reason, we have proposed another criterion to exclude hydrazones with low solubility in water, that is, log S greater than -2.5 (i.e. approximately 10 times higher than that of the lead compound). Only the *N*-acylhydrazones that are in accordance to all the reference values of the studied parameters and this proposed value of calculated solubility were selected for synthesis, characterization and study in the context of the present work. Figure 9 is a bar graph showing the solubility of the proposed hydrazones. The bar representing the lead compound INHHQ (**1h**) is depicted in red. As expected, compounds belonging to row **d** (synthesized from 1-methyl-1H-imidazole-2-carboxaldehyde) present much higher solubility. However, compound **5d**'s solubility in water is too high, and its log S is a positive value. We then decided to not synthesize this compound as well, since some lipophilicity is also important for a drug designed to cross the BBB and reach the brain. Light gray bars represent the 18 compounds selected for the next step of the project, i.e. synthesis and chemical characterization. Besides the hydrazones belonging to row **d**, two other important clusters of potentially suitable compounds were found within groups **1** and **5**, i.e. those derived, respectively, from isoniazid and 4-methyl-1-piperazinecarboxylic acid hydrazide.

From this point forward, it has been established that, from the 55 starting drug candidates, only 19 of them (18 + lead compound **1h** for control purposes) would be synthesized and, according to their observed physicochemical properties, experimentally evaluated regarding their performance as MPACs.

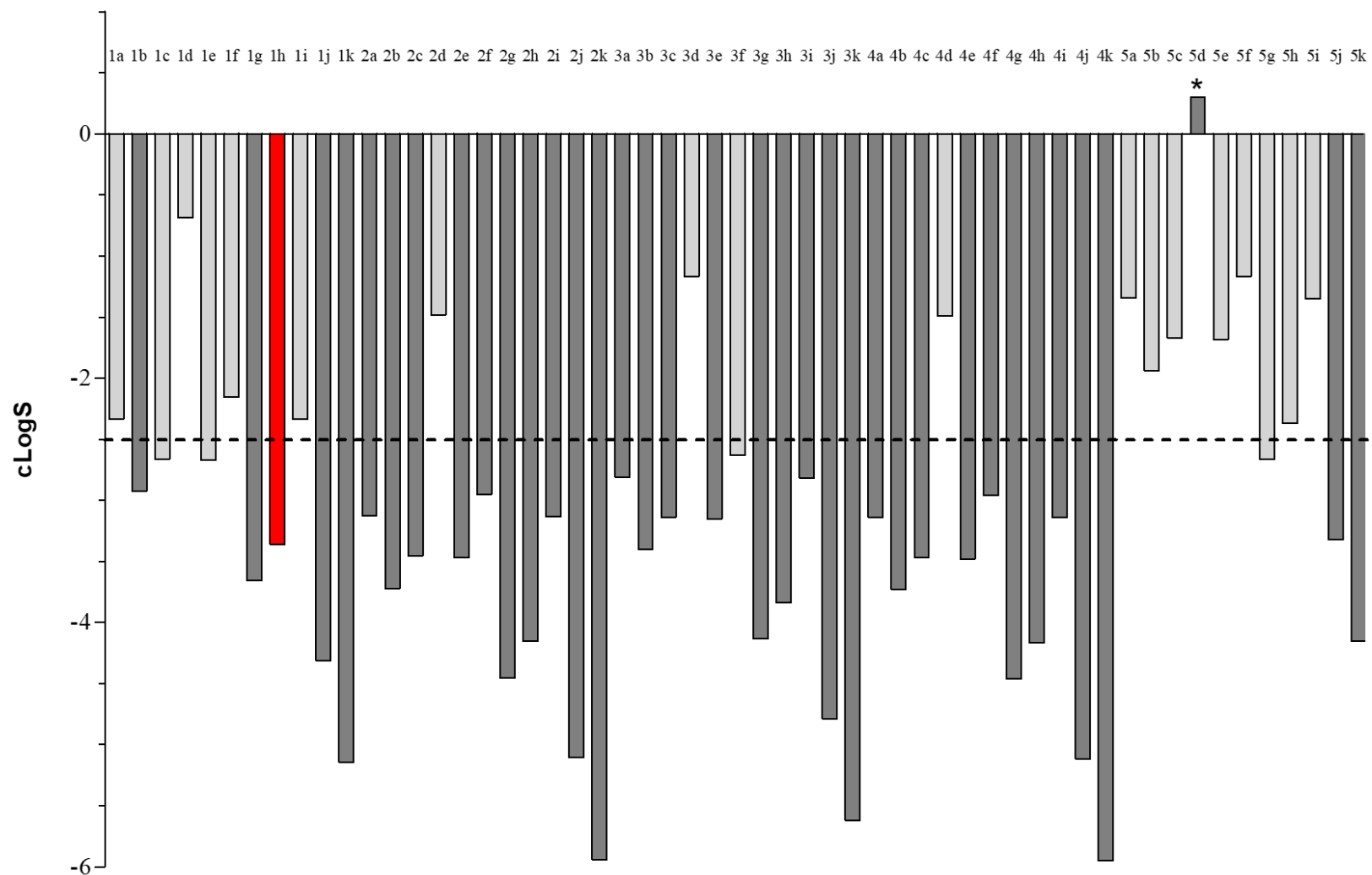


Figure 9. cLog S of the 55 hydrazones. The lead compound (**1h**) is shown in red and the hydrazones selected for synthesis are shown in light gray. The (*) symbol highlights the compound with undesired positive cLog S.

5.2. Syntheses and chemical characterization

The ligands were synthesized similarly, through Schiff base condensation reactions between a carbonyl compound and a hydrazide. Whenever possible, thermogravimetry and elemental analyses were used as analytical tools to confirm the presence or absence of solvent molecules, i.e., the state of hydration of these solids, which has direct implications on the exact molar masses of the compounds. Moreover, Nuclear Magnetic Resonance (NMR) and mid-infrared (IR) vibrational spectroscopies were employed to structurally characterize the molecules. X-ray diffraction structure of the obtained single crystals are also discussed herein. These data are presented separately for each compound, except for the group of the 1-methylimidazole-derived, and the group of the pyridine-2-carboxaldehyde-derived *N*-acylhydrazones, for which comparative discussions were done due to their very closely related structures. Selected NMR absorptions, common to all hydrazones, were also further discussed comparatively.

With respect to the NMR data, we have recently conducted and published a series of papers that present detailed studies of the characterization of structure-related *N*-acylhydrazones in solution, including different two-dimensional NMR experiments which allowed for the assignment of their signals (Cukierman *et al.*, 2018; Cukierman *et al.*, 2019; Cukierman *et al.*, 2020; Cukierman *et al.*, 2021). Based on these assignments, and due to the similarity of the inhere described compounds, for the sake of simplicity, only the 1D ^1H NMR data will be presented and discussed in this thesis. The complete set of ^{13}C and 2D spectra can be found in the cited literature. Assignments were also performed based on the spectra of the precursors, which are not shown.

5.2.1. Compound 1a:

3,4-dihydroxybenzaldehyde isonicotinoyl hydrazone

This orange solid was obtained after the condensation between 3,4-dihydroxybenzaldehyde and isoniazid in ethanol, with precipitation occurring immediately upon addition of 1 drop of HCl. The catechol moiety seems to oxidate to an *ortho*-quinone around 274 °C, evidenced by a pronounced change of color to black. Thus, the melting point of compound **1a** could not be determined.

Thermogravimetric curve of compound **1a** (Appendix Figure 1) suggests the presence of two hydration water molecules (loss of 11.44% until 200 °C). Thus, its chemical formula corresponds to $C_{13}H_{11}N_3O_3 \cdot 2 H_2O$ (MW = 293.24 g mol⁻¹). The decomposition of the organic ligand occurs in two steps of similar percentage weight loss. There is no considerable stable residue after 700 °C.

Compound **1a**'s infrared spectrum is shown in Appendix Figure 2. The absorption related to the newly formed azomethine bond (C=N), can be observed at 1650 cm⁻¹, while the characteristic C=O stretching appears at 1677 cm⁻¹ in the spectrum. A large band centered at 3442 cm⁻¹ indicates the stretching of O–H bond, confirming the presence of hydration water, as well as the expected catechol moiety. Another important band is seen at 3215 cm⁻¹, corresponding to the stretching of the N–H bond. Taken together, these data confirm the identity of the solid obtained, and these attributions are also in accordance to the literature (Suvarapu *et al.*, 2011).

The ¹H-NMR spectrum of **1a** in DMSO-*d*₆ solution, together with the corresponding assignments, is shown in Figure 10. Two sets of signals can be observed in the spectrum, being the proportion between them around 80% for the major signals and 20% for the minor ones. This probably represents an equilibrium between the (*E*)-amido [-OC-(NH)-N=C-] and (*E*)-iminol [-(HO)C=N-N=C-] tautomers (Mohammed, 2012; Coman *et al.*, 2018). We do not exclude the possibility, however, that this secondary set of signals represents an equilibrium between *anti*- and *syn*- conformations around the amide bond (Oliveira *et al.*, 2017). No (*Z*) isomer is observed, since there is no *ortho* substituent that could favor its stabilization (Syakaev *et al.*, 2006; Patorski *et al.*, 2013; Yuan and Zheng, 2019).

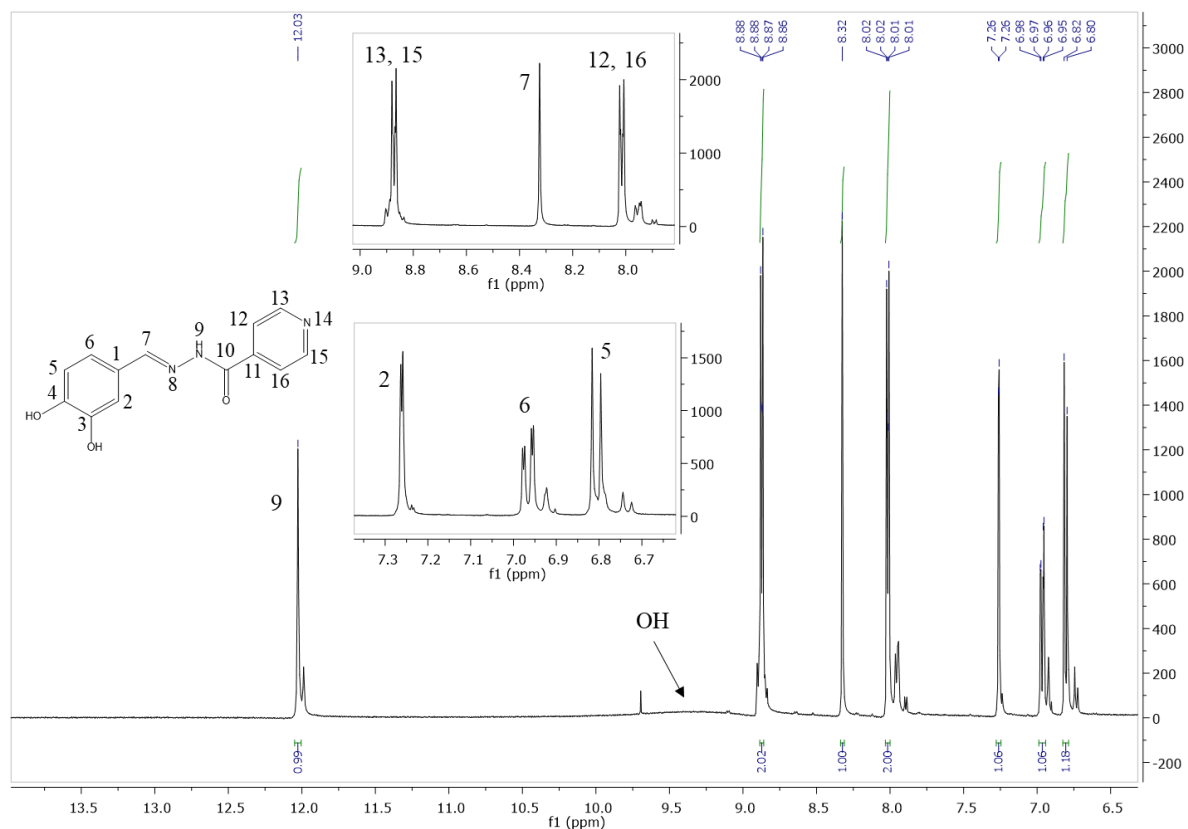


Figure 10. ^1H NMR spectrum of **1a** (400 MHz) in $\text{DMSO-}d_6$ at room temperature.

5.2.2. Compound **1c**:

2-(1H-pyrazol-1-yl)benzaldehyde isonicotinoyl hydrazone (**1c**)

Compound **1c** was isolated as a yellow crystalline solid after the condensation between 2-(1H-pyrazol-1-yl)benzaldehyde and isoniazid in ethanol at room temperature. This aldehyde was synthesized by Prof. Jones Limberger's group, at PUC-Rio. When an attempt on the synthesis of **1c** was conducted under reflux and strong acidic conditions, an unexpected dihydrazone, constituted by two units of the aldehyde-derived structure, was obtained as product. This compound was also thoroughly characterized and will be, from this point on, referred to as compound **1c'**: 1,2-bis[2-(1H-pyrazol-1-yl)benzylidene]hydrazone.

Single crystals of both compounds were isolated, which allowed for their complete solid-state characterization. The crystal structure investigations of compounds **1c** and **1c'** indicate that both crystallize in the monoclinic system, although in different space groups: $P2_1/c$ and $P2_1/c$, respectively, containing four molecules per unit cell. Figure 11 exhibits the molecular representation of the molecular structures and the crystallographic details for these compounds are listed

in Table 6. No protonation, counter-ions or solvent molecules are observed in either structures. The lack of solvent molecules in the crystal networks of **1c** and **1c'** is confirmed by the thermal decomposition patterns of both compounds, with no mass loss below 200 °C. The solution NMR spectra showed that, as expected, the (*E*) configuration is predominant around the C=N bonds, due to its greater stability. Selected geometrical parameters for these compounds are displayed in Table 7.

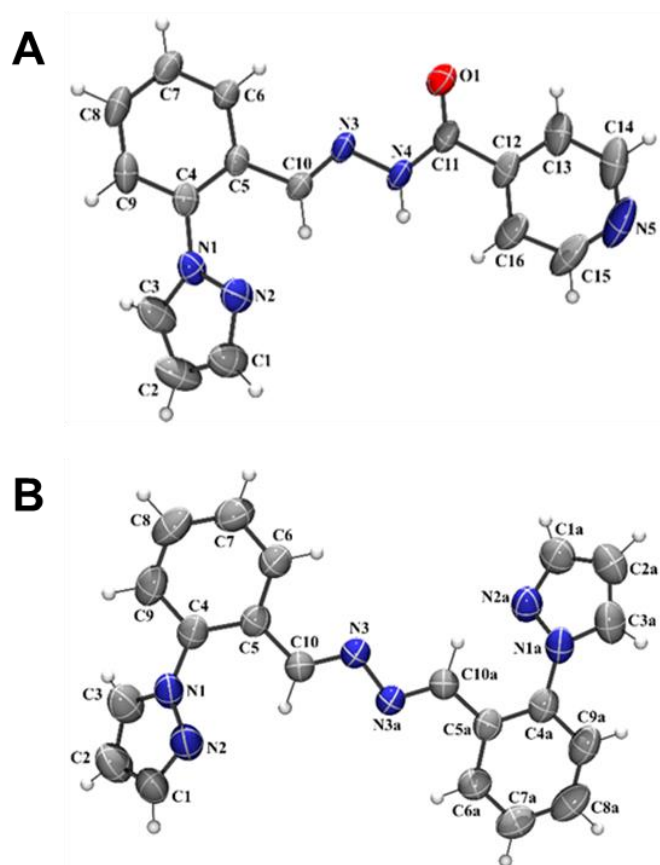


Figure 11. Molecular structure representations of (A) compound **1c** and (B) compound **1c'**. The ellipsoids were drawn at the 50% probability level.

Table 6. Crystal data and refinement parameters for compounds **1c** and **1c'**.

Compound	1c	1c'
Formula	C ₁₆ H ₁₃ N ₅ O	C ₂₀ H ₁₆ N ₆
Formula weight (g mol⁻¹)	291.31	340.39
Crystal system, space group	Monoclinic, <i>P2/c</i>	Monoclinic, <i>P2₁/c</i>
Temperature (K)	293	293
<i>a</i> (Å)	12.3523(6)	7.9805(5)
<i>b</i> (Å)	7.9564(4)	22.589(1)
<i>c</i> (Å)	15.3018(8)	10.3283(5)
β (°)	96.325(5)	107.618(6)
V (Å³)	1494.7(1)	1774.5(2)
Z	4	4
Radiation type	Mo Kα	Mo Kα
μ (mm⁻¹)	0.086	0.081
Crystal size (mm)	0.26 x 0.20 x 0.14	0.90 × 0.38 × 0.20
Measured / Independent reflections	38444 / 4054	37675 / 4752
Observed reflections / R_{int}	3187 / 0.0304	2963 / 0.0491
Number of parameters	200	238
R_{obs}, R_{all}	0.0505, 0.0654	0.0540, 0.0909
wR_{obs}, wR_{all}, S	0.1378, 0.1460, 1.081	0.1429, 0.1667, 1.063
Δp_{max}, Δp_{min} (e Å⁻³)	0.227, -0.173	0.157, -0.154

In the solid-state, the molecule of the dihydrazone **1c'** is not symmetric as one would expect, and the main difference between each phenyl-pyrazole fragment is in the torsion angles amid the planes defined by N1(a), N2(a), C1(a), C2(a) and C3(a) - pyrazole ring - and C4(a), C5(a), C6(a), C7(a), C8(a) and C9(a) - phenyl ring. In one fragment, the angle is equal to 51.5° and, in the other, to 53.7°. The phenyl rings from each fragment are also not in the same plane, displaying a dihedral angle of 9.3°. The C=N–N=C link between the fragments, showing average C=N distances of 1.272(2) Å, present a torsion angle of 176.1°. The crystal stability is guaranteed by non-conventional CH⋯N hydrogen bond interactions between the pyrazole rings of two dihydrazone molecules, giving rise to a dimeric arrangement. A number of these dimers, on the other hand, are linked by CH⋯π interactions involving phenyl and pyrazole rings, respectively, which generates a one-dimensional network along the crystallographic axis *a* (Figure 12A).

Concerning the originally desired compound **1c**, the torsion angles between aromatic rings are 28.1° (phenyl-pyridyl) and 47.4° (phenyl-pyrazole). In this case, the carbon-nitrogen distances in the CNNC group are different [1.267(2) and 1.348(2) Å], which indicates that one linkage has double bond character while the other is a single bond. For this reason, N4 is protonated, contrary to what is observed in compound **1c'**. It is precisely the occurrence of the hydrazoneic N4H group which stabilizes the crystal structure of **1c**, acting as a hydrogen donor in weak $\text{NH}\cdots\text{N}$ hydrogen bonds involving pyrazole N2 atoms as the acceptors. These interactions generate, as was also observed in the structure of **1c'**, dimers. Non-conventional $\text{CH}\cdots\text{O}$ and $\text{CH}\cdots\text{N}$ contacts involving the heteroatoms O1, N5 and N3 link the dimers, giving rise to a more complex tri-dimensional network (Figure 12B).

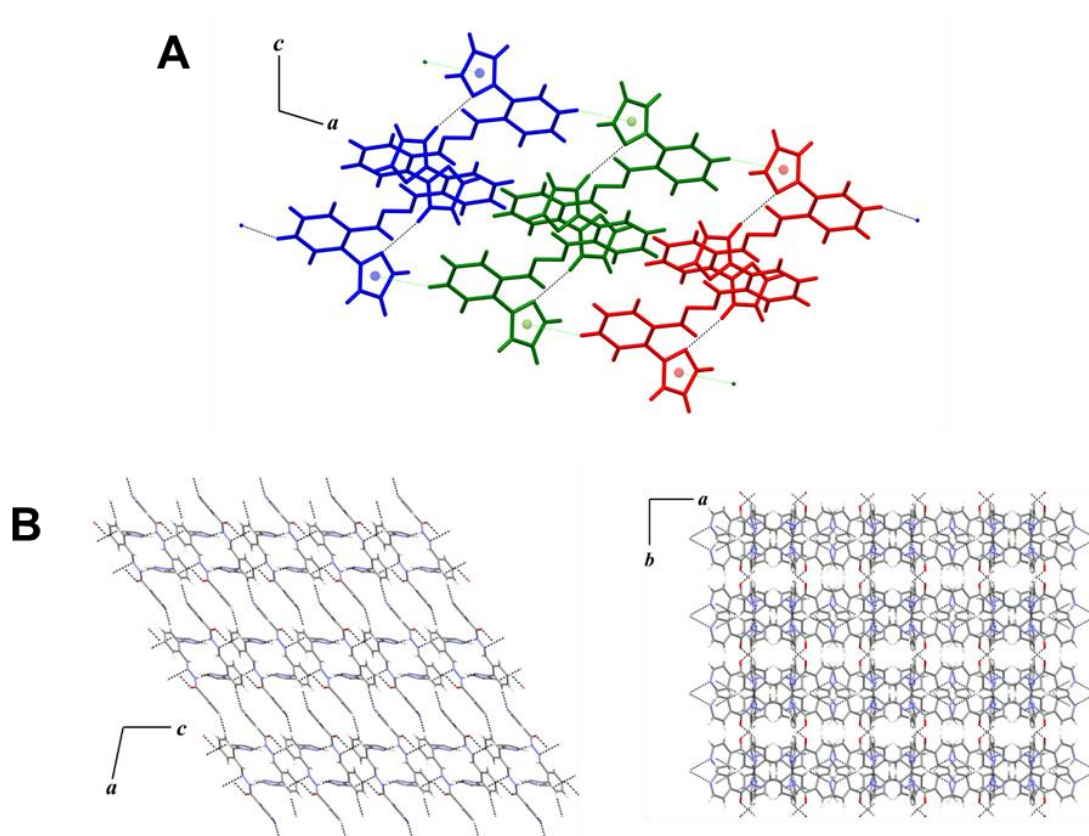


Figure 12. Intermolecular interactions in (A) compound **1c'**, where each color represents a dimeric unit linked in a one-dimensional network along the crystallographic axis *a* and (B) compound **1c**. The intricate tridimensional network can be observed along axis *b* (left) and *c* (right). Extracted from (Cukierman *et al.*, 2021).

Table 7. Selected bond distances and angles for compounds **1c** and **1c'**.

Compound	1c	1c'		
Bond distances (Å)				
N1–N2	1.357(2)	1.359(2)		
N3–N3a / N3–N4	1.375(1)	1.407(2)		
N1a–N2a	-	1.361(2)		
C10–N3	1.267(2)	1.273(2)		
C10a–N3a / C11–N4	1.348(2)	1.270(2)		
C11–O1	1.211(2)	-		
Bond angles (°)				
C4–N1–N2	121.5(1)	121.7(1)		
C5–C4–N1	96.03(1)	118.0(2)		
C4–C5–C10	121.5(1)	123.1(1)		
C5–C10–N3	119.2(1)	119.8(1)		
C10–N3–N3a / C10–N3–N4	115.9(1)	112.9(1)		
N3–N3a–C10a / N3–N4–C11	118.4(1)	111.4(1)		
N3a–C10a–C5a / N4–C11–C12	115.4(1)	121.5(1)		
C4a–N1a–N2a	-	121.1(1)		
C5a–C4a–N1a	-	121.1(1)		
C4a–C5a–C10a	-	121.6(1)		
O1–C11–C12	120.6(1)	-		
N4–C11–O1	123.9(1)	-		
Intermolecular interactions				
D–H⋯A	D–H (Å)	H⋯A (Å)	D⋯A (Å)	D–H⋯A (°)
1c				
N4–H4⋯N2ⁱ	0.89	2.12	3.005(2)	177.0
C7–H7⋯O1ⁱⁱ	0.93	2.43	3.194(2)	140.0
C9–H9⋯N5ⁱⁱⁱ	0.93	2.52	3.426(2)	166.0
C3–H3⋯N3^{iv}	0.93	2.74	3.494(2)	138.0
1c'				
C3a–H3a⋯N2ⁱ	0.93	2.46	3.378(2)	170.0
C8–H8⋯π (pyraz.)ⁱⁱ	0.93	3.16	4.031(2)	157.0

Symmetry codes: **1c** - *i* (-x, y, ½ - z); *ii* (-x, 2 - y, -z); *iii* (x - 1, 1 - y, z - ½); *iv* (-x, 1 - y, -z).
1c' - *i* (1 - x, -y, -z); *ii* (1 + x, y, z).

This unforeseen reaction was further investigated and was the subject of a very recent publication in Journal of Molecular Structure (Cukierman *et al.*, 2021). Our proposition is that the isonicotinoyl hydrazone may actually be formed at first, since imine generation usually occurs immediately upon the mixture of the

reactants, especially under acid catalysis conditions. However, further protonation on the carbonyl group increases the carbon's electrophilicity, making it susceptible to a nucleophilic attack by a solvent molecule (i.e., ethanol). The subsequent intramolecular electron rearrangement results in breaking of the N–C bond, thus producing a terminal hydrazone derived from the structure of the aldehyde. Since free aldehyde is still present in the reaction mixture, a new C=N bond is formed, yielding the dihydrazone **1c'**. In this publication, we present a comprehensive study on the structure of these compounds, including Hirshfeld surface and energy framework analyses, as well as gas-phase calculations and a thorough discussion on the different contributions from coupled vibrational modes to the main bands in their IR spectra. For the sake of simplicity and focus, these data will not be discussed herein. Moreover, we worked with another *ortho*-substituted benzaldehyde, also synthesized in collaboration with Prof. Jones Limberger, with which the same unexpected dihydrazone formation was observed. Additional ¹H NMR experiments and computational thermodynamic calculations afforded some mechanistic insights for these reactions. The identification of signals related to the formation of ethyl isonicotinate is consistent with the expected by-product resulting from the attack on the aroylhydrazone's carbonyl by ethanol, depicting thus a classic solvolysis reaction, followed by condensation of the ensuing hydrazone to a second free aldehyde molecule (Cukierman *et al.*, 2021).

The mid-IR spectra of the compounds confirm some of the structural aspects observed in the crystal structures. The spectrum of the precursor aldehyde (data not shown) shows the well-known aldehyde $\nu(\text{C-H})$ absorptions at around 2880 and 2765 cm^{-1} . These modes, however, are completely absent in the spectra of products **1c** (Appendix Figure 3) and **1c'** (Appendix Figure 4). Likewise, the lack of the aldehyde $\nu(\text{C=O})$ band at 1685 cm^{-1} was observed in the spectrum of **1c'**. However, it cannot be confirmed for aroylhydrazone **1c**, since this compound presents intense carbonyl coupled modes [$\nu(\text{C=O}) + \beta(\text{H-N-C})$] in the region. Another important vibrational mode observed in **1c** but not in **1c'** is the distinguishing $\nu(\text{N-H})$ absorption at 3185 cm^{-1} . On the other hand, coupled azomethine modes can be found in the spectra of both hydrazones, at 1619 [$\nu_{\text{as}}(\text{C=N}) + \beta(\text{H-C=N})$] for **1c'** and 1640 [$\nu(\text{C=N}) + \beta(\text{H-C=N})$] / 1562 [$\beta(\text{H-N-N}) + \beta(\text{H-C=N})$] cm^{-1} for the aroylhydrazone **1c**. These absorptions are in accordance with our previously

published isonicotinoyl hydrazones (González-Baró *et al.*, 2012; De Freitas *et al.*, 2013; Cukierman *et al.*, 2018). Characteristic pyrazole bands were assigned at 1394 (**1c'**) / 1397 (**1c**) cm^{-1} [$\nu(\text{N-N})$] and at 767 (**1c'**) / 768 (**1c**) cm^{-1} [$\gamma(\text{H-C})$].

With respect to the characterization of the compounds in solution, their ^1H NMR spectra in $\text{DMSO-}d_6$ are displayed in Figure 13 and Figure 14, respectively for **1c** and **1c'**. A secondary set of signals in the spectrum of *N*-acylhydrazone **1c** can be seen, being more easily observed near the deshielded NH signal around 12 ppm. These resonances are considerably small with respect to the major set, indicating low concentration in solution. Thus, only the main set of signals were quantified and marked in the spectrum. The aldehyde, characterized through its typical de-shielded hydrogen at 9.93 ppm (not shown), is clearly converted into azomethines, observed at 8.39 ppm in **1c** and at 8.52 ppm in **1c'**. In the former, a characteristic aroylhydrazone -NH singlet appears at 12.16 ppm, in accordance to previously published isonicotinoyl hydrazones (Cukierman *et al.*, 2018; Cukierman *et al.*, 2019). The equivalent hydrogens of the pyridinic ring derived from isoniazid, on the other hand, can be detected as a pair of doublets of doublets at 8.76 and 7.80 ppm in compound **1c**, also in accordance with our previous studies. They are obviously absent in the spectrum of **1c'**. Table 8 presents a thorough report of all the chemical shifts and couplings for the ^1H nuclei of both compounds.

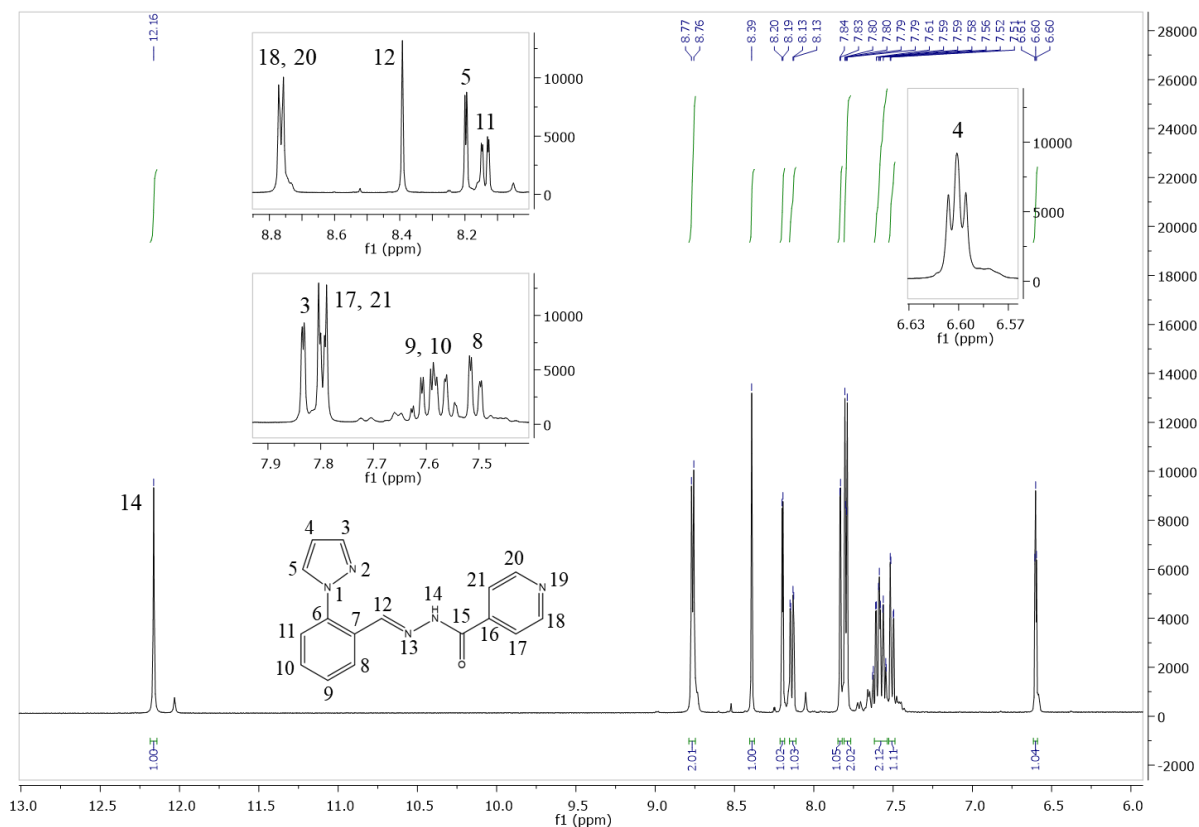


Figure 13. ^1H NMR spectrum of **1c** (400 MHz) in $\text{DMSO-}d_6$ at room temperature.

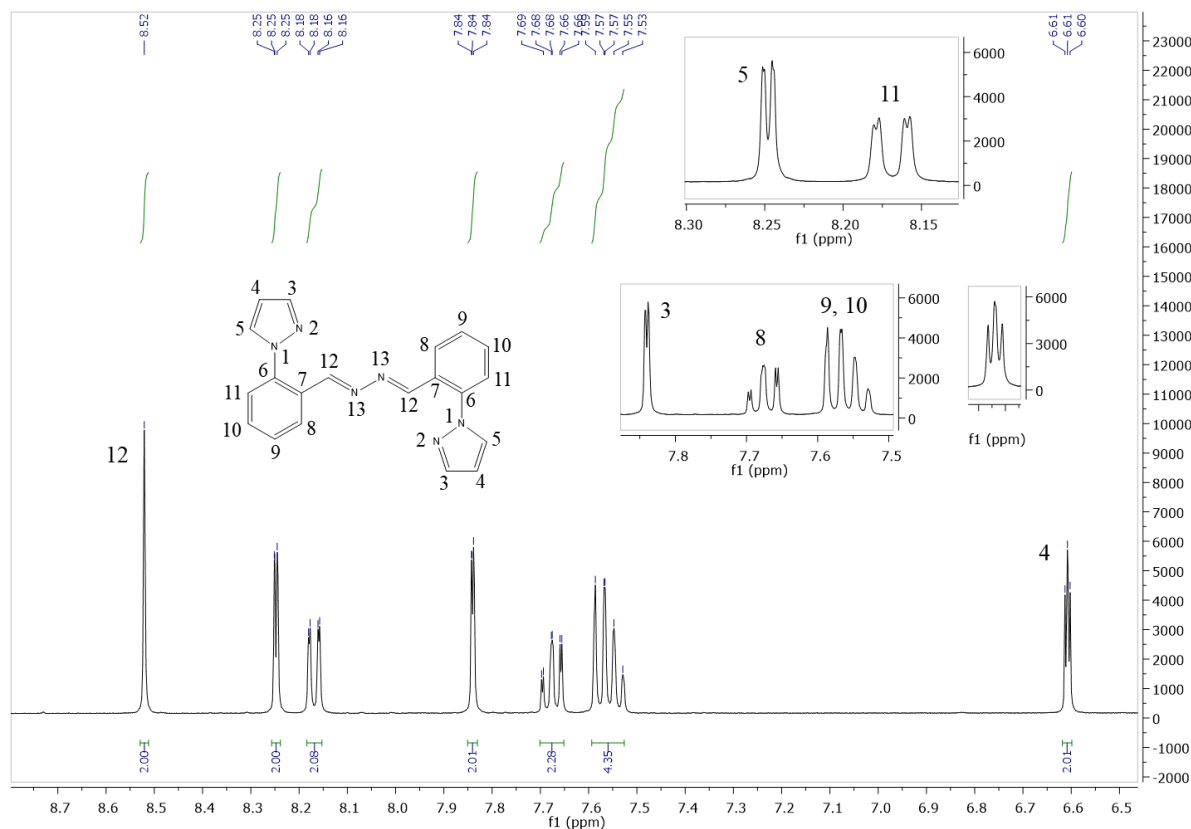


Figure 14. ^1H NMR spectrum of **1c'** (400 MHz) in $\text{DMSO-}d_6$ at room temperature.

Table 8. ^1H (400 MHz) data for compounds **1c** and **1c'** in $\text{DMSO-}d_6$ at room temperature.

^1H	1c δ (ppm)	1c' δ (ppm)
3	7.83 (d, 1H, $^3J = 2.0$ Hz)	7.84 (dd, 2H, $^3J = 1.9$ Hz, $^4J = 0.4$ Hz)
4	6.60 (t, 1H, $^3J = 2.0$ Hz)	6.61 (dd, 2H, $^3J = 1.9$ Hz, $^3J = 2.4$ Hz)
5	8.20 (d, 1H, $^3J = 2.0$ Hz)	8.25 (dd, 2H, $^3J = 2.4$ Hz, $^4J = 0.4$ Hz)
8	7.51 (dd, 1H, $^3J = 7.8$ Hz, $^4J = 1.5$ Hz)	7.68 (ddd, 2H, $^3J = 8.2$ Hz, $^4J = 7.3$ Hz, $^5J = 1.4$ Hz)
9	7.63-7.55 (m, 2H)*	7.59-7.53 (m, 4H)
10	7.63-7.55 (m, 2H)*	7.59-7.53 (m, 4H)
11	8.14 (dd, 1H, $^3J = 7.6$ Hz, $^4J = 1.6$ Hz)	8.17 (dd, 2H, $^3J = 7.8$ Hz, $^5J = 1.4$ Hz)
12	8.39 (s, 1H)	8.52 (s, 2H)
14	12.16 (s, 1H)	-
17	7.80 (dd, 2H, $^3J = 4.5$ Hz, $^5J = 1.4$ Hz)	-
18	8.76 (dd, 2H, $^3J = 4.5$ Hz, $^5J = 1.4$ Hz)	-
20	8.76 (dd, 2H, $^3J = 4.5$ Hz, $^5J = 1.4$ Hz)	-
21	7.80 (dd, 2H, $^3J = 4.5$ Hz, $^5J = 1.4$ Hz)	-

s: singlet, d: doublet, dd: doublet of doublets, ddd: doublet of doublet of doublets, t: triplet, m: multiplet.

* H7 is overlapped with H8. For this reason, C7 and C8 could not be specifically assigned.

Although structurally interesting, compound **1c** does not bind copper(II) efficiently [Cukierman *et al.* (18th International Conference on Biological Inorganic Chemistry, 2017)]. Figure 15 shows the UV-Vis spectrum of this compound, which presents a main band at around 300 nm. Upon addition of equimolar amount of CuCl_2 , only an effect of dilution can be observed in the spectrum, even after 3h30 under constant stirring. This clearly indicates the lack of significant interaction between **1c** and copper(II). Moreover, $^1\text{H} \times ^{15}\text{N}$ HSQC NMR spectra acquired for the system $\text{A}\beta$ peptide + Cu^{2+} showed no signal recovery upon addition of 1, 2, 3, 4, 5 or 10 equivalents of **1c** (data not shown). This was done in collaboration with the group of Prof. Dr. Claudio O. Fernández, from the Max Planck Laboratory for Structural Biology, Chemistry and Molecular Biophysics of Rosario, Argentina. For these reasons, the studies involving compound **1c** were limited to its structural characterization and additional dihydrazone formation. Thus, *N*-acylhydrazone **1c** was excluded from further steps of the project.

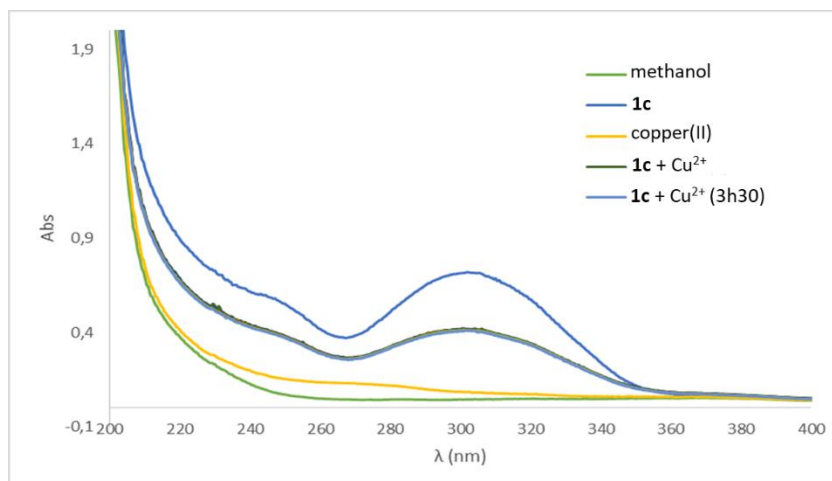


Figure 15. Study of the complexation potential of compound **1c** towards copper(II): Absorption UV-Vis spectra of compound **1c** in methanol, in the absence (dark blue) and presence (gray) of CuCl₂, and after 3h30 kept under constant stirring (light blue). Absorptions of methanol (green) and CuCl₂ methanolic solution (yellow) are shown for control purposes.

5.2.3. Compounds **1d**, **2d**, **3d** and **4d**: 1-methyl-1H-imidazole-2-carboxaldehyde *N*-acylhydrazones

The 1-methylimidazole-containing hydrazones differ from each other only with respect to the hydrazone-derived moiety, which can be 4-pyridyl, phenyl, 2-furanyl and 2-thiophenyl, respectively for compounds **1d**, **2d**, **3d** and **4d** (Figure 16). For this reason, their syntheses and characterization are discussed together herein, comparatively.

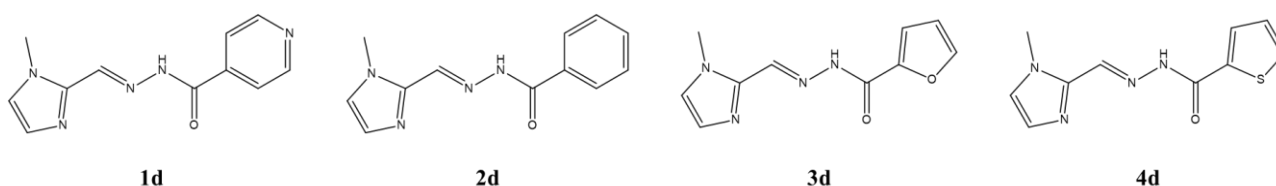


Figure 16. Structure of the 1-methyl-1H-imidazole-2-carboxaldehyde-derived *N*-acylhydrazones (i.e. compounds **1d**, **2d**, **3d** and **4d**)

The first 1-methylimidazole-containing compound, **1d** (namely 1-methyl-1H-imidazole-2-carboxaldehyde isonicotinoyl hydrazone), was obtained upon slow evaporation of the solvent after the reaction between 1-methyl-1H-imidazole-2-carboxaldehyde and isoniazid without the use of acid catalyst. The solid is composed of elongated and very thin needle-shaped microcrystals, resembling a

cotton-like morphology. Since this was the only 1-methylimidazole-containing compound that was not obtained as single crystals at first try, its hydrochloride form, from now on referred to as **1d'**, was prepared using 1 drop of HCl, thus fulfilling this goal. This isoniazid-derived system was recently described in a publication in a Special Issue of Dalton Transactions, which included not only chemical characterizations but also biological activity in a cellular model of synucleinopathy, which will be further described (Cukierman *et al.*, 2020).

Regarding the compound from the second series, **2d** (namely 1-methyl-1H-imidazole-2-carboxaldehyde benzoyl hydrazone), a white crystalline solid was obtained after the reaction between 1-methyl-1H-imidazole-2-carboxaldehyde and benzoyl hydrazone in ethanol at reflux and with 1 drop of HCl. During the 4 hours of reflux, no precipitation was observed but after slow evaporation of the solvent, the solid was formed. Single crystals were isolated from the mother-liquor.

Compound **3d** (namely 1-methyl-1H-imidazole-2-carboxaldehyde 2-furoyl hydrazone) was also obtained as a hydrochloride in the form of single crystals after slow precipitation of the reaction mixture. The brown solid is the product of the acid-catalyzed reaction between 1-methyl-1H-imidazole-2-carboxaldehyde and 2-furoic hydrazide, in ethanol.

Finally, the sulfur-containing compound **4d** (1-methyl-1H-imidazole-2-carboxaldehyde 2-thiophenyl hydrazone) was also obtained as yellow single crystals in its hydrochloride form isolated from the mother liquor of the reaction mixture between 1-methyl-1H-imidazole-2-carboxaldehyde and 2-thiophenyl hydrazone, in ethanol after 4 hours in reflux and in the presence of 1 drop of HCl.

All 1-methylimidazole-containing hydrazones crystallize as hydrochlorides in the monoclinic system, in different space groups, i.e. $P2_1$, $P2_1/c$, $P2_1/c$ and $P2_1/n$ respectively for compounds **1d'**, **2d**, **3d** and **4d**. Crystal, data collection and refinement parameters are summarized in Table 9, while selected bond distances, as well as important bond and dihedral angles, can be found in Table 10. The ORTEP representations of the crystal structures are displayed in Figure 17. As expected, only the (*E*) stereoisomer of the amido tautomeric form of all compounds is observed in the solid state due to its, *a priori*, higher stability related to a less steric hindrance. Likewise, the CO–NH bond *anti-periplanar* conformation is

adopted by these *N*-acylhydrazones. In compounds **1d'**, **3d** and **4d**, this is probably stabilized by non-conventional hydrogen bonds involving the chloride anion (Figure 18), with N4...Cl distances of 3.126(3), 3.155(1) and 3.193(1) Å, respectively (Table 11). Compound **2d**, on the other hand, presents a more complex hydrogen bond pattern, in which interactions between N4-H4n...O3 [2.818(2) Å] and O3-H3b...Clⁱⁱ [3.141(2) Å, symmetry code: (ii) -x, -y, -z] stabilize the *anti*-conformation with the presence of three water molecules in the crystal network.

Protonation of the compounds occur in the imidazole ring, at the N2 nitrogen. In the structure of **1d'**, this generates a network of moderate, mostly electrostatic (Steiner, 2002) intermolecular hydrogen interactions of the type N2-H2n...N5ⁱ [2.754(4) Å, symmetry code: (i) 1 - x, 1/2 + y, -z], in which the nitrogen atom from the pyridine ring of a neighboring hydrazone acts as a hydrogen acceptor. This interaction keeps the protonated **1d** units together, along zigzag chains running parallel to the crystallographic axis *b* (Figure 18A). It is worth noting that compound **1d'** is the only one from this group that presents no crystallization water, no π -stacking interactions and that the methyl group is pointed at the same direction of the carbonyl moiety, instead of opposed to it as observed in the other three structures, due to rotated C3-C4 bond. This suggests that these N2-H2n...N5 intermolecular interactions are stronger than the N2-H2n...Ox interactions that occur between compounds **2d**, **3d** and **4d** and water molecules. Moreover, π - π stacking probably also plays a role in this conformation in the latter compounds.

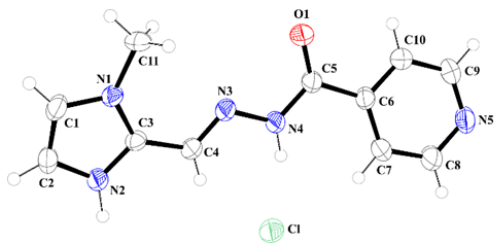
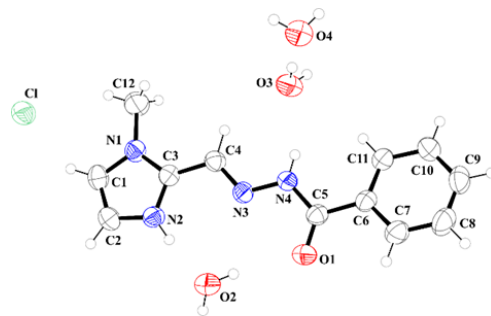
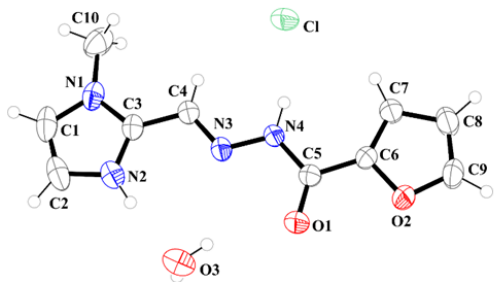
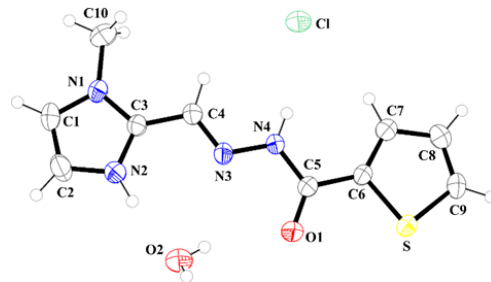
A**B****C****D**

Figure 17. ORTEP representation of the crystal structures of (A) **1d'**, (B) **2d**, (C) **3d** and (D) **4d**. The ellipsoids were drawn with 50% probability level.

Table 9. Crystal, data collection and refinement parameters for compounds **1d'**, **2d**, **3d** and **4d**.

Compound	1d'	2d	3d	4d
Formula	C ₁₁ H ₁₂ N ₅ OCl	C ₁₂ H ₁₉ N ₄ O ₄ Cl	C ₁₀ H ₁₃ N ₄ O ₃ Cl	C ₁₀ H ₁₃ N ₄ O ₂ SCl
Formula weight (g mol⁻¹)	265.71	318.76	272.69	288.75
Crystal system	Monoclinic	Monoclinic	Monoclinic	Monoclinic
Space group	P2 ₁	P2 ₁ /c	P2 ₁ /c	P2 ₁ /n
<i>a</i> (Å)	4.3066(4)	9.4095(6)	8.4271(2)	7.0656(4)
<i>b</i> (Å)	17.7428(11)	23.9779(10)	18.8539(5)	18.0958(6)
<i>c</i> (Å)	8.1657(5)	7.4947(5)	8.2549(2)	10.6824(4)
$\alpha = \gamma$ (°)	90.00	90.00	90.00	90.00
β (°)	102.475(7)	110.961(8)	102.381(3)	101.665(4)
<i>V</i> (Å³)	609.22(8)	1579.05(18)	1281.07(2)	1337.67(10)
<i>Z</i>	2	4	4	4
Temperature (K)	293(2)	293(2)	293(2)	293(2)
Crystal size (mm)	0.12 x 0.26 x 0.54	0.42 x 0.52 x 1.00	0.34 x 0.60 x 1.08	0.26 x 0.52 x 1.01
μ(Mo Kα) (mm⁻¹)	0.309	0.263	0.305	0.442
Refl. measured/ independent	7384 / 3951	20662 / 4022	33691 / 3451	2331 / 3383
<i>R</i>_{int}	0.0389	0.0322	0.0301	0.0363
Refined parameters	163	191	164	164
<i>R</i>_{obs} [<i>F</i>_o>2σ(<i>F</i>_o)]	0.0493	0.0436	0.0385	0.0344
<i>R</i>_{all}	0.815	0.0668	0.0494	0.0480
<i>wR</i>_{obs} [<i>F</i>_o²>2σ(<i>F</i>_o)²]	0.0919	0.1043	0.0985	0.0854
<i>wR</i>_{all}	0.1077	0.1185	0.1036	0.0936
<i>S</i>	1.047	1.020	1.072	1.052
$\Delta\rho_{\max}, \Delta\rho_{\min}$ (e Å⁻³)	0.262 / -0.239	0.310 / -0.226	0.263 / -0.215	0.260 / -0.215

Table 10. Selected geometric parameters for compounds **1d'**, **2d**, **3d** and **4d**.

Bond distance (Å)				
	1d'	2d	3d	4d
C3–C4	1.449(4)	1.447(2)	1.445(2)	1.442(2)
C4–N3	1.272(4)	1.272(2)	1.277(2)	1.275(2)
N3–N4	1.272(4)	1.356(2)	1.277(2)	1.356(2)
N4–C5	1.364(4)	1.365(2)	1.364(2)	1.367(2)
C5–O1	1.217(4)	1.223(2)	1.220(2)	1.221(2)
C5–C6	1.504(4)	1.489(2)	1.464(2)	1.466(2)
Bond angle (°)				
C3–C4–N3	120.0(3)	115.6(1)	116.6(1)	116.3(1)
C4–N3–N4	115.3(2)	118.2(1)	117.1(1)	117.3(1)
N3–N4–C5	117.5(2)	117.6(1)	117.1(1)	117.0(1)
N4–C5–C6	115.3(2)	116.4(1)	113.8(1)	115.4(1)
N4–C5–O1	123.1(3)	121.5(1)	123.0(2)	122.5(1)
C6–C5–O1	121.6(3)	122.5(1)	123.2(1)	122.2(1)
Torsion angle (°)				
C3–C4–N3–N4	179.7(3)	-178.9(1)	179.0(1)	178.0(1)
C4–N3–N4–C5	177.1(3)	176.7(1)	-179.1(1)	-178.5(1)
N3–N4–C5–C6	174.8(3)	-178.9(1)	-179.1(1)	177.9(2)
N3–N4–C5–O1	-4.7(5)	1.2(2)	2.9(2)	-2.6(2)
C7–C6–C5–O1	171.8(4)	-14.2(2)	177.4(2)	172.3(2)

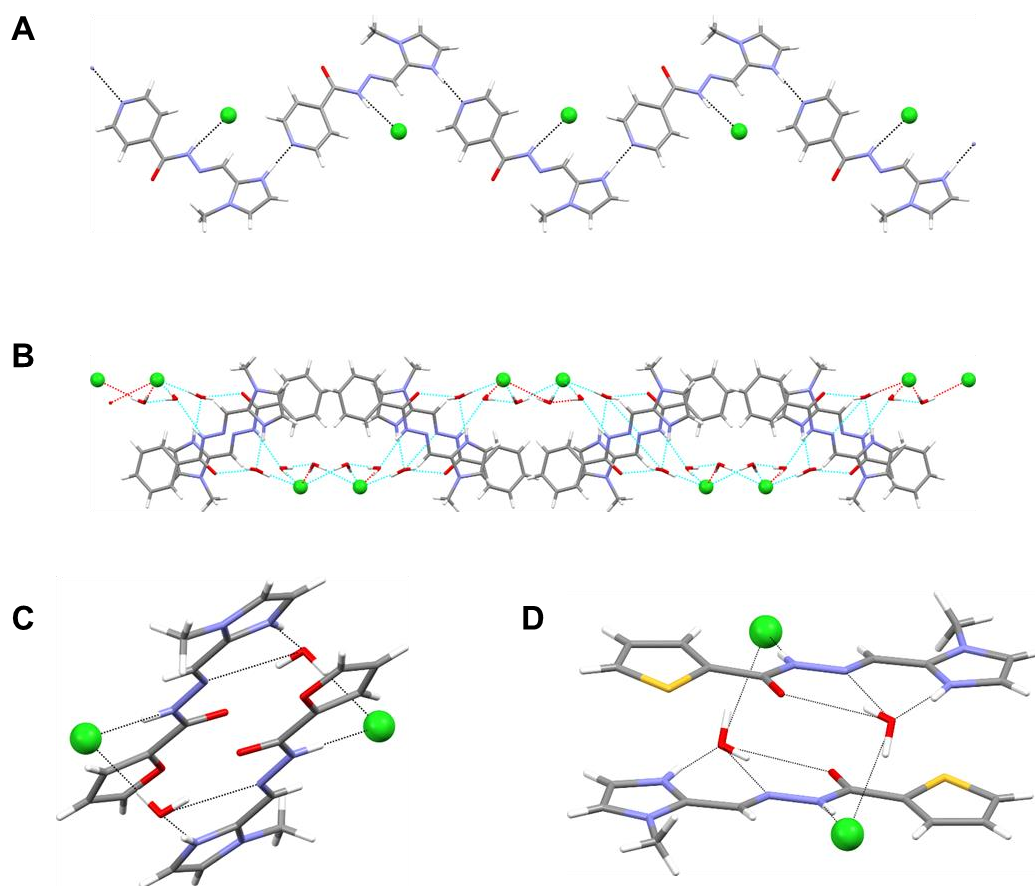


Figure 18. Hydrogen bond interactions in the crystal networks of compounds (A) 1d', (B) 2d, (C) 3d and (D) 4d.

Table 11. Hydrogen bond geometric parameters for compounds **1d'**, **2d**, **3d** and **4d**.

D–H⋯A	D–H (Å)	H⋯A (Å)	D⋯A (Å)	D–H⋯A (°)
1d'				
N2–H2n⋯N5 ⁱ	1.02	1.74	2.754(4)	171.0
N4–H4n⋯Cl	0.97	2.18	3.126(3)	165.0
Symmetry code: <i>i</i> (1 - <i>x</i> , ½ + <i>y</i> , - <i>z</i>)				
2d				
N2–H2n⋯O2	0.86	1.87	2.727(2)	173.0
N4–H4n⋯O3	0.80	2.05	2.818(2)	159.0
O2–H2a⋯Cl ⁱ	0.91	2.22	3.130(2)	174.0
O2–H2b⋯O1	0.83	2.15	2.959(2)	163.0
O2–H2b⋯N3	0.83	2.47	2.975(2)	120.0
O3–H3a⋯O4	0.88	1.91	2.786(2)	174.0
O3–H3b⋯Cl ⁱⁱ	0.85	2.30	3.141(2)	170.0
O4–H4a⋯Cl ⁱⁱⁱ	0.79	2.44	3.223(2)	174.0
O4–H4b⋯Cl ^{iv}	0.84	2.34	3.178(2)	174.0
Symmetry code: <i>i</i> (1 + <i>x</i> , <i>y</i> , <i>z</i>); <i>ii</i> (- <i>x</i> , - <i>y</i> , - <i>z</i>); <i>iii</i> (- <i>x</i> , ½ + <i>y</i> , ½ - <i>z</i>); <i>iv</i> (- <i>x</i> , - <i>y</i> , 1 - <i>z</i>)				
3d				
N2–H2n⋯O3	0.86	1.93	2.775(2)	169.0
N4–H4n⋯Cl	0.89	2.29	3.155(1)	163.0
O3–H3a⋯N3	0.82	2.43	3.025(2)	130.0
O3–H3a⋯O1	0.82	2.29	3.074(2)	161.0
O3–H3b⋯Cl ⁱ	0.87	2.23	3.097(1)	177.0
Symmetry code: <i>i</i> (1 - <i>x</i> , 1 - <i>y</i> , 1 - <i>z</i>)				
4d				
N2–H2n⋯O2	0.86	1.91	2.759(2)	172.0
N4–H4n⋯Cl	0.85	2.37	3.193(1)	166.0
O2–H2a⋯N3	0.76	2.44	2.985(2)	130.0
O2–H2a⋯O1	0.76	2.30	3.021(2)	160.0
O2–H2b⋯Cl ⁱ	0.86	2.34	3.216(1)	172.0
Symmetry code: <i>i</i> (1 - <i>x</i> , - <i>y</i> , 1 - <i>z</i>)				

As mentioned before, compounds **2d**, **3d** and **4d** presented π - π stacking interactions in their network always involving the contact between the 1-methylimidazole ring with the hydrazide-derived aromatic ring, i.e. benzene, furan and thiophene respectively, as can be observed in Figure 19. Geometric parameters for such interactions are displayed in Table 12.

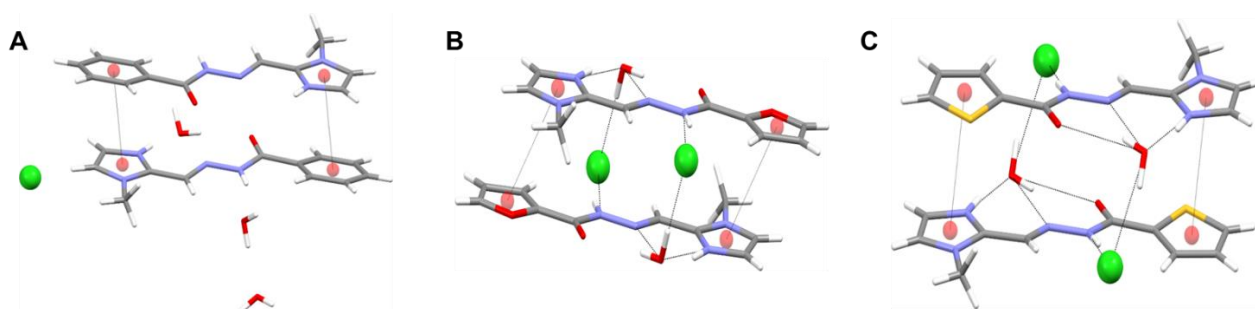


Figure 19. π - π stacking interactions in the structures of compounds **2d**, **3d** and **4d**.

Table 12. π - π stacking geometric parameters for compounds **2d**, **3d** and **4d**.

Compound	Centroid-centroid distance (Å)	Centroid-plane distance (Å)	Horizontal displacement (Å)
2d	3.532	3.449	0.76
3d	3.635	3.304	1.52
4d	3.632	3.392	1.30

Elemental analyses of carbon, hydrogen and nitrogen of the polycrystalline **1d** and single crystals **1d'**, **2d**, **3d** and **4d** were performed to evaluate the state of hydration of the former and to confirm the homogeneity of the crystalline samples. For the crystals, theoretical values were calculated using the protonation state, counter-ions and crystallization solvents observed in the XRD structures. Table 13 shows the calculated and experimental values of each of these elements for all the 1-methylimidazol-containing *N*-acylhydrazones. All percentages are in accordance with their proposed calculated values.

Table 13. Calculated and experimental elemental analyses of the 1-methylimidazole-derived compounds **1d**, **1d'**, **2d**, **3d** and **4d**.

	C		H		N	
	Calc	Exp	Calc	Exp	Calc	Exp
(1d) C ₁₁ H ₁₇ N ₅ O ₄	46.6%	47.2%	6.0%	6.0%	24.7%	25.4%
(1d') C ₁₁ H ₁₂ N ₅ OCl	49.7%	50.8%	4.6%	4.8%	26.4%	27.4%
(2d) C ₁₂ H ₁₉ N ₄ O ₄ Cl	45.2%	45.4%	6.0%	6.0%	17.6%	18.1%
(3d) C ₁₀ H ₁₃ N ₄ O ₃ Cl	44.0%	43.7%	4.8%	4.8%	20.6%	20.5%
(4d) C ₁₀ H ₁₃ N ₄ O ₂ SCl	41.6%	41.4%	4.5%	4.5%	19.4%	19.3%

Thermal decomposition of the polycrystalline solid occurs in two well-defined steps. The **1d** TG curve (Appendix Figure 5) indicates the loss of three water molecules under 100 °C, corresponding to 18.5% of the total mass, in agreement with the CHN elemental analysis. Its monocrystals **1d'**, on the other hand, presents only the thermal degradation of the organic moiety, in two steps, between 200 and 700 °C (Appendix Figure 6), consistent with the lack of solvent observed in the crystal lattice. With respect to compound **2d**, its crystal structure is composed of a very complex and intricate hydrogen bond network, as evidenced in Figure 18, which is reflected in its thermogravimetric curve (Appendix Figure 7): the loss of one hydration water molecule initiates the whole process of thermal degradation. Compounds **3d** and **4d**, on the other hand, present very similar structures and hydrogen bond patterns, as well as TG curves, which show two mass losses between 200 and 300 °C corresponding to the release of a hydration water molecule followed by the loss of HCl, being these curves more pronounced in the latter compound (Appendix Figure 8 and Appendix Figure 9).

Still in the solid state, the IR spectra of compounds **1d**, **1d'**, **2d**, **3d** and **4d** can be observed in Appendix Figure 10, Appendix Figure 11, Appendix Figure 12, Appendix Figure 13 and Appendix Figure 14, respectively. Typical aroylhydrazone bands, such as $\nu(\text{N-H})$, $\nu(\text{C=O})$, $\nu(\text{C=N})$, $\nu(\text{N-N})$, as well as imidazole vibrations, are common to all spectra and summarized in Table 14. It is important to note that imidazole C–N and C–C bonds are usually seen as coupled bands (Di Santo *et al.*, 2018). Additionally, specific absorptions rising from the aromatic substituent in the hydrazide-derived moieties are also present. The thiophene C–S–C stretching, for

example, occurs at 852 cm⁻¹ in compound **4d** (Nogueira *et al.*, 2016), while a pair of bands related to $\nu(\text{C-O})$ modes of the furan ring are noted at 1033 and 957 cm⁻¹ in compound **3d**'s spectrum (Kwiatkowski *et al.*, 1997).

Table 14. Selected infrared frequencies of compounds **1d**, **1d'**, **2d**, **3d** and **4d**, along with their assignments. Samples were prepared as KBr pellets.

Assignment	1d	1d'	2d	3d	4d
	IR (cm ⁻¹)				
$\nu(\text{N-H})$	3103	3130	3102	3091	3102
$\nu(\text{C=O})$	1684	1671	1680	1658	1672
$\nu(\text{C=N})_{\text{azomethine}}$	1615	1614	1619	1621	1629
$\nu(\text{N-N})$	1162	1131	1133	1131	1137
$\nu(\text{C-N}) / \nu(\text{C-C})_{\text{imidazole}}$	1498, 1473 and 1460	1520, 1497 and 1475	1524, 1494 and 1481	1483, 1467 and 1454	1508, 1478 and 1467
$\nu(\text{N}^+-\text{H})_{\text{imidazole}}$	–	3141	3153	3148	3127

As mentioned before, isoniazid-derived compound **1d** was obtained both in its polycrystalline free-base and single crystal hydrochloric (**1d'**) forms. Due to the huge difference in the yields of each synthesis, the free-base form, **1d**, was produced in a larger amount and, therefore, employed in all the future assays described in this work. The hydrochloric **1d'** was proposed for solid state characterization purposes only. However, in order to compare the solution ¹H NMR of all methylimidazole-derived *N*-acylhydrazones, a ¹H NMR spectrum of **1d'** was also obtained, since all the other compounds are also protonated as hydrochlorides. Moreover, due to the use of free-base **1d** in solutions employed in the future steps of the project, this compound was also characterized in DMSO-*d*₆ solution (Figure 20).

The ¹H NMR spectrum of **1d** (Figure 20A) shows two corresponding sets of signals, probably referring to the presence of tautomers amido and iminol in solution. Our proposition is that the (*E*)-amido form predominates significantly and, for this reason, the assignment of only the main set of signals present in the spectrum was performed. On the other hand, the spectra of hydrochlorides **1d'**, **2d**, **3d** and **4d** show only one quantifiable set of signals. The protonated imidazole N–H signal was not observed in these spectra, probably due to fast proton exchange in

the presence of water in the DMSO- d_6 solvent. Moreover, it is worth noting that all hydrogens are slightly more shielded in compound **1d** when compared to its hydrochloride **1d'**, being this effect more relevant for the imidazole C–H absorptions (signals 4 and 5), as well as the azomethine C–H6 signal (Figure 20B). Protonation in the imidazole nitrogen promotes inductive and electron delocalization effects, making the neighboring hydrogens more deshielded in **1d'**. Characteristic hydrazoneic N–H, nevertheless, also shows a pronounced difference in chemical shift of 0.9 ppm when comparing both forms of this isoniazid-derived hydrazone. All chemical shifts and signals attribution are described in Table 15. Spectra of compounds **2d**, **3d** and **4d** can be seen in Figure 21, Figure 22 and Figure 23, respectively.

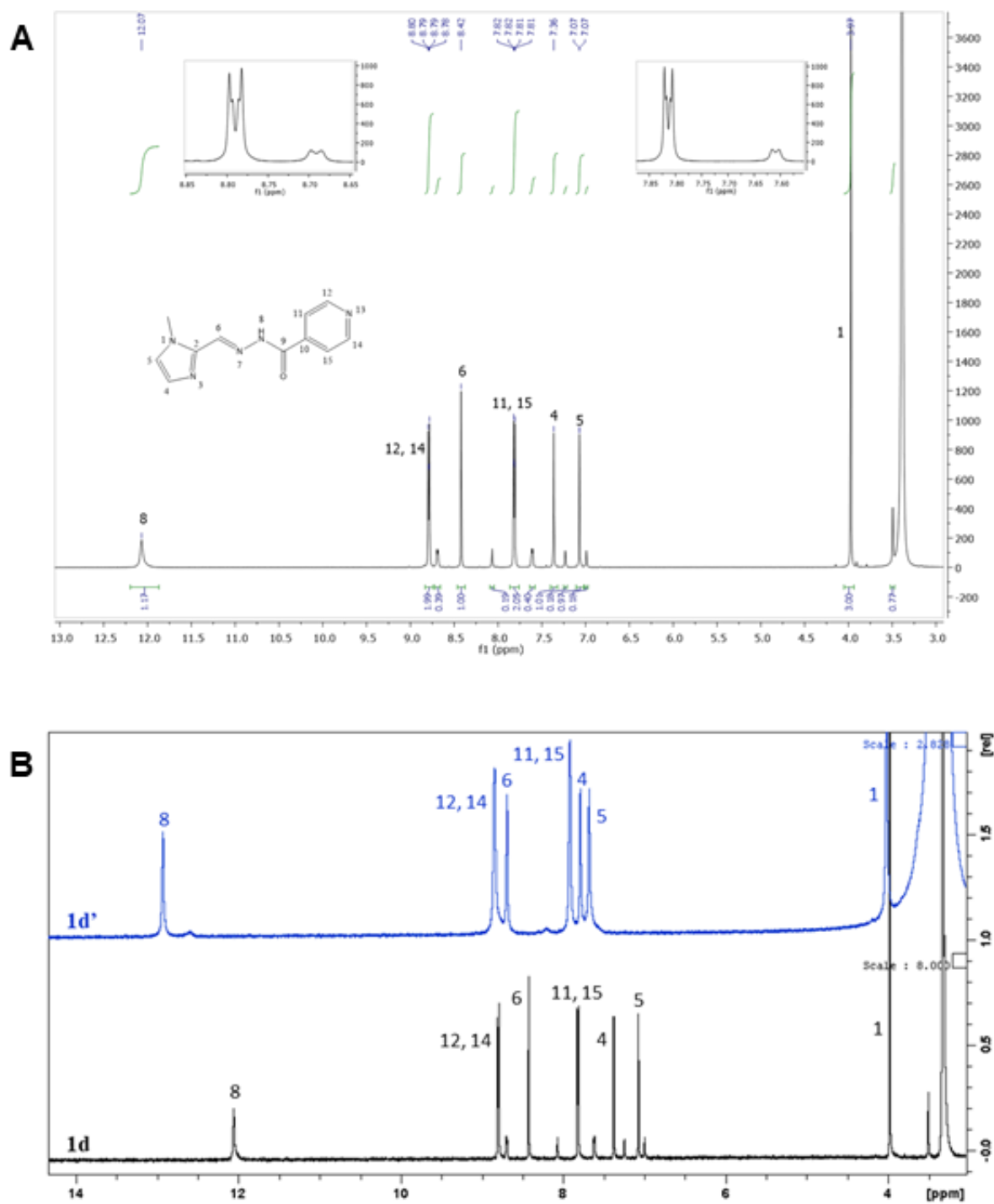


Figure 20. (A) ¹H NMR spectrum of compound **1d** (400 MHz) in DMSO-*d*₆ at room temperature. (B) Comparison between the ¹H NMR spectra (400 MHz) of **1d** and its hydrochloride **1d'** in DMSO-*d*₆ at room temperature.

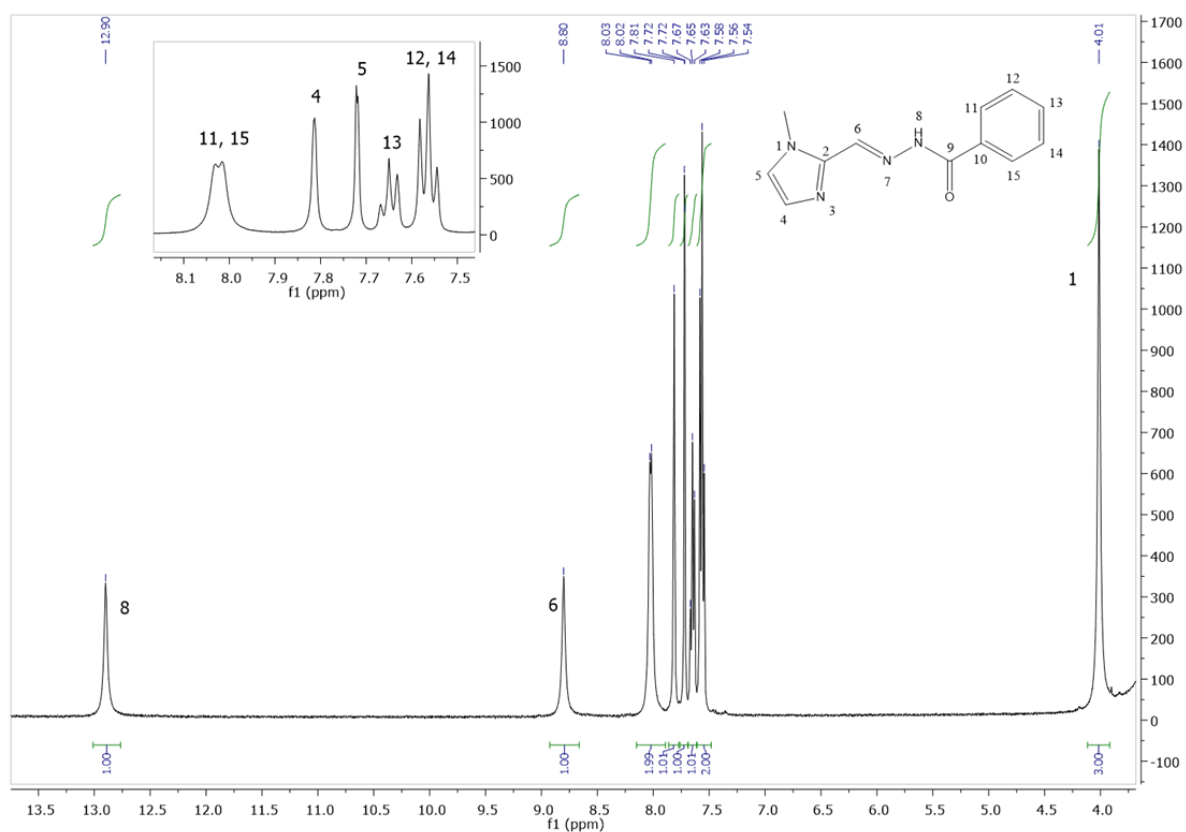


Figure 21. ^1H NMR spectrum of **2d** (400 MHz) in $\text{DMSO-}d_6$ at room temperature.

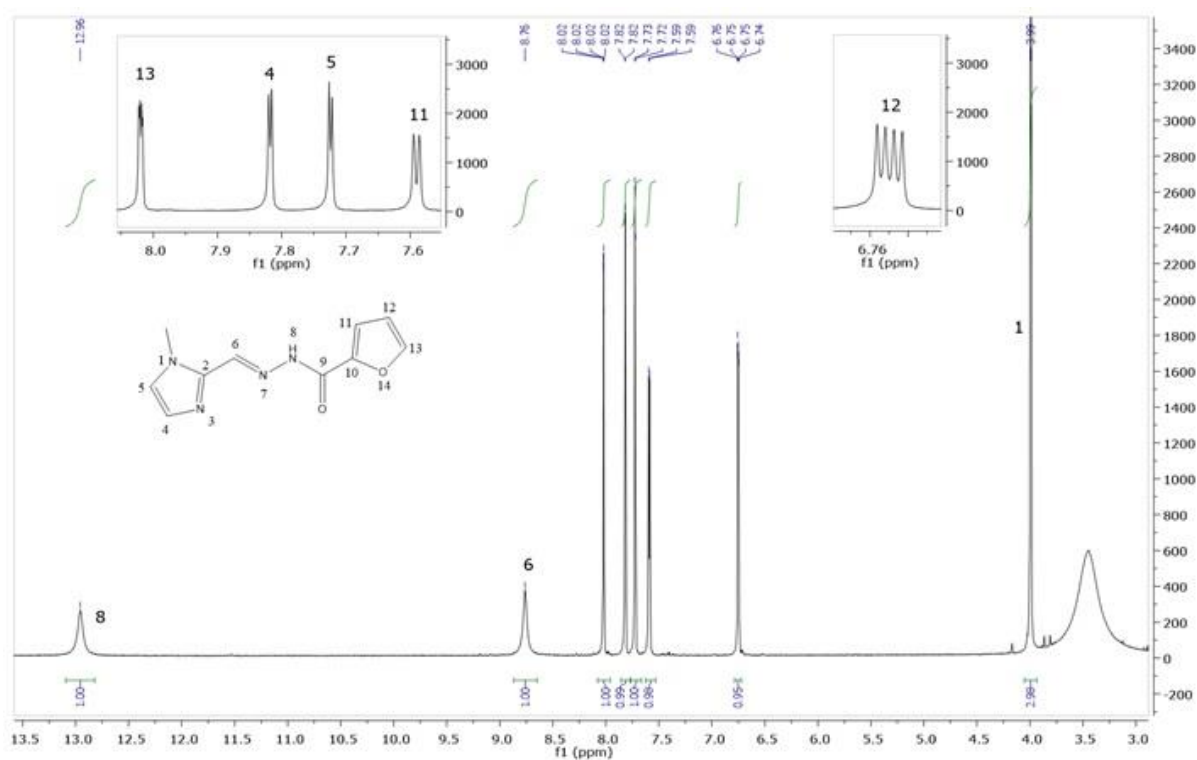


Figure 22. ^1H NMR spectrum of **3d** (400 MHz) in $\text{DMSO-}d_6$ at room temperature.

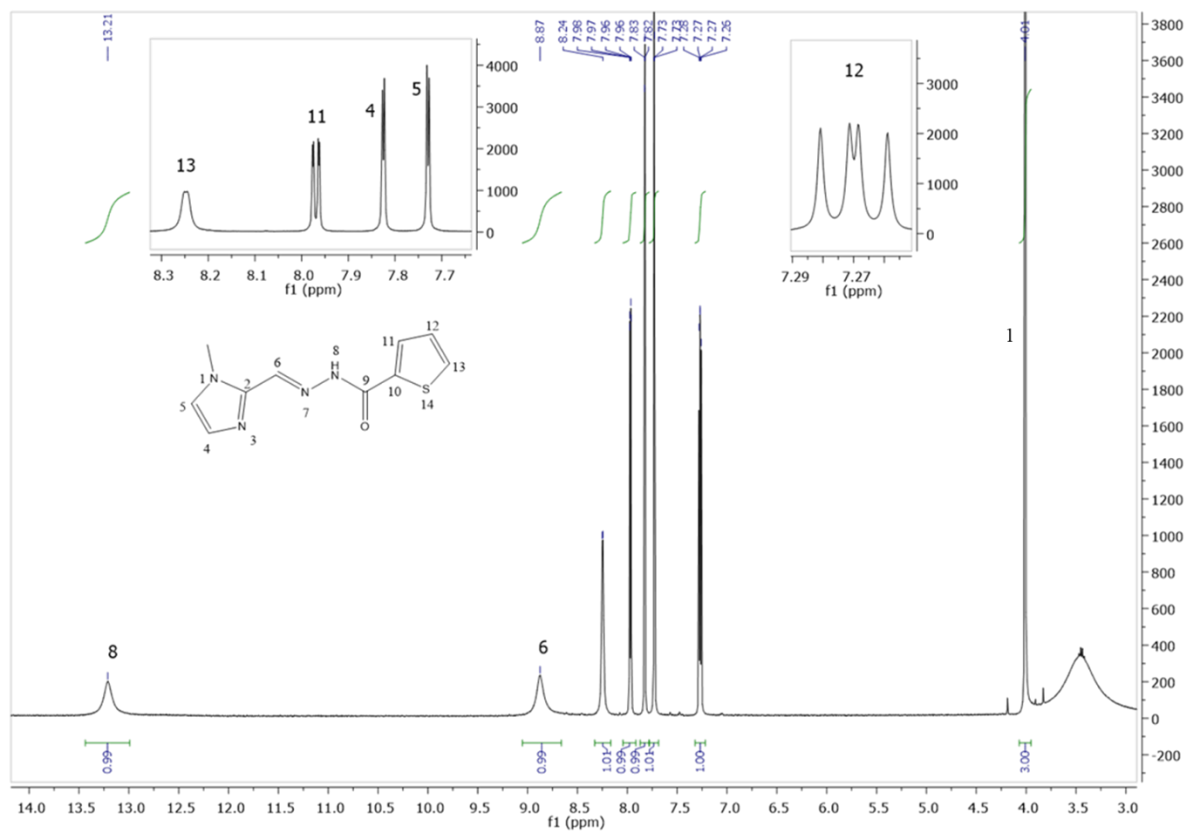


Figure 23. ^1H NMR spectrum of **4d** (400 MHz) in $\text{DMSO-}d_6$ at room temperature.

Table 15. Comparative ^1H (400 MHz) signal attribution for the 1-methyl-1H-imidazole-2-carboxaldehyde-derived compounds (i.e. compounds **1d**, **1d'**, **2d**, **3d** and **4d**), in DMSO- d_6 solution at room temperature.

H / δ (ppm)	1d	1d'	2d	3d	4d
1	3.97 (s, 3H)	4.01 (s, 3H)	4.01 (s, 3H)	3.99 (s, 3H)	4.01 (s, 3H)
2	-	-	-	-	-
3	-	-	-	-	-
4	7.36 (s, 1H)	7.79 (s, 1H)	7.81 (s, 1H)	7.82 (d, 1H)	7.83 (d, 1H)
5	7.07 (d, 1H)	7.68 (s, 1H)	7.72 (d, 1H)	7.73 (d, 1H)	7.73 (d, 1H)
6	8.42 (s, 1H)	8.69 (s, 1H)	8.80 (s, 1H)	8.76 (s, 1H)	8.87 (s, 1H)
7	-	-	-	-	-
8	12.07 (s, 1H)	12.93 (s, 1H)	12.90 (s, 1H)	12.96 (s, 1H)	13.21 (s, 1H)
9	-	-	-	-	-
10	-	-	-	-	-
11	7.82 (dd, 2H)	7.92 (b, 2H)	8.02 (d, 2H)	7.59 (d, 1H)	7.97 (dd, 1H)
12	8.79 (dd, 2H)	8.84 (b, 2H)	7.56 (t, 2H)	6.75 (dd, 1H)	7.27 (dd, 1H)
13	-	-	7.65 (t, 1H)	8.02 (dd, 1H)	8.25 (d, 1H)
14	8.79 (dd, 2H)	8.84 (b, 2H)	7.56 (t, 2H)	-	-
15	7.82 (dd, 2H)	7.92 (b, 2H)	8.02 (d, 2H)	-	-

s: singlet, d: doublet, dd: doublet of doublets, t: triplet, b: broad signal.

5.2.4. Compound 1e: 2-hydroxy-3-methoxy-benzaldehyde isonicotinoyl hydrazone

This *N*-acylhydrazone has been the subject of a previous detailed solution study in our research group, which has proven its very low stability against hydrolysis (De Falco, 2017). Figure 24 displays its UV-Vis absorption profile over 30 hours, together with that of the precursor 2-hydroxy-3-methoxy-benzaldehyde (*ortho*-vanillin), showing that the hydrazone is rapidly hydrolyzed over time. The presence of an isosbestic point at 272 nm indicates the equilibrium between two absorbing species (the hydrazone itself and its hydrolysis product *ortho*-vanillin). Thus, although considered suitable from the theoretical point of view, compound **1e** was excluded from the present project due to its low stability in solution.

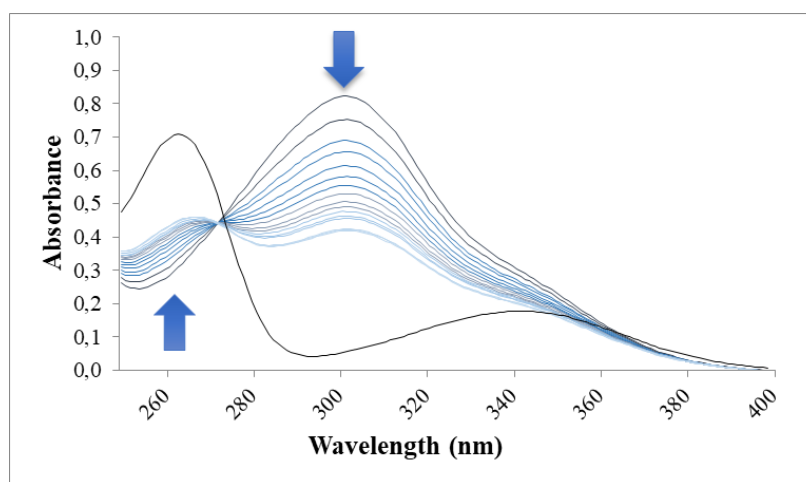


Figure 24. Electronic molecular absorption spectra of compound **1e** in 10% DMSO taken at regular intervals for 30 hours. The spectrum of the precursor 2-hydroxy-3-methoxy-benzaldehyde, in the same solvent, is shown in black. Blue arrows indicate the temporal changes that occur. Reproduced with the author's approval (De Falco, 2017).

5.2.5. Compounds **1f** and **3f**: pyridine-2-carboxaldehyde *N*-acylhydrazone

The syntheses and characterization of both ligands have already been described in the literature and they were prepared accordingly (Richardson *et al.*, 1999; Richardson *et al.*, 2006; Zamani *et al.*, 2006; Bernhardt *et al.*, 2007). Both solids are white and correspond to the products of the condensation between pyridine-2-carboxaldehyde and isoniazid (**1f**) or 2-furoic acid hydrazide (**3f**). The aldehyde must be distilled immediately prior to its use due to its rapid oxidation when exposed to the atmosphere. We have characterized compound **1f**, also known in the literature as HPCIH, in detail in a recent publication in *Journal of Biological Inorganic Chemistry*, together with its evaluation as an MPAC for the treatment of Alzheimer's (Cukierman *et al.*, 2018). Since its crystal structure was already described by other groups, single crystals obtained during the synthesis were not further analyzed (Richardson *et al.*, 1999). Likewise, we have also published the characterization of compound **3f** (also called HPCFur) in the same journal one year later, regarding its potential as a peptide protecting agent against the copper-catalyzed oxidation in the context of prion diseases (Cukierman *et al.*, 2019).

Thermal decomposition of **1f** occurs in two steps (Appendix Figure 15). The mass loss percentage of the first step, around 100 °C, is consistent with the presence of two water molecules, which confirms the results obtained by elemental analysis

and the composition described in the original patent application about this ligand (Richardson *et al.*, 2006) ($C_{12}H_{10}N_4O \cdot 2 H_2O$, MW = 262.26 g mol⁻¹). The second mass loss step corresponds to the total degradation of the organic ligand. After 350 °C, there is no more residue left. With respect to compound **3f**, its decomposition occurs in three steps, as shown in the TG curve of Appendix Figure 16. The first stage around 100 °C is also related to the loss of hydration water, in this case one molecule only, originating the formula $C_{11}H_9N_3O_2 \cdot H_2O$, with molecular weight of 233.20 g mol⁻¹. The ligand then decomposes in two steps, presenting no stable residue after 650 °C.

The two ligands inhere described are very closely related to one another. Thus, as expected, their IR spectra share great similarities. They are displayed in Appendix Figure 17 and Appendix Figure 18, while the main bands of both hydrazones and their assignments are displayed in Table 16.

Table 16. Selected infrared frequencies of compounds **1f** and **3f**, along with their assignments. Samples were prepared as KBr pellets.

Assignment	1f IR (cm ⁻¹)	3f IR (cm ⁻¹)
v(NH)	3450	3425
v(OH) _{water}	3270	3235
v(CH) _{aromatic}	3072 / 3030	3135 / 3055
v(CH) _{azomethyne}	2853	2859
v(C=O)	1663	1660
v(C=N) _{azomethyne}	1621	1640
v(C=N) _{pyridine}	1606	1600
v(C=C) _{aromatic}	1571 / 1472	1580 / 1469
v(N-N)	1146	1141
v(CO) _{furan}	–	1085

The vibrations of the foremost chemical groups present were identified, such as the C=N_{azomethine} bond, which is formed upon reaction between pyridine-2-carboxaldehyde and the respective aroylhydrazide and constitutes the main band to determine the success of the syntheses. The key difference between the ligands is the presence of the furan ring, which can be observed only in **3f**'s spectrum, at

around 1085 cm^{-1} , as a characteristic stretching band involving the carbon-oxygen bond (Kwiatkowski *et al.*, 1997). Both ligands contain aromatic and pyridine-related absorptions, as well as bands arising from the presence of hydration water in the structure, in agreement with the thermogravimetric analyses.

In solution, the ^1H NMR spectrum of compound **1f** clearly shows three sets of signals (Figure 25), which indicates the presence of three species in solution. For each of the three systems, it is possible to observe eight different resonances corresponding to the ten hydrogens of the molecule, since there are two cases of magnetic equivalence. The relative integration of the signals led us to propose that there are 85% of the (*E*)-amido and 14% of the (*E*)-iminol tautomers and 1% of the (*Z*)-amido isomer. The most deshielded signals in the ^1H spectrum correspond either to the N9–H (amido) or to the O11–H (iminol) nucleus. For the (*E*)-amido isomer, this signal is observed at 12.26 ppm due to the interaction of N9–H with the solvent, with a slight overlap of the signal of O11–H of its (*E*)-iminol tautomer. In contrast, the (*Z*)-amido isomer shows the most deshielded signal, at 15.75 ppm, due to an N9–H \cdots N2 intramolecular hydrogen bond. As for all compounds described herein, additional ^{13}C and two-dimensional experiments such as COSY, HSQC and HMBC were employed to unequivocally assign all the signals and these data are not shown for the sake of simplicity. They are, however, in this case, available in the literature (Cukierman *et al.*, 2018; Cukierman *et al.*, 2019). Compound **3f**, on the other hand, presents only one quantifiable main species in DMSO- d_6 solution – the (*E*)-amido tautomer, although minor species seems to be present in extremely low amounts, as can be observed in Figure 26. Overall the spectrum of **3f** is remarkably similar to that of **1f**, as expected, with a slight deshielded NH signal for the latter. Moreover, characteristic furan absorptions are present, such as the double of duplets C–H14 at 6.72 ppm.

Table 17 summarizes the signals and attributions made for the ^1H spectra of both compounds.

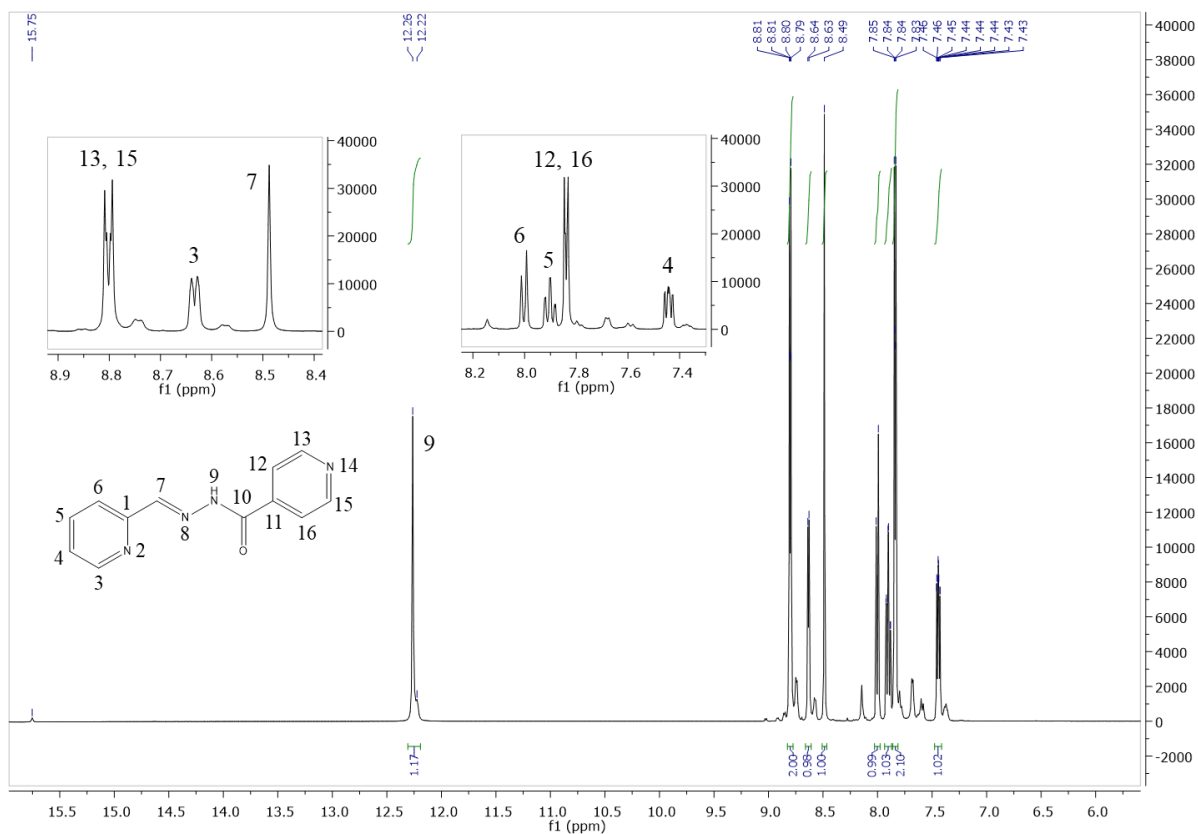


Figure 25. ^1H NMR spectrum of **1f** (400 MHz) in $\text{DMSO}-d_6$ at room temperature.

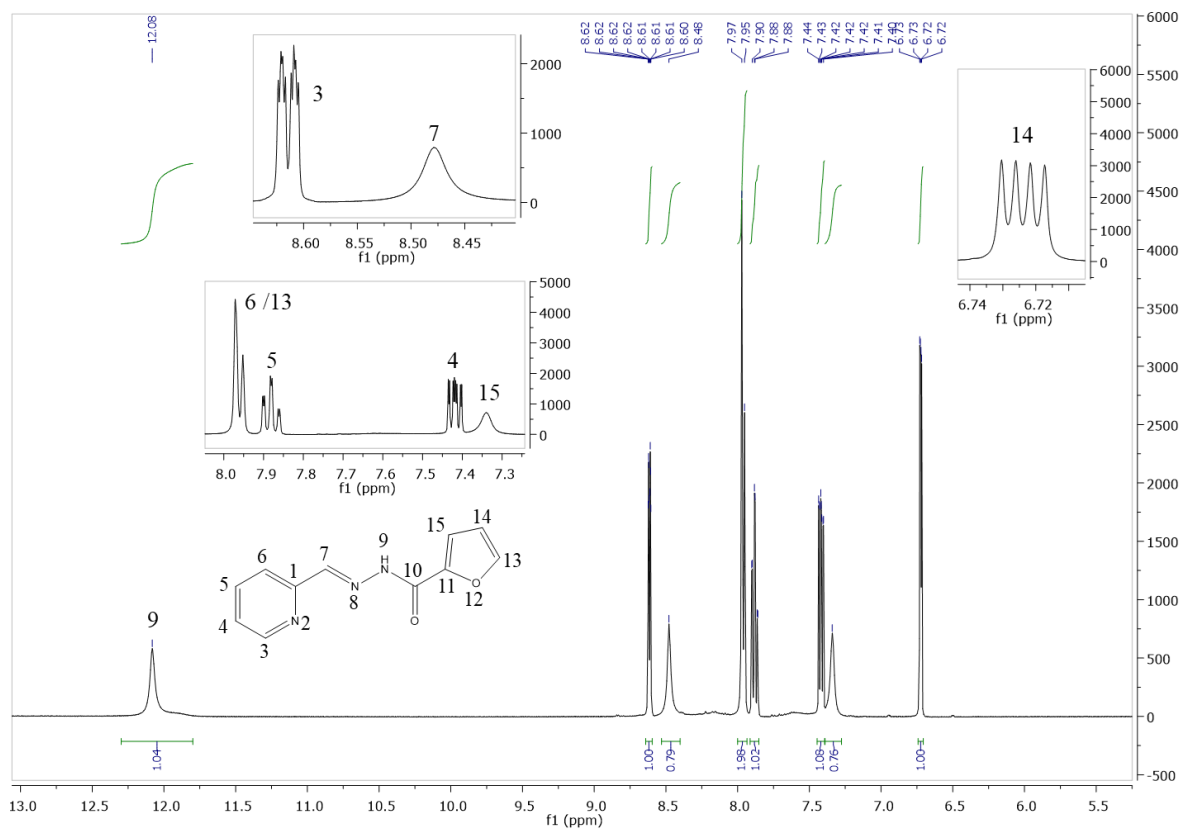


Figure 26. ^1H NMR spectrum of **3f** (400 MHz) in $\text{DMSO}-d_6$ at room temperature.

Table 17. Comparative ^1H (400 MHz) signal attribution for compounds **1f** and **3f** in $\text{DMSO-}d_6$, at room temperature.

H / δ (ppm)	1f	3f
1	-	-
2	-	-
3	8.63 (dd, 1H, $^3J = 4.9$ Hz, $^4J = 1.5$ Hz)	8.62 (ddd, 1H, $^3J = 4.8$ Hz, $^4J = 1.6$ Hz, $^5J = 1.0$ Hz,)
4	7.45 (ddd, 1H, $^3J = 7.4$ Hz, $^3J = 4.9$ Hz, $^4J = 1.1$ Hz)	7.42 (ddd, 1H, $^3J = 7.7$ Hz, $^3J = 4.8$ Hz, $^4J = 1.3$ Hz)
5	7.90 (td, 1H, $^3J = 7.9$ Hz, $^3J = 7.4$ Hz, $^4J = 1.5$ Hz)	7.88 (td, 1H, $^3J = 7.7$ Hz, $^4J = 1.6$ Hz)
6	8.00 (dd, 1H, $^3J = 7.9$ Hz, $^4J = 1.1$ Hz)	7.96 (d, 1H, $^3J = 7.7$ Hz)
7	8.49 (s, 1H)	8.48 (s, 1H)
8	-	-
9	12.26 (s, 1H)	12.08 (s, 1H)
10	-	-
11	-	-
12	7.84 (d, 2H, $^3J = 4.5$ Hz, $^4J = 1.6$ Hz)	-
13	8.80 (dd, 2H, $^3J = 4.5$ Hz, $^4J = 1.6$ Hz)	7.97 (b, 1H)
14	-	6.72 (dd, 1H, $^3J = 3.5$ Hz, $^3J = 1.7$ Hz)
15	8.80 (dd, 2H, $^3J = 4.5$ Hz, $^4J = 1.6$ Hz)	7.34 (b, 1H)
16	7.84 (d, 2H, $^3J = 4.5$ Hz, $^4J = 1.6$ Hz)	-

s: singlet, d: doublet, dd: doublet of doublets, ddd: doublet of doublet of doublets
td: triplet of doublets, b: broad signal.

Since compounds **1f** and **3f** are closely related, the electronic effect of their heterocyclic substituents can be evaluated through ^{13}C NMR, as the chemical shift of the vicinal carbonyl group. For **1f**, carbonyl resonates at 162.90 ppm, while for **3f**, this group is more shielded, being registered at 154.35 ppm (data not shown). The carbonyl's electronic environment may have direct impact on the intensity of electron donation in metal coordination, resulting in different binding affinities.

**5.2.6. Compound 1h (lead compound):
8-hydroxyquinoline-2-carboxaldehyde isonicotinoyl
hydrazone**

Compound **1h** (INHHQ) is the lead compound of the present study. It has been extensively studied by our research group (De Freitas *et al.*, 2013; Hauser-Davis *et al.*, 2015; Cukierman *et al.*, 2017; De Falco *et al.*, 2020). This crystalline light-yellow compound was obtained after recrystallization of the product of the reaction between 8-hydroxyquinoline-2-carboxaldehyde and isoniazid as described by de Freitas *et al.* (De Freitas *et al.*, 2013). Characterization was based on the literature and the author's long experience in working with this compound and will not be discussed again in herein.

**5.2.7. Compound 1i:
4-chloro-3-formylcoumarin isonicotinoyl hydrazone**

This yellow solid was obtained after the condensation between 4-chloro-3-formylcoumarin and isoniazid in ethanol, without any acid catalyst, with precipitation occurring 15 minutes after the dropwise addition of the hydrazide over the lactone. When heated at 215 °C, the solid turns black, indicating decomposition and thus precluding its melting point determination. This also imposed some difficulties in studying the thermal degradation of this organic ligand.

In solution, its ¹H NMR spectrum (Figure 27) shows the presence of at least two sets of signals, demonstrating that an equilibrium occurs in DMSO-*d*₆. All 10 hydrogens that compose the main set of signals were assigned based on the literature (Angelova *et al.*, 2016) and confirmed using bidimensional spectra (not shown). Characteristic hydrazonic N–H and H–C=N singlets resonate in the expected region, similarly to all *N*-acylhydrazones described in this project, in 12.34 and 8.66 ppm, respectively. Distinctive *para*-pyridine doublets are also in accordance with their likely chemical shift. It is worth noting that the initially yellow solution turned dark red inside the NMR tube within a few days, indicating low stability of this sample in solution, which was later demonstrated by UV-Vis analyses.

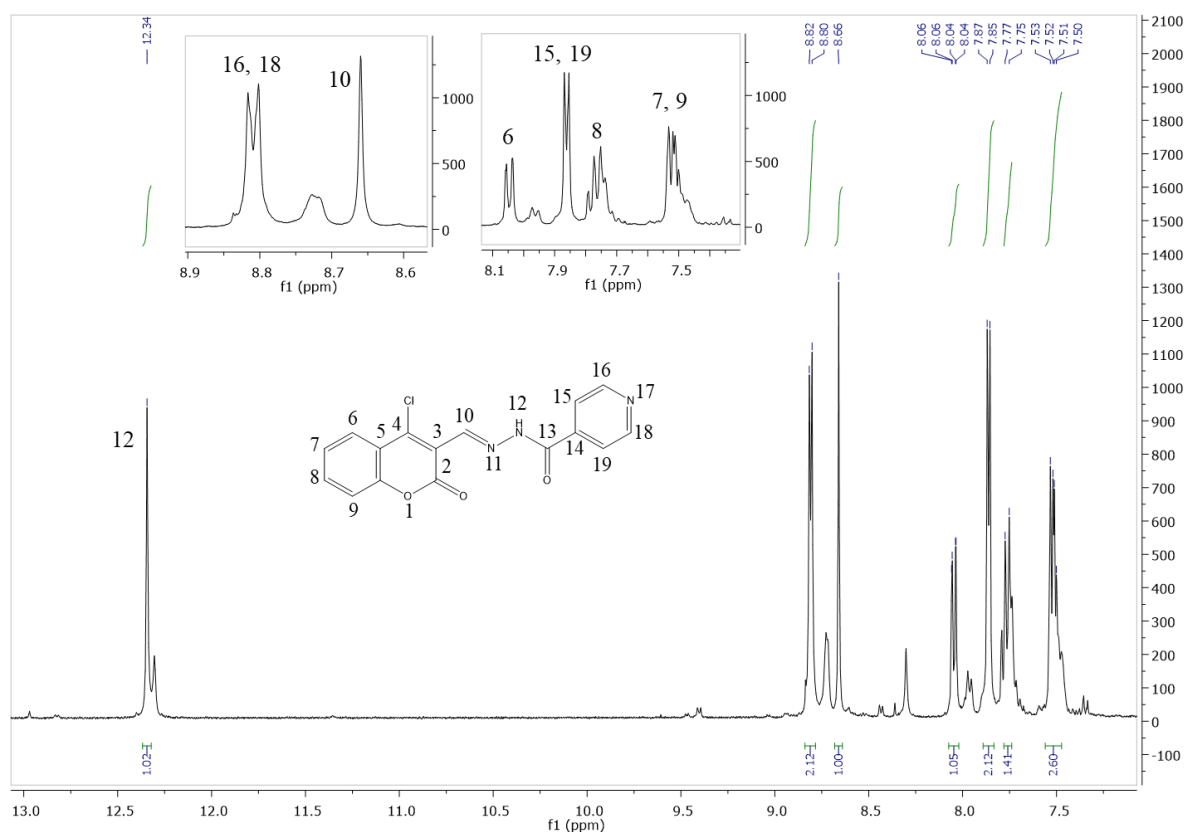


Figure 27. ^1H NMR spectrum of **1i** (400 MHz) in $\text{DMSO-}d_6$ at room temperature.

5.2.8. 4-methylpiperazine-derived hydrazones (series 5)

Although very promising, this series could not be prepared for this work due to the complexity to obtain the key precursor 4-methyl-1-piperazinecarboxylic acid hydrazide. This compound is not commercially available in Brazil and presents high costs of importation. Its synthesis from the 4-methylpiperazine acid chloride is also complicated to perform, since it requires the use of liquid hydrazine, which is also not sold freely in Brazil, although many failed attempts were performed using the commercially available hydrazine dihydrochloride. Nevertheless, a small amount of the hydrazide was prepared by Prof. Dr. Nicolás A. Rey during his postdoctoral period in the NMR-Based Structural Biology Department of the Max Planck Institute for Biophysical Chemistry, in Göttingen, Germany. However, the solid is not stable at room temperature, and its transportation to Brazil imposed some difficulties. For the reasons exposed above, the synthesis of 4-methylpiperazine-derived hydrazones became the sole purpose of a new project in our research group and was excluded from this thesis.

Thus, from the 19 compounds (18 + INHHQ) suitable for synthesis, 10 of them (9 + INHHQ) were successfully prepared and fully characterized. **1e**'s known low stability was decisive for its elimination from the synthetic step of the project.

5.3. Nuclear Magnetic Resonance

Concerning the NMR data, most *N*-acylhydrazones showed the presence of different species in DMSO-*d*₆ solution (Oliveira *et al.*, 2017), with the exception of the hydrochlorides **1d'**, **2d**, **3d** and **4d**. *N*-acylhydrazones have (*E*) and (*Z*) isomers, as well as *anti* and *syn* conformations, and amido-iminol tautomers, which results in rich equilibriums in solution (Figure 28). In practice, usually the (*Z*) isomers are absent or present in extremely low quantities. An exception occurs when R' = 2-pyridyl, due to the presence of strong intramolecular hydrogen bonds (Syakaev *et al.*, 2006), as we have shown for compound **1f** (Cukierman *et al.*, 2018). With respect to the conformation, the less hindered *anti* form usually predominates in solutions of aroylhydrazones derived from aromatic aldehydes, as proven by NMR experiments (Mangia *et al.*, 1983; Palla *et al.*, 1986).

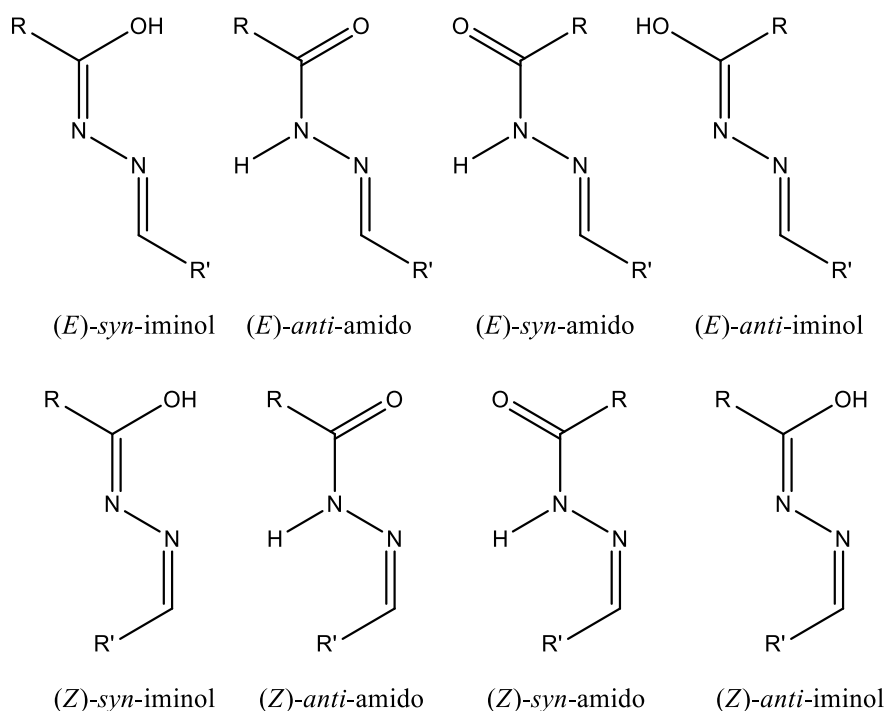


Figure 28. Scheme of the possible species of *N*-acylhydrazones present in solution. Both substituents, R and R', must be aromatic but may be different from each other.

Overall, hydrochloride salts **1d'**, **2d**, **3d** and **4d** presented more deshielded hydrazonic -NH signals. Hydrazone-specific resonances for the -H-C=N- and -NH hydrogen nuclei for the 10 ligands synthesized are selectively shown in Table 18 for the sake of comparison, since they were previously discussed separately.

Table 18. Comparative ¹H (400 MHz) hydrazonic azomethine and -NH attribution for all the synthesized compounds, in DMSO-*d*₆ solution at room temperature.

	1a	1c	1c'	1d	1d'	1f	1h	1i	2d	3d	3f	4d
H-C=N	8.32	8.39	8.52	8.42	8.69	8.49	8.65	8.66	8.80	8.76	8.48	8.87
H-N	12.03	12.16	-	12.07	12.93	12.26	12.45	12.34	12.90	12.96	12.08	13.21

5.4. Electronic spectroscopy and hydrolytic stability

From all the 10 synthesized compounds (i.e. **1a**, **1c**, **1d**, **1f**, **1h**, **1i**, **2d**, **3d**, **3f** and **4d**), the solution behavior of **9** (8 + INHHQ) were studied through molecular absorption spectroscopy under UV-Visible light. As mentioned before, compound **1c** was precociously eliminated from the project due to its proven weak interaction with copper(II) ions, which is one of the main goals of the project.

The main goal of this step was to evaluate the compounds' stability against hydrolysis in aqueous medium. The compounds were initially prepared in 100% DMSO (stock solutions 25 mmol L⁻¹), then they were diluted to lower concentrations (~5 x 10⁻⁵ mol L⁻¹) in solutions containing 1% DMSO / 99% ultra-pure water. This percentage was chosen due to its usage in *in vitro* assays. In this latter condition, for all the studied *N*-acylhydrazones, the spectra were acquired at regular intervals for 12 hours and a final spectrum was obtained after 4 days. In the first and the last spectra, a Gaussian curve fitting was performed in order to obtain the exact wavelengths of maximum absorptions.

Additionally, the stock solutions (which were kept at 4 °C) were followed for 2 weeks in order to simulate the conditioning that would be further employed in the cellular assays (spectra not shown). Figure 29A-C shows representative photos of the stock solutions over time. Compound **1i** is highlighted due to its clear instability in solution, which was previously observed during characterization in the NMR tube. The change of color observed may possibly be due to a photo-dimerization process, that has been reported to occur to coumarins when irradiated at 365 nm

(near UV) (Rivero *et al.*, 2015). Structurally similar lawsones have also been shown to form dimers (Bustamante *et al.*, 2013). This dimerization might increase the conjugation in the molecule which would explain the observed bathochromic shift. For this reason, **1i** was also excluded from the project in this step and, consequently, was not assessed at 1% DMSO. All the other *N*-acylhydrazones were completely stable under these conditions.

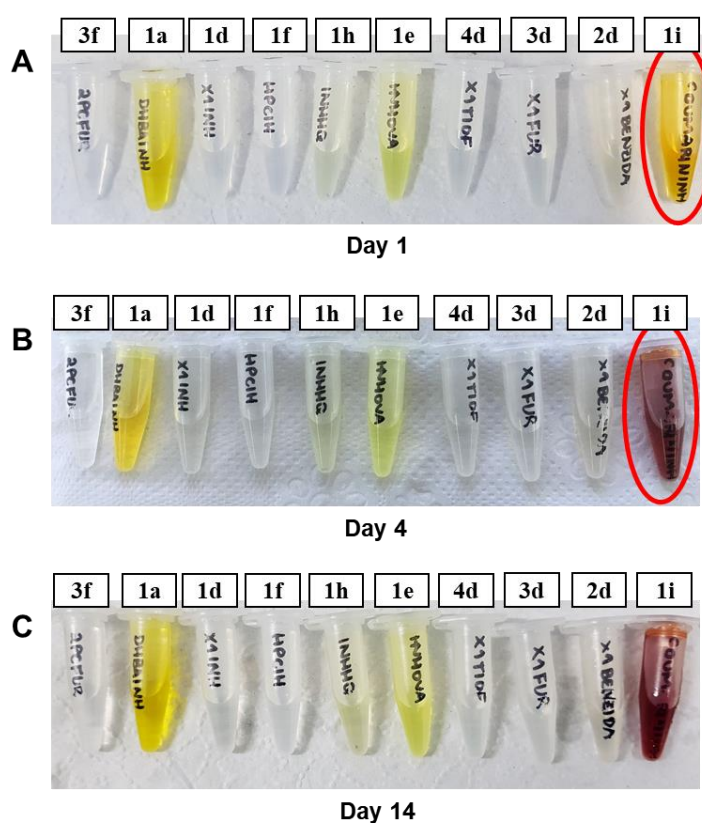


Figure 29. Photos at different timepoints of the stock solutions (25 mmol L^{-1}) in 100% DMSO, used for dilution to 1% DMSO/ultra-pure water stability assays. All vials were kept at 4°C , mimicking the conditions of storage that would be employed for the cellular assays. (A) Solutions immediately after preparation. (B) Solutions after 4 days and (C) after 14 days. Compound **1i** is highlighted in red circle due to its evident change of color over time. Additionally, compound **1e** was also excluded and not evaluated at 1% DMSO solution due to its known low stability under these conditions, as demonstrated in Section 5.2.4.

Figure 30 shows the structure of the *N*-acylhydrazones selected for the next step of the project, with the purpose of making it clearer for the readership which are the remaining compounds after these first rounds of selection and funneling.

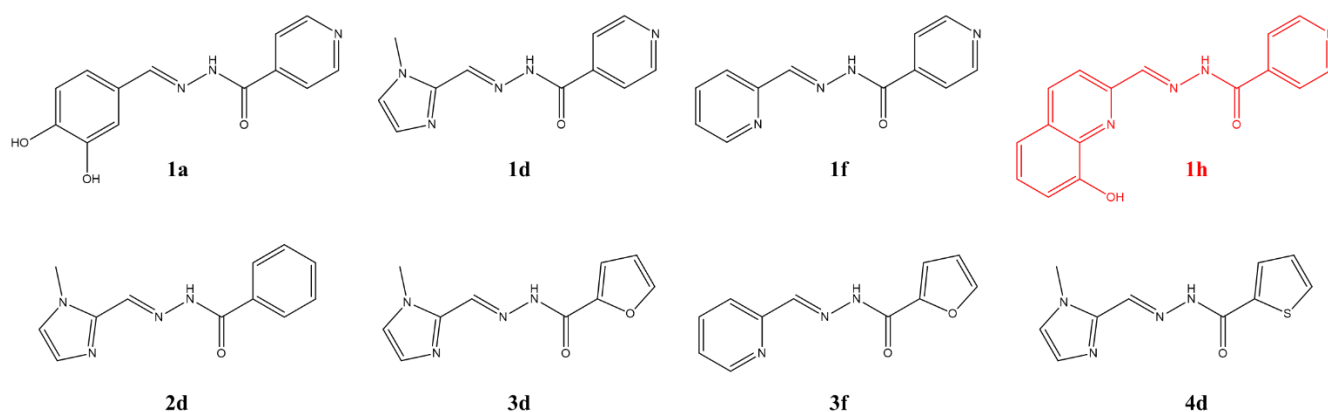
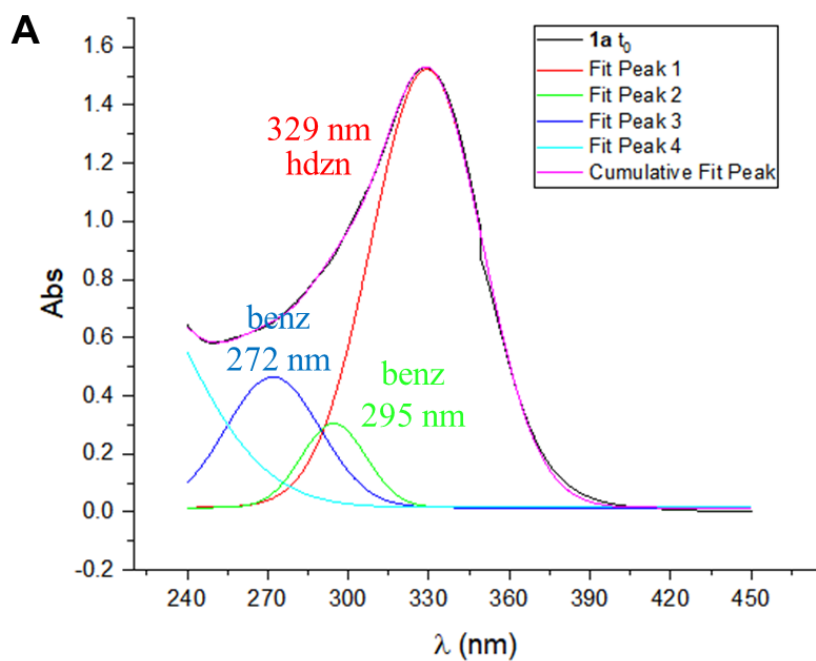


Figure 30. Structures of the 8 *N*-acylhydrazones (7 + INHHQ, which is highlighted in red) selected for the next steps of the present work.

The UV-Vis absorption spectrum of compound **1a** is composed of two apparent bands that, when deconvoluted, were proven to actually be formed by three absorptions (Figure 31A). The most intense one, at 329 nm, was attributed to the hydrazone moiety, while the most energetic ones, at 295 and 272 nm, seem to be precursor-related, since 3,4-dihydroxybenzaldehyde absorbs at 310 and 279 nm. Moreover, these bands' absorbances increase over time, suggesting a hydrolysis process. Isoniazid's absorption, on the other hand, occurs at 263 nm. Compound **1a** hydrolysis' rate is very high: in the first 12 hours of experiments, there is a decrease in more than 15% of absorbance of the main band, and a small increase in the band at 272 nm can be observed (Figure 31B). After four days, two isosbestic points can clearly be seen in the spectra, at 283 and 258 nm, and the main band, at lower energies, presents only around 50% of its initial absorbance. The presence of isosbestic points means that there are two absorbing species in solution, proving, thus, that an equilibrium between precursors and hydrazone is established.



Model	Gaussian			
Equation	$y = y_0 + A/(w*\sqrt{\pi/(4*\ln(2))}) * \exp(-4*\ln(2)*(x-xc)^2/w^2)$			
Plot	Peak1(B)	Peak2(B)	Peak3(B)	Peak4(B)
y0	0.01503 ± 0.00116	0.01503 ± 0.00116	0.01503 ± 0.00116	0.01503 ± 0.00116
xc	329.17885 ± 0.40956	294.56247 ± 8.55327	271.92078 ± 19.3862	201.28604 ± 1010.83758
A	78.19857 ± 2.30509	8.73862 ± 40.4026	19.77402 ± 238.0694	88.2204 ± 2873.15163
w	48.69432 ± 0.30995	28.41913 ± 15.41034	41.34496 ± 148.74905	78.06717 ± 1408.35037
Reduced Chi-Sqr	1.70219E-4			
R-Square (COD)	0.99935			
Adj. R-Square	0.99933			

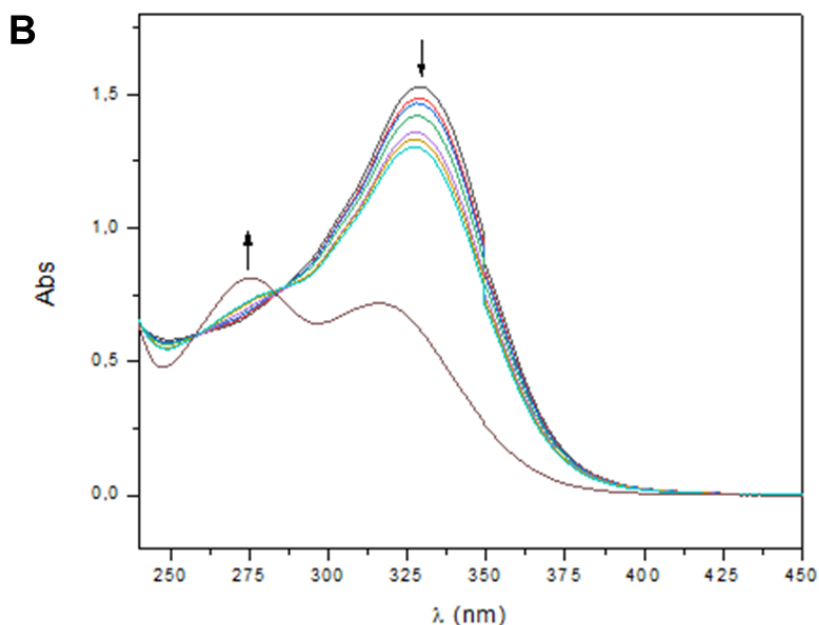


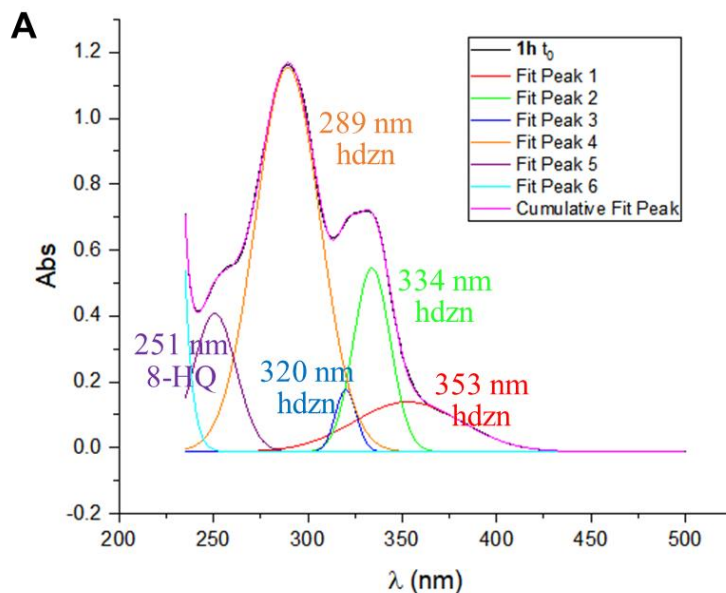
Figure 31. Absorption UV-Vis spectra of **1a** in 1% DMSO/H₂O. **(A)** Deconvolution of the bands in the spectrum at t_0 . Fitting was performed using the software Origin. **(B)** Spectra taken at regular intervals of 1 hour during the first 12 hours and then after 4 days, at room temperature.

Compound **1h**, which is the lead compound of this study, is the second least stable of the evaluated compounds under these conditions, presenting a 17% decrease in absorbance in the band at 289 nm after four days (Figure 32B). This is one of the reasons why the present study was proposed: to make chemical modifications that can improve this feature. This compound, however, is much less prone to hydrolyze than the previous one, especially in the first 12 hours, in which it is almost completely stable. The spectrum of **1h** is more complex: curve fitting showed the contribution of 5 absorptions, with 4 of them proposed as being hydrazone-related, as can be seen in Figure 32A. Once again, the most energetic band (251 nm) is precursor-related, as suggested by comparison to the spectrum of 8-HQ-2-CA, and since it suffers an increase in absorbance of around 23% over time.

Structurally similar to **1h** is compound **1f**, both isoniazid-derived and *ortho*-pyridine-containing ligands. This *N*-acylhydrazone presents a hydrolytic profile in aqueous solution comparable to that of our lead compound, maintaining its absorbance values in the hydrazone band, centered at 302 nm, in the first 12 hours and presenting a slight decrease of around 10% after four days (Figure 33B). Deconvolution of the asymmetric band (Figure 33A) showed the presence of a second absorption at 273 nm, that does not seem to be much affected by hydrolysis. This is in accordance to previous studies which have demonstrated that this band is derived from both pyridine-containing precursors (Cukierman *et al.*, 2018). However, a third band was also identified at 316 nm, which decreases around 23% over time and was also attributed to the hydrazone moiety.

The influence of the aldehyde-derived *ortho*-pyridine moiety in the hydrolysis rate of *N*-acylhydrazones is confirmed in the third ligand that contains this portion in its structure. Although compound **3f**'s UV-Vis spectrum is apparently similar to that of **1f**, it is composed of four absorptions instead of just three (Figure 34A). The most intense hydrazone band occurs at 307 nm and suffers an overall reduction of 7% in its absorbance after four days, as can be observed in Figure 34B. Lower energy bands at 317 and 328 nm also decrease around 17% and 10% in absorbance, respectively, also corresponding to hydrazone-centered transitions. Higher energy band at 276 nm, related to pyridine-2-carboxaldehyde, however, presented a slight increase of 3% after hydrolysis. It is worth noting that when a band is present both in reagent and product, since there is an equilibrium, a

change in its absorbance should only occur if there is a notable difference between the molar absorptivities of said species.



Model	Gaussian					
Equation	$y = y_0 + A/(w \cdot \sqrt{\pi}) \cdot \exp(-4 \cdot \ln(2) \cdot ((x-xc)^2/w^2))$					
Plot	Peak1(B)	Peak2(B)	Peak3(B)	Peak4(B)	Peak5(B)	Peak6(B)
y0	-0.01215 ± 3.56015E-4	-0.01215 ± 3.56015E-4	-0.01215 ± 3.56015E-4	-0.01215 ± 3.56015E-4	-0.01215 ± 3.56015E-4	-0.01215 ± 3.56015E-4
xc	352.90648 ± 1.41952	333.95482 ± 0.14006	320.17334 ± 0.11409	289.39803 ± 0.05868	250.70404 ± 0.25626	194.65235 ± 31.70807
A	10.72362 ± 0.50709	13.64003 ± 0.36247	2.61146 ± 0.17307	50.0045 ± 0.32313	11.9169 ± 0.40901	2422.76278 ± 10358.83544
w	66.5638 ± 1.70568	22.98975 ± 0.29918	13.07265 ± 0.28538	40.27225 ± 0.18382	26.66915 ± 0.57691	30.30375 ± 11.93105
Reduced Chi-Sqr	1.6271E-5					
R-Square (COD)	0.99989					
Adj. R-Square	0.99988					

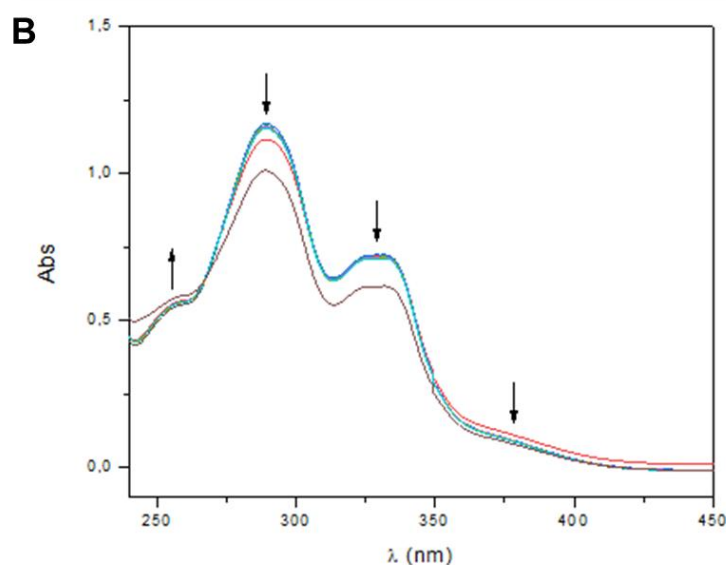
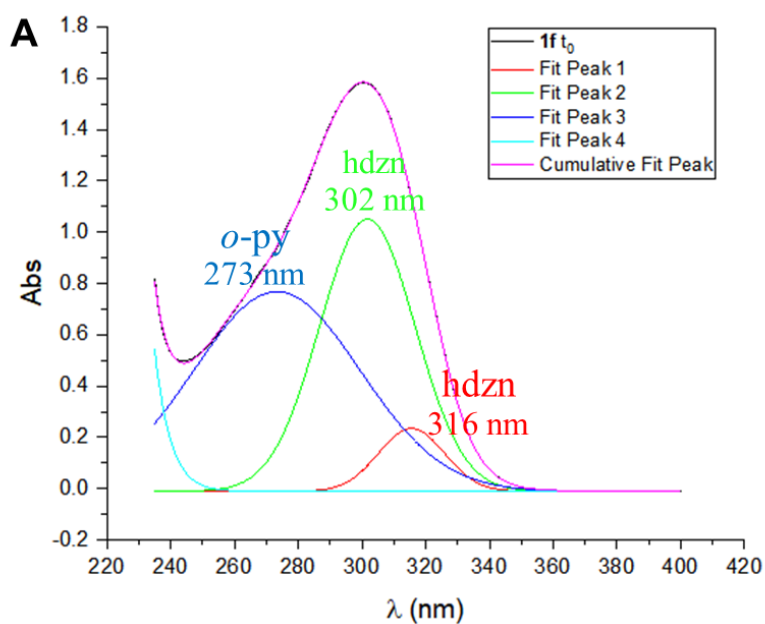


Figure 32. Absorption UV-Vis spectra of **1h** in 1% DMSO/H₂O. **(A)** Deconvolution of the bands in the spectrum at t_0 . Fitting was performed using the software Origin. **(B)** Spectra taken at regular intervals of 1 hour during the first 12 hours and then after 4 days, at room temperature.



Model	Gaussian			
Equation	$y = y_0 + A/(w \cdot \sqrt{\pi/(4 \cdot \ln(2))}) \cdot \exp(-4 \cdot \ln(2) \cdot (x-xc)^2/w^2)$			
Plot	Peak1(B)	Peak2(B)	Peak3(B)	Peak4(B)
y0	-0.01046 ± 4.40513E-4	-0.01046 ± 4.40513E-4	-0.01046 ± 4.40513E-4	-0.01046 ± 4.40513E-4
xc	315.57221 ± 0.23998	301.72933 ± 0.57556	273.34379 ± 0.73451	139.97227 ± 59.59359
A	6.35084 ± 1.652	39.84322 ± 2.91322	50.87637 ± 1.50992	352004.79404 ± 2204259.3457
w	24.39271 ± 1.03013	35.2769 ± 0.74487	61.41907 ± 0.99897	51.7192 ± 16.01965
Reduced Chi-Sqr	1.12424E-5			
R-Square (COD)	0.99996			
Adj. R-Square	0.99996			

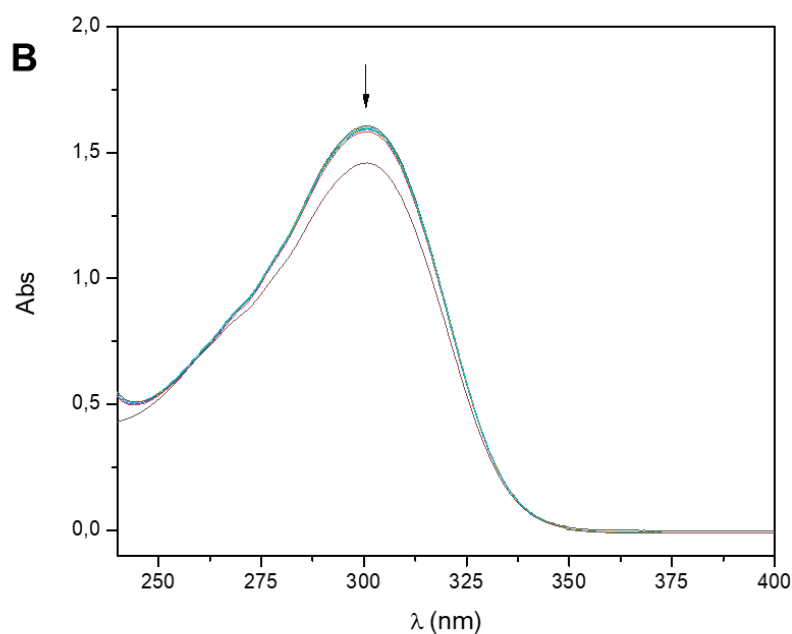
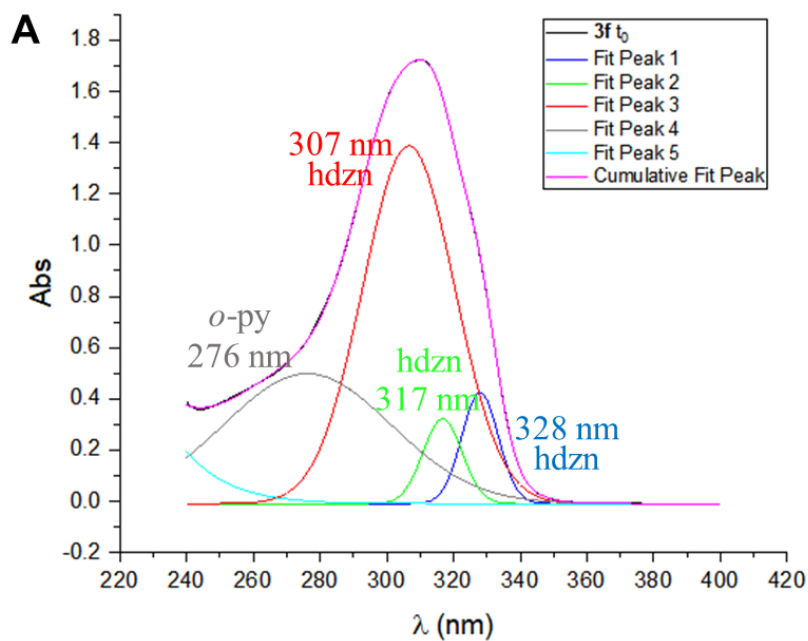


Figure 33. Absorption UV-Vis spectra of **1f** in 1% DMSO/H₂O. **(A)** Deconvolution of the bands in the spectrum at t_0 . Fitting was performed using the software Origin. **(B)** Spectra taken at regular intervals of 1 hour during the first 12 hours and then after 4 days, at room temperature.



Model	Gaussian				
Equation	$y = y_0 + A/(w*\sqrt{\pi/(4*\ln(2))}) * \exp(-4*\ln(2)*(x-xc)^2/w^2)$				
Plot	Peak1(B)	Peak2(B)	Peak3(B)	Peak4(B)	Peak5(B)
y0	-0.00925 ± 3.5749E-4	-0.00925 ± 3.5749E-4	-0.00925 ± 3.5749E-4	-0.00925 ± 3.5749E-4	-0.00925 ± 3.5749E-4
xc	328.00485 ± 0.11326	316.74913 ± 0.15982	306.61186 ± 0.10185	276.2051 ± 2.43911	80.57055 ± 981.60017
A	5.9535 ± 0.23139	4.87167 ± 0.23863	48.1535 ± 1.26232	31.95215 ± 2.24822	8919.25891 ± 344459.33996
w	12.90511 ± 0.16563	13.83342 ± 0.26322	32.40331 ± 0.30838	59.20745 ± 1.60978	109.01183 ± 347.34542
Reduced Chi-Sqr	7.90777E-6				
R-Square (COD)	0.99998				
Adj. R-Square	0.99998				

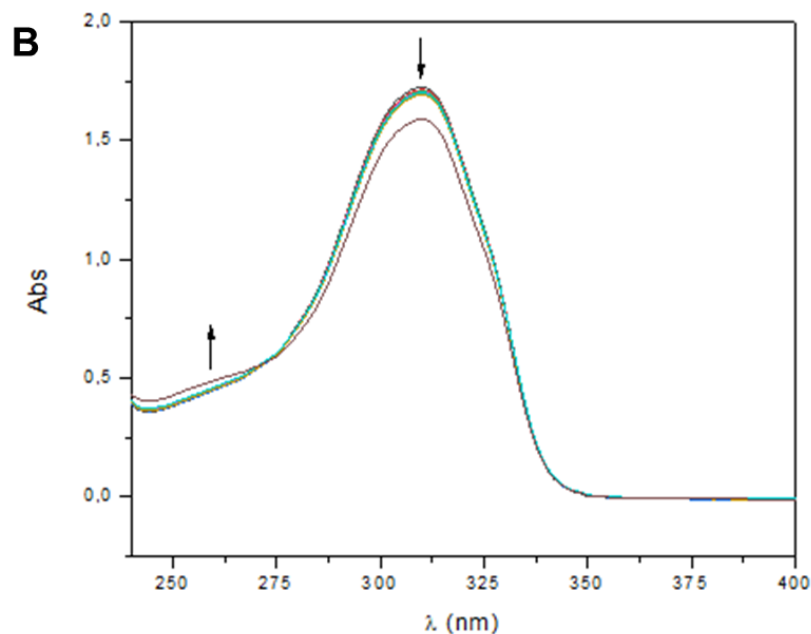
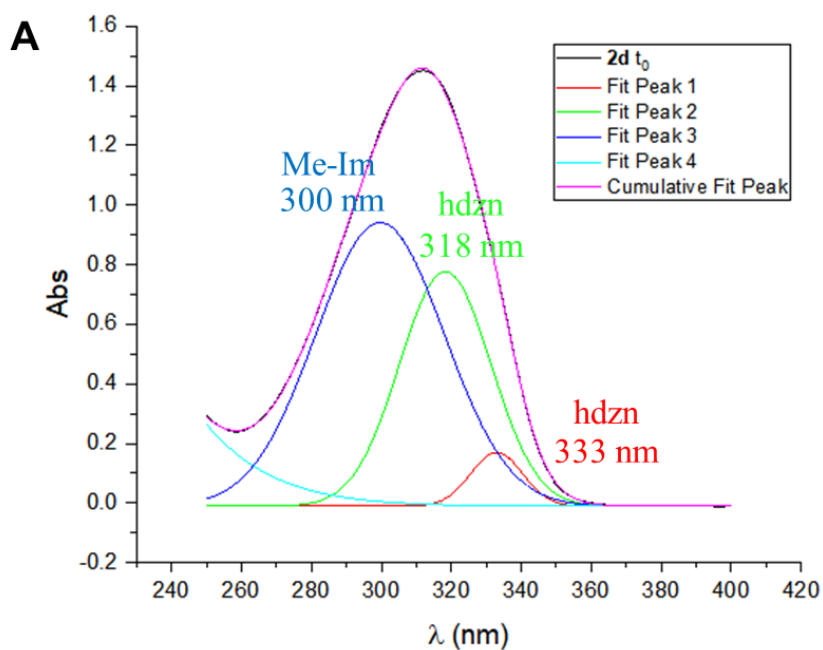


Figure 34. Absorption UV-Vis spectra of **3f** in 1% DMSO/H₂O. **(A)** Deconvolution of the bands in the spectrum at t_0 . Fitting was performed using the software Origin. **(B)** Spectra taken at regular intervals of 1 hour during the first 12 hours and then after 4 days, at room temperature.

The second series of compounds, which are derived from benzoylhydrazide, was proposed due to its theoretically higher stability. This group's lower solubility, however, allowed only for the synthesis of one hydrazone, **2d**, which contains the highly hydrophilic 1-methylimidazole group. With the use of benzoylhydrazide, a much better stability profile was obtained when compared to most of the 4-pyridine-containing (isonicotinoyl hydrazide-derived) ligands. However, the presence of the benzoyl substituent is not the one accountable for this result. The only isoniazid-derived hydrazone that is more stable than **2d** is compound **1d**, which is derived from the same 1-methyl-1H-imidazole-2-carboxaldehyde, indicating that it is in fact this moiety the one responsible not only for a better water solubility, but also for the hydrazones' general stability against hydrolysis.

Regarding compound **2d**, three absorptions contribute to its observable spectrum: 300, 318 and 333 nm (Figure 35A). The most energetic was attributed to precursor-related 1-methylimidazole ring, while the other two were proposed to be hydrazonic-derived bands. After four days, more than 92% of the main observable band's absorbance at 312 nm is maintained, as can be observed in Figure 35B.

Compounds **4d** and **3d** are structurally remarkably similar to each other, being the only difference in one atom substitution: sulfur on thiophen-derived **4d** and oxygen on furan-containing **3d**. Indeed, this resemblance is clearly seen in their spectra, both presenting four absorptions almost in the same positions: three hydrazonic bands and one precursor-related band at higher energy (Figure 36A and Figure 37A). Regarding their hydrolytic profile, both compounds also act comparably: following the good resistance in the first 12 hours, after four days **4d** presents an overall decrease of 6% in its absorbance (Figure 36B), while **3d** decreases 4% in its main band (Figure 37B). An increase of absorbance in the furan-related band (266 nm) is also observed in the latter.



Model	Gaussian			
Equation	$y = y_0 + A/(w*\sqrt{\pi/(4*\ln(2))}) * \exp(-4*\ln(2)*(x-xc)^2/w^2)$			
Plot	Peak1(B)	Peak2(B)	Peak3(B)	Peak4(B)
y0	-0.01096 ± 5.05474E-4	-0.01096 ± 5.05474E-4	-0.01096 ± 5.05474E-4	-0.01096 ± 5.05474E-4
xc	332.96693 ± 0.16048	318.27746 ± 0.1752	299.65352 ± 2.77794	46.37987 ± 870.56054
A	3.35458 ± 0.80647	25.78558 ± 8.58092	43.81615 ± 9.16787	8083.36764 ± 197363.68093
w	17.47659 ± 0.87931	30.76551 ± 2.09792	43.23234 ± 3.16177	148.34333 ± 318.47506
Reduced Chi-Sqr	1.34843E-5			
R-Square (COD)	0.99995			
Adj. R-Square	0.99995			

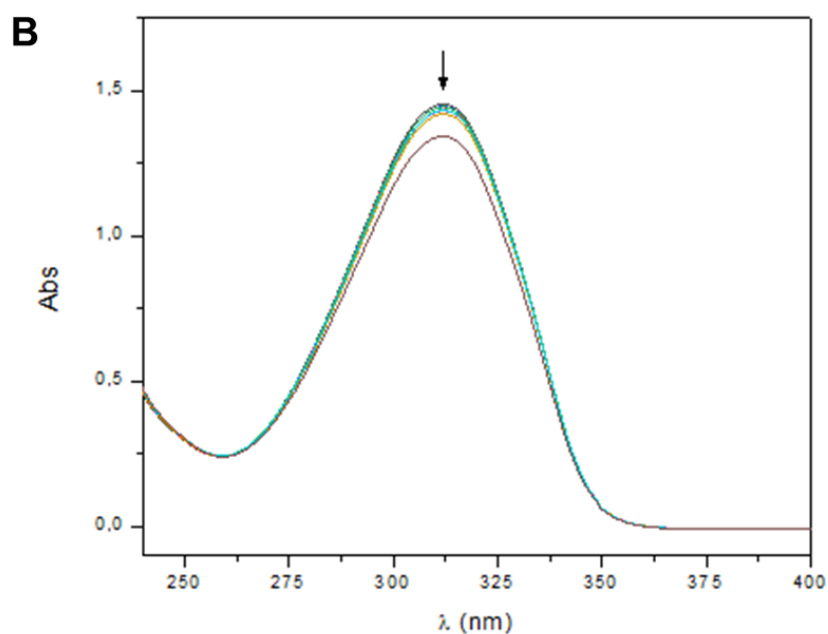
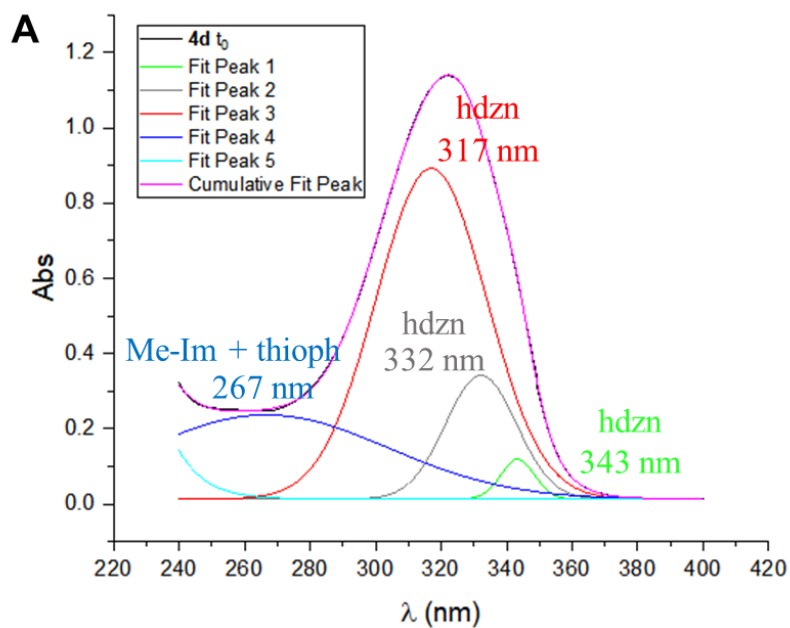


Figure 35. Absorption UV-Vis spectra of **2d** in 1% DMSO/H₂O. **(A)** Deconvolution of the bands in the spectrum at t_0 . Fitting was performed using the software Origin. **(B)** Spectra taken at regular intervals of 1 hour during the first 12 hours and then after 4 days, at room temperature.



Model	Gaussian				
Equation	$y = y_0 + A/(w*\sqrt{\pi(4*\ln(2))}) * \exp(-4*\ln(2)*(x-xc)^2/w^2)$				
Plot	Peak1(B)	Peak2(B)	Peak3(B)	Peak4(B)	Peak5(B)
y0	0.01299 ± 0.00102	0.01299 ± 0.00102	0.01299 ± 0.00102	0.01299 ± 0.00102	0.01299 ± 0.00102
xc	343.40253 ± 0.07973	332.20813 ± 0.28447	317.04633 ± 0.78272	266.6699 ± 4.35097	65.76343 ± 948.85769
A	1.36883 ± 0.18871	8.94705 ± 1.9658	37.2091 ± 2.64703	20.91159 ± 2.37548	351009.32324 ± 2.02695E7
w	12.1784 ± 0.48804	25.57745 ± 1.34582	39.75769 ± 0.90495	87.81771 ± 7.33515	90.63535 ± 251.30313
Reduced Chi-Sqr	7.90663E-6				
R-Square (COD)	0.99995				
Adj. R-Square	0.99994				

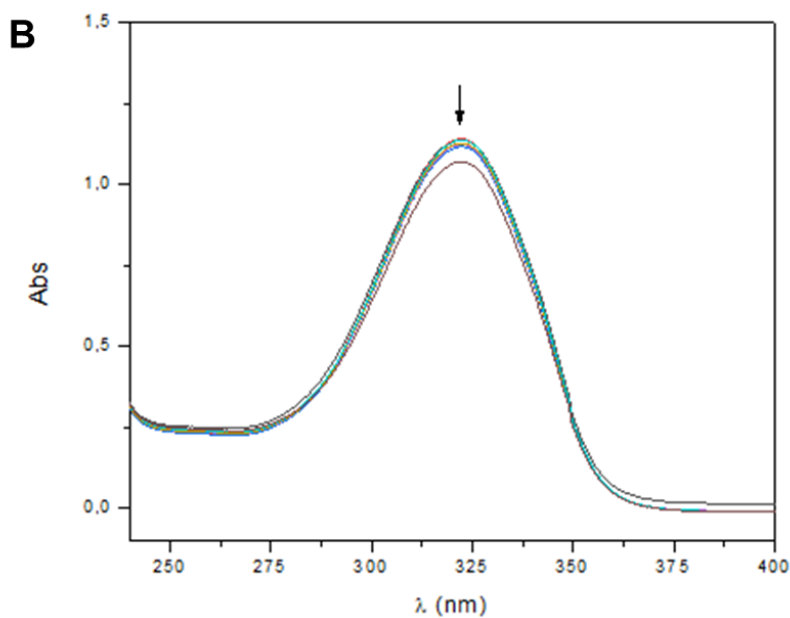
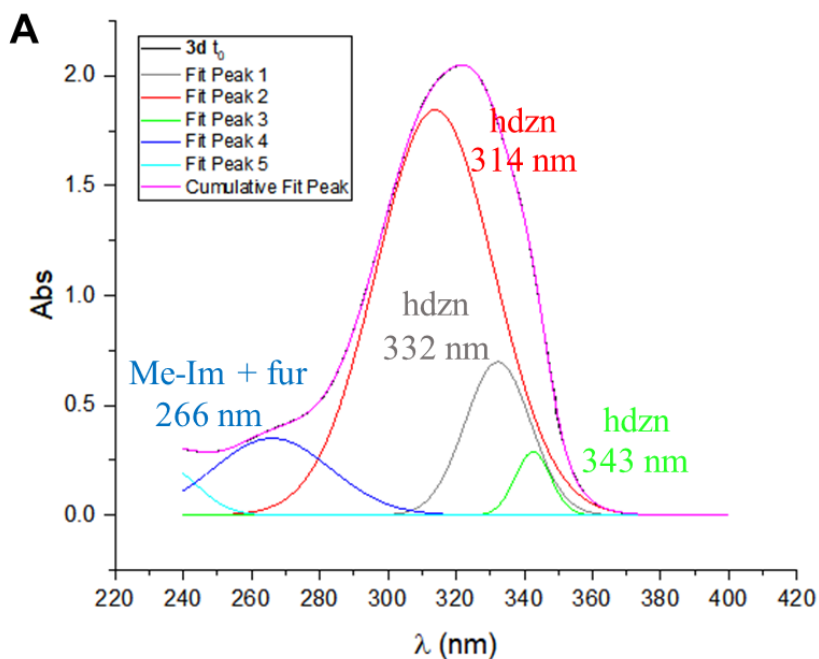


Figure 36. Absorption UV-Vis spectra of **4d** in 1% DMSO/H₂O. **(A)** Deconvolution of the bands in the spectrum at t_0 . Fitting was performed using the software Origin. **(B)** Spectra taken at regular intervals of 1 hour during the first 12 hours and then after 4 days, at room temperature.



Model	Gaussian				
Equation	$y = y_0 + A / (w \cdot \sqrt{\pi / (4 \cdot \ln(2))}) \cdot \exp(-4 \cdot \ln(2) \cdot (x - x_c)^2 / w^2)$				
Plot	Peak1(B)	Peak2(B)	Peak3(B)	Peak4(B)	Peak5(B)
y0	$1.31206E-4 \pm 4.71997E-4$	$1.31206E-4 \pm 4.71997E-4$	$1.31206E-4 \pm 4.71997E-4$	$1.31206E-4 \pm 4.71997E-4$	$1.31206E-4 \pm 4.71997E-4$
xc	332.309 ± 0.17594	313.91059 ± 0.13998	342.58104 ± 0.04117	265.991 ± 0.20368	234.78831 ± 1.18184
A	16.82574 ± 0.82833	79.92123 ± 0.66557	3.75357 ± 0.27016	15.09414 ± 0.41017	5.21715 ± 0.87387
w	22.676 ± 0.4034	40.70579 ± 0.18176	12.24464 ± 0.23704	40.54982 ± 0.95542	22.37468 ± 1.92395
Reduced Chi-Sqr	1.09715E-5				
R-Square (COD)	0.99998				
Adj. R-Square	0.99998				

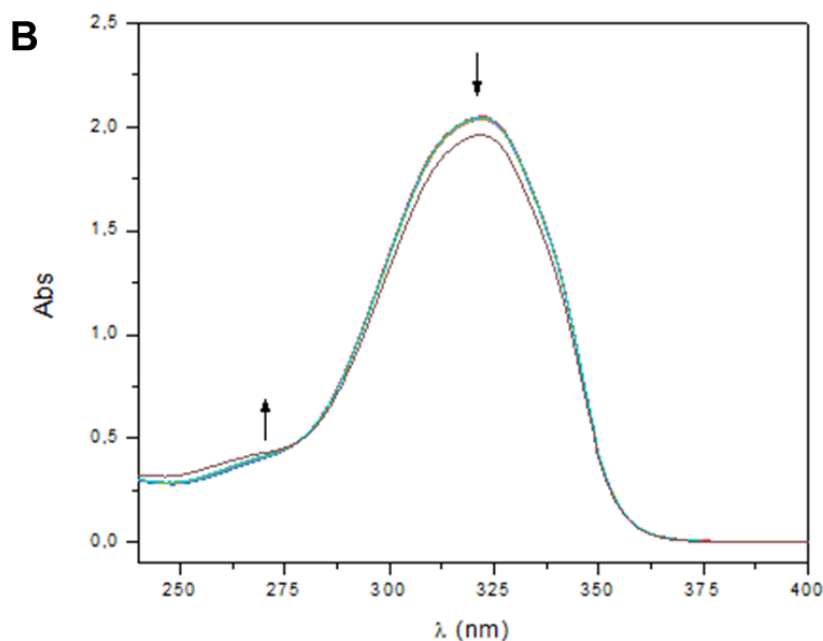


Figure 37. Absorption UV-Vis spectra of **3d** in 1% DMSO/H₂O. **(A)** Deconvolution of the bands in the spectrum at t_0 . Fitting was performed using the software Origin. **(B)** Spectra taken at regular intervals of 1 hour during the first 12 hours and then after 4 days, at room temperature.

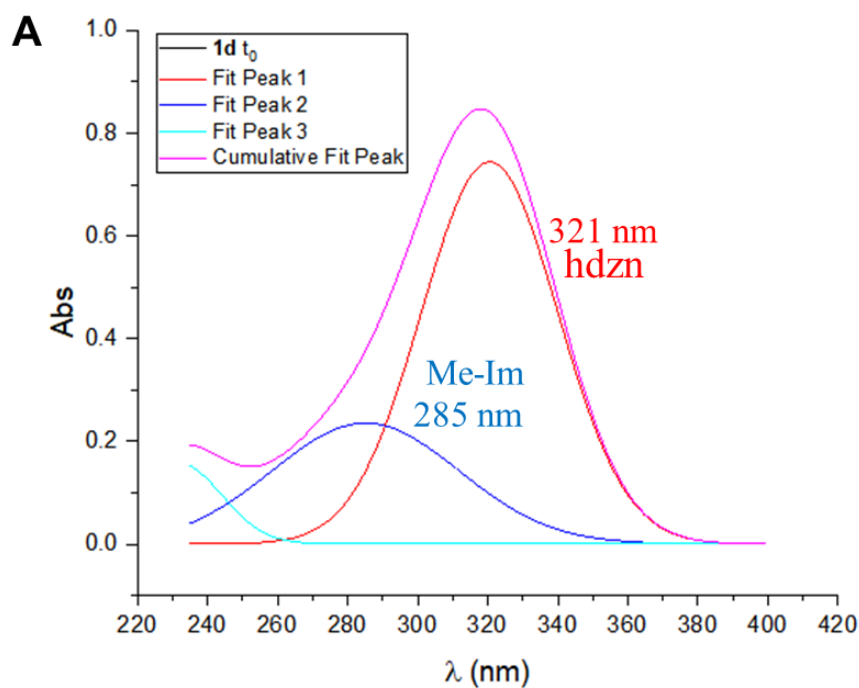
Finally, **1d** is the most stable among all the evaluated *N*-acylhydrazones in aqueous solutions. It is also the one with the most simple spectrum, presenting only two bands at 285 and 321 nm, as shown in the fitting in Figure 38A. During the four days of experiment, an absorbance decrease of only 3% in the main band (hydrazonic) was observed (Figure 38B). Moreover, a slight increase can be noticed in the higher energy band centered at 285 nm, which is probably related to the 1-methylimidazole group, since the free aldehyde absorbs at 289 nm. This hydrazone is also the most soluble one, according to both *in silico* calculations and experimental observations. This indicates the potentiality of this compound for the following development steps.

As a whole, the following order of increasing stability was established:



Interestingly, when comparing the hydrolysis resistance of the 4 synthesized 1-methylimidazole-containing *N*-acylhydrazones, the ones with the highest stability (**1d** and **3d**) are also the ones with the most shielded azomethine (H–C=N) NMR absorption. This makes sense since these carbons remain less electrophilic and thus, less prone to undergo an attack by a water molecule.

Overall, the 1-methylimidazole-derived ligands (highlighted in blue color in the box above) presented good stability, besides the expected better solubility, which is a great indicative of the potentiality of this five-membered heteroaromatic moiety in the field of Medicinal Chemistry. Consequently, hydrazones **1d**, **2d**, **3d** and **4d**, and, more generally, a representative Markush structure, were the subject of a very recent Brazilian patent application (BR1020200054236) in the agency *Instituto Nacional da Propriedade Industrial* (INPI) (Rey and Cukierman, 2020).



Model	Gaussian		
Equation	$y = y_0 + A/(w*\sqrt{\pi/(4*\ln(2))}) * \exp(-4*\ln(2)*(x-xc)^2/w^2)$		
Plot	Peak1(B)	Peak2(B)	Peak3(B)
y0	$3.71526E-4 \pm 3.17294E-4$	$3.71526E-4 \pm 3.17294E-4$	$3.71526E-4 \pm 3.17294E-4$
xc	320.56626 ± 0.3195	285.1243 ± 3.51999	231.90353 ± 0.59878
A	36.3024 ± 2.22832	15.70232 ± 2.48875	4.79368 ± 0.46395
w	45.85642 ± 0.39943	62.74213 ± 5.74311	28.76273 ± 1.44848
Reduced Chi-Sqr	5.25886E-6		
R-Square (COD)	0.99993		
Adj. R-Square	0.99993		

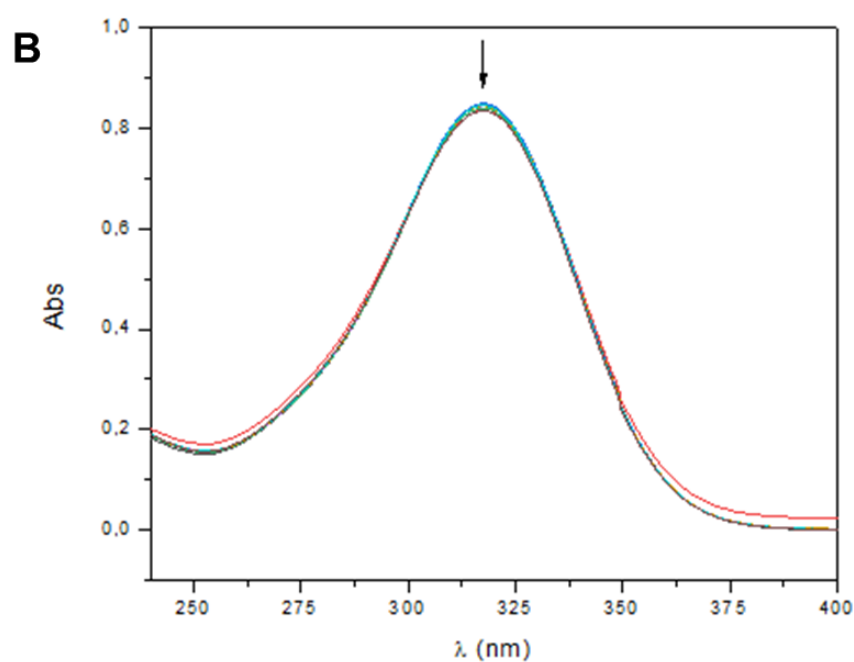


Figure 38. Absorption UV-Vis spectra of **1d** in 1% DMSO/H₂O. **(A)** Deconvolution of the bands in the spectrum at t_0 . Fitting was performed using the software Origin. **(B)** Spectra taken at regular intervals of 1 hour during the first 12 hours and then after 4 days, at room temperature.

In summary, 8 *N*-acylhydrazones were evaluated regarding their stability towards hydrolysis and selected to the next step of the project. Although less stable, compound **1a** was still considered due to its structural similarity to L-dopa, which fueled our interest in seeing its activity in a cellular model of synucleinopathy.

5.5. Experimental log P

The partition coefficient (P) is defined as the ratio of concentrations of a compound in a mixture of two immiscible solvents at equilibrium, and it is commonly expressed as its log value. It is important to note that the partition coefficient refers to unionized species, while the distribution coefficient (log D) counts with a rectification to involve all species of the compound, using its pKa value. This parameter is important because it represents the hydrophilic-lipophilic balance of a molecule, which can be used to predict membrane-crossing abilities.

Log P is frequently calculated *in silico* (referred to as cLog P), as described in item 5.1. However, the experimental values of the partition coefficient of some of the most promising compounds were also estimated through the shake flask method (Bravo-Gómez *et al.*, 2009). A Tris buffer pH 7.40 was employed as the aqueous phase and 1-octanol was used as the organic phase. This method is limited by the solubility of the *N*-acylhydrazones in these solvents at the necessary concentration for UV-Vis detection. Unfortunately, not all compounds presented such adequate features and, thus, were not assessed. Table 19 summarizes the experimental values of log P obtained for the evaluated compounds and a comparison to the calculated ones.

The Lipinski's rule of five is a guideline for some physico-chemical features of a compound that is widely employed in medicinal chemistry to help predict the oral bioavailability profile and permeability of new drug candidates (Lipinski *et al.*, 2001). According to this "rule", log P values should be less than or equal to 5. However, since Lipinski's first description of such parameters, new, updated recommendations have arisen. Nowadays, optimal range for blood-brain barrier crossing is considered for log P values between 0 and 3 (Pajouhesh and Lenz, 2005).

Table 19. Comparison between experimental and calculated partition coefficient values (log P and cLogP) for the studied *N*-acylhydrazones.

Compound	log P	cLog P
1a *	–	1.5093
1d	0.67 ± 0.03	0.3832
1f	0.91 ± 0.12	1.2538
1h *	–	2.2250
2d	1.49 ± 0.13	1.3841
3d *	–	0.5728
3f	1.08 ± 0.01	1.4434
4d *	–	1.2507

*Compound **1a** is not very stable in aqueous solutions. Compound **1h**, on the other hand, is insoluble in the buffer solution, whereas compounds **3d** and **4d** are insoluble in 1-octanol at the concentration needed for this assay.

In general, good agreement was found between experimental and calculated partition coefficients for the assessed hydrazones. A log P value of 0.67 ± 0.03 was obtained for compound **1d**, which is even better than the calculated one of 0.38. Compound **2d** also presents an ideal hydrophilic-lipophilic balance. This means that, although the 1-methylimidazole moiety is responsible for an exponential increase in water solubility of the *N*-acylhydrazones, it still allows the compounds to cross the BBB and penetrate cellular membranes. Structurally similar *ortho*-pyridine-derived hydrazones **1f** and **3f** are also in the range of good log P for the desired purpose and possess comparable values (0.91 and 1.08, respectively).

5.6. Is it possible to correlate spectroscopic trends with calculated physicochemical properties for *N*-acylhydrazones?

Some important calculated molecular descriptors, such as solubility in water (cLog S), octanol-water partition coefficient (cLog P) and polar surface area (PSA), were systematically plotted against selected spectroscopic parameters related to the *N*-acylhydrazonic moiety -HC=N-NH-CO-, namely, ¹H NMR chemical shifts (in DMSO-*d*₆) of amide -NH and azomethine H-C=N and IR wavenumber of carbonyl C=O stretching. The goal was to identify the presence of any correlation that could aid in the spectroscopic prediction of such pharmacologically relevant properties.

1-methylimidazole-containing *N*-acylhydrazones showed a good correlation ($R^2 = 0.8514$) between the azomethine hydrogen chemical shift and their solubility in water, as can be observed in Figure 39. Being all these compounds derived from 1-methyl-1H-imidazole-2-carboxaldehyde, it is fair to conclude that the aromatic substituent derived from the hydrazide moiety has also a direct impact on the chemical shift of the azomethine hydrogen and on the hydrazone's solubility. Our results show that the most deshielded the azomethine's hydrogen, the less soluble the 1-methylimidazole-derived *N*-acylhydrazone is. The most soluble derivative is the one containing the *para*-pyridine substituent.

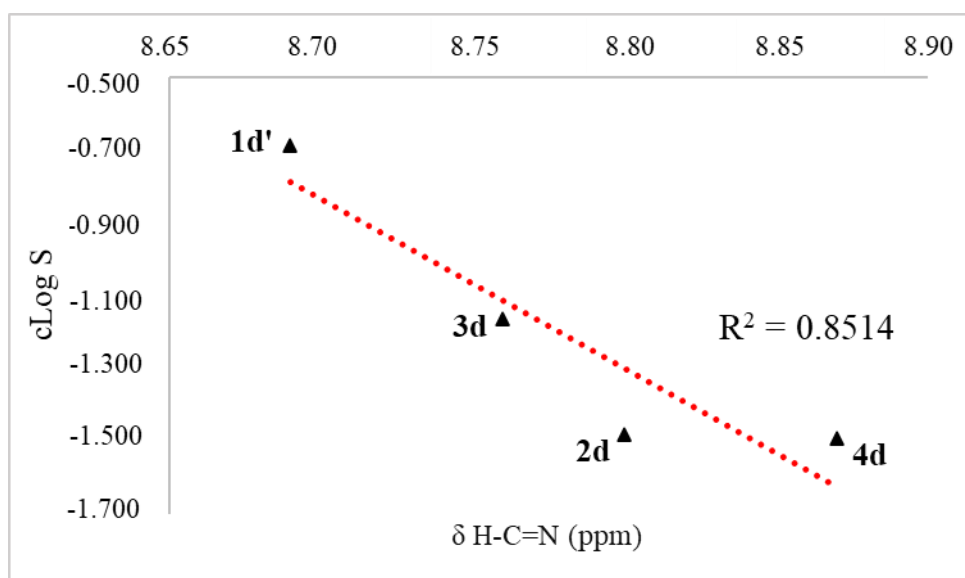


Figure 39. Chemical shift of azomethine's hydrogen *versus* calculated solubility of 1-methylimidazole-containing *N*-acylhydrazones. In order to compare compounds of the same type, data regarding the protonated form of **1d**, i.e., **1d'**, were employed.

This trend was also inversely proven using the correlation between these chemical shifts and the calculated log P values for the same set of compounds. In this case, an ascending tendency ($R^2 = 0.7151$) was obtained, showing that the more deshielded, the higher the partition coefficient was, indicating higher liposolubility. These outcomes suggest that the chemical shift of one single hydrazoneic ^1H NMR signal, H-C=N, can be employed to estimate the water solubility and octanol-water partition coefficient of 1-methylimidazole-containing *N*-acylhydrazones.

Additionally, a very strong correlation was found between the solubility of pyridine-containing *N*-acylhydrazones and the position of the C=O bond stretching

band (Figure 40). With an R^2 of 0.9995, we found that the higher the double bond character (i.e., higher wavenumber) of the carbonyl group, the more soluble the compounds are. It is important to note, however, that although all of these compounds present the pyridinic moiety in their structure, this substituent could be either *ortho*- or *para*-pyridine, or even both. Nevertheless, such a robust correlation involving four datapoints in the graph must have, beyond any reasonable doubt, some real physical significance, which is probably related to the involvement of the carbonyl oxygen in hydrogen bonds with the surrounding water molecules. This was once again inversely observed concerning the cLog P property ($R^2 = 0.9693$).

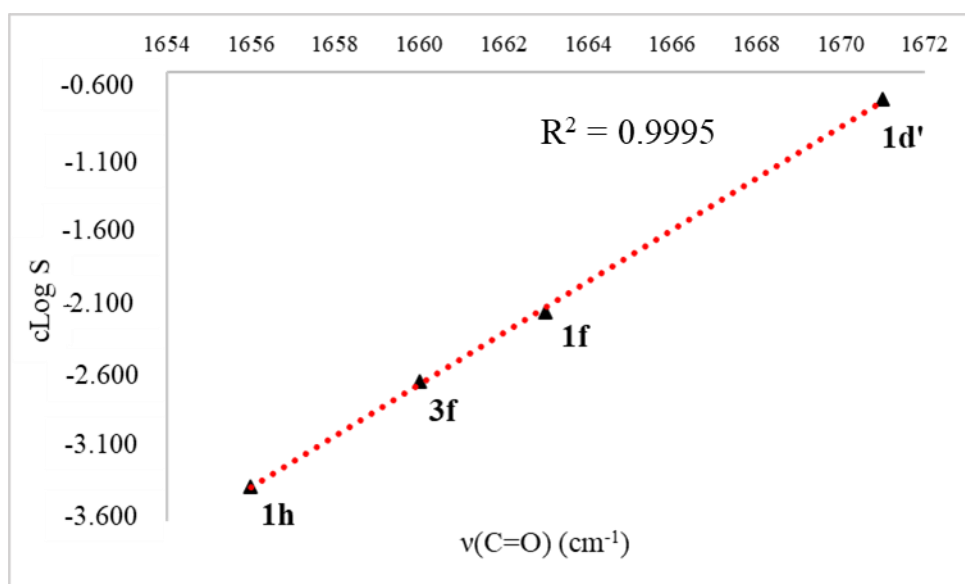


Figure 40. Wavenumber of carbonyl's stretching vibration *versus* calculated solubility of pyridine-containing *N*-acylhydrazones. In order to compare compounds of the same type, data regarding the protonated form of **1d**, i.e., **1d'**, were employed.

On the other hand, PSA, another important pharmacological descriptor, only yielded a horizontal line when plotted against any of the evaluated hydrazone spectroscopic parameters, indicating that this property is mainly defined by the aromatic substituents derived from the aldehyde and the hydrazide.

5.7. *In silico* prediction of the toxic potential of *N*-acylhydrazones

The toxic potential (endocrine and metabolic disruption; carcinogenicity and cardiotoxicity) of drugs can be estimated using the OpenVirtualToxLab™ software, which is freely available upon license request. The program calculates the binding affinity of an input molecule towards a series of 16 proteins, which are known or suspected to trigger adverse effects. With these data, a toxic potential is calculated and classified into a scale of 0-1 (with values close to 0 indicating non-toxic compounds and those close to 1 suggesting a remarkably high toxicity). Table 20 summarizes such classification and its possible interpretations. Moreover, the software allows for the molecular docking to be visualized by the user, so that ligand-protein binding sites and modes can be thoroughly studied.

Table 20. Toxic Potential (TP) classification over the binding affinity of the tested compound for 16 selected proteins. Extracted from the OpenVirtualToxLab™ User and Reference Manual – Version 5.8, freely available at <http://www.biograf.ch/downloads/VirtualToxLab.pdf>.

Class	Toxic Potential	Classification	Possible Interpretation
0	≤ 0.3	None	Unlikely to show any adverse effects triggered by any of the 16 target proteins tested in the VirtualToxLab™
	$0.3 < TP \leq 0.4$	Low	Compound binds weakly to one target protein
	$0.4 < TP \leq 0.5$	Moderate	Compound binds moderately to one target protein or weakly to several target proteins
I	$0.5 < TP \leq 0.6$	Elevated	Compound binds substantially to one target protein or moderately to several targets
II	$0.6 < TP \leq 0.7$	High	Compound binds at least to two target protein classes, e.g. nuclear receptor classes I+II
III	$0.7 < TP \leq 0.8$	Very High	Compound binds at least to three target protein classes, e.g. nuclear receptor classes I+II and cytochromes
IV	> 0.8	Extreme	Compound binds at least to four target protein classes, e.g. nuclear receptor classes I+II, cytochromes and hERG/AhR. So far, no compound has been identified in this class.

The 16 proteins that are simulated by the software are: the androgen (AR), aryl hydrocarbon (AhR), estrogen α (ER α), estrogen β (ER β), glucocorticoid (GR), hERG, liver X (LXR), mineralocorticoid (MR), progesterone (PR), thyroid α (TR α), thyroid β (TR β), and the peroxisome proliferator-activated receptor γ (PPAR γ), as well as the enzymes cytochrome P450 1A2, 2C9, 2D6 and 3A4 (CYP).

These proteins are considered anti-targets in medicinal chemistry due to their role in metabolism and physiological regulation. Thus, binding to such macromolecules is undesirable, since interfering with these processes can lead to toxicity. For example, hERG is an ion channel that is responsible for maintaining the electrical activity of the heart. Obstructing this channel's ability to conduct electricity may lead to cardiotoxicity, as has been observed for many drug candidates and even approved ones (Sanguinetti and Tristani-Firouzi, 2006). For this reason, the FDA now recommends pre-clinical evaluation of possible drug candidate–hERG interactions (F.D.A., 2005). Another important example of the selected anti-target proteins is the superfamily of cytochromes P450. These enzymes contain the heme group as a cofactor and its redox-active iron center allows for the oxidation of steroids, fatty acids and even xenobiotics such as drugs. The term “P450” refers to a peak of maximum spectrophotometric absorption at 450 nm. These are the main enzymes involved in drug metabolism (Guengerich, 2008). Interference with the cytochrome activity, specially by its inactivation, is undesired, since this constitutes the major cause of adverse drug interactions and toxicity in the organism, due to possible drug accumulation.

The OpenVirtualToxLab™ software combines automated, flexible docking and mQSAR to calculate the toxic potential (TP) of prospective drugs. Initially, the small molecule is flexibly docked to the three-dimensional structure of the protein. The potential binding modes are sampled into a 4D data set, which is then used as input for 4D Boltzmann scoring, for quantifying the binding affinities. Finally, the toxic potential is derived from the normalized binding affinities towards these proteins, their standard deviation and the predictive r^2 of the underlying model. These information were extracted from the OpenVirtualToxLab™ User and Reference Manual 5.8 (<http://www.biograf.ch/downloads/VirtualToxLab.pdf>).

The toxic potential was calculated for the 8 selected *N*-acylhydrazones. Once again, 1-methylimidazole-containing compounds showed the most promising results. Compounds **1d** and **4d** presented absolutely no calculated toxicity. With a TP of 0.300 and 0.250, respectively, the compounds do not seem to significantly bind to any of the anti-target proteins considered. It is important to highlight that *N*-acylhydrazone **4d** was the only compound judged as deprotonated at pH 7.4 by the calculations (**4d**⁻), and that all inputs were performed with the free-base form

of the compounds. However, upon forcing the user-defined protonation state of **4d** to maintain its hydrazoneic -NH, the compound interacted with more anti-target proteins and presented a TP of 0.356, which still characterizes a low toxicity drug. Compounds **2d** and **3d** also remained in the low toxicity range.

Interestingly, all the *ortho*-pyridine containing compounds (**1f**, **1h** and **3f**) presented higher TP values, in the $0.4 < TP \leq 0.5$ range, being classified as a Class 0 moderate toxicity compounds in this computational model.

Compound **1a**, on the other hand, presented a TP higher than 0.5, being classified as a Class I elevated toxicity compound, binding substantially to the androgen receptor and weakly to several other anti-targets. Nevertheless, important everyday drugs such as fluoxetine have been reported in the same range of TP. Compound **1a** binds moderately to the androgen receptor (AR), with $K_d = 0.0672 \mu\text{mol L}^{-1}$. The AR is a nuclear receptor with the main function of regulating gene expression, that is activated by binding to androgenic hormones. Its contacts involved the *meta*-OH acting as both donor and acceptor of hydrogen bond to residues asparagine N705 and threonine T877, respectively, as well as *para*-pyridine nitrogen bound to arginine R752 and the carbonyl oxygen bound to a water molecule in the network (Figure 41).

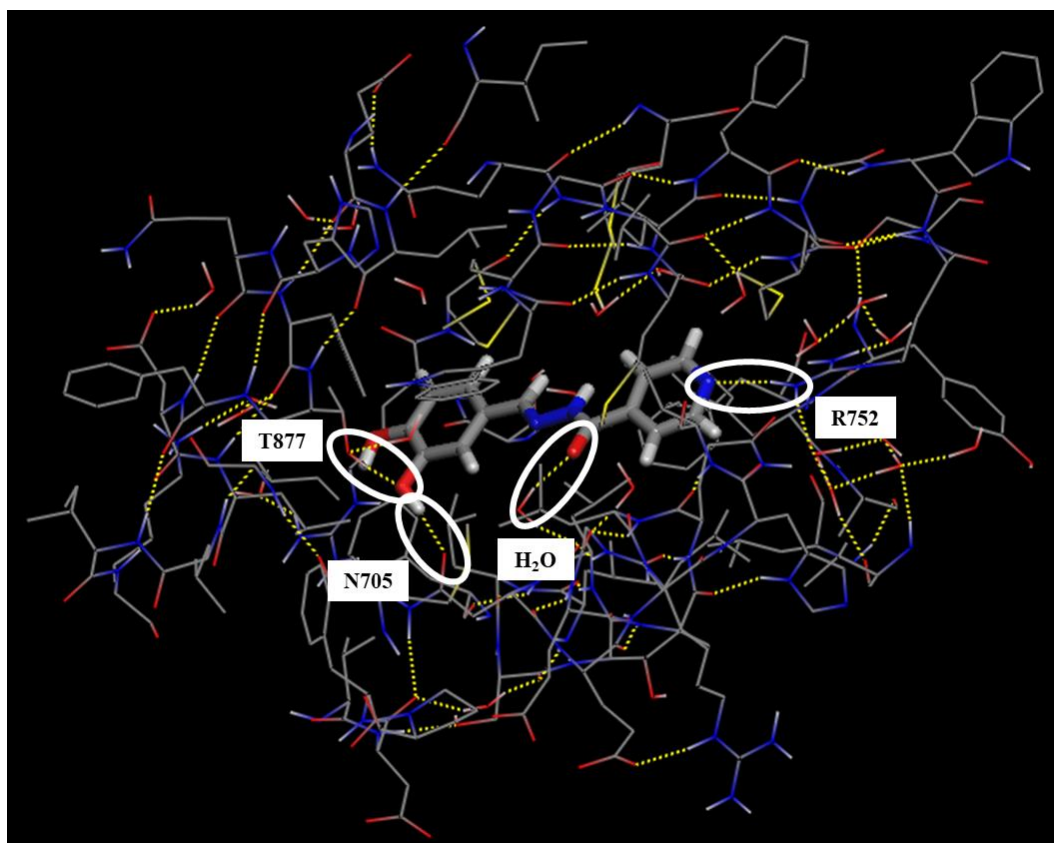


Figure 41. Hydrogen bond interactions between androgen receptor and compound **1a**.

Lead compound **1h** also bound to the androgen receptor (AR), presenting $K_d = 0.716 \mu\text{mol L}^{-1}$, which also characterizes a moderate affinity, but lower than **1a**'s. The hydrogen bond interactions with compound **1h** occur through arginine and threonine residues R752 and T877 in the C-terminus steroid-binding domain with *para*-pyridine and phenol, respectively, as can be seen in Figure 42. Moreover, this compound presented weak affinity ($K_d = 1.49 \mu\text{mol L}^{-1}$) for another hormone-related target, progesterone. In this interaction, a single hydrogen bond was identified between the phenolic -OH from **1h** and K822.

It is important to highlight that other relevant types of contacts, such as hydrophobic and π - π stacking interactions, are not shown in the figures.

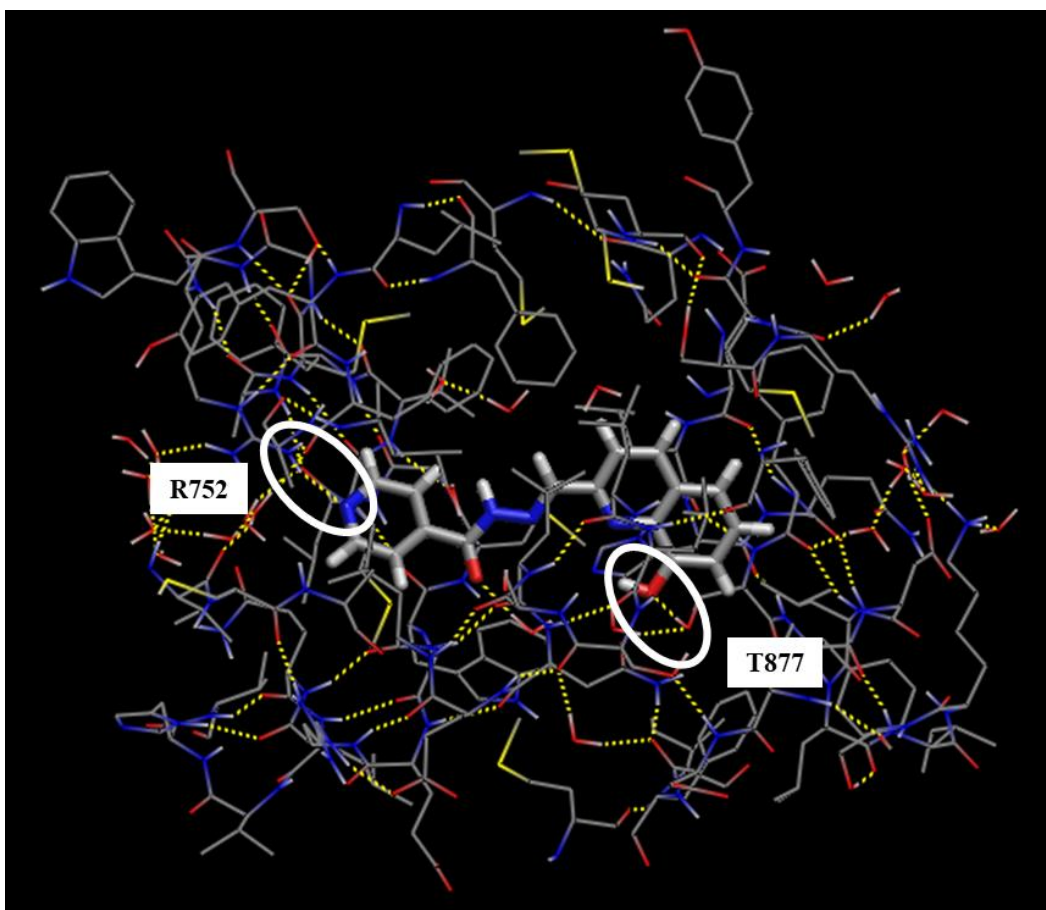


Figure 42. Hydrogen bond interactions between androgen receptor and lead compound **1h**.

Overall, the aryl hydrocarbon receptor (AhR) was the protein that interacted the most with the *N*-acylhydrazones, presenting either weak or moderate affinity and binding to all the evaluated compounds with the exception of deprotonated *N*-acylhydrazone **4d⁻**. AhR is known for its role in metabolism, binding to aromatic xenobiotics as well as endogenous indoles, and in gene expression, immunity and homeostasis (Kawajiri and Fujii-Kuriyama, 2017). Among the *N*-acylhydrazones that interacted with this receptor, the most relevant was **3f**, with $K_d = 0.196 \mu\text{mol L}^{-1}$. This moderate interaction is partially explained by the three observable hydrogen bonds, displayed in Figure 43. The glutamine residue Q100 acts as a double hydrogen bond donor with its $-\text{NH}_2$, interacting simultaneously with the *ortho*-pyridinic nitrogen and the carbonyl oxygen of **3f**. This latter atom from the ligand also interacts with a serine $-\text{OH}$ in residue S82.

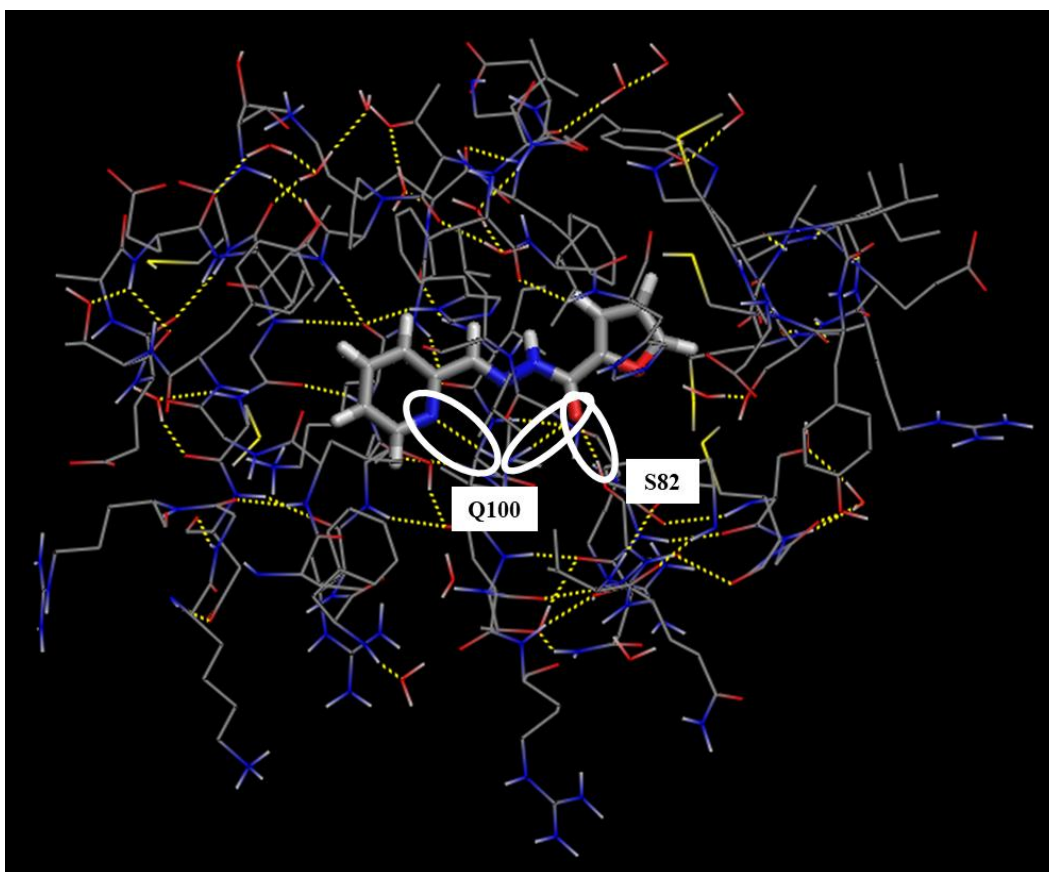


Figure 43. Hydrogen bond interactions between aryl hydrocarbon receptor and compound **3f**.

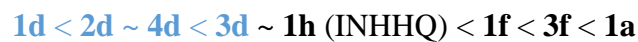
Interestingly, structure-related compound **1f** presents more hydrogen bond interactions with this receptor than **3f**, but lower affinity ($K_d = 0.407 \mu\text{mol L}^{-1}$). This is important to show that all types of interactions and conformations are relevant for protein binding, specially to this receptor which is expected to bind to aromatic xenobiotics. Besides the same contacts observed in **3f**, compound **1f** also shows a hydrogen bond between the hydrazonic -NH and histidine residue H8.

On the whole, binding to cytochrome P450 family was not relevant. The same occurs for hERG, which is related to possible cardiotoxicity, which does not seem to be a problem for the *N*-acylhydrazones considered herein. For the sake of simplicity, all interactions are described through their dissociation constant values in Table 21, which also shows the calculated TP for all compounds.

Table 21. Affinity constant (K_d) values, in $\mu\text{mol L}^{-1}$, calculated for the binding of the 8 *N*-acylhydrazones to each of the 16 proteins – OpenVirtualToxLab™. Red color indicates elevated predicted toxicity, which was only observed for compound **1a**.

	TP	AR	AhR	CYP1A2	CYP2C9	CYP2D6	CYP3A4	ER α	ER β	GR	hERG	LXR	MR	PPAR γ	PR	TR α	TR β
1a	0.509	0.0672	21.2	–	–	–	–	29.1	20.6	39.2	3.52	83.6	39.3	24.3	2.66	3.67	33.9
1d	0.300	–	15.9	–	–	–	–	–	8.71	–	–	–	–	–	70.9	25.9	–
1f	0.431	–	0.407	–	–	–	–	–	–	–	–	–	–	–	11.2	56.4	10.1
1h	0.412	0.716	2.83	67.1	–	–	–	66.5	–	22.8	13.5	–	–	7.69	1.49	–	63.7
2d	0.341	–	7.95	–	–	–	–	22.4	63.7	–	–	40.6	–	28.5	3.56	60.9	–
3d	0.400	–	0.835	–	–	–	–	–	–	–	–	24.3	–	–	–	–	–
3f	0.463	–	0.196	–	–	–	–	56.4	–	–	45.9	–	–	–	34.5	–	–
4d	0.250	–	–	–	–	–	–	–	–	–	–	–	–	–	25.1	–	64.2
4d	0.356	–	2.21	–	–	–	–	–	22.0	–	–	–	–	–	–	–	–

Overall, the following order of increasing potential toxicity was established:



Once again, the 1-methylimidazole-containing compounds (highlighted in blue color in the box above) appear to be the most promising, less toxic derivatives.

It is important to highlight at this point that these computational estimations of toxicity should always be discussed along with pharmacokinetic data (ADME – absorption, distribution, metabolism and excretion), as bioavailability is essential to the molecular mechanisms of toxicity proposed. With respect to the calculated physico-chemical properties, indeed compound **1a** presented PSA higher than the recommended value of 90 \AA^2 . Also, the four compounds with $TP > 400$ were the ones with the lowest Druglikeness score and the least stable ones as well. However, ADME analyses that assess permeability, blood-plasma partitioning, microsomal binding and metabolite profile, for example, are essential to draw more conclusions.



PUC-Rio - Certificação Digital Nº 1712623/CA

RESULTS AND DISCUSSION II

6. Results and discussion: Part II – Effects of the selected *N*-acylhydrazones on synucleinopathies-related models

6.1. *In cell* assays

6.1.1. Cellular viability in H4 cells (MTT)

The cytotoxicity of the *N*-acylhydrazones in H4 cells was estimated using the MTT assay, which assess the metabolic activity of cells through the colorimetric reduction of 3-(4,5-dimethylthiazol-2-yl)-2,5-diphenyltetrazolium bromide into formazan, through NAD(P)H-dependent cellular oxidoreductase enzymes.

Results are presented in Figure 44, in which absorbances were normalized to the untreated control cells. The dashed line indicates the normal cell death caused by the presence of 1% DMSO treatment, which is around 20%. The most toxic *N*-acylhydrazone is the lead compound INNHQ (**1h**), being toxic to H4 cells from low concentrations of 10 $\mu\text{mol L}^{-1}$. The other analogues are well tolerated by these neuroglioma cells, showing that the new hydrazones are not only, in most cases, more soluble and more stable in water, but also less toxic and probably more biocompatible for this model. The second compound that presented higher toxicity was compound **1f**, whose structure is the most closely related to that of INNHQ (**1h**) from the selected hydrazones. These results give a hint about the structure that might be related to *in cell* toxicity, which would be the 8-hydroxyquinoline, as well as the presence of the aldehyde-derived *ortho*-pyridine ring, since a trace of toxicity is also observed in the structure-related compound **3f**. Other hydrazones presented no toxicity at all for H4 cells under these conditions. However, cytotoxicity represents a simplified, unicellular model, so the absence of toxicity herein should be interpreted carefully.

The calculation of the IC_{50} of the compounds was not performed because, due to their low toxicity, higher concentrations would be required to do so, and precipitation could be observed in the culture medium for some of the compounds starting from 500 $\mu\text{mol L}^{-1}$.

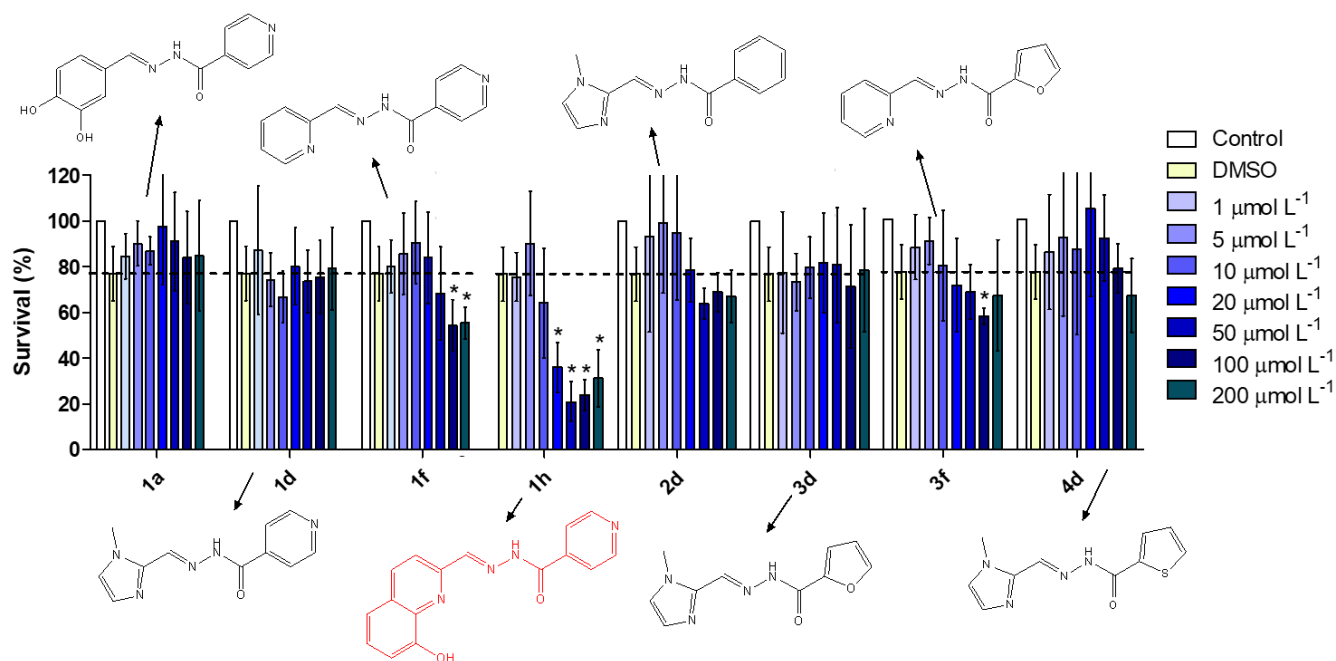


Figure 44. Cytotoxicity of *N*-acylhydrazones in human neuroglioma (H4) cells, at different concentrations. Dashed line represents the threshold for cell death caused by the presence of 1% DMSO. Significant differences (2-way ANOVA) are shown with (*) for $p < 0.05$ with respect to the 1% DMSO control.

From this point on, the concentrations of 1, 20 and 50 $\mu\text{mol L}^{-1}$ were chosen as the range of safe concentrations to evaluate the effect of the hydrazones on models of α -synuclein aggregation. Although compounds **1f** and **1h** presented higher toxicity, they constitute important structural models for the understanding of the role of the widely employed *ortho*-pyridine ring in hydrazones. The latter is also the lead compound and main comparative element of the present work. Thus, all 8 tested compounds were selected for the next step of development.

6.1.2. Intracellular α -syn aggregation: SynT + Sph1 model

The fusion of the initial 83 amino acids of EGFP at the C-terminus of α -synuclein, together with its co-expression with synphilin-1 forms α -synuclein-positive inclusions in H4 cells, which can be observed through fluorescence microscopy after immunostaining. This robust model was employed to assess the effect of the non-toxic compounds in the aggregation of the protein in cells, since the amount of insoluble aggregates can be quantified and compared.

6.1.2.1. Immunocytochemistry (ICC)

Treatment with the compounds affected the number and size of the observed inclusions. Transfected cells were divided into four categories: cells with no inclusions, cells with 1 to 4 inclusions, those with 5 to 9, and with 10 or more inclusions. The average size of the inclusions were also noted and these were qualitatively classified into small, medium and big inclusions. The representative images of the cells treated with different compounds in different concentrations are shown below, in Figure 45 and Figure 46. It is possible to observe the effect on the amount and size of the inclusions that are formed in the presence of the treatments. However, a quantitative bar graph (Figure 47) was plotted in order to statistically compare the differences observed. Cells treated only with 1% DMSO show a distribution of around 30% of the total cells presenting no inclusion at all, 30% with more than ten inclusions, and the other 40% is divided into groups with less aggregation, although these numbers may vary a little due to the complexity of the biological system. For this reason, each experiment is compared to its own control, instead of using just one averaged control bar.

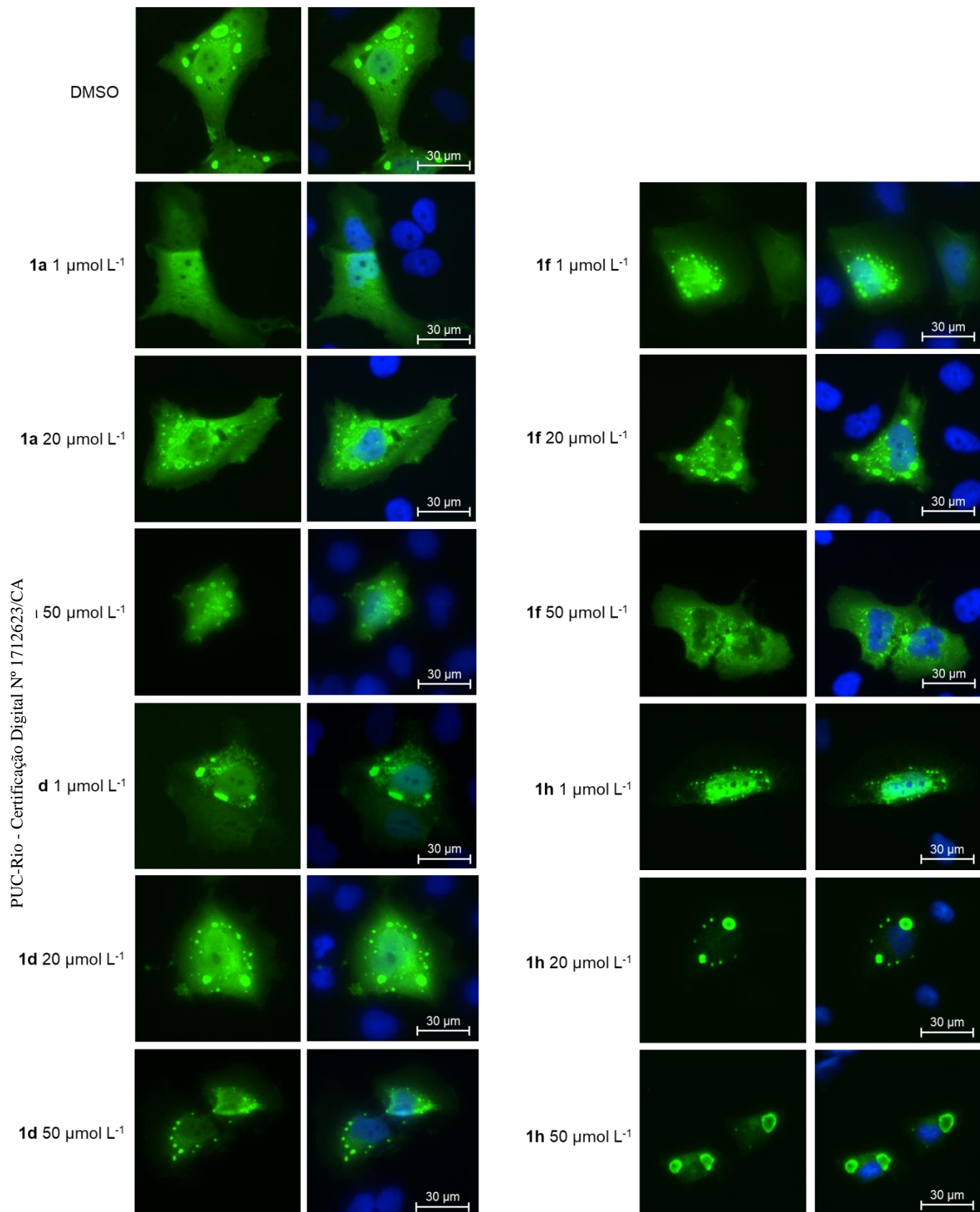


Figure 45. Representative images of the inclusion pattern in transfected cells: effect of 1% DMSO control and different concentrations of hydrazones **1a**, **1d**, **1f** and **1h** in SynT inclusions. α -Syn localization is highlighted in green, while the cell nuclei are colored in blue.

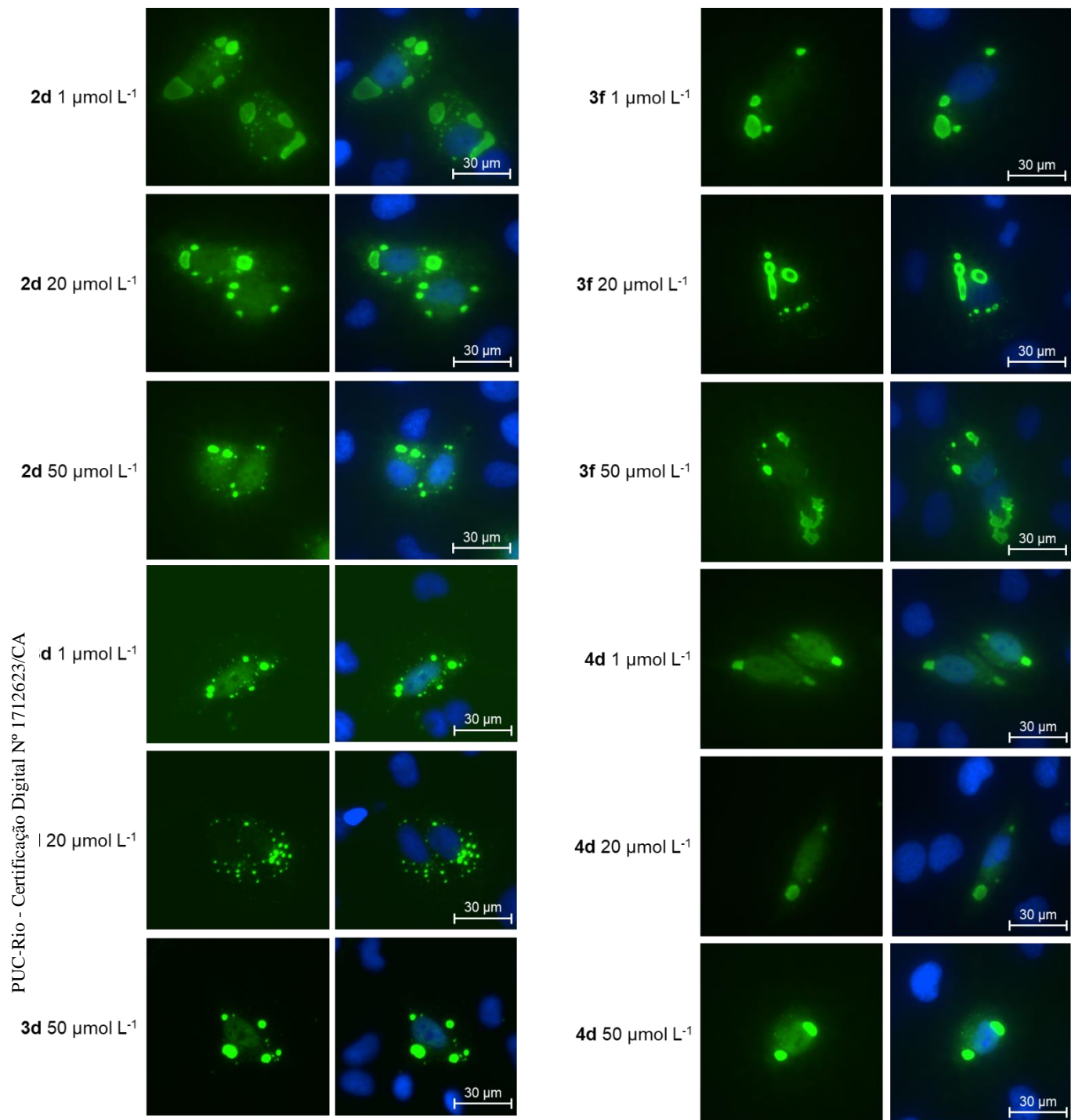


Figure 46. Representative images of the inclusion pattern in transfected cells: effect of different concentrations of hydrazones **2d**, **3d**, **3f** and **4d** in SynT inclusions. α -Syn localization is highlighted in green, while the cell nuclei are colored in blue.

The most pronounced, concentration-dependent effect in the amount of inclusions can be observed for compound **1d**, which reduces the number of cells without inclusions and increases those with more than 10. This, coupled with the observation that the compound presented smaller aggregates upon increasing its concentration, could mean that **1d** might be either inhibiting the fusion of smaller aggregates into bigger inclusions, or breaking bigger ones into smaller inclusions.

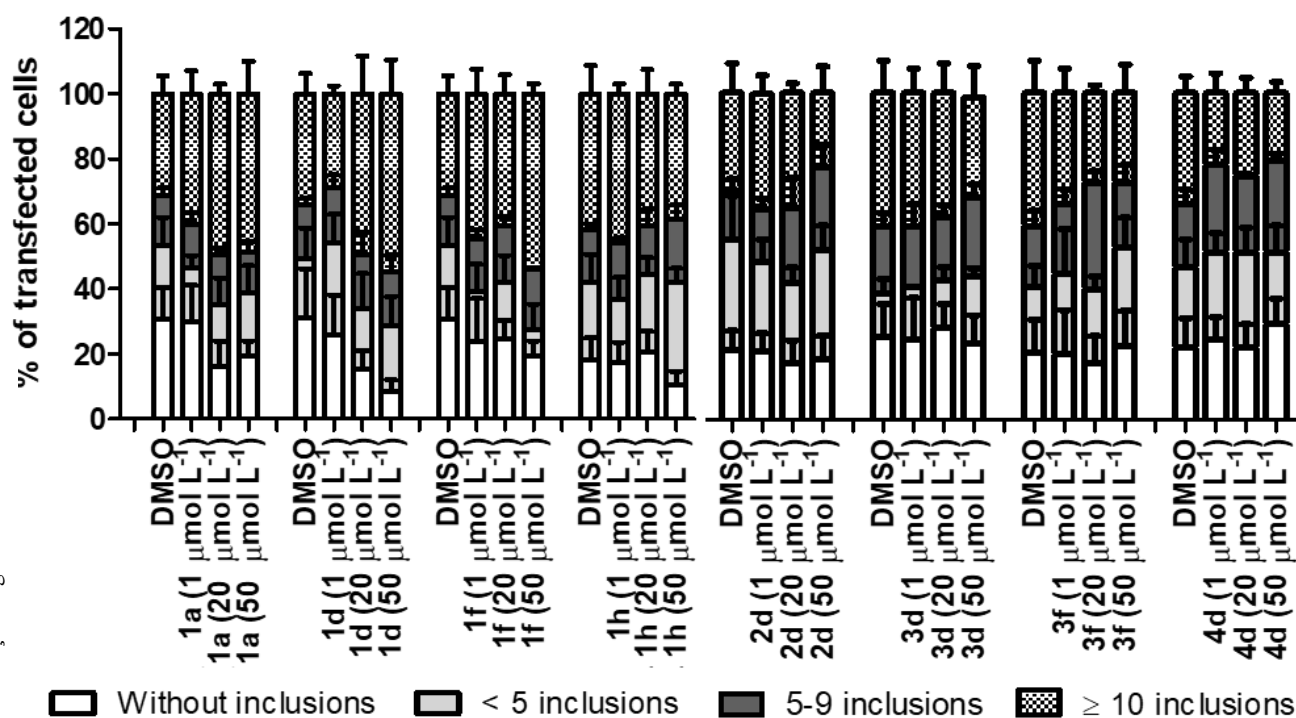


Figure 47. Quantification of effect of the treatments in SynT inclusions in the transfected cells, divided into the defined categories.

For statistical analysis, the groups of inclusions were separated (Figure 48A-D) and *t* test was performed. Statistically significant differences can be observed for compound **1a** and **1d**, lowering the number of cells without inclusions, compounds **1f** and **1h** also lowering the amount of cells with 1-4 inclusions, for compound **2d**, increasing the amount of cells with 5-9 aggregates, and compound **1f** also increasing the number of cells with more than 10 inclusions.

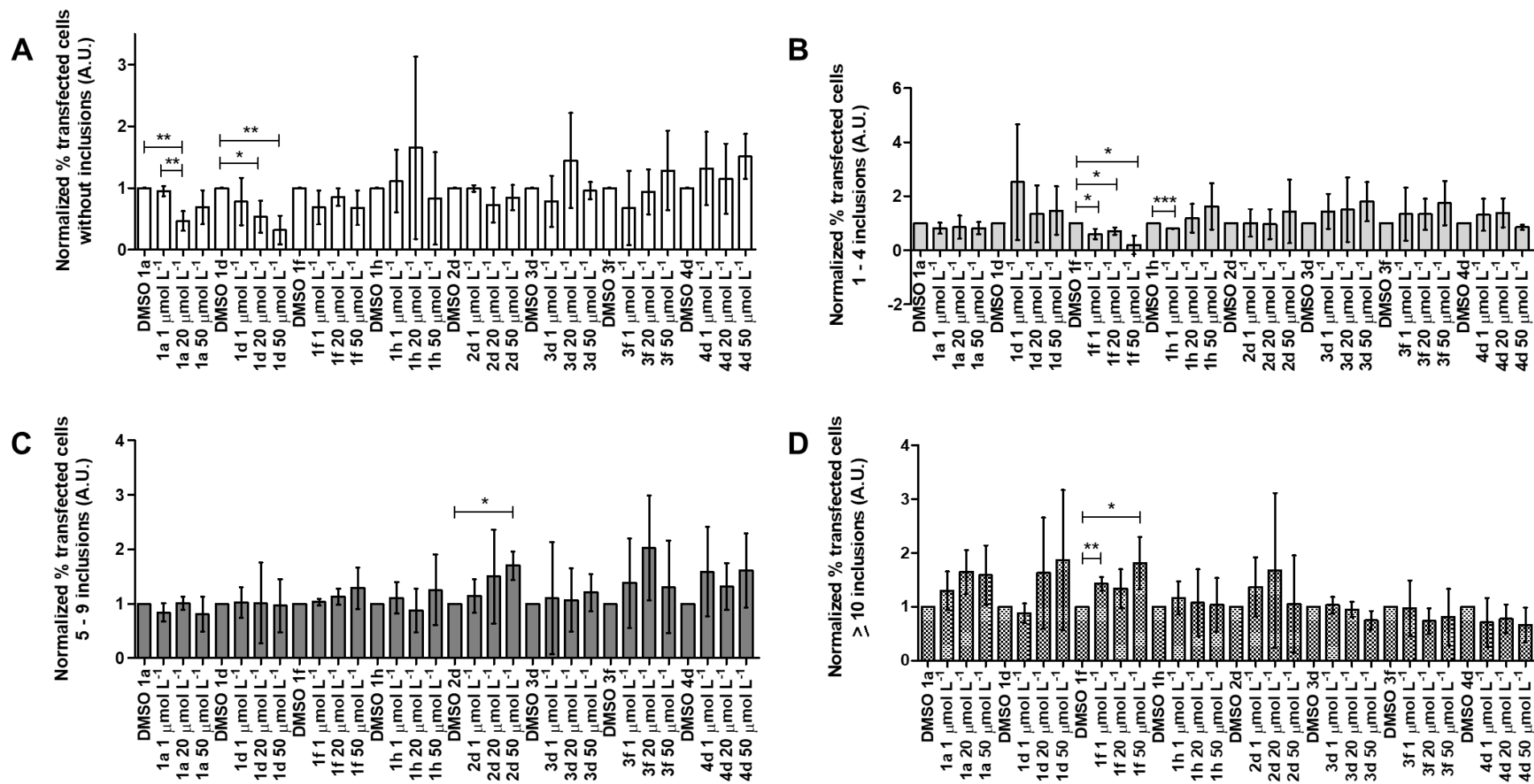


Figure 48. Statistical *t* test analyses, with significance level of $p < 0.05$, of the number of inclusions in each group (GraphPad Prism software). (A) Cells without inclusions, (B) cells with 1-4 inclusions, (C) cells with 5-9 inclusions and (D) cells with more than 10 inclusions.

Currently, oligomers of α -Syn are considered the most neurotoxic species formed during the aggregation cascade (Winner *et al.*, 2011), so an interesting approach is to reduce soluble oligomers, preventing thus further damage. We have previously shown that $1 \mu\text{mol L}^{-1}$ of INHHQ (**1h**) is able to reduce oligomerization of α -Syn in H4 cells, as observed through the Bimolecular Fluorescence Complementation assay (BiFC) (Cukierman *et al.*, 2017), thus indicating that *N*-acylhydrazones could exert their effects through this mechanism of action.

6.1.2.2. Western Blot

In order to characterize this system in more detail, some molecular biology assays were performed, such as western blots, Triton-X solubility and PK digestion. Due to the complexity of the assays and the limited time of the “sandwich doctorate”, only compounds **1d**, which presented the most marked results and tendencies, and **1h**, which is the lead compound INHHQ, were more deeply studied. Also, for the sake of simplicity, only the lowest and the highest concentrations of treatment were employed.

The goal of analyzing a simple western blot is to verify whether the compounds affect the total amount of protein in the cells. For this, after 24 hours of treatment post-transfection, cells were lysed and collected, treated with lysis buffer and sonicated. The total amount of protein was quantified through the colorimetric Bradford assay. This step is important in electrophoresis since the exact same amount of protein must be loaded into the wells for a quantitative analysis. Once the loading dye was added, samples were boiled and loaded into the gels. These steps are important in order to denature the proteins so they can run according to their size, and not structure. After the run, proteins are transferred to a membrane which can then be treated with specific antibodies that will help identify the desired protein. These experiments were performed in triplicates and representative images of the membranes were selected (Figure 49A and B).

SynT (the fusion of α -Syn and a truncated version of EGFP) runs at around 35 kDa, as identified in the membranes. In this assay, glyceraldehyde 3-phosphate dehydrogenase (GAPDH) was employed as a loading control, since this protein is stably expressed in all cells at high levels. The loading control is used to normalize the levels of the protein in each condition. Both compounds, **1d** and **1h**, do not statistically affect α -Syn levels (Figure 49C). This means that the total amount of

protein does not change upon treatment with the *N*-acylhydrazones. This suggests, thus, that the differences observed in terms of inclusion numbers might be due to an effect specifically on the aggregation process, and not in the degradation or production pathways of the protein. It is worth noting that the amount of protein found for different assays may vary due to each transfection rate. For this reason, each assay has its own control (treatment with 1% DMSO), which is used for statistic comparison.

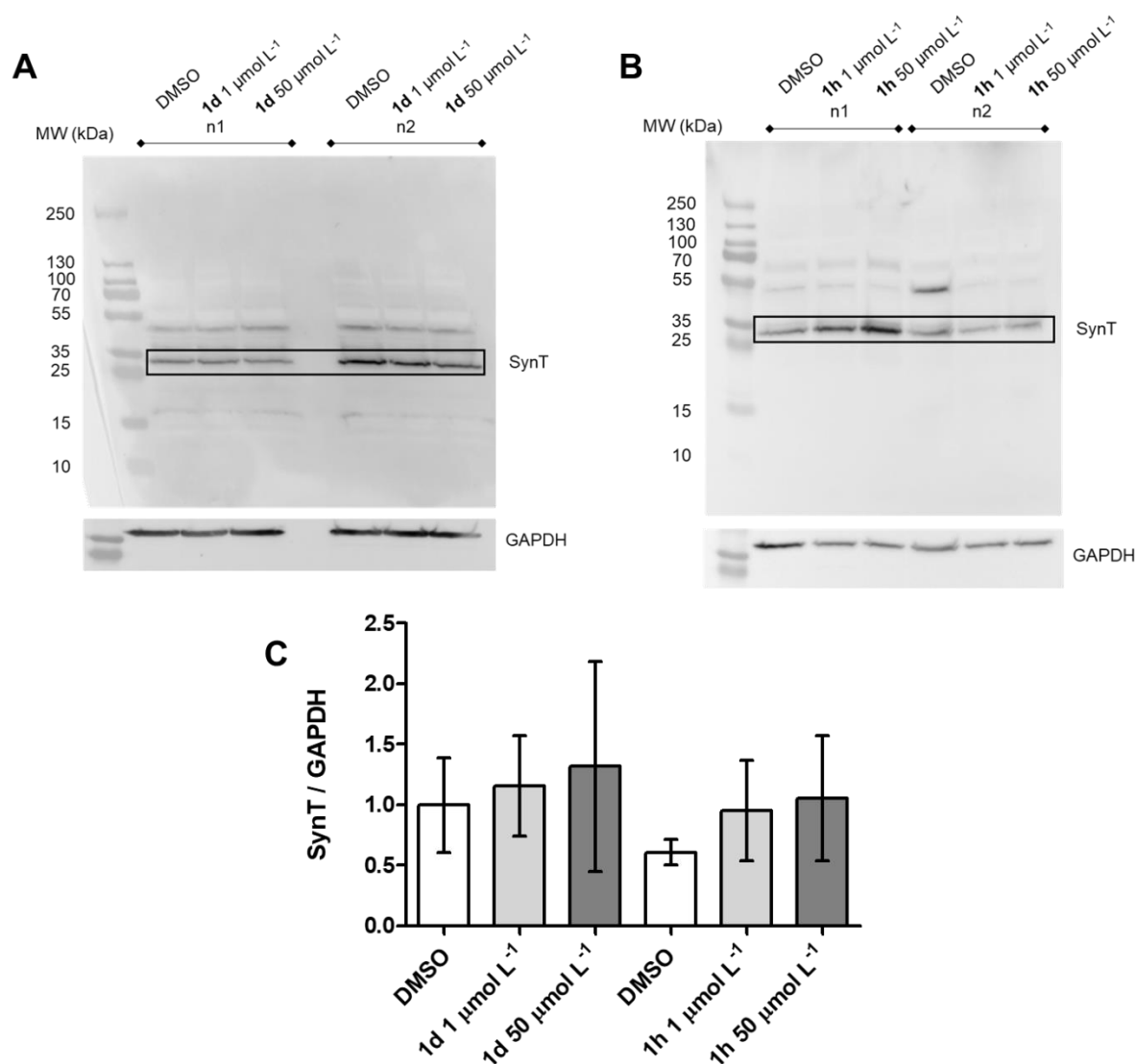


Figure 49. Levels of Syn-T after **1d** and **1h** treatments. **(A)** Representative immunoblot showing the expression levels of SynT and GAPDH after treatment with **1d**. **(B)** Representative immunoblot showing the expression levels of SynT and GAPDH after treatment with lead compound INHHQ (**1h**). **(C)** Expression levels of Syn-T normalized to GAPDH for the treatment with both compounds.

6.1.2.3. Triton-X100 solubility

One way of verifying the state of aggregation of a protein is through its solubility in Triton-X100. Aggregated α -Syn molecules are less soluble in this detergent. This has been well-established and these insoluble species can be detected in human diseased brain, as well as in transgenic models of PD (Campbell *et al.*, 2000; Kahle *et al.*, 2001). For this assay, collected cells were incubated with Triton-X100 on ice and centrifuged in order to separate soluble and insoluble phases. Since there is no consensus regarding the phase separation of GAPDH, this protein cannot be used as a control. The membrane is thus stained with Ponceau S {3-hydroxy-4-[2-sulfo-4-(4-sulfophenylazo)phenylazo]-2,7-naphthalenedisulfonic acid sodium salt}, which is a dye that binds to all proteins on the membrane. This is used as a qualitative loading control, as shown in Figure 50A and C.

Once again, there are no statistically significant differences between the controls and the treatments (Figure 50B, D and E), indicating that the compounds do not affect the partitioning or the total amount of soluble and insoluble α -Syn.

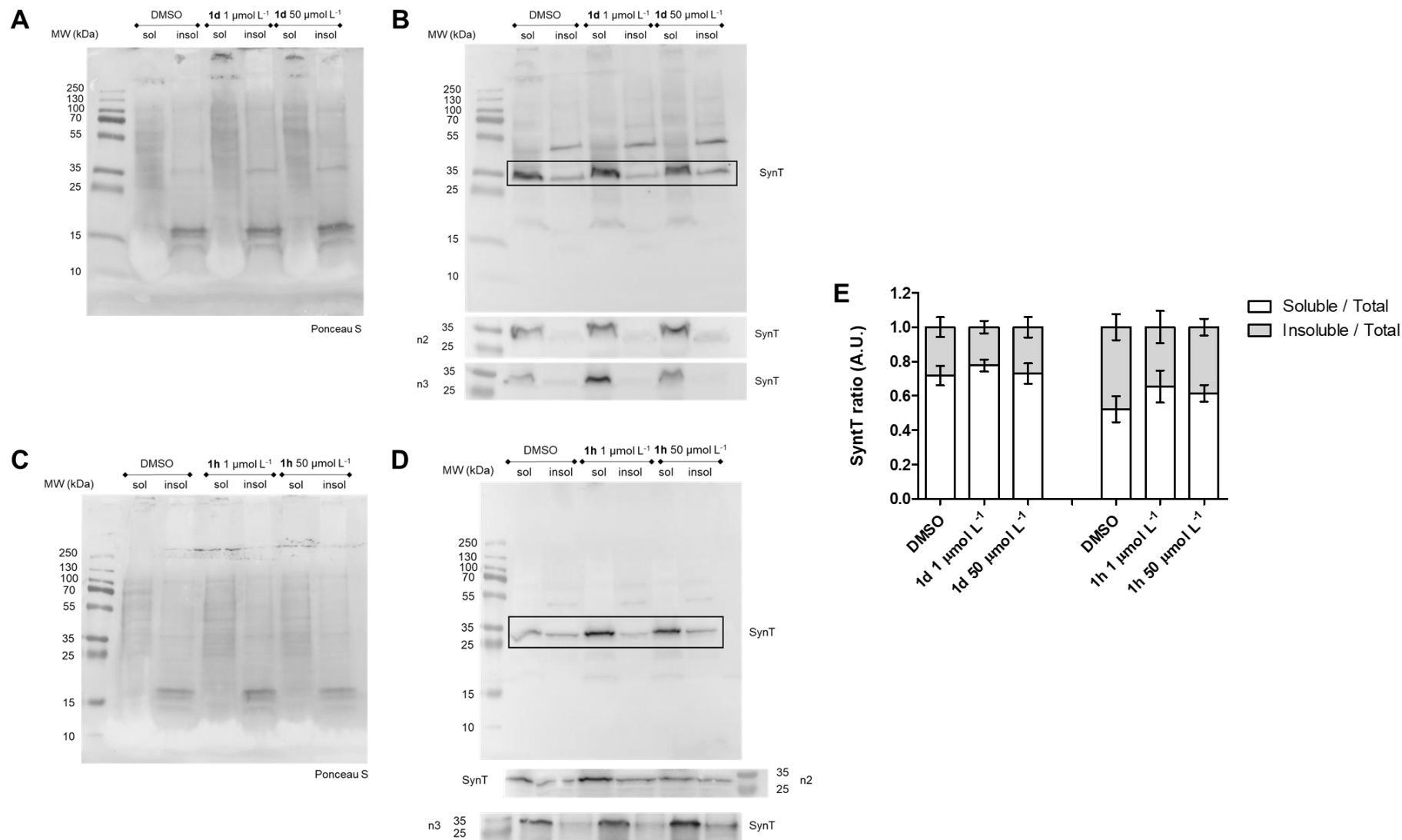


Figure 50. Levels of Syn-T partition in Triton-X100 soluble/insoluble fractions after **1d** and **1h** treatments. **(A)** Representative immunoblot after treatment with compound **1d** showing Ponceau S staining for control purposes. **(B)** Representative immunoblot showing the levels of Syn-T in Triton-X100 soluble and insoluble fractions after treatment with **1d**. **(C)** Representative immunoblot after treatment with compound **1h** showing Ponceau S staining for control purposes. **(D)** Representative immunoblot showing the levels of Syn-T in Triton-X100 soluble and insoluble fractions after treatment with **1h**. **(E)** Triton-X100 soluble and insoluble fractions normalized to total amount of Syn-T after treatment with both compounds **1d** and **1h**.

6.1.2.4. Proteinase-K (PK) digestion

In order to further investigate the effect of the *N*-acylhydrazones on the aggregation state of α -Syn, we performed Proteinase-K (PK) assays and western blot analyses (Figure 51). PK is an enzyme that cleaves peptide bonds, presenting very broad cleavage specificity, being used to digest proteins in various biological contexts. Samples are incubated with Proteinase-K for different timepoints. Treatment with **1d** reduces the resistance of α -Syn to PK (Figure 51B and C). These results suggest that, although compound **1d** does not change α -Syn solubility in Triton-X100, inclusions may be less compact, thus more accessible to be cleaved by PK. These effects were more prominent upon treatment with a 50 $\mu\text{mol L}^{-1}$ dose.

The same was not observed for the lead compound **1h**. No statistically significant differences were observed in the SynT levels of cells treated with INHHQ in both studied concentrations in comparison to its 1% DMSO control, indicating that the lead *N*-acylhydrazone does not affect the aggregation state of α -Syn in this model (Figure 51E and F). Once again, it is important to stress that the amount of protein varies a lot in each assay due to different transfection efficacies, thus a control is always performed in each experiment for statistical comparison.

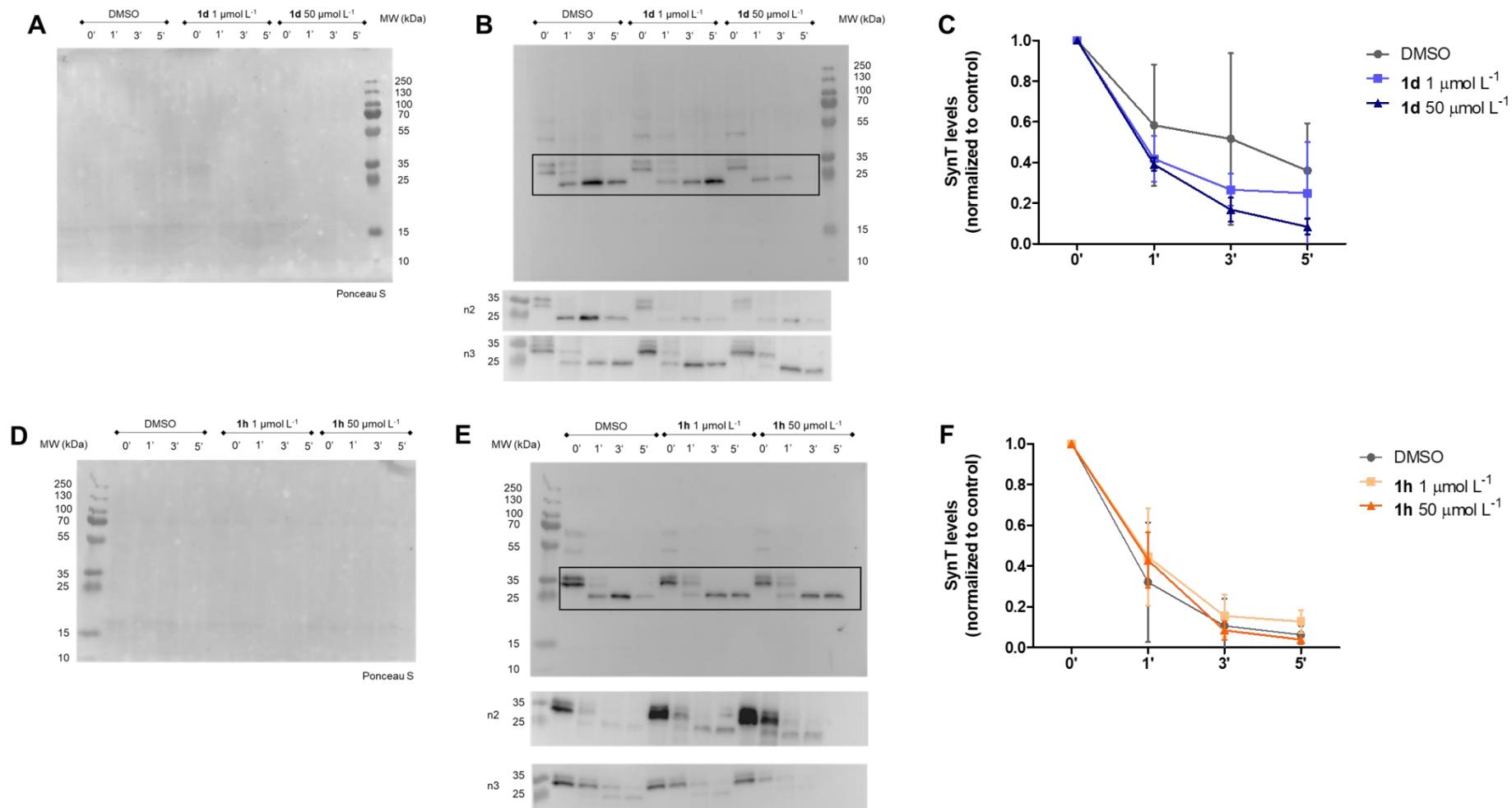


Figure 51. Effect of the compounds' treatments on α -Syn inclusion digestion by Proteinase-K. **(A)** Representative immunoblot after treatment with compound **1d** showing Ponceau S staining for control purposes. **(B)** Representative immunoblot stained for α -Syn after 1, 3 and 5 minutes of PK digestion for each treatment with compound **1d**. **(C)** Syn-T levels normalized to samples without Proteinase K for the treatment with **1d**. **(D)** Representative immunoblot after treatment with compound **1h** showing Ponceau S staining for control purposes. **(E)** Representative immunoblot stained for α -Syn after 1, 3 and 5 minutes of PK digestion for each treatment with lead compound **1h**. **(F)** Syn-T levels normalized to samples without Proteinase K for the treatment with **1h**.

6.2. Biophysical characterizations

6.2.1. Interaction between **1d** and aggregated forms of α -Syn

Complementary NMR STD experiments (Saturation Transfer Difference) were executed by Prof. Dr. Nicolás A. Rey, with the help of the author of this thesis, at the NMR-based Structural Biology Department, in the Max Planck Institute for Biophysical Chemistry, Göttingen, Germany. This preliminary study demonstrated the preference of compound **1d** for aggregated α -Syn instead of monomers of the protein. STD is based on the nuclear Overhauser effect that describes the transfer of nuclear spin polarization through cross-relaxation and is nowadays widely employed as a tool for studying small molecule-protein interactions. In summary, the protein is selectively saturated through irradiation in a region that no absorption from the ligand occurs. For weak binding, with K_d in the range 10^{-8} - 10^{-3} mol L⁻¹, the protein transfers its magnetization to the compound hydrogens that are interacting with it (Viegas *et al.*, 2011). The STD profile is then obtained from the subtraction of the saturated protein's spectrum from the one without this irradiation. Consequently, only the signals of the hydrogens of the small molecule will appear in this spectrum, making it possible to assign the moiety responsible for interaction.

The STD experiment was performed with monomeric and aggregated α -Syn in the presence of the most promising compound **1d**. First, a simple ¹H spectrum of a solution containing **1d** and aggregates of the protein was recorded, without specific irradiation, and signals corresponding to the compound were assigned and highlighted (Figure 52, green). Then, an STD spectrum was obtained for monomers of α -Syn and **1d**, irradiating the protein at 0.85 ppm. As can be seen in Figure 52 (blue), no interaction was observed between the small molecule and α -Syn in this condition. However, when the protein was previously aggregated and irradiated in the same region, magnetization is transferred to **1d**, and its hydrogens can be seen in the red spectrum of the same figure. It was not possible to assign a specific binding epitope since the whole molecule seems to be interacting with the protein. This, associated with unidimensional ¹H NMR experiments (Hauser-Davis *et al.*, 2015; Cukierman *et al.*, 2020), point to a selectivity of *N*-acylhydrazones for aggregated forms of α -Syn. This is also in accordance with the cellular experiments, which showed interaction between **1d** and SynT inclusions.

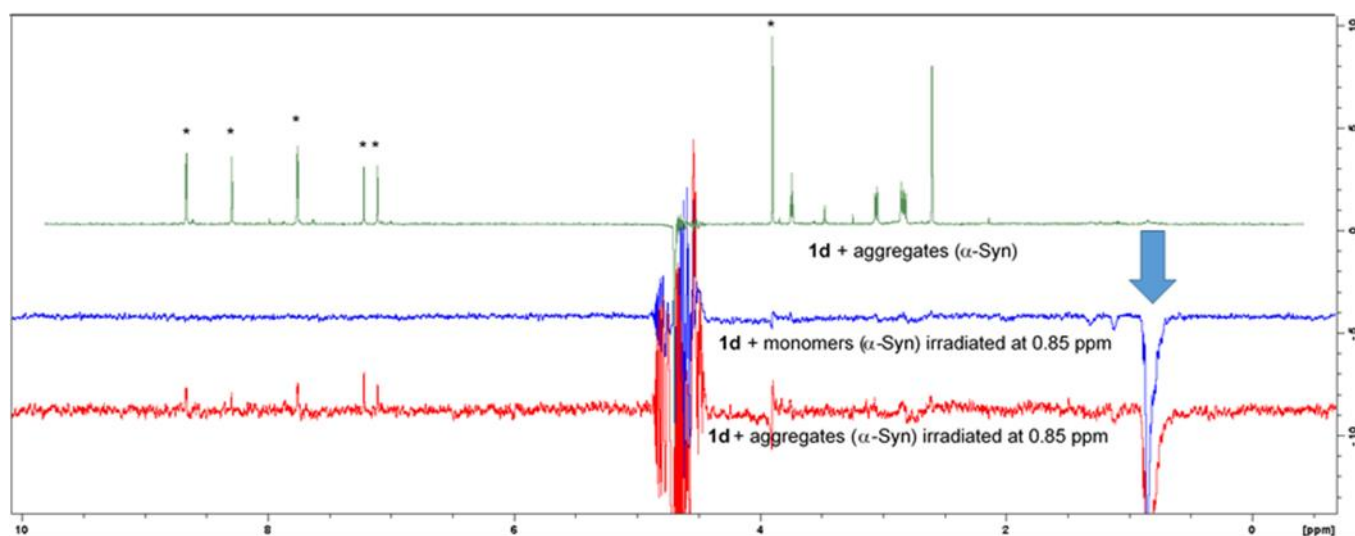


Figure 52. STD-NMR experiment. Green: ^1H spectrum of the mixture containing **1d** and aggregates of $\alpha\text{-Syn}$ without specific irradiation. The signals of the compound are highlighted with the (*) symbol. Blue: STD spectrum of the compound in the presence of monomers of the protein, irradiated at 0.85 ppm. Red: STD spectrum of **1d** and aggregated $\alpha\text{-Syn}$, irradiated at 0.85 ppm.

6.2.2. Interactions of *N*-acylhydrazones with copper in the absence and presence of monomeric, *N*-acetylated $\alpha\text{-Syn}$

The *N*-acylhydrazone moiety was chosen as the pharmacophore of the present study due to its potential in moderate coordination of physiological metal ions copper(I), copper(II) and zinc(II). This well-established coordination has been extensively studied and applied to a wide spectrum of pharmacological activities. For example, our research group, led by Prof. Nicolás A. Rey, has shown that dinuclear copper(II) complexes of non-symmetric binucleating aroylhydrazone ligands comprise a promising structural motif for enhanced antiproliferative activity in human cancer cell lines (Rada *et al.*, 2019; Rada *et al.*, 2020; Rey *et al.*, 2020). Moreover, a new oxidovanadium(V) complex prepared from an isoniazid-derived *N*-acylhydrazone showed moderate cytotoxicity against the chronic myelogenous leukemia K562 cell line (González-Baró *et al.*, 2017).

The aroylhydrazone HPCIH (inhere compound **1f**, which presents a structure very closely related to that of the lead compound INHHQ – **1h**) has been extensively studied concerning its metal coordination abilities. In 2003, Armstrong *et al.* described a sequence of complexes with divalent metal ions of the first transition series, from Mn^{2+} to Zn^{2+} , coordinated by HPCIH in a diversity of ways,

including the complex $[\text{Cu}(\text{PClIH})_2]$ and a polymeric structure of the type $[\text{Zn}(\text{HPClIH})\text{SO}_4]_n$ (Armstrong *et al.*, 2003). Complexes with two and even three metal ions (di- and trinuclear, respectively) were also obtained, as in the case of a symmetric Mn^{2+} compound. More recently, mono- and dinuclear copper complexes of HPClIH have been reported, the former being obtained in the ML_2 stoichiometric ratio (Satyajit Mondal, 2013). In 2015, Khandar *et al.* synthesized a series of coordination polymers containing HPClIH and the Cd^{2+} ion (Khandar *et al.*, 2015). This metal is also interesting because although it does not belong to the first transition series, it is of the same family as zinc, and therefore, has similar chemical properties. In 2016, Li *et al.* published the crystal structure of the complex $[\text{ZnCl}_2(\text{HPClIH})]$ (Li *et al.*, 2016).

In 2018, we published a work describing a detailed solution and solid-state study of the coordination of this ligand with Zn^{2+} ions, as well as its *in vitro* binding ability towards this metal in the presence of the Alzheimer's related $\text{A}\beta_{(1-40)}$ peptide (Cukierman *et al.*, 2018). Concerning the binding to zinc(II), both mononuclear (discrete) and polymeric complexes were observed in the solid state. In this context, the crystal structure of the novel 1D coordination polymer $\{[\text{Zn}_2\text{Cl}_2(\text{HPClIH})_2]\text{Cl}_2\}_n$ was described. In a $\text{DMSO}-d_6$ solution of the ML complex $[\text{ZnCl}_2(\text{HPClIH})]$, both (*E*)-protonated (85%) and (*E*)-deprotonated (15%) species were identified. In addition to these entities, ESI-MS studies performed in a methanol/DMSO mixture allowed for the identification of the ML_2 stoichiometry species. In all the cases, HPClIH acts as a tridentate ligand through the pyridine and azomethine nitrogen atoms, and the carbonyl oxygen. ITC-based calculations were carried out to determine the formation constant of the ML_2 species, $\log \beta = 14.33$, which is in accordance with the literature. Like the lead compound INHHQ (**1h**), HPClIH (**1f**) is able to efficiently compete with $\text{A}\beta_{(1-40)}$ for Zn^{2+} ions *in vitro*, performing as expected for an MPAC, mainly because of its affinity for zinc, which is in the same order of magnitude of that of the $\text{A}\beta$ peptide (Cukierman *et al.*, 2018).

With respect to Parkinson's disease, structural characterization of the interactions between α -Syn and metal ions actively associated with the onset of this disease has been recently explored (Binolfi *et al.*, 2006). Among these, copper is the most relevant, since interaction between zinc and α -Syn is very weak (Valiente-Gabioud *et al.*, 2012), and copper has been implicated in highly efficient α -Syn aggregation (Paik *et al.*, 1999), being able to selectively fibrillate the protein

(Wright *et al.*, 2009). Copper could be present in physiological medium as Cu^{2+} and Cu^+ . Although copper transporter 1 protein (CTR1) binds both oxidation states of the element, it specifically transports Cu^+ across the cell membrane. Extracellular Cu^{2+} must be reduced prior to CTR1-mediated uptake (Lee *et al.*, 2002; Kaplan and Lutsenko, 2009). Recently, it has been proposed that CTR1 could also act as a copper reductase (Schwab *et al.*, 2016). Once inside the cell, copper interacts with α -Syn, triggering a redox cascade of reactions that, ultimately, produce ROS and oxidative damage. For α -Syn- Cu^{2+} complexes, the metal ion is firstly reduced at the protein site by electron donors such as NADH, ascorbate or the protein itself. Then, Cu^+ catalyzes the reduction of molecular oxygen, generating ROS, which in turn oxidize neighboring amino acid residues, resulting in α -Syn damage (Binolfi *et al.*, 2012). It is worth noting that the Met1 site of the *N*-terminally acetylated physiological form of α -Syn has poor affinity for Cu^{2+} when compared to the nonacetylated protein (Moriarty *et al.*, 2014).

In this sense, characterizing the interactions between *N*-acylhydrazones and both oxidation states of copper is of interest, both in the absence and presence of the protein α -Syn. Due to the promising prospect of **1d**, this compound was chosen as a model to study such interactions in more details.

Since biological chemistry occurs in solution, the Method of Continuous Variations (Job method), inhere monitored through UV-Vis spectroscopy, was employed. A Job Plot – a plot of absorbance *versus* molar fraction – is constructed in order to confirm the stoichiometry of the main generated complex. The maximum absorbance at 0.5 molar fraction (Figure 53A) proves that the ML stoichiometry is formed favorably under these conditions. Selected representative spectra (from molar fractions 0.5 to 1 with respect to the ligand) are shown in Figure 53B. Only two absorbent species can be observed: the free ligand **1d**, absorbing at 318 nm, and the complex, showing a band centered at 375 nm. No copper(II) characteristic *d-d* band was observed due to the low concentration employed in this assay.

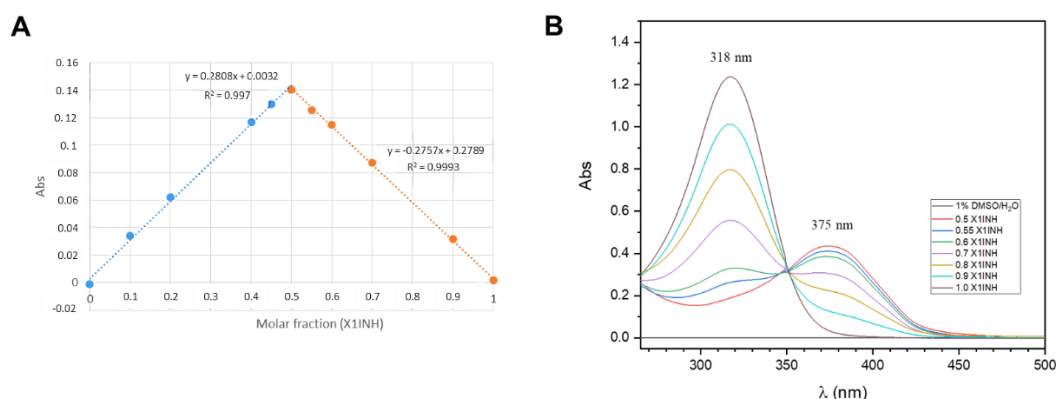


Figure 53. Method of Continuous Variations for the binding of **1d** to copper(II). **(A)** Job Plot: absorbance *versus* molar fraction. **(B)** Selected UV-Vis spectra of molar fractions from 0.5 to 1.0 of **1d** : $\text{CuCl}_2 \cdot 2\text{H}_2\text{O}$ in 1% DMSO/ H_2O , at room temperature. Reference: (Cukierman *et al.*, 2020).

From the Method of Continuous Variations, it is possible to estimate an apparent affinity constant for the formation of the copper complex. A $\log K_{\text{app}}$ of 5.66 ± 0.08 was determined, from triplicates of the experiments. This value indicates that **1d** presents a moderate affinity for copper(II) binding, which is expected for an MPAC that cannot indiscriminately bind copper in the biological system. Although this methodology may not provide an absolute value for the stability constant, it certainly allows for a valuable comparison of affinities between structure-related compounds such as the inhere studied *N*-acylhydrazones. A higher $\log K_{\text{app}}$ of 6.03 ± 0.01 has been estimated for compound **1f** under the same experimental conditions. Unfortunately, the same could not be done for our lead compound **1h**, since both ligand and complex absorb at the same region, a limitation for this method. This was also the case for copper(I) complexes.

Since no buffer solution was employed, due to either absorption in the spectral region of interest or undesired coordination to copper(II) ions, the apparent pH values of the solutions were measured for the different metal-to-ligand ratios. For the solutions of free ligands ($5.0 \times 10^{-5} \text{ mol L}^{-1}$), **1d** and **1f**, in 1% DMSO/ H_2O , apparent pH values of 8.39 and 9.15 were found, respectively. This is in accordance to the more basic character of **1f** when compared to **1d**. At the same concentration, the solution of CuCl_2 possesses an apparent pH of around 8. The unexpected slight basicity of the metal solution is probably related to the presence of DMSO. When mixing the solutions at equimolar ratios, pH drops to 6.60 for both ligands. This

indicates that the complexation process releases protons to the medium through a process involving the metal-mediated deprotonation of **1d** or **1f**, which coordinate copper(II) in their iminolate form. The fact that the stoichiometric pH for Cu^{2+} -**1d** and Cu^{2+} -**1f** systems is the same suggests a related structure for both complexes.

With the use of 1-methyl-1H-imidazole-derived *N*-acylhydrazones, it is expected a slight increase in the bite angle observed for the copper(II) complex, as well as a series of changes in the electronic structure of the ligand, which are responsible for the smaller, optimized affinity constant displayed by **1d**. To determine the primary interaction site for copper(II) in **1d**, we performed a ^1H NMR titration of the ligand using a solution of copper(II) chloride dihydrate as the titrant. Since d^9 copper(II) is paramagnetic, sub-stoichiometric amounts were employed to avoid an excessive, beyond detection broadening of the ligand's hydrogen signals. Figure 54 shows a series of ^1H NMR spectra obtained during the treatment of a $\text{DMSO-}d_6$ solution of **1d** with increasing amounts of copper(II), dissolved in D_2O .

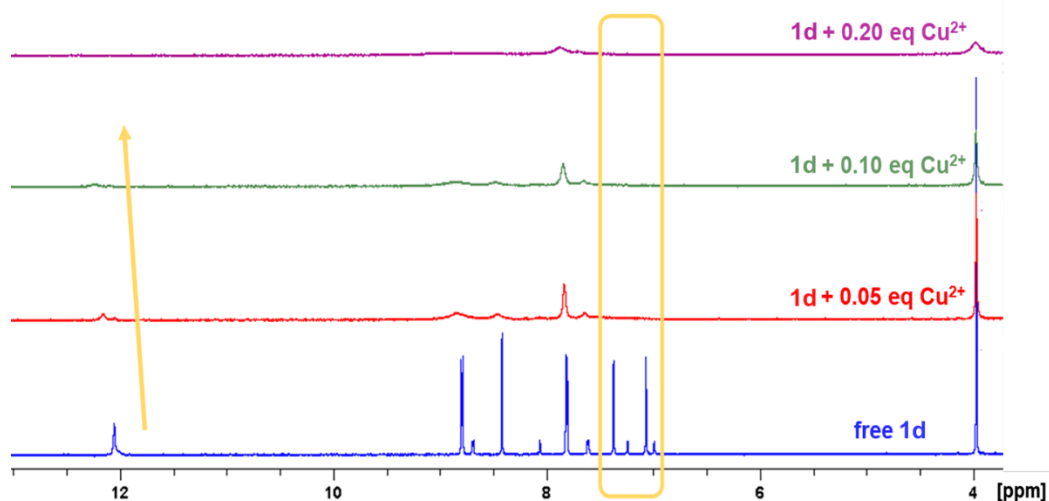


Figure 54. ^1H (400 MHz) spectra of **1d** in $\text{DMSO-}d_6$ in the absence (blue) and presence of 0.05 eq. (red), 0.10 eq. (green) and 0.20 eq. (purple) of copper(II) chloride dihydrate, at room temperature. Adapted from (Cukierman *et al.*, 2020).

The presence of paramagnetic copper(II), even at the substoichiometric amount of just 0.05 eq., causes the broadening of most of the ligand's signals. The most evident effect occurs at the signals related to the aromatic imidazole hydrogen atoms, which are originally observed at 7.365 and 7.072 ppm and disappear

completely after the first metal addition (yellow box). This suggests that the primary anchoring point for copper(II) ions in compound **1d** is, in fact, the 1-methyl-1H-imidazole moiety. Subsequent copper(II) additions progressively affect all the ligand's resonances and, at 0.20 eq. of metal, only the most shielded hydrogens from pyridine and those from the methyl group are still observable. Another interesting feature observed along the titration was the gradual de-shielding effect upon the amide hydrogen signal from 12.066 to 12.158 ppm, and then to 12.242 ppm (yellow arrow), which indicates that the presence of copper(II) weakens the N–H bond, and probably fully deprotonates the ligand at the stoichiometric coordination ratio ML, as evidenced by the decrease in the apparent pH observed after the Job Plot measurements. When the same set of experiments was performed in 10% DMSO-*d*₆/D₂O (% v/v), **1d**'s signals were broadened beyond detection upon the addition of 0.10 eq. copper(II) and, for this reason, the spectra are not shown herein.

In the presence of α -Syn, compound **1d** was evaluated with respect to its metal sequestering potential towards the Cu²⁺ / Cu⁺ redox active couple. The details of copper binding to α -Syn were explored at single residue resolution by NMR spectroscopy. Initially, the ¹H-¹⁵N HSQC spectrum of the paramagnetic α -Syn-Cu²⁺ complexes was recorded, from which the measured intensities profile confirms His50 as the main copper(II) anchoring residue ($K_d = 35 \mu\text{mol L}^{-1}$) at the *N*-terminal region of α -Syn, as well as the location of multiple copper(II) binding sites at the *C*-terminus, with affinities in the millimolar range (Figure 55A, blue line) (Binolfi *et al.*, 2010). Then, ascorbate was added as reducing agent to generate the α -Syn-Cu⁺ complexes. As shown in Figure 55B (black bars), the chemical shifts profile of α -Syn-Cu⁺ binding revealed the occurrence of very large chemical shift changes in a discrete number of residues located at the 1–10 segment of the *N*-terminal region, reflecting the binding of copper(I) ions to the high-affinity binding site Met1-Met5 ($K_d = 10 \mu\text{mol L}^{-1}$) (Miotto *et al.*, 2015).

Interestingly, increasing amounts of the *N*-acylhydrazone **1d** were shown to compete quite efficiently with the protein for the binding of copper(I) at the high-affinity Met1-Met5 motif, removing substantially the metal-induced perturbations from α -Syn backbone amides upon addition of 5 eq. of the compound (Figure 55B, progressively: red, green, purple, and blue bars). In addition, the features of the 1D

^1H NMR spectrum of the protein is not modified in the presence of **1d**, indicating that the compound does not interact directly with α -Syn monomers. Taken together, these results demonstrate that compound **1d** is able to disrupt copper(I) interactions with α -Syn by a mechanism that probably involves metal ion sequestering. The affinity of **1d** for copper(I) ions seems to be comparable to that of α -Syn, consistent with this *N*-acylhydrazone acting as an MPAC.

On the other hand, for the higher oxidation state of copper, addition of up to 5 eq. of compound **1d** affected differently the spectral features of residues located around the high-affinity site of α -Syn towards Cu^{2+} (Figure 55A, gradually: red, purple and green lines): whereas the His50 and Gly51 signals remained broadened beyond detection, the resonances of other residues located in the vicinity (i.e. valines 48 and 52) of the metal-binding site showed a complete recovery of their intensities. The observed behavior is consistent with the role of His50 as the main anchoring residue for copper(II) binding and the conceivable formation of a ternary complex in which Gly51 and **1d** might provide additional groups for copper(II) coordination. In fact, in a very recent publication by our research group, we identified, in solution, a ternary complex involving copper(II), an *N*-acylhydrazone and a model decapeptide for a fragment of human prion protein (Cukierman *et al.*, 2019). Finally, the addition of only 1 eq. of **1d** was enough to remove completely copper(II) from the low affinity sites at the C-terminus of α -Syn (Figure 55A, red line above residue #80).

The results obtained from this set of experiments allow us to conclude that the compound **1d** actually possesses a lower, optimized affinity for copper(II). Once again, this was achieved by the use of the 1-methyl-1H-imidazole moiety as the primary metal anchoring site in the ligand. Comparing the performance of **1d** to that of the lead compound INHHQ (**1h**), it is evident that the latter has a much higher affinity for copper(II) ions than **1d**, since 3 eq. of INHHQ are sufficient to remove most of the metal-induced perturbations from α -Syn backbone amides, including those at residues His50 and Gly51. Moreover, the clear preference of **1d** for copper(I) is an interesting property, as α -Syn inclusions are mostly intracellular in PD and copper must be reduced to copper(I) before entering cells through a CTR1-mediated transport process. Additionally, the compound could impact copper(I) ions even before they enter the cell, since this reduced state is formed

transiently during redox reactions, as reducing agents (e.g. ascorbate) are also present extracellularly (Rice, 2000).

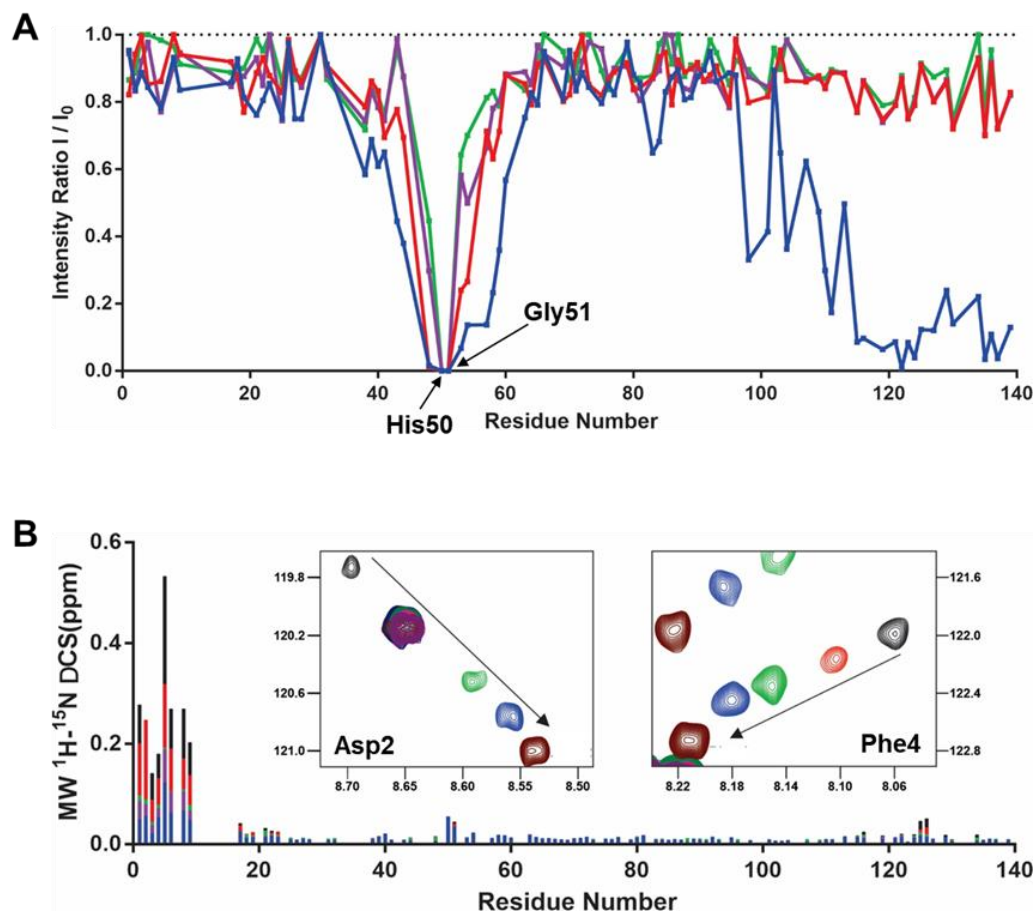


Figure 55. (A) Effect of **1d** on α -Syn- Cu^{2+} complexes. I/I_0 intensity profiles for the backbone amide resonances of $50 \mu\text{mol L}^{-1}$ α -Syn in the presence of 1 equivalent of Cu^{2+} (blue), followed by the addition of 1 (red), 3 (purple) and 5 (green) equivalents of compound **1d**. (B) Effect of **1d** on the high-affinity α -Syn- Cu^+ complex. Differences in the mean weighted chemical shift displacements ($\text{MW } ^1\text{H}-^{15}\text{N}\Delta\text{CS}$) between free and Cu^+ -complexed α -Syn at a molar ratio of 1:1 (black), followed by the addition of 1 (red), 2 (green), 3 (purple) and 5 (blue) equivalents of compound **1d**. Insets show the chemical shift changes on the resonances of Asp2 and Phe4 residues from the metal-complexed state (black) induced by increasing levels of **1d**: 1 (red), 3 (green) and 5 (blue) equivalents. Cross-peaks colored in brown correspond to metal-free α -Syn. Extracted from (Cukierman *et al.*, 2020).

Although there are no conclusive evidences concerning the binding of copper to α -Syn intracellularly under physiological conditions, mainly due to the highly reducing character of the cytosol and the presence of amino acid-based soft chelating agents such as metallothioneins (Meloni and Vařák, 2011) and GSH

(Morgan *et al.*, 2017), disregarding the importance of copper in PD pathology may signify neglecting an important paradigm in the pursue for novel therapies.

Increasing evidence of the presence of α -Syn in the extracellular medium has been reported (Vekrellis and Stefanis, 2012; Lee *et al.*, 2014; Ottolini *et al.*, 2017; Wilkaniec *et al.*, 2019), and the importance of these findings for PD pathology is yet to be unveiled. Besides, in a pathological (therefore not physiological) condition, one might expect that intracellular redox and metal balance are completely disturbed in a way that frontline defense entities such as metallothioneins and GSH can be fully overcome. Moreover, the recent publication of Lothian *et al.* leaves the possibility open that copper may serve to induce a small percentage of α -Syn molecules to trigger the nucleation process that lead to oligomerization and the subsequent formation of fibrils, and only a local misbalance of copper homeostasis is enough to initiate aggregation (Lothian *et al.*, 2019).

Taken together, the results discussed in this chapter, along with the previous one, point to the indisputable potentiality of 1-methylimidazole-containing *N*-acylhydrazones as moderate, optimized chelators for the prospective management of PD and other related synucleinopathies.



PUC-Rio - Certificação Digital Nº 1712623/CA

RESULTS AND DISCUSSION III

7. Results and discussion: Part III – Effects of the selected *N*-acylhydrazones on models for other aggregopathies

7.1. Impact of pyridine-2-carboxaldehyde-derived aroylhydrazones on the copper-catalyzed oxidation of M112A PrP₁₀₃₋₁₁₂ fragment

Although metal-enhanced aggregopathies present common features, such as proteins that are prone to aggregate upon interaction with metal ions, these diseases are multifactorial, and one could expect that structurally different *N*-acylhydrazones would have distinct activities for diverse models of such pathologies. While pyridine-2-carboxaldehyde-derived *N*-acylhydrazones did not present significant results on the aggregation of Syn-T model, it does not mean that these compounds are not interesting from an Inorganic Medicinal Chemistry point of view.

Structure-related compounds **1f** and **3f** (from here on referred to as HPCIH and HPCFur, respectively, following the literature nomenclature –

Figure 56) were evaluated as peptide protecting agents toward the deleterious metal-catalyzed oxidation effects in a mutant fragment of human PrP (Ac-SKPKTNMKHA-NH₂, abbreviated dMKHA – Figure 57), which mimics some relevant structural features that may play an important role in the neurotoxicity observed in prion pathologies. For simplification purposes due to the name of the peptide employed, the amino acid residues here are named following their one letter code. These studies were done in collaboration with the research group of Prof. Dr. Csilla Kállay, from the Department of Inorganic and Analytical Chemistry of the University of Debrecen, in Hungary. The NMR and ESI-MS experiments involved in this project were performed at the NMR-based Structural Biology Department, in the Max Planck Institute for Biophysical Chemistry - Göttingen, Germany. These results were described in a recent publication in the special issue “Metal Ions and Degenerative Diseases” of Journal of Biological Inorganic Chemistry (Cukierman *et al.*, 2019).

In terms of coordination chemistry, the use of dMKHA is also very suitable since this mutant maintains all the donor atoms involved in the coordination sphere of copper(II) observed in the human WT 103–112 fragment. Furthermore, in a very recent publication by Sánchez-López *et al.*, the preference of copper(II) for the H111 residue instead of the H96 one was demonstrated, and the fact was associated with the presence of M109 in the vicinity of the former site (Sánchez-López *et al.*, 2018). This constitutes an additional support for the use of the short dMKHA fragment, which displays the M112A mutation but keeps the auxiliary anchoring methionine residue at the 109 position.

Before assessing the compounds, we studied the copper(II) coordination chemistry of dMKHA, to confirm, by complementary means, the involvement of the methionine thioether sulfur atom in the metal anchoring system constituted by the H111 side chain. In the present work, 1D and 2D NMR spectroscopy were employed to pursue this goal. The intrinsic absorptions of the HEPES buffer prevented the observation of the peptide's signals between 4.0 and 2.7 ppm. However, the most important resonances regarding the present study are located outside of this region. The aromatic hydrogens of the histidine residue are observed as a pair of doublets ($^4J = 1.1$ Hz) at 7.729 and 6.934 ppm. Cross peaks in the ^1H – ^1H TOCSY contour plot confirm the assignments (data not shown). The most shielded of those aromatic nuclei also couples with a resonance at around 3 ppm, which should correspond to the histidine β -methylene hydrogen atoms. Thus, the signal at 6.934 ppm was assigned to the $\delta 2$ imidazole hydrogen. On the other hand, the ϵ methyl hydrogens from the methionine residue resonate at 2.022 ppm and those from the *N*-terminal acetyl group, at 1.992 ppm. Amide hydrogens from the side chain of asparagine (N108) are observed as two broad signals at 7.526 and 6.827 ppm. Figure 58A shows the main assignments concerning the $\text{H}\alpha$ (in a ^1H – ^{13}C HSQC contour plot) and some “key” hydrogen signals belonging to potentially coordinating side chains in the peptide (highlighted in the ^1H spectrum of dMKHA).

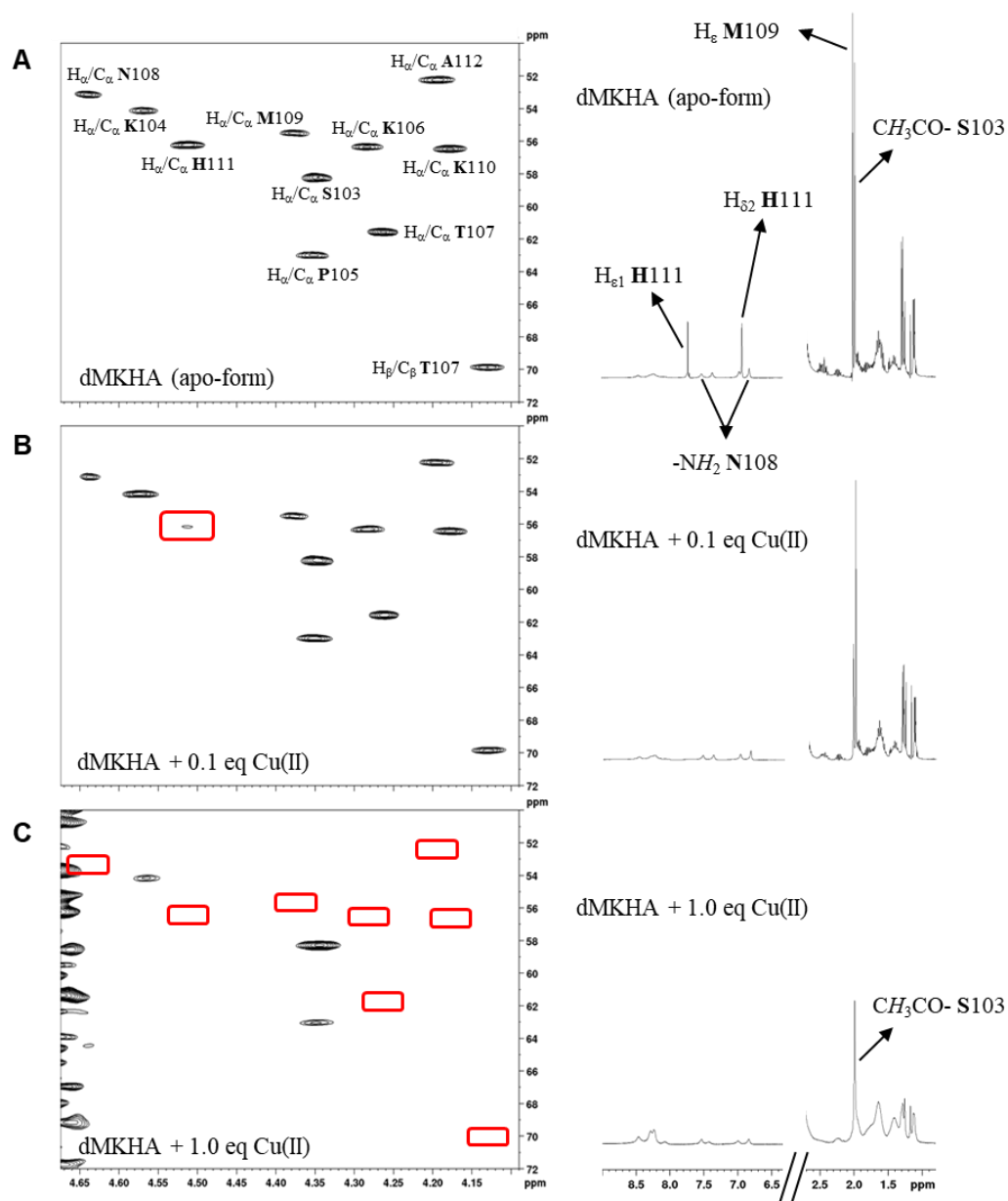


Figure 58. NMR study of the coordination of copper(II) by dMKHA. ^1H - ^{13}C HSQC contour plots and ^1H NMR spectra of (A) dMKHA apo-form, (B) dMKHA + 0.1 eq copper(II) and (C) dMKHA + 1.0 eq copper(II). pH 7.4 at 25 °C. Extracted from (Cukierman *et al.*, 2019).

Usually, the loss of NMR signals due to the paramagnetic effects related to this cation occurs within 9–10 Å, affecting the peptide's nuclei in a relatively local manner. The addition of 0.1 eq copper(II) disturbed immediately the $\text{H}_\alpha/\text{C}_\alpha$ H111 cross peak in the ^1H - ^{13}C HSQC map, as well as the signals from histidine's $\delta 2$ and $\varepsilon 1$ aromatic hydrogens in the ^1H NMR spectrum of dMKHA, which were broadened almost beyond detection (Figure 58B). This confirms the high affinity of histidine for copper(II) as well as its role as an anchoring site for this metal, and is in

accordance to data previously published for the PrP_{106–113} fragment (Belosi *et al.*, 2004). Additionally, a significant intensity decrease is observed in the ϵ methyl signal from methionine, which could indicate a weak interaction with the sulfur atom of this residue as a part of the coordination process. Increasing the copper concentration until reaching 1.0 eq (Figure 58C), we observed that only three out of ten H $_{\alpha}$ /C $_{\alpha}$ cross peaks seem to be not directly affected by the metal. They are, as expected, those from S103, K104, and P105, which confirm the idea that *N*-terminal residues are not involved in the interaction with copper(II) ions due to the presence of proline, a well-known break point for metal coordination. At this 1:1 stoichiometry, also the ϵ methyl signal of methionine is severely affected. This strongly supports the propositions regarding a methionine contribution to coordination. However, other signals considered in the present study, as those related to the $-NH_2$ hydrogens from the amide side chain of asparagine, remain quite unchanged, which allows to rule out the involvement of this residue in the dMKHA–metal interaction. From the protonation equilibria studies published by Csire *et al.*, we assume that, at pH 7.4, an almost equimolar mixture of the [Cu(H $_{-2}$ dMKHA)]³⁺ and [Cu(H $_{-3}$ dMKHA)]²⁺ species occurs (Csire *et al.*, 2017). The conditional stability constants for these complexes are, respectively, -7.95 and -15.43 . Therefore, we can conclude that the most likely donor atoms in the coordination sphere of copper(II) at this pH value are an imidazole nitrogen from histidine and two (in H $_{-2}$ dMKHA, where dMKHA represents the peptide protonated at the three lysine residues) or three (in the case of H $_{-3}$ dMKHA) deprotonated amide nitrogens from the main-chain peptide bonds involving H111, K110 and, for the species [Cu(H $_{-3}$ dMKHA)]²⁺, also M109. It is well known that copper(II) is able to deprotonate and bind amide nitrogen atoms when anchored to imidazole groups from histidine residues (Kozłowski *et al.*, 2005), a process which, for this system, happens above pH 5 in a cooperative manner (Csire *et al.*, 2017). The thioether sulfur atom from methionine should be axially coordinated. Figure 59 shows the proposed structures for the metal–peptide adducts at pH 7.4. Special attention should be paid to the labile equatorial site displaying a coordinated water molecule in [Cu(H $_{-2}$ dMKHA)]³⁺, since it constitutes a putative spot for the interaction and subsequent oxidation of H₂O₂ to the O₂⁻ radical, giving rise to a reduced copper(I) center which, in turn, could be able to trigger dMKHA oxidation through Fenton-type reactions (Zhao *et al.*, 1997; Schöneich, 2000). Finally, a

contact with the hydroxyl oxygen atom from the T107 side chain, alternating with the apical water molecule in a supposed multipart equilibrium, cannot be completely discarded at this point, as the cross peak related to threonine H_{β}/C_{β} coupling is also very affected by the presence of copper.

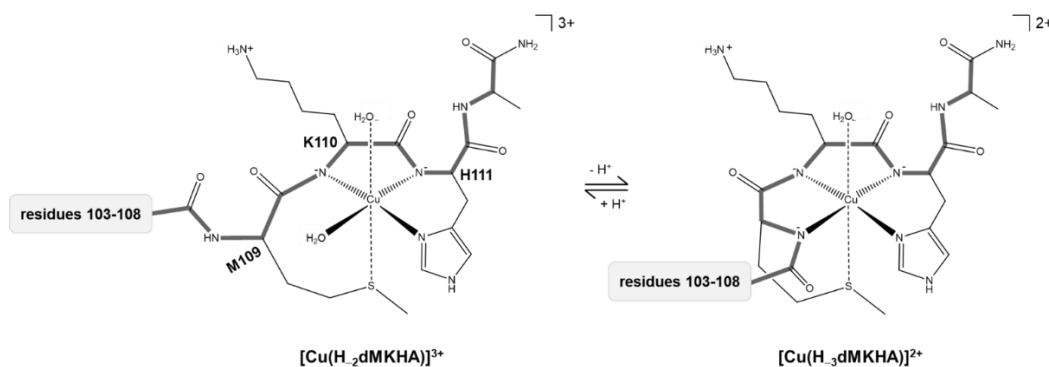


Figure 59. Proposed structures for the main species present in equilibrium at pH 7.4 in the dMKHA–copper(II) system. The peptide’s main-chain is highlighted in bold grey, while the main amino acid residues involved in coordination are labelled. Reference: (Cukierman *et al.*, 2019).

The oxidation of dMKHA in the presence of copper(II) and hydrogen peroxide has been previously investigated by RP-HPLC and mass spectrometry (Csire *et al.*, 2017). Figure 60A presents a series of representative chromatograms involving the studied systems after 30 min of oxidation. The ratio of the main products at the end of this period is presented in Figure 60B. For the system containing only the peptide and copper(II), oxidation does not occur at significant extent under our experimental conditions. In the presence of H_2O_2 , however, the product dM(O)KHA, observed at a retention time of 13.2 min, is generated, corresponding to the oxidation of the methionine residue to methionine sulfoxide. The number of oxidation sites present, as well as their precise identification, was determined by MS/MS measurements. The fragment ions are indicated by *b* if the charge is retained on the N terminus and by *y* if the charge is maintained on the C terminus, as proposed by Roepstorff and Fohlman (Roepstorff and Fohlman, 1984). The subscript refers to the number of amino acid residues in the fragment. The fragmentation of the singly oxidized product at the methionine residue is displayed in Figure 61A. The m/z value at 599.822 (calculated value: m/z 599.822) corresponds to the doubly charged singly oxidized molecular ion of dMKHA (i.e.,

$[y_{10} + O]^{2+}$). The most convincing proof of methionine oxidation is the elimination of a CH_3SOH molecule (63.998 Da) from the $[y_{10} + O]^{2+}$ and $[y_8 + O]^{2+}$ ions, as it is considered a diagnostic evidence for the formation and presence of methionine sulfoxide (Bridgewater and Vachet, 2005). Furthermore, the formation of $[y_4 + O]^+$ supports that the oxygen atom is attached to one of the four amino acids at the C terminus. Since the $[y_2]^+$ ion was observed in the MS/MS spectrum, the oxidation of the histidine residue can be ruled out.

When an excess of ascorbic acid is present, more products are formed: besides dM(O)KHA ($t_R = 13.1$ min), oxidation of the histidine residue also takes place, giving rise to the doubly oxidized product, [dMKHA + 2O], and the singly histidine oxidized product dMKH(O)A. These species elute at 13.4 min and 16.6 min, respectively. The m/z value of the product in which the histidine residue is oxidized is equal to the previous one (m/z 599.822), but it is detected at a different retention time: 16.6 instead of 13.1 min. The oxidation of histidine is also proved in the doubly oxidized product ($[y_{10} + 2O]^{2+}$, with m/z 607.814, calculated value: m/z 607.819), as can be seen in Figure 61B. Additionally, the $[y_3 + O]^+$ ion, with the amino acid sequence –KHA–, is only singly oxidized, being the oxygen atom consequently attached to the histidine residue. From the results discussed above, one can conclude that the presence of ascorbic acid slightly hinders the oxidation of methionine, promoting that of histidine (Figure 60B). This effect is not favorable since the methionine oxidation can be easily reversed by the methionine sulfoxide reductase systems (methionine sulfoxide reductase A or B), but the one involving histidine is irreversible.

A similar effect on the oxidation of dMKHA is observed when an equimolar amount (with respect to the peptide) of the *N*-acylhydrazone HPCIH (**1f**) is added. However, the compound promotes the oxidation of histidine to a lesser extent than ascorbic acid. Only a small amount of the doubly oxidized product is generated (around 3%), while the single oxidized product dMKH(O)A is negligible. Even if the amount of this compound is decreased to one-tenth, its effect is still significant.

The protecting role of HPCFur (**3f**) is even more expressive. When this compound is present at the same concentration as dMKHA, almost 85% of the peptide remains unchanged, being only 15% of it oxidized, but exclusively on the

methionine residue. In the presence of ascorbic acid, the protective effect of HPCFur (**3f**) remains, although to a lesser degree. Analyzing the effect of this ligand on the oxidation profile of the system dMKHA : Cu(II) : H₂O₂ : ascorbic acid, we observe almost 10% more of unoxidized peptide, due to the reduction of histidine-associated oxidation products, since the amount of methionine-oxidized peptide remains almost the same.

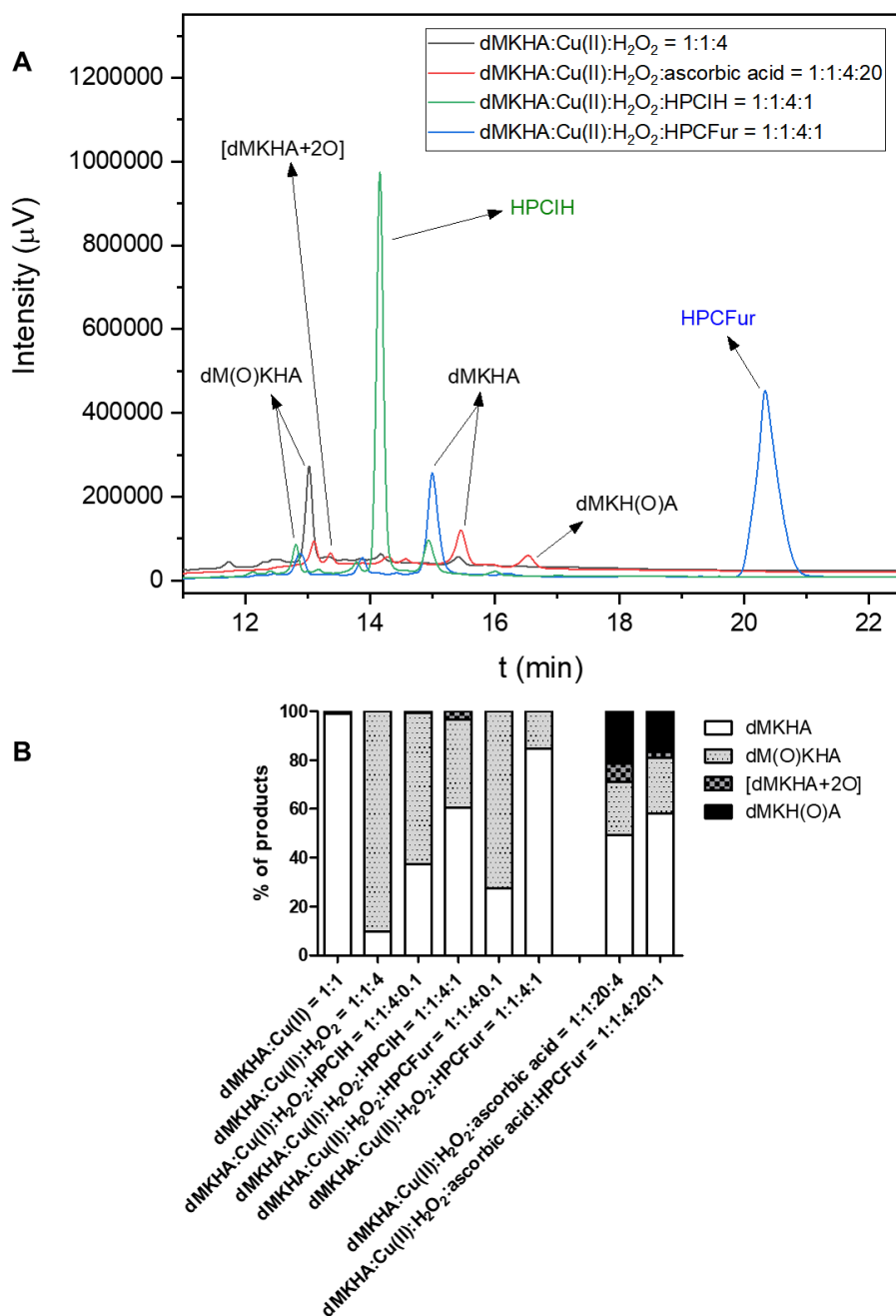


Figure 60. HPLC study of the oxidation of dMKHA in the presence of copper(II) and H₂O₂. **(A)** Representative chromatograms of the different studied systems after 30 min of reaction. **(B)** Ratio of products at the end of this timepoint. Extracted from (Cukierman *et al.*, 2019).

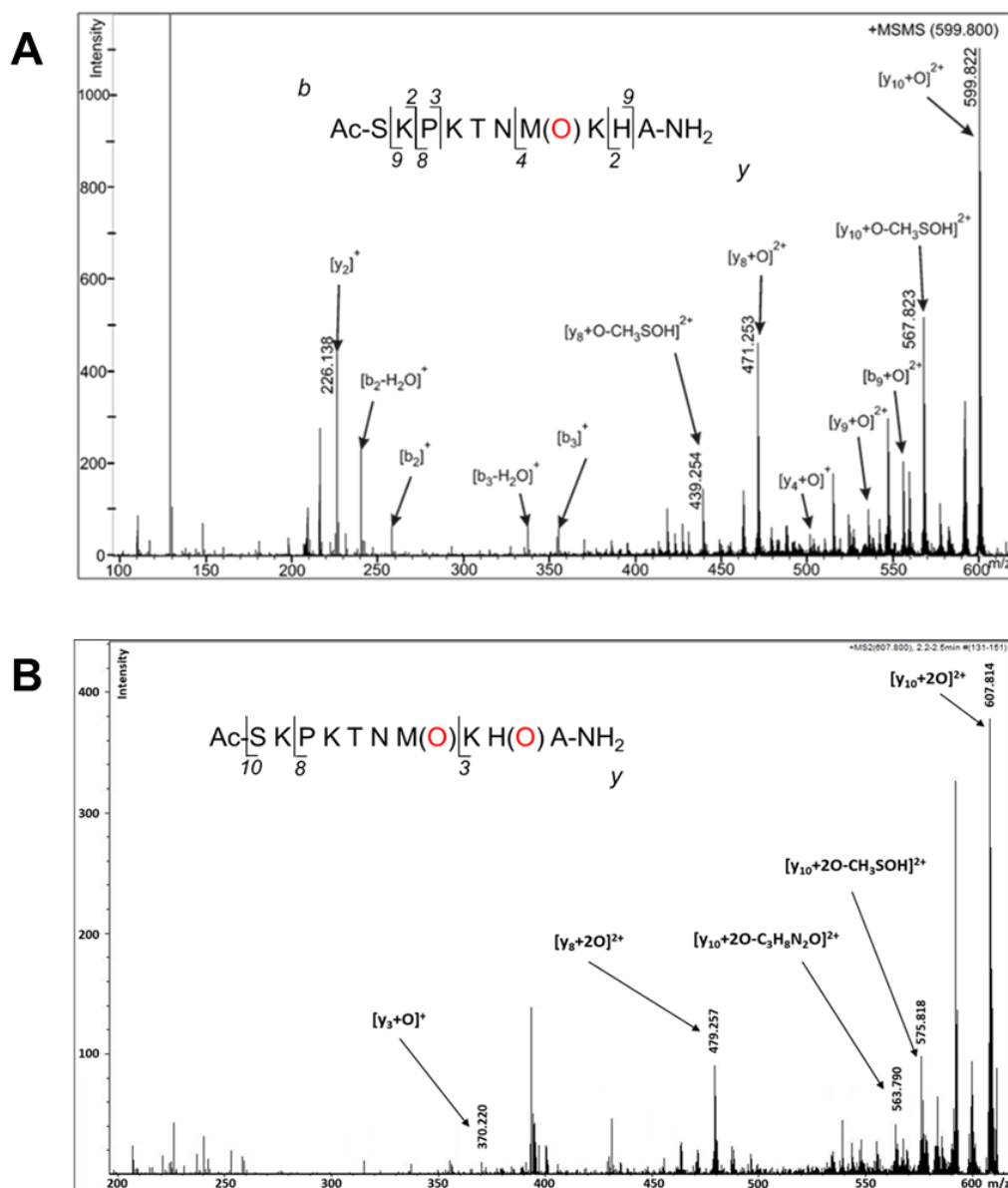


Figure 61. MS/MS spectrum of (A) the methionine oxidized dM(O)KHA species and of (B) the doubly oxidized dM(O)KH(O)A product. Extracted from (Cukierman *et al.*, 2019).

To further characterize the oxidation of the peptide, NMR spectroscopy was employed. As stated above, both methionine and histidine residues of dMKHA are sensitive to oxidation in the presence of hydrogen peroxide, a reaction catalyzed by copper(II) ions. Methionine is an amino acid highly susceptible to oxidation, even under mild conditions, and the methionine sulfoxide-containing derivative constitutes the main product identified by RP-HPLC and mass spectrometry experiments. Therefore, the oxidation of this residue of the peptide at 25 °C was followed by ^1H NMR, in a reaction mixture containing 0.1 eq Cu^{2+} and excess (4.0 eq) of H_2O_2 .

Throughout the oxidation process of dMKHA, the decrease in intensity of the ϵ methyl hydrogens' signal from the methionine residue at 2.02 ppm was accompanied by the rise of an asymmetric absorption at 2.65 ppm, which was assigned to the ϵ methyl hydrogens from the methionine sulfoxide of the oxidized product (Figure 62A). These outcomes agree with the observations made on the single amino acid which, after oxidation to methionine sulfoxide, displays two very close singlets for the methyl group, which are shifted by around 0.60 ppm downfield when compared to the signal related to the methyl group in unoxidized methionine (Concetti and Gariboldi, 1990). He *et al.* also found a similar NMR spectral behavior when studying the methionine oxidation in peptides by peroxovanadium complexes (He *et al.*, 2015). A qualitative analysis of the results obtained was performed by measuring the peak intensities related to radiofrequency absorptions, since the strong signal overlapping prevented accurate integrations to be carried out. After 45 min of reaction, intensities corresponding to the oxidized and unoxidized forms of dMKHA seem to reach a plateau (Figure 62A, inset). At this point, approximately 87% of the peptide units contain methionine sulfoxide. However, if the reaction is additionally followed until 120 min, a second oxidation phase, probably related to the formation of the doubly oxidized product, occurs (Figure 62B, black line). During this second step, another 6% of unoxidized dMKHA are lost. Besides those related to the methyl group of the methionine residue, other minor changes were observed in the spectra as well, probably related to the generation of a new stereogenic center in the sulfur atom introduced by the oxidation of methionine (Concetti and Gariboldi, 1990). A series of magnetic anisotropy effects related to the presence of the sulfoxide group can be identified too, being also responsible for these small alterations.

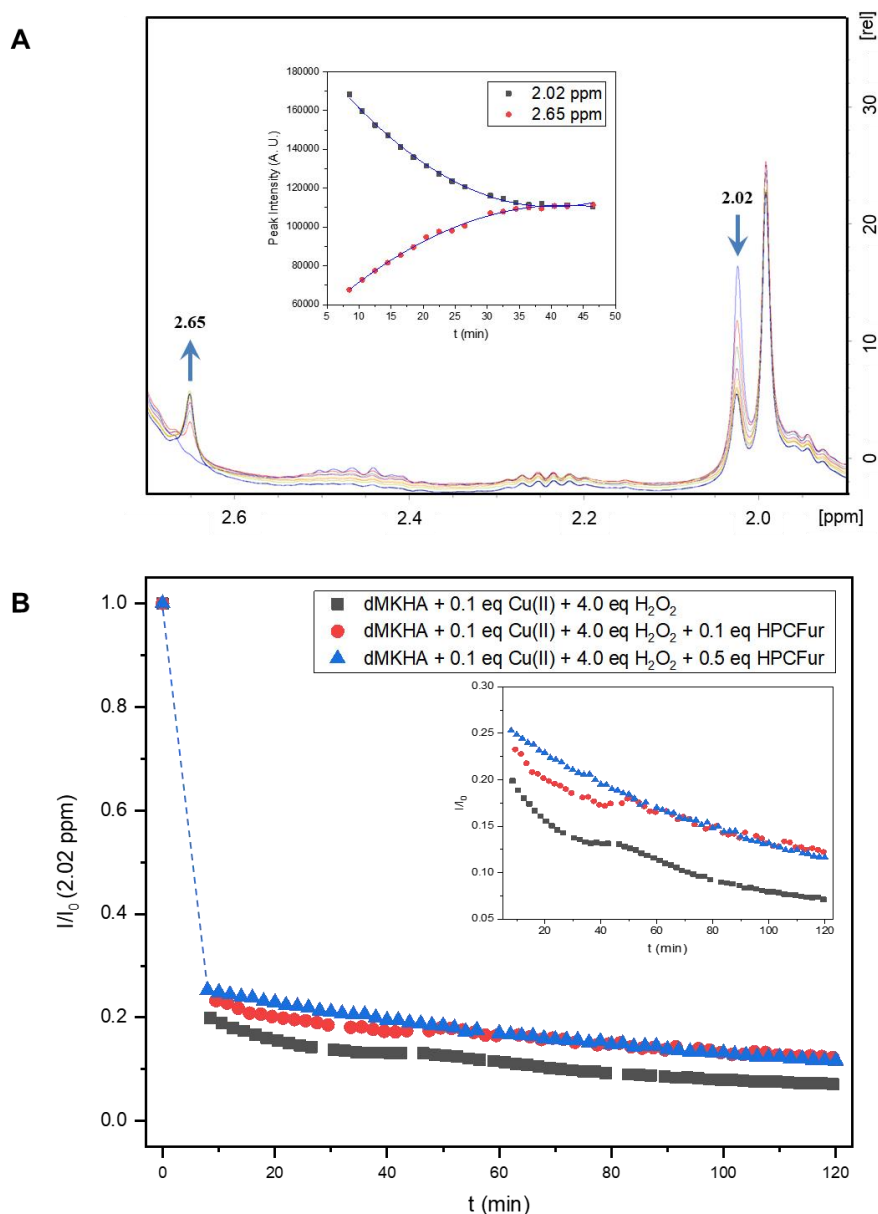


Figure 62. NMR study of the oxidation of dMKHA in the presence of copper(II) and H_2O_2 . **(A)** A series of ^1H NMR acquired at regular intervals for 45 min, at 25°C and pH 7.4. Inset: Peak intensities of the ϵ methyl hydrogens' signal from methionine at 2.02 ppm (black) and the oxidized product formed (methionine sulfoxide) at 2.65 ppm (red). **(B)** Normalized intensity of the ϵ methyl hydrogens' signal from methionine at 2.02 ppm (black), in the presence of 0.1 eq (red) and 0.5 eq (blue) HPCFur (**3f**). Inset: Magnification of the methionine ϵ methyl signal intensity *versus* reaction time curves. Extracted from (Cukierman *et al.*, 2019).

As the compound HPCFur (**3f**) showed the most promising prospect regarding its protecting role toward dMKHA oxidation, the effect of 0.1 and 0.5 eq of this ligand was also evaluated through NMR in the system constituted by 1:0.1:4 dMKHA (5.0 mmol L^{-1}) : Cu^{2+} : H_2O_2 . As shown in Figure 62B (red and blue lines), this aroylhydrazone is able to prevent methionine oxidation to some extent, as

assessed by the peak intensity of the signal at 2.02 ppm. After 120 min of reaction, around 12% of the peptide remains unoxidized for both concentrations (0.5 and 2.5 mmol L⁻¹) of HPCFur (**3f**), which represents a protection of around 70% (0.12 against 0.07) compared to dMKHA oxidation in the absence of the compound. It is worth noting that these values are not directly comparable to those obtained by RP-HPLC, since solvent system and reactant concentrations are not the same. However, the protective effect of HPCFur (**3f**) is nonetheless confirmed by the NMR results. Probably more relevant is the corroboration of the compound inhibition effect in histidine oxidation, which seems to occur in a concentration-dependent manner. The inset of Figure 62B shows a magnification of the methionine ϵ methyl signal intensity versus reaction time curve, in which one can observe that, upon addition of 0.5 eq HPCFur (**3f**) (blue line), the second oxidation step detected for dMKHA (black line) is completely abolished. This is again in agreement with the data obtained from RP-HPLC and mass spectrometry experiments.

The observed HPCFur (**3f**) protective effect toward dMKHA oxidation certainly deserves some deeper considerations regarding this ligand's interactions with the peptide–copper(II) system. First of all, ¹H NMR spectra showed that HPCFur (**3f**) does not interact directly with dMKHA under the experimental conditions employed in the present study (data not shown). Upon addition of 0.1 eq of Cu²⁺ to a mixture constituted by dMKHA (5.0 mmol L⁻¹) and 0.5 eq HPCFur (**3f**), all the NMR signals related to the hydrogen atoms in the ligand, altogether with the imidazole signals of the peptide, are broadened beyond detection, indicating the interaction with the paramagnetic ion. The ϵ methyl group from M109 is also affected, although to a lesser extent. This is in accordance with ¹H NMR titration experiments performed for the dMKHA (5 mmol L⁻¹) : Cu²⁺ (0.1 eq) : HPCFur (**3f**) (0.1–0.5 eq) system (Figure 63A). However, in the absence of the compound, the H111 imidazole signals, while broadened and slightly shifted, are not completely abolished (Figure 63A, inset). This seems to indicate that the presence of the ligand at the [HPCFur (**3f**)] : [Cu²⁺] = 1 : 1 ratio strengthens the interaction of dMKHA with copper instead of preventing it, probably through the formation of a ternary complex whose proposed structure can be observed in Figure 63B. Coordination of copper to dMKHA is, in this sense, modulated by HPCFur (**3f**). This is reflected in the large amount of signal loss detected after the first ligand

addition. Increasing amounts of HPCFur (**3f**) (up to a ligand-to-metal stoichiometry of 5 : 1, limited by solubility issues) are able to rescue the signals' intensities only to the level registered after the addition of copper(II). Recovery of M109 methyl signal, on the other hand, is more significant and, at the end of the titration, the observed signal was around 65% higher than that measured after Cu^{2+} addition (Figure 63A, inset).

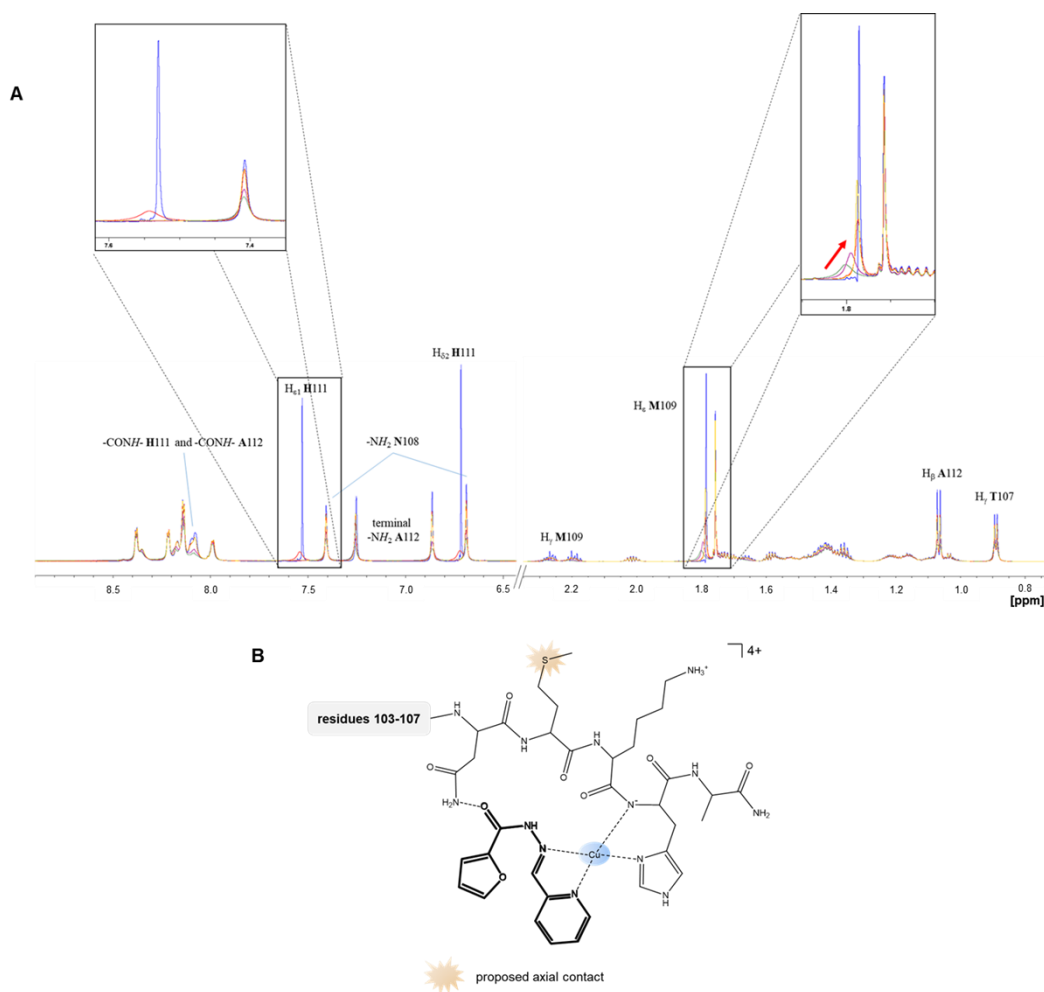


Figure 63. Suggested interactions in the ternary system dMKHA–copper(II)–HPCFur (**3f**). **(A)** ^1H NMR titration performed for the dMKHA (5 mmol L^{-1}) : Cu^{2+} (0.5 mmol L^{-1}) : HPCFur ($0.5\text{-}2.5 \text{ mmol L}^{-1}$) system, at $5 \text{ }^\circ\text{C}$ and pH 7.4. Insets: Zooms of the $\text{H}_{\epsilon 1}$ signal from H111 (left) and H_{ϵ} from M109 (right). **(B)** Proposed schematic structure for the ternary complex $[\text{Cu}(\text{H-1dMKHA})(\text{HPCFur})]^{4+}$. Extracted from (Cukierman *et al.*, 2019).

It is worth noting that the ternary coordination compound was identified via ESI–MS(+) measurements, through the peak at m/z 499.32 (Figure 64), assigned to the $[\text{Cu}(\text{H-1dMKHA})(\text{HPCFur})\text{Cl}]^{3+}$ species (calculated: m/z 499.54). This may

represent a different mechanism of action from the one usually associated with “classical” MPACs, in which competition with the peptide for the binding to the metal ion is replaced by an active modulation of such interactions. Our proposition is that steric- or kinetic-related factors may impair the production of a coordinated hydroxyl radical, proposed to be the actual ROS involved in amino acid oxidation catalyzed by copper in the presence of hydrogen peroxide (Zhao *et al.*, 1997). In fact, in a very recent publication by the groups of Luigi Casella and Bilha Fischer, the potential of an aminomethylene-phosphonate derivative to inhibit the 4-methylcatechol oxidation induced by the PrP₈₄₋₁₁₄-copper(II) system was associated to the formation of a ternary, redox inactive, PrP₈₄₋₁₁₄-copper(II)-ligand complex (Pariente Cohen *et al.*, 2019).

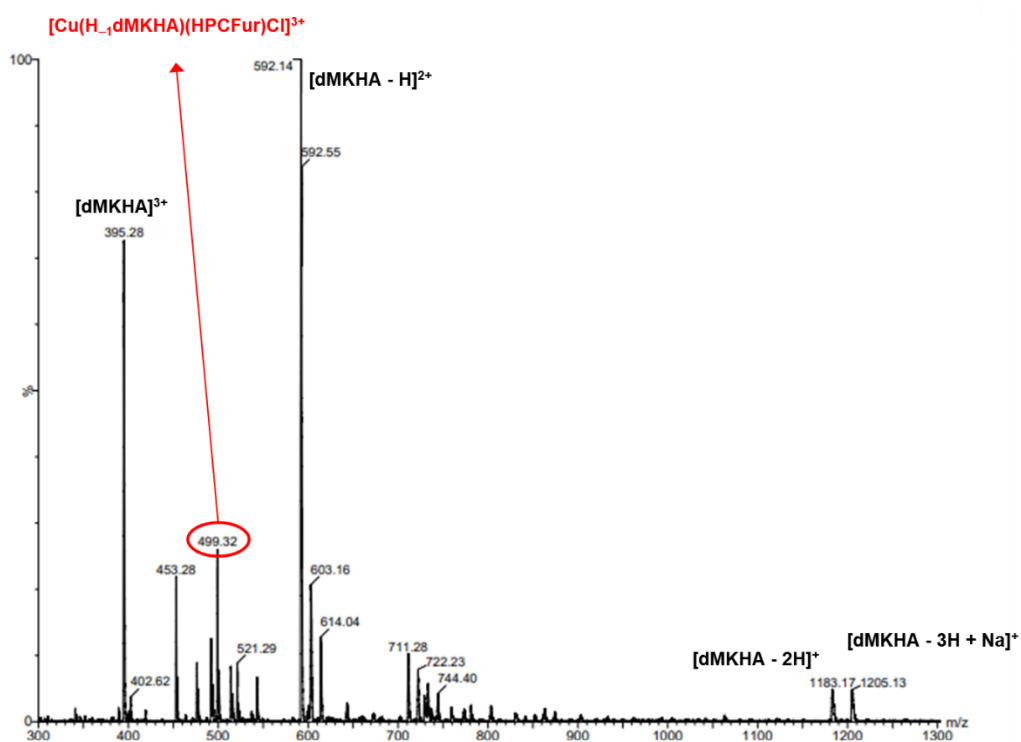


Figure 64. ESI-MS(+) spectrum of a mixture of dMKHA (5 mmol L⁻¹), Cu²⁺ (0.5 mmol L⁻¹) and HPCFur (**3f**) (2.5 mmol L⁻¹), at pH 7.4. The ternary species [Cu(H₁dMKHA)(HPCFur)Cl]³⁺ is observed at *m/z* 499.32. Extracted from (Cukierman *et al.*, 2019).

7.2. Prospective effect of *N*-acylhydrazones in Stress Granules

While on one hand specific protein aggregation in neurodegenerative diseases is considered a key factor for cell death, for RNA binding proteins (RBPs) this constitutes a physiological process in protein synthesis, through the formation of Stress Granules (SGs). These are membraneless aggregates in the cytosol that contain RNA and proteins, and are formed when the cell is under stress, with the proposed goal of protecting RNA under such conditions. These proteins associate through their glycine rich domains in a reversible and regulated pathway, through liquid-liquid phase separation (LLPS). However, RBPs mutations and prolonged stress conditions have been associated with accelerated pathological protein aggregation in neurodegenerative diseases such as amyotrophic lateral sclerosis and frontotemporal lobar degeneration (Irwin et al., 2015; Taylor et al., 2016).

The 8 initially selected *N*-acylhydrazones were also evaluated against a cellular model of SGs, generated in the presence of arsenous acid. Arsenite is thought to be responsible for the oxidation of cysteine residues in target proteins, altering their conformation and activity, causing, thus, its known toxicity (Thompson, 1993; McEwen *et al.*, 2005). Consequently, the use of sodium *meta*-arsenite to induce the formation of SGs has become protocol. Figure 65 shows the effect of this oxidative stress in HEK cells: nuclei are shown in blue color in DAPI channel, while TIA1 was immunostained and is presented in red. As can be observed in the water negative control, in which arsenite was not added, TIA1 is diffuse in the cytosol of the cells. However, in the presence of NaAsO₂, this RNA-binding protein is concentrated as cytoplasmatic inclusions, visualized as small red dots. The effect of 1% DMSO treatment was also assessed as a control for the experiments involving the compounds. As can be observed, the solvent has no effect whatsoever upon the formation of SGs.

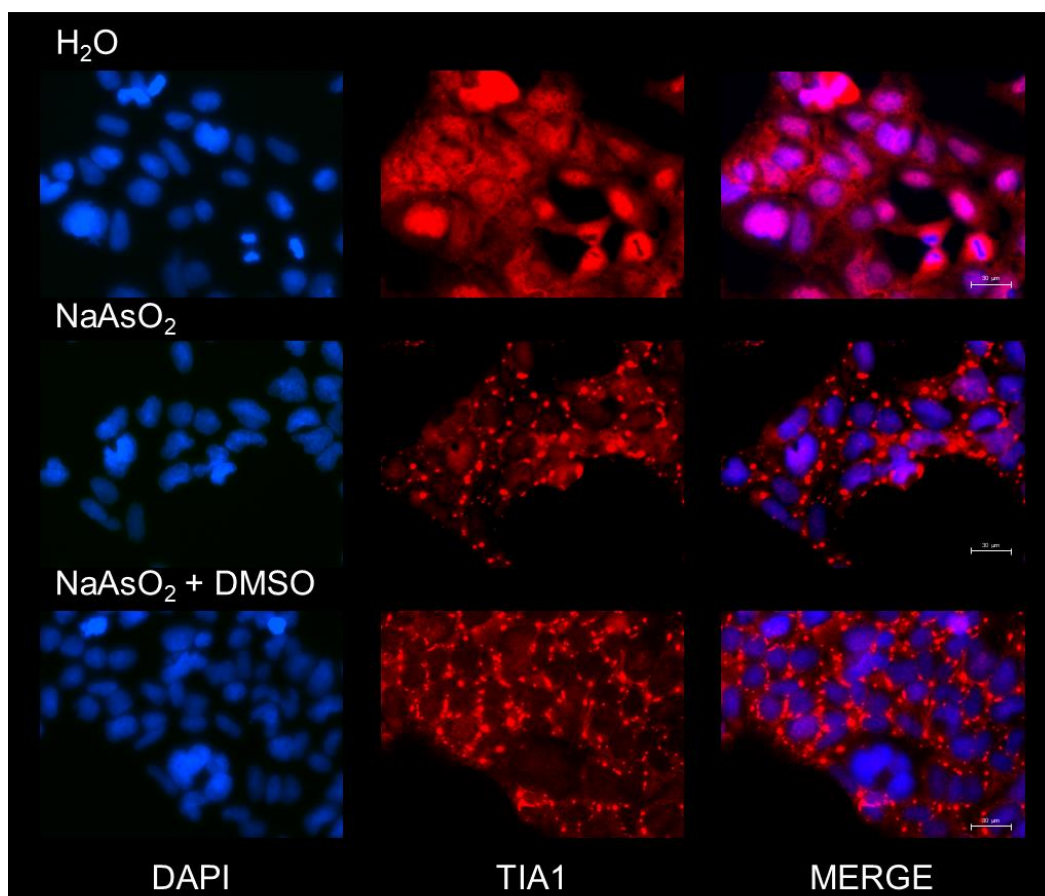


Figure 65. Representative images of the stress granules pattern in HEK cells: effect of positive and negative controls. TIA1 is shown in red, while the cell nuclei are colored in blue.

The proposed involvement of SGs in such diseases opens the perspective of new targets for new therapeutic strategies. In this sense, Figure 66, Figure 67, Figure 68 and Figure 69 show a qualitative prospect of the effect of the studied hydrazones upon the arsenite-generated SG model in HEK cells. Since SG pathway is reversible and inclusions are quickly dissolved upon stress removal (not shown), treatment with the compounds were preventive, i.e. cells were treated with the hydrazones or their 1% DMSO solution control for 24 hours prior to the addition of NaAsO₂ for 2 hours.

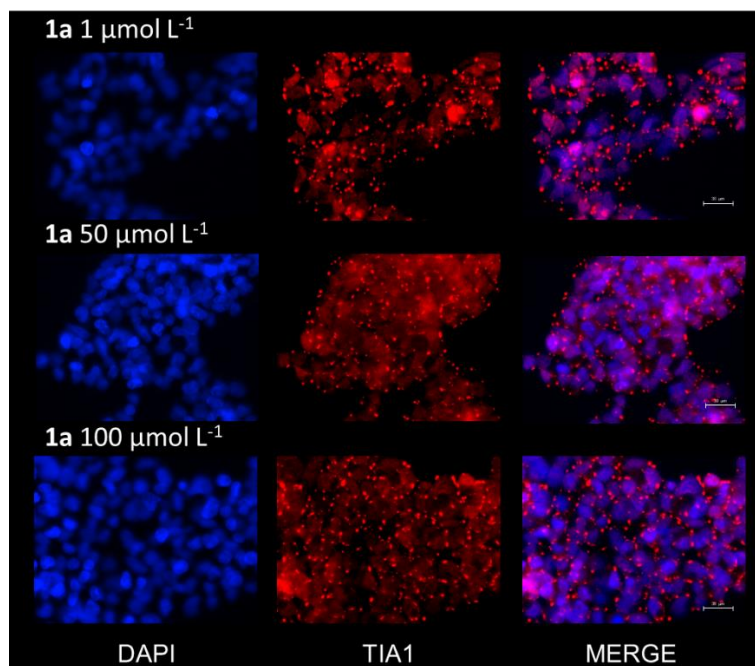


Figure 66. Representative images of the stress granules pattern in HEK cells: effect of different concentrations of compound **1a**. TIA1 is shown in red, while the cell nuclei are colored in blue.

Compound **1a** has no effect upon the formation of SGs (Figure 66). Treatment with lead compound **1h** also presents no significant effect in this model, as displayed in Figure 67. Compound **1f**, however, seems to reduce the amount of observable SG inclusions in the highest concentration of $100 \mu\text{mol L}^{-1}$. The same was not observed in the structure-related, 2-pyridine-derived, *N*-acylhydrazone **3f**, as can be seen in Figure 68.

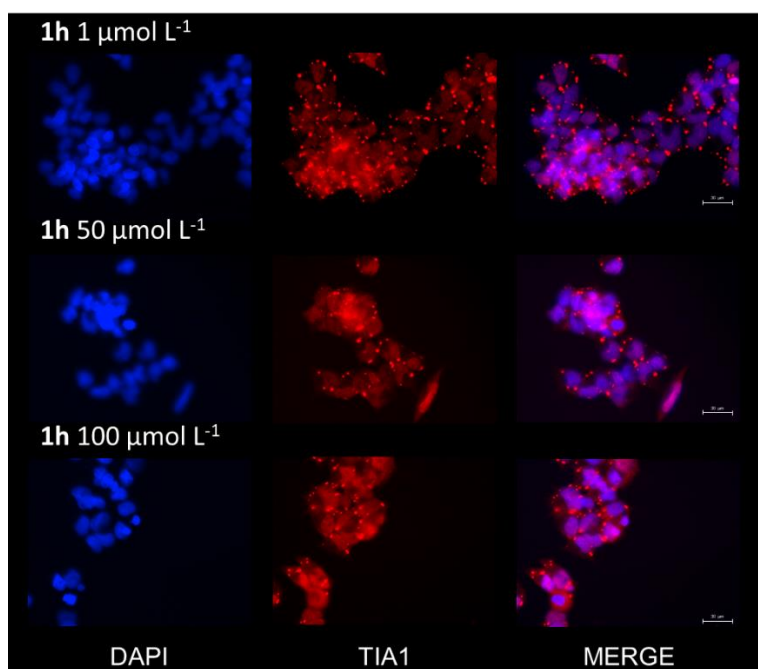


Figure 67. Representative images of the stress granules pattern in HEK cells: effect of different concentrations of lead compound **1h** (INHHQ). TIA1 is shown in red, while the cell nuclei are colored in blue.

PUC-Rio - Certificação Digital Nº 1712623/CA

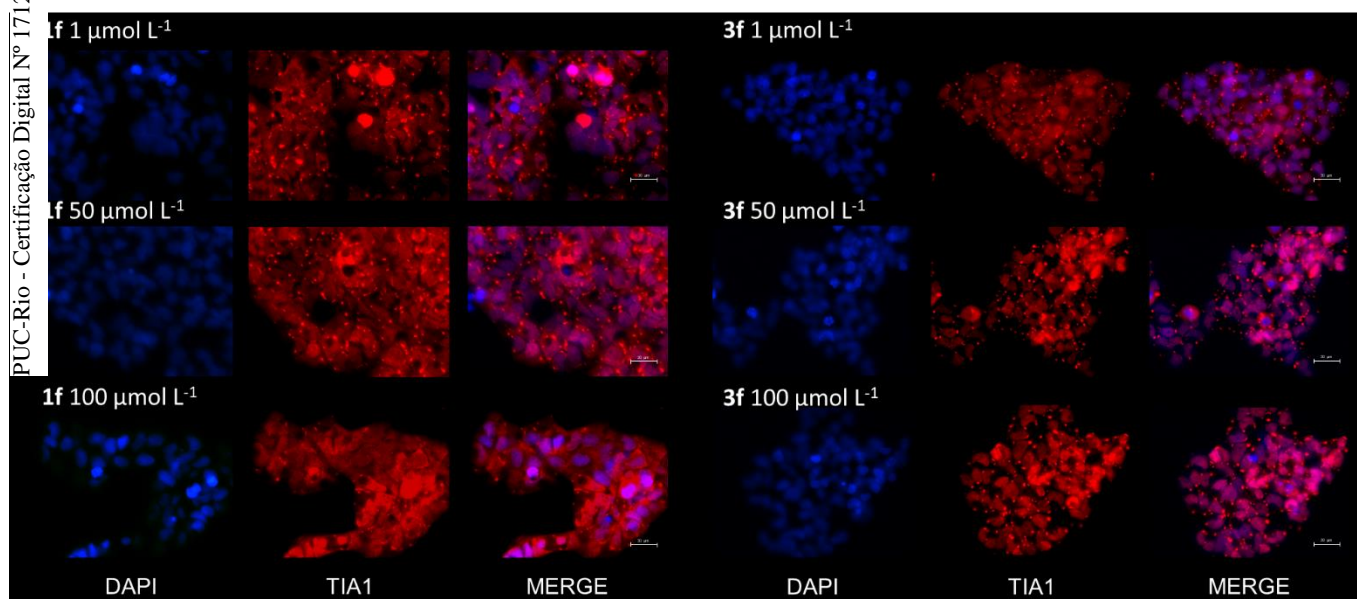


Figure 68. Representative images of the stress granules pattern in HEK cells: effect of different concentrations of pyridine-2-carboxaldehyde-derived compounds **1f** and **3f**. TIA1 is shown in red, while the cell nuclei are colored in blue.

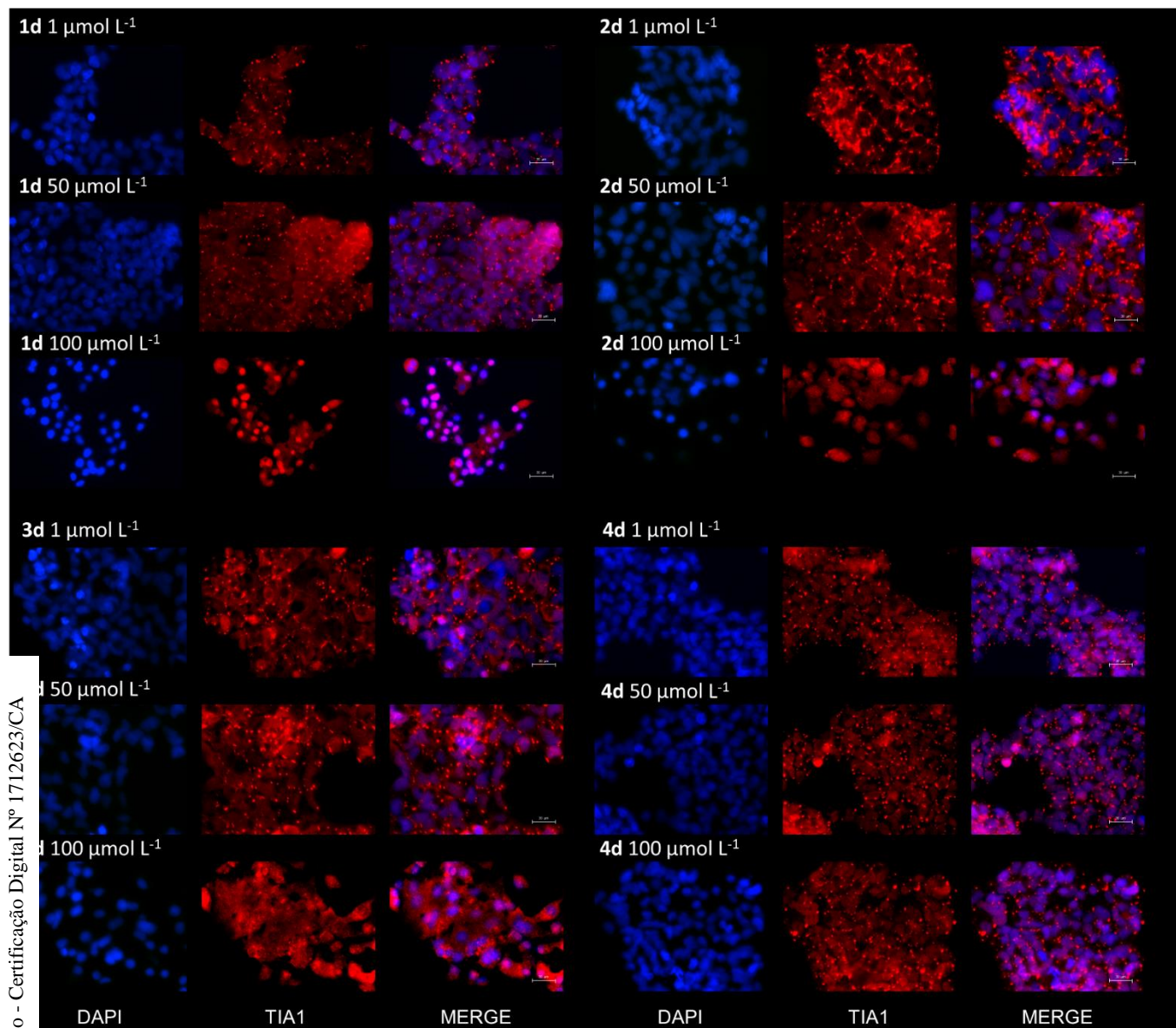


Figure 69. Representative images of the stress granules pattern in HEK cells: effect of different concentrations 1-methylimidazole-containing compounds **1d**, **2d**, **3d** and **4d**. TIA1 is shown in red, while the cell nuclei are colored in blue.

Regarding the four 1-methylimidazole-containing compounds, presented in Figure 69, results were more encouraging, reinforcing the promising potential of this class of compounds in the field of neurodegeneration. The only compound that did not present any effect in this model was compound **4d**. This indicates that the observed effect of the treatment with the *N*-acylhydrazones is not due to chelation of arsenic and consequent prevention of the formation of SG inclusions, since this ligand contains a sulfur donor atom and should present some preference for As coordination, considering both compose a pair of soft acid-base.

Compounds **1d**, **2d** and **3d**, on the other hand, drastically reduce the formation of such inclusions upon treatment with $100 \mu\text{mol L}^{-1}$, as shown by their representative images that resemble those of the negative water control, in which TIA1 is completely diffuse in the cytosol.

Although the “RBP cascade hypothesis”, as it is usually referred to, still needs to be proven *in vivo* (i.e., it needs formal target validation), many small molecules have been tested against SG models, specially *via* high throughput screening (Wolozin and Ivanov, 2019). Aquinnah Pharmaceuticals Inc., for example, is a company that specializes in the study, development and testing of new prospective treatments for neurodegenerative diseases such as ALS and AD, specifically focusing on the SG pathway. In this sense, although these results are merely qualitative, they open a new perspective of hit compounds that can be used in such development processes.

In summary, we were able to show that, although all compounds described herein belong to the class of *N*-acylhydrazones, each of them, with their own particularities, may or may not be adequate for a certain model of aggregopathy.



CONCLUSIONS

8. Conclusions

In the present work, fifty-five *N*-acylhydrazones were initially evaluated *in silico* regarding their physico-chemical pharmacological profiles. The compounds were designed through rationally thought changes in the lead compound's structure (INHHQ, **1h**) in order to improve their performance as moderate metal chelators with potential to be used as drugs in the context of metal-enhanced aggregopathies. After a primary round of selection based on calculated theoretical blood-brain barrier (BBB) crossing reference values and water solubility, nineteen compounds (eighteen + lead compound **1h**) were considered adequate for the next step, which involved their syntheses and chemical characterization. Although theoretically promising, hydrazones derived from precursor 4-methyl-1-piperazinecarboxylic acid hydrazide could not be synthesized due to issues involving its obtention. Consequently, ten compounds (nine + **1h**) were successfully prepared and fully characterized, both in solution and in the solid state. Five crystal structures of novel *N*-acylhydrazones were obtained and analyzed through X-ray diffraction.

Two compounds, **1c** and **1i**, were excluded from the next steps. The first did not show appreciable binding to copper(II), while the latter is unstable even in 100% DMSO solution. The eight (seven compounds + **1h**) remaining *N*-acylhydrazones were evaluated regarding their hydrolysis resistance profile in a 1% DMSO/H₂O solution. Catechol containing ligand **1a** was the only one with a substantial decrease in the hydrazonic band's absorption in the first 12 hours of experiment. Second comes lead compound **1h**, whose lower stability was one of the driving forces for the proposal of the present work. In general, the analogues are more stable and much more water soluble than **1h**, with special attention to 1-methylimidazole-containing *N*-acylhydrazones **1d**, **2d**, **3d** and **4d**. Nevertheless, all eight compounds were maintained for the next steps.

The experimental log P values could be determined only for four of these hydrazones, namely **1d**, **1f**, **2d** and **3f**, and they are indeed in good agreement with the calculated values and within the optimum range for BBB crossing. Moreover, the collection of spectroscopic data regarding the selected compounds allowed the search for correlations with some important calculated molecular descriptors. From the obtained pseudo-linear relationship between the azomethine hydrogen chemical

shift and calculated water solubility for the series of 1-methylimidazole-containing *N*-acylhydrazones, we concluded that the most deshielded the H–C=N hydrogen, the less soluble the 1-methylimidazole-derived hydrazone is, a correlation that is also observed, although in an inverse manner, with the related parameter cLog P. Furthermore, a very strong linear relationship between the solubility of pyridine-containing *N*-acylhydrazones and the position of the C=O bond stretching band showed that the higher the double bond character of the carbonyl group, the more soluble the compounds are, which may be related to hydrogen bonding with water.

Still for the eight selected *N*-acylhydrazones, the *in silico* toxic potential (TP) was calculated, with the 1-methylimidazole-containing compounds once again presenting the most promising results. Compounds **1d** and **4d** showed absolutely no computed toxicity, while **2d** and **3d** also remained in the low toxicity range. Interestingly, the *ortho*-pyridine containing hydrazones **1f**, **1h** and **3f** presented higher TP values. Compound **1a**, on the other hand, showed a TP higher than 0.5, being classified as a Class I elevated toxicity ligand. The experimental cytotoxicity of the selected *N*-acylhydrazones was estimated in H4 cells using the MTT assay. In general, these data are in agreement with the predicted toxicity: both studies point to hydrazone **1d** as being the least toxic compound among those considered in this step. Furthermore, this promising isoniazid-derived *N*-acylhydrazone affects α -Syn aggregation in a cellular model of synucleinopathy, producing a higher number of smaller, less compact inclusions. Lead compound **1h**, on the other hand, presented only marginal results in this system, but has recently shown encouraging results in a mice model of sporadic AD. Since each condition involves its own aggregating entity with particular affinities for specific metal ions, it is most probable that an *N*-acylhydrazone presenting a good activity in a PD model might not be ideal for the treatment of another neurodegenerative disease, opening the field for the rational design of a multitude of structure-related compounds that can perform as moderate chelators in the context of several metal-enhanced aggregopathies.

In fact, compound **1d** showed a moderate, optimized, affinity for copper(II) ions in 1% DMSO/H₂O solution, with an apparent stability constant of 4.57×10^5 for the predominant ML complex at 25 °C. NMR titrations indicate that the primary anchoring site for copper(II) binding in **1d** is the imidazole ring. Additionally, the metal sequestering potential of this compound towards α -Syn was proven on the

Cu²⁺/Cu⁺ redox active couple, relevant for PD pathology, as assessed by high-field NMR spectroscopy, through ¹H-¹⁵N HSQC experiments. This novel hydrazone showed a clear preference for copper(I) ions, removing substantially the metal-induced perturbations from α -Syn upon addition of 5 eq. of the compound. The lower affinity of **1d** for copper(II) ions, on the other hand, was evidenced by its inability to remove the oxidized form of the metal from the α -Syn high affinity Cu²⁺-binding site. These biophysical results are in accordance with the low stability constant reported herein for the Cu²⁺-**1d** complex, which indicates that the affinity for this metal's specific oxidation state was successfully optimized, since copper(I) is the relevant form in the intracellular medium, where α -Syn is mainly found. Conversely, strong interactions with copper(II) can lead to undesired side-effects and toxicity. For the sake of comparison, regarding the Cu²⁺-**1f** complex, an apparent stability constant more than twice higher (1.07×10^6) was estimated.

Overall, the new 1-methylimidazole-containing *N*-acylhydrazones reported herein present a much higher solubility in water, are more hydrolysis-resistant, less toxic and show an improved selectivity towards copper(I) ions than our first designed, lead compound **1h**. This fulfills the expectations that gave rise to the proposition of the present research project. For these reasons, we strongly believe that, not only compound **1d**, but indeed the whole family of related 1-methyl-1H-imidazole-derived *N*-acylhydrazones constitutes a promising and, up until now, completely unexplored set of moderate metal-chelators for a potential treatment of Parkinson's disease and other synucleinopathies.

As an additional development of our original research proposal, we have evaluated the effect of two of our selected pyridine-2-carboxaldehyde-derived *N*-acylhydrazones, **1f** and **3f**, on the copper-catalyzed oxidation of the human M112A PrP₁₀₃₋₁₁₂ short mutant fragment (dMKHA), a model which has implications for the treatment of prion diseases. When only the peptide, copper(II) and H₂O₂ are present, one major product is formed, corresponding to the oxidation of the methionine 109 residue to methionine sulfoxide. On the other hand, the presence of compounds such as ascorbic acid hinders the oxidation of methionine, promoting the oxidation of histidine. Surprisingly, **3f** not only prevented the irreversible oxidation of histidine, but it also protected 85% of the peptide from undergoing methionine oxidation. Although *N*-acylhydrazones are able to compete for the binding of

copper with some amyloidogenic proteins, experimental evidence seems to point to a different mechanism in the present case, through the formation of a dMKHA–Cu(II)–**3f** ternary complex. This opens a new avenue of investigation.

N-acylhydrazones can readily be obtained from the reaction between an aldehyde or ketone and an aroylhydrazide, being this synthetic simplicity the key for an extraordinary chemical diversity. In this sense, we consider that there are many still unexplored possibilities for the structural improvement of such a class of compounds. Therefore, new agents, even more potent than those described herein, can be expected in the coming years.



PUC-Rio - Certificação Digital Nº 1712623/CA

BIBLIOGRAPHY

9. Bibliography

18th International Conference on Biological Inorganic Chemistry. **J Biol Inorg Chem**, v. 22, n. Suppl 1, p. 1-278, Jul 2017. ISSN 1432-1327. Available at: < <https://www.ncbi.nlm.nih.gov/pubmed/28710546> >.

AARSLAND, D.; ZACCAI, J.; BRAYNE, C. A systematic review of prevalence studies of dementia in Parkinson's disease. **Mov Disord**, v. 20, n. 10, p. 1255-63, Oct 2005. ISSN 0885-3185. Available at: < <http://www.ncbi.nlm.nih.gov/pubmed/16041803> >.

ADLARD, P. A. et al. Rapid restoration of cognition in Alzheimer's transgenic mice with 8-hydroxy quinoline analogs is associated with decreased interstitial A β . **Neuron**, v. 59, n. 1, p. 43-55, Jul 2008. ISSN 1097-4199. Available at: < <http://www.ncbi.nlm.nih.gov/pubmed/18614028> >.

ALEXANDER, G. E. Biology of Parkinson's disease: pathogenesis and pathophysiology of a multisystem neurodegenerative disorder. **Dialogues Clin Neurosci**, v. 6, n. 3, p. 259-80, Sep 2004. ISSN 1294-8322. Available at: < <https://www.ncbi.nlm.nih.gov/pubmed/22033559> >.

ALZHEIMER, A. Über einen eigenartigen schweren Erkrankungsprozeß der Hirnrinde. **Neurol Central.**, v. 25, p. 1134, 1907.

ANAND, P.; SINGH, B. A review on cholinesterase inhibitors for Alzheimer's disease. **Arch Pharm Res**, v. 36, n. 4, p. 375-99, Apr 2013. ISSN 0253-6269. Available at: < <https://www.ncbi.nlm.nih.gov/pubmed/23435942> >.

ANGELOVA, V. T. et al. Antiproliferative and antioxidative effects of novel hydrazone derivatives bearing coumarin and chromene moiety. v. 25, n. 9, p. 2082-2092, 2016. Available at: < <https://doi.org/10.1007/s00044-016-1661-4> >.

ANNAMALAI, B. et al. Role of S-nitrosoglutathione mediated mechanisms in tau hyper-phosphorylation. **Biochem Biophys Res Commun**, v. 458, n. 1, p. 214-9, Feb 2015. ISSN 1090-2104. Available at: < <http://www.ncbi.nlm.nih.gov/pubmed/25640839> >.

ARMSTRONG, C. M. et al. Structural Variations and Formation Constants of First-Row Transition Metal Complexes of Biologically Active Aroylhydrazones. **European Journal Of Inorganic Chemistry**, v. 2003, n. 6, p. 1145-1156, 2003.

ATRIÁN-BLASCO, E.; CONTE-DABAN, A.; HUREAU, C. Mutual interference of Cu and Zn ions in Alzheimer's disease: perspectives at the molecular level. **Dalton Trans**, v. 46, n. 38, p. 12750-12759, Oct 2017. ISSN 1477-9234. Available at: < <https://www.ncbi.nlm.nih.gov/pubmed/28937157> >.

AZIMI, S.; RAUK, A. On the involvement of copper binding to the N-terminus of the amyloid Beta Peptide of Alzheimer's disease: a computational study on model

systems. **Int J Alzheimers Dis**, v. 2011, p. 539762, 2011. ISSN 2090-0252. Available at: < <http://www.ncbi.nlm.nih.gov/pubmed/22191059> >.

BACHLI, M. B. et al. Evaluating the reliability of neurocognitive biomarkers of neurodegenerative diseases across countries: A machine learning approach. v. 208, p. 116456, 2020. Available at: < <https://www.sciencedirect.com/science/article/pii/S105381191931047X> >.

BAREGGI, S. R.; CORNELLI, U. Clioquinol: review of its mechanisms of action and clinical uses in neurodegenerative disorders. **CNS Neurosci Ther**, v. 18, n. 1, p. 41-6, Jan 2012. ISSN 1755-5949. Available at: < <http://www.ncbi.nlm.nih.gov/pubmed/21199452> >.

BARNES, C. ORTEP-3 for Windows - a version of ORTEP-III with a Graphical User Interface (GUI) by J. Farrugia. **J Appl Crystallogr**, v. 30, n. 5 Part 1, p. 568, 1997. ISSN 0021-8898. Available at: < <https://doi.org/10.1107/S0021889897006638> >.

BARNES, D. E.; YAFFE, K. Vitamin E and donepezil for the treatment of mild cognitive impairment. **N Engl J Med**, v. 353, n. 9, p. 951-2; author reply 951-2, Sep 2005. ISSN 1533-4406. Available at: < <http://www.ncbi.nlm.nih.gov/pubmed/16135844> >.

BARNHAM, K. J.; BUSH, A. I. Metals in Alzheimer's and Parkinson's diseases. **Curr Opin Chem Biol**, v. 12, n. 2, p. 222-8, Apr 2008. ISSN 1367-5931. Available at: < <http://www.ncbi.nlm.nih.gov/pubmed/18342639> >.

BARNHAM, K. J.; MASTERS, C. L.; BUSH, A. I. Neurodegenerative diseases and oxidative stress. **Nat Rev Drug Discov**, v. 3, n. 3, p. 205-14, Mar 2004. ISSN 1474-1776. Available at: < <http://www.ncbi.nlm.nih.gov/pubmed/15031734> >.

BECKER, E.; RICHARDSON, D. R. Development of novel aroylhydrazone ligands for iron chelation therapy: 2-pyridylcarboxaldehyde isonicotinoyl hydrazone analogs. **J Lab Clin Med**, v. 134, n. 5, p. 510-21, Nov 1999. ISSN 0022-2143. Available at: < <https://www.ncbi.nlm.nih.gov/pubmed/10560945> >.

BELOSI, B. et al. Copper binding to the neurotoxic peptide PrP106-126: thermodynamic and structural studies. **Chembiochem**, v. 5, n. 3, p. 349-59, Mar 2004. ISSN 1439-4227. Available at: < <https://www.ncbi.nlm.nih.gov/pubmed/14997527> >.

BENSON, M. D. et al. Amyloid nomenclature 2018: recommendations by the International Society of Amyloidosis (ISA) nomenclature committee. **Amyloid**, v. 25, n. 4, p. 215-219, Dec 2018. ISSN 1744-2818. Available at: < <https://www.ncbi.nlm.nih.gov/pubmed/30614283> >.

_____. Amyloid nomenclature 2020: update and recommendations by the International Society of Amyloidosis (ISA) nomenclature committee. **Amyloid**, v. 27, n. 4, p. 217-222, 2020. Available at: < <https://doi.org/10.1080/13506129.2020.1835263> >.

BERNHARDT, P. V. et al. Hydrazone chelators for the treatment of iron overload disorders: iron coordination chemistry and biological activity. **Dalton Trans**, n. 30, p. 3232-44, Aug 2007. ISSN 1477-9226. Available at: < <https://www.ncbi.nlm.nih.gov/pubmed/17893768> >.

BINOLFI, A. et al. Bioinorganic chemistry of copper coordination to alpha-synuclein: Relevance to Parkinson's disease. **Metal Ions in Neurodegenerative Diseases**, v. 256, n. 19–20, p. 2188-2201, 2012. Available at: < <http://www.sciencedirect.com/science/article/pii/S0010854512001221> >.

_____. Interaction of alpha-synuclein with divalent metal ions reveals key differences: a link between structure, binding specificity and fibrillation enhancement. **J Am Chem Soc**, v. 128, n. 30, p. 9893-901, Aug 2006. ISSN 0002-7863. Available at: < <http://www.ncbi.nlm.nih.gov/pubmed/16866548> >.

_____. Bioinorganic chemistry of Parkinson's disease: structural determinants for the copper-mediated amyloid formation of alpha-synuclein. **Inorg Chem**, v. 49, n. 22, p. 10668-79, Nov 2010. ISSN 1520-510X. Available at: < <http://www.ncbi.nlm.nih.gov/pubmed/20964419> >.

_____. Exploring the structural details of Cu(I) binding to α -synuclein by NMR spectroscopy. **J Am Chem Soc**, v. 133, n. 2, p. 194-6, Jan 2011. ISSN 1520-5126. Available at: < <https://www.ncbi.nlm.nih.gov/pubmed/21158432> >.

BLESA, J. et al. Oxidative stress and Parkinson's disease. **Front Neuroanat**, v. 9, p. 91, 2015. ISSN 1662-5129. Available at: < <https://www.ncbi.nlm.nih.gov/pubmed/26217195> >.

BOLOGNIN, S.; MESSORI, L.; ZATTA, P. Metal ion physiopathology in neurodegenerative disorders. **Neuromolecular Med**, v. 11, n. 4, p. 223-38, 2009. ISSN 1559-1174. Available at: < <http://www.ncbi.nlm.nih.gov/pubmed/19946766> >.

BRAVO-GÓMEZ, M. E. et al. Antiproliferative activity and QSAR study of copper(II) mixed chelate [Cu(N–N)(acetylacetonato)]NO₃ and [Cu(N–N)(glycinato)]NO₃ complexes, (Casiopéinas®). v. 103, n. 2, p. 299-309, 2009. Available at: < <http://www.sciencedirect.com/science/article/pii/S0162013408002481> >.

BRIDGEWATER, J. D.; VACHET, R. W. Metal-catalyzed oxidation reactions and mass spectrometry: The roles of ascorbate and different oxidizing agents in determining Cu–protein-binding sites. v. 341, n. 1, p. 122-130, 2005. Available at: < <http://www.sciencedirect.com/science/article/pii/S0003269705001697> >.

BROWN, D. R. Prion and prejudice: normal protein and the synapse. v. 24, n. 2, p. 85-90, 2001. Available at: < <http://www.sciencedirect.com/science/article/pii/S0166223600016891> >.

BUDIMIR, A. Metal ions, Alzheimer's disease and chelation therapy. **Acta Pharm**, v. 61, n. 1, p. 1-14, Mar 2011. ISSN 1846-9558. Available at: < <http://www.ncbi.nlm.nih.gov/pubmed/21406339> >.

BURLA, M. C. et al. Crystal structure determination and refinement via SIR2014. **J Appl Crystallogr**, v. 48, n. 1, p. 306-309, 2015. ISSN 1600-5767. Available at: < <https://doi.org/10.1107/S1600576715001132> >.

BUSCIGLIO, J. et al. beta-amyloid fibrils induce tau phosphorylation and loss of microtubule binding. **Neuron**, v. 14, n. 4, p. 879-88, Apr 1995. ISSN 0896-6273. Available at: < <http://www.ncbi.nlm.nih.gov/pubmed/7718249> >.

BUSH, A. I. Metals and neuroscience. **Curr Opin Chem Biol**, v. 4, n. 2, p. 184-91, Apr 2000. ISSN 1367-5931. Available at: < <http://www.ncbi.nlm.nih.gov/pubmed/10742195> >.

BUSH, A. I. et al. Rapid induction of Alzheimer A beta amyloid formation by zinc. **Science**, v. 265, n. 5177, p. 1464-7, Sep 1994. ISSN 0036-8075. Available at: < <http://www.ncbi.nlm.nih.gov/pubmed/8073293> >.

BUSTAMANTE, F. L. S. et al. Lawsons Dimerization in Cobalt(III) Complexes toward the Design of New Prototypes of Bioreductive Prodrugs. **Inorganic Chemistry**, v. 52, n. 3, p. 1167-1169, 2013. Available at: < <https://doi.org/10.1021/ic302175t> >.

CAMPBELL, B. C. et al. Accumulation of insoluble alpha-synuclein in dementia with Lewy bodies. **Neurobiol Dis**, v. 7, n. 3, p. 192-200, Jun 2000. ISSN 0969-9961. Available at: < <https://www.ncbi.nlm.nih.gov/pubmed/10860784> >.

CDC, C. F. D. C. A. P. Prion Diseases. <https://www.cdc.gov/prions/index.html>, 2018. Accessed on: March, 2021.

_____. Creutzfeldt-Jakob Disease: Treatment. <https://www.cdc.gov/prions/cjd/treatment.html>, 2019. Accessed on: March 2021.

CHAUDHURI, K. R.; CLOUGH, C. G.; SETHI, K. D. **Fast facts : Parkinson's disease**. 3rd ed. Abingdon: Health Press, 2011. ISBN 9781905832880 (pbk.).

CHENG, F.; VIVACQUA, G.; YU, S. The role of α -synuclein in neurotransmission and synaptic plasticity. **J Chem Neuroanat**, v. 42, n. 4, p. 242-8, Dec 2011. ISSN 1873-6300. Available at: < <http://www.ncbi.nlm.nih.gov/pubmed/21167933> >.

CHERNY, R. A. et al. Treatment with a copper-zinc chelator markedly and rapidly inhibits beta-amyloid accumulation in Alzheimer's disease transgenic mice. **Neuron**, v. 30, n. 3, p. 665-76, Jun 2001. ISSN 0896-6273. Available at: < <http://www.ncbi.nlm.nih.gov/pubmed/11430801> >.

CHITI, F.; DOBSON, C. M. Protein misfolding, functional amyloid, and human disease. **Annu Rev Biochem**, v. 75, p. 333-66, 2006. ISSN 0066-4154. Available at: < <http://www.ncbi.nlm.nih.gov/pubmed/16756495> >.

CITRON, M. et al. Mutation of the beta-amyloid precursor protein in familial Alzheimer's disease increases beta-protein production. **Nature**, v. 360, n. 6405, p. 672-4, Dec 1992. ISSN 0028-0836. Available at: < <http://www.ncbi.nlm.nih.gov/pubmed/1465129> >.

CJD-FOUNDATION, C.-J. D. F. Types of Prion Diseases. <https://cjd.foundation.org/types-prion-diseases>, 2021. Accessed on: March 2021.

COMAN, A. G. et al. Conformation-induced light emission switching of N-acylhydrazone systems. **New Journal of Chemistry**, v. 42, n. 17, p. 14111-14119, 2018. Available at: < <http://dx.doi.org/10.1039/C8NJ01880D> >.

CONCETTI, A.; GARIBOLDI, P. Methionine sulfoxide formation in proteins: NMR study. v. 3, n. 2, p. 125-126, 1990. Available at: < <https://doi.org/10.1007/BF01179519> >.

CRADDOCK, T. J. et al. The zinc dyshomeostasis hypothesis of Alzheimer's disease. **PLoS One**, v. 7, n. 3, p. e33552, 2012. ISSN 1932-6203. Available at: < <http://www.ncbi.nlm.nih.gov/pubmed/22457776> >.

CROUCH, P. J.; BARNHAM, K. J. Therapeutic redistribution of metal ions to treat Alzheimer's disease. **Acc Chem Res**, v. 45, n. 9, p. 1604-11, Sep 2012. ISSN 1520-4898. Available at: < <http://www.ncbi.nlm.nih.gov/pubmed/22747493> >.

CROUCH, P. J. et al. The Alzheimer's therapeutic PBT2 promotes amyloid- β degradation and GSK3 phosphorylation via a metal chaperone activity. **J Neurochem**, v. 119, n. 1, p. 220-30, Oct 2011. ISSN 1471-4159. Available at: < <http://www.ncbi.nlm.nih.gov/pubmed/21797865> >.

CSIRE, G. et al. Copper(II) interaction with the Human Prion 103-112 fragment - Coordination and oxidation. **J Inorg Biochem**, v. 170, p. 195-201, 05 2017. ISSN 1873-3344. Available at: < <https://www.ncbi.nlm.nih.gov/pubmed/28260678> >.

CUKIERMAN, D. S. **LIGANTES AROILHIDRAZÔNICOS: Uma nova classe de promissores MPACs na terapia da doença de Alzheimer**. 2016. (Bachelor). Departamento de Química PUC-Rio, PUC-Rio

CUKIERMAN, D. S. et al. Aroylhydrazones constitute a promising class of 'metal-protein attenuating compounds' for the treatment of Alzheimer's disease: a proof-of-concept based on the study of the interactions between zinc(II) and pyridine-2-carboxaldehyde isonicotinoyl hydrazone. **J Biol Inorg Chem**, v. 23, n. 8, p. 1227-1241, Dec 2018. ISSN 1432-1327. Available at: < <https://www.ncbi.nlm.nih.gov/pubmed/30145655> >.

_____. Impact of pyridine-2-carboxaldehyde-derived aroylhydrazones on the copper-catalyzed oxidation of the M112A PrP. **J Biol Inorg Chem**, v. 24, n. 8, p. 1231-1244, 12 2019. ISSN 1432-1327. Available at: < <https://www.ncbi.nlm.nih.gov/pubmed/31401689> >.

_____. Mildness in preparative conditions directly affects the otherwise straightforward syntheses outcome of Schiff-base isoniazid derivatives: Aroylhydrazones and their solvolysis-related dihydrazones. **Journal of Molecular Structure**, v. 1228, p. 129437, 2021. Available at: < <http://www.sciencedirect.com/science/article/pii/S002228602031752X> >.

_____. XIINH, an improved next-generation affinity-optimized hydrazone ligand, attenuates abnormal copper(I)/copper(II)- α -Syn interactions and affects protein aggregation in a cellular model of synucleinopathy. **Dalton Trans**, v. 49, n. 45, p. 16252-16267, Nov 2020. ISSN 1477-9234. Available at: < <https://www.ncbi.nlm.nih.gov/pubmed/32391542> >.

_____. A moderate metal-binding hydrazone meets the criteria for a bioinorganic approach towards Parkinson's disease: Therapeutic potential, blood-brain barrier crossing evaluation and preliminary toxicological studies. **J Inorg Biochem**, v. 170, p. 160-168, May 2017. ISSN 1873-3344. Available at: < <https://www.ncbi.nlm.nih.gov/pubmed/28249224> >.

DANISHUDDIN; KHAN, A. U. Descriptors and their selection methods in QSAR analysis: paradigm for drug design. **Drug Discov Today**, v. 21, n. 8, p. 1291-302, 08 2016. ISSN 1878-5832. Available at: < <https://www.ncbi.nlm.nih.gov/pubmed/27326911> >.

DAVIES, K. M. et al. Copper pathology in vulnerable brain regions in Parkinson's disease. **Neurobiol Aging**, v. 35, n. 4, p. 858-66, Apr 2014. ISSN 1558-1497. Available at: < <https://www.ncbi.nlm.nih.gov/pubmed/24176624> >.

DE FALCO, A. **Activity evaluation and toxicological profile of new potential "Metal Protein Attenuating Compounds" in biological models of Alzheimer's disease**. 2017. 158 (PhD). Departamento de Química PUC-Rio, PUC-Rio

DE FALCO, A. et al. DOENÇA DE ALZHEIMER: HIPÓTESES ETIOLÓGICAS E PERSPECTIVAS DE TRATAMENTO. **Química Nova**, v. 39, p. 63-80, 2016. ISSN 0100-4042. Available at: < http://www.scielo.br/scielo.php?script=sci_arttext&pid=S0100-40422016000100063&nrm=iso >.

_____. The aroylhydrazone INHHQ prevents memory impairment induced by Alzheimer's-linked amyloid- β oligomers in mice. **Behavioural Pharmacology**, v. 31, n. 8, 2020. Available at: < https://journals.lww.com/behaviouralpharm/Fulltext/2020/12000/The_aroylehydrazone_INHHQ_prevents_memory.4.aspx >.

DE FREITAS, L. V. et al. Structural and vibrational study of 8-hydroxyquinoline-2-carboxaldehyde isonicotinoyl hydrazone--a potential metal-protein attenuating compound (MPAC) for the treatment of Alzheimer's disease. **Spectrochim Acta A Mol Biomol Spectrosc**, v. 116, p. 41-8, Dec 2013. ISSN 1873-3557. Available at: < <http://www.ncbi.nlm.nih.gov/pubmed/23896296> >.

DEDEOGLU, A. et al. Preliminary studies of a novel bifunctional metal chelator targeting Alzheimer's amyloidogenesis. **Exp Gerontol**, v. 39, n. 11-12, p. 1641-9, 2004 Nov-Dec 2004. ISSN 0531-5565. Available at: < <http://www.ncbi.nlm.nih.gov/pubmed/15582280> >.

DEIBEL, M. A.; EHMANN, W. D.; MARKESBERY, W. R. Copper, iron, and zinc imbalances in severely degenerated brain regions in Alzheimer's disease: possible relation to oxidative stress. **J Neurol Sci**, v. 143, n. 1-2, p. 137-42, Nov 1996. ISSN 0022-510X. Available at: < <http://www.ncbi.nlm.nih.gov/pubmed/8981312> >.

DEUTSCH, J. A. The cholinergic synapse and the site of memory. **Science**, v. 174, n. 4011, p. 788-94, Nov 1971. ISSN 0036-8075. Available at: < <http://www.ncbi.nlm.nih.gov/pubmed/4330469> >.

DEXTER, D. T. et al. Alterations in the levels of iron, ferritin and other trace metals in Parkinson's disease and other neurodegenerative diseases affecting the basal ganglia. **Brain**, v. 114 (Pt 4), p. 1953-75, Aug 1991. ISSN 0006-8950. Available at: < <http://www.ncbi.nlm.nih.gov/pubmed/1832073> >.

DEZSI, L.; VECSEI, L. Monoamine Oxidase B Inhibitors in Parkinson's Disease. **CNS Neurol Disord Drug Targets**, v. 16, n. 4, p. 425-439, 2017. ISSN 1996-3181. Available at: < <https://www.ncbi.nlm.nih.gov/pubmed/28124620> >.

DI SANTO, A. et al. Exploring weak intermolecular interactions in thiocyanate-bonded Zn(ii) and Cd(ii) complexes with methylimidazole: crystal structures, Hirshfeld surface analysis and luminescence properties. **RSC Advances**, v. 8, n. 42, p. 23891-23902, 2018. Available at: < <http://dx.doi.org/10.1039/C8RA04452J> >.

DORAISWAMY, P. M.; FINEFROCK, A. E. Metals in our minds: therapeutic implications for neurodegenerative disorders. **Lancet Neurol**, v. 3, n. 7, p. 431-4, Jul 2004. ISSN 1474-4422. Available at: < <http://www.ncbi.nlm.nih.gov/pubmed/15207800> >.

DUGGER, B. N.; DICKSON, D. W. Pathology of Neurodegenerative Diseases. **Cold Spring Harb Perspect Biol**, v. 9, n. 7, Jul 2017. ISSN 1943-0264. Available at: < <https://www.ncbi.nlm.nih.gov/pubmed/28062563> >.

EL-HAWASH, S. A.; ABDEL WAHAB, A. E.; EL-DEMELLAWY, M. A. Cyanoacetic acid hydrazones of 3-(and 4-)acetylpyridine and some derived ring systems as potential antitumor and anti-HCV agents. **Arch Pharm (Weinheim)**, v. 339, n. 1, p. 14-23, Jan 2006. ISSN 0365-6233. Available at: < <https://www.ncbi.nlm.nih.gov/pubmed/16411172> >.

ELMALLAH, M. I. Y. et al. Impact of methionine oxidation as an initial event on the pathway of human prion protein conversion. **Prion**, v. 7, n. 5, p. 404-411, 2013. Available at: < <https://doi.org/10.4161/pri.26745> >.

F.D.A. **S7B Nonclinical Evaluation of the Potential for Delayed Ventricular Repolarization (QT Interval Prolongation) by Human Pharmaceuticals.** FDA-2004-D-0366. ADMINISTRATION, U. F. A. D. 2005.

FALLER, P.; HUREAU, C. A bioinorganic view of Alzheimer's disease: when misplaced metal ions (re)direct the electrons to the wrong target. **Chemistry**, v. 18, n. 50, p. 15910-20, Dec 2012. ISSN 1521-3765. Available at: < <http://www.ncbi.nlm.nih.gov/pubmed/23180511> >.

FARRUGIA, L. J. WinGX and ORTEP for Windows: an update. **J Appl Crystallogr**, v. 45, n. 4, p. 849-854, 2020/05/11 2012. Available at: < <https://doi.org/10.1107/S0021889812029111> >.

FAUVET, B. et al. α -Synuclein in central nervous system and from erythrocytes, mammalian cells, and Escherichia coli exists predominantly as disordered monomer. **J Biol Chem**, v. 287, n. 19, p. 15345-64, May 2012. ISSN 1083-351X. Available at: < <https://www.ncbi.nlm.nih.gov/pubmed/22315227> >.

FAUX, N. G. et al. PBT2 rapidly improves cognition in Alzheimer's Disease: additional phase II analyses. **J Alzheimers Dis**, v. 20, n. 2, p. 509-16, 2010. ISSN 1875-8908. Available at: < <http://www.ncbi.nlm.nih.gov/pubmed/20164561> >.

FERREIRA, C. et al. **(Un)suitability of the use of pH buffers in biological, biochemical and environmental studies and its interaction with metal ions – a review.** 2015.

FINKELSTEIN, D. et al. PBT434 Prevents α -synuclein Aggregation, Neuron Loss, Motor Dysfunction and Reduces Glial Cell Inclusions in a Transgenic Mouse Model of Multiple System Atrophy (P5.8-006). **Neurology**, v. 92, n. 15 Supplement, p. P5.8-006, 2019. Available at: < http://n.neurology.org/content/92/15_Supplement/P5.8-006.abstract >.

FINKELSTEIN, D. I. et al. The novel compound PBT434 prevents iron mediated neurodegeneration and alpha-synuclein toxicity in multiple models of Parkinson's disease. **Acta Neuropathol Commun**, v. 5, n. 1, p. 53, Jun 2017. ISSN 2051-5960. Available at: < <https://www.ncbi.nlm.nih.gov/pubmed/28659169> >.

FÄNDRICH, M. On the structural definition of amyloid fibrils and other polypeptide aggregates. **Cell Mol Life Sci**, v. 64, n. 16, p. 2066-78, Aug 2007. ISSN 1420-682X. Available at: < <https://www.ncbi.nlm.nih.gov/pubmed/17530168> >.

GAETA, A.; HIDER, R. C. The crucial role of metal ions in neurodegeneration: the basis for a promising therapeutic strategy. **Br J Pharmacol**, v. 146, n. 8, p. 1041-59, Dec 2005. ISSN 0007-1188. Available at: < <http://www.ncbi.nlm.nih.gov/pubmed/16205720> >.

GAGGELLI, E. et al. Copper homeostasis and neurodegenerative disorders (Alzheimer's, prion, and Parkinson's diseases and amyotrophic lateral sclerosis). **Chem Rev**, v. 106, n. 6, p. 1995-2044, Jun 2006. ISSN 0009-2665. Available at: < <http://www.ncbi.nlm.nih.gov/pubmed/16771441> >.

GANDY, S. The role of cerebral amyloid beta accumulation in common forms of Alzheimer disease. **J Clin Invest**, v. 115, n. 5, p. 1121-9, May 2005. ISSN 0021-9738. Available at: < <http://www.ncbi.nlm.nih.gov/pubmed/15864339> >.

GESCHWIND, M. D. Prion Diseases. **Continuum (Minneap Minn)**, v. 21, n. 6 Neuroinfectious Disease, p. 1612-38, Dec 2015. ISSN 1538-6899. Available at: < <https://www.ncbi.nlm.nih.gov/pubmed/26633779> >.

GOMES, L. M. et al. 8-Hydroxyquinoline Schiff-base compounds as antioxidants and modulators of copper-mediated A β peptide aggregation. **J Inorg Biochem**, v. 139, p. 106-16, Oct 2014. ISSN 1873-3344. Available at: < <https://www.ncbi.nlm.nih.gov/pubmed/25019963> >.

GONZÁLEZ-BARÓ, A. C. et al. A novel oxidovanadium(V) compound with an isonicotinohydrazide ligand. A combined experimental and theoretical study and cytotoxicity against K562 cells. **Polyhedron**, v. 135, p. 303-310, 2017. Available at: < <http://www.sciencedirect.com/science/article/pii/S0277538717304965> >.

_____. Spectroscopic and theoretical study of the o-vanillin hydrazone of the mycobactericidal drug isoniazid. **J Mol Struct**, v. 1007, p. 95–101, 2012.

GUENGERICH, F. P. Cytochrome p450 and chemical toxicology. **Chem Res Toxicol**, v. 21, n. 1, p. 70-83, Jan 2008. ISSN 0893-228X. Available at: < <https://www.ncbi.nlm.nih.gov/pubmed/18052394> >.

HANE, F.; LEONENKO, Z. Effect of metals on kinetic pathways of amyloid- β aggregation. **Biomolecules**, v. 4, n. 1, p. 101-16, 2014. ISSN 2218-273X. Available at: < <http://www.ncbi.nlm.nih.gov/pubmed/24970207> >.

HANE, F. et al. Cu(2+) affects amyloid- β (1-42) aggregation by increasing peptide-peptide binding forces. **PLoS One**, v. 8, n. 3, p. e59005, 2013. ISSN 1932-6203. Available at: < <http://www.ncbi.nlm.nih.gov/pubmed/23536847> >.

HARDY, J. A.; HIGGINS, G. A. Alzheimer's disease: the amyloid cascade hypothesis. **Science**, v. 256, n. 5054, p. 184-5, Apr 1992. ISSN 0036-8075. Available at: < <http://www.ncbi.nlm.nih.gov/pubmed/1566067> >.

HARRIS, E. D. Basic and clinical aspects of copper. **Crit Rev Clin Lab Sci**, v. 40, n. 5, p. 547-86, Oct 2003. ISSN 1040-8363. Available at: < <https://www.ncbi.nlm.nih.gov/pubmed/14653357> >.

HAUSER-DAVIS, R. A. et al. Disruption of zinc and copper interactions with A β (1-40) by a non-toxic, isoniazid-derived, hydrazone: a novel biometal homeostasis restoring agent in Alzheimer's disease therapy? **Metallomics**, v. 7, p. 743-747, April 01 2015. ISSN 1756-591X. Available at: < <http://www.ncbi.nlm.nih.gov/pubmed/25860559> >.

HE, L. et al. Methionine oxidation of amyloid peptides by peroxovanadium complexes: inhibition of fibril formation through a distinct mechanism.

Metallomics, v. 7, n. 12, p. 1562-72, Dec 2015. ISSN 1756-591X. Available at: < <https://www.ncbi.nlm.nih.gov/pubmed/26444976> >.

HE, W.; BARROW, C. J. The A beta 3-pyroglutamyl and 11-pyroglutamyl peptides found in senile plaque have greater beta-sheet forming and aggregation propensities in vitro than full-length A beta. **Biochemistry**, v. 38, n. 33, p. 10871-7, Aug 1999. ISSN 0006-2960. Available at: < <http://www.ncbi.nlm.nih.gov/pubmed/10451383> >.

HOERNKE, M.; KOKSCH, B.; BREZESINSKI, G. Influence of the hydrophobic interface and transition metal ions on the conformation of amyloidogenic model peptides. **Biophys Chem**, v. 150, n. 1-3, p. 64-72, Aug 2010. ISSN 1873-4200. Available at: < <http://www.ncbi.nlm.nih.gov/pubmed/20347516> >.

HOFFMAN, R. E. Standardization of chemical shifts of TMS and solvent signals in NMR solvents. **Magn Reson Chem**, v. 44, n. 6, p. 606-16, Jun 2006. ISSN 0749-1581. Available at: < <https://www.ncbi.nlm.nih.gov/pubmed/16534833> >.

HONG-QI, Y.; ZHI-KUN, S.; SHENG-DI, C. Current advances in the treatment of Alzheimer's disease: focused on considerations targeting A β and tau. **Transl Neurodegener**, v. 1, n. 1, p. 21, 2012. ISSN 2047-9158. Available at: < <http://www.ncbi.nlm.nih.gov/pubmed/23210837> >.

HOYER, W. et al. Impact of the acidic C-terminal region comprising amino acids 109-140 on alpha-synuclein aggregation in vitro. **Biochemistry**, v. 43, n. 51, p. 16233-42, Dec 2004. ISSN 0006-2960. Available at: < <https://www.ncbi.nlm.nih.gov/pubmed/15610017> >.

HU, X. et al. Tau pathogenesis is promoted by A β 1-42 but not A β 1-40. **Mol Neurodegener**, v. 9, p. 52, 2014. ISSN 1750-1326. Available at: < <http://www.ncbi.nlm.nih.gov/pubmed/25417177> >.

HUANG, W.; WEI, W.; SHEN, Z. Drug-like chelating agents: a potential lead for Alzheimer's disease. **RSC Adv.**, v. 4, n. 94, p. 52088-52099, 2014. ISSN 2046-2069.

HUANG, X. et al. Trace metal contamination initiates the apparent auto-aggregation, amyloidosis, and oligomerization of Alzheimer's Abeta peptides. **J Biol Inorg Chem**, v. 9, n. 8, p. 954-60, Dec 2004. ISSN 0949-8257. Available at: < <http://www.ncbi.nlm.nih.gov/pubmed/15578276> >.

_____. Zinc-induced Alzheimer's Abeta1-40 aggregation is mediated by conformational factors. **J Biol Chem**, v. 272, n. 42, p. 26464-70, Oct 1997. ISSN 0021-9258. Available at: < <http://www.ncbi.nlm.nih.gov/pubmed/9334223> >.

INGELSSON, M. Alpha-Synuclein Oligomers-Neurotoxic Molecules in Parkinson's Disease and Other Lewy Body Disorders. **Front Neurosci**, v. 10, p. 408, 2016. ISSN 1662-4548. Available at: < <https://www.ncbi.nlm.nih.gov/pubmed/27656123> >.

IQBAL, K. et al. Tau pathology in Alzheimer disease and other tauopathies. **Biochim Biophys Acta**, v. 1739, n. 2-3, p. 198-210, Jan 2005. ISSN 0006-3002. Available at: < <http://www.ncbi.nlm.nih.gov/pubmed/15615638> >.

JENKINS, E. C. et al. Fine mapping of an Alzheimer disease-associated gene encoding beta-amyloid protein. **Biochem Biophys Res Commun**, v. 151, n. 1, p. 1-8, Feb 1988. ISSN 0006-291X. Available at: < <http://www.ncbi.nlm.nih.gov/pubmed/3279948> >.

JOHNSON, M.; GEEVES, M. A.; MULVIHILL, D. P. Production of amino-terminally acetylated recombinant proteins in E. coli. **Methods Mol Biol**, v. 981, p. 193-200, 2013. ISSN 1940-6029. Available at: < <https://www.ncbi.nlm.nih.gov/pubmed/23381863> >.

JOMOVA, K.; BAROS, S.; VALKO, M. Redox active metal-induced oxidative stress in biological systems. v. 37, n. 2, p. 127-134, 2012. Available at: < <https://doi.org/10.1007/s11243-012-9583-6> >.

KAHLE, P. J. et al. Selective insolubility of alpha-synuclein in human Lewy body diseases is recapitulated in a transgenic mouse model. **Am J Pathol**, v. 159, n. 6, p. 2215-25, Dec 2001. ISSN 0002-9440. Available at: < <https://www.ncbi.nlm.nih.gov/pubmed/11733371> >.

KAJAL, A. et al. Therapeutic potential of hydrazones as anti-inflammatory agents. **Int J Med Chem**, v. 2014, p. 761030, 2014. ISSN 2090-2069. Available at: < <https://www.ncbi.nlm.nih.gov/pubmed/25383223> >.

KALIA, J.; RAINES, R. T. Hydrolytic stability of hydrazones and oximes. **Angew Chem Int Ed Engl**, v. 47, n. 39, p. 7523-6, 2008. ISSN 1521-3773. Available at: < <https://www.ncbi.nlm.nih.gov/pubmed/18712739> >.

KAPLAN, J. H.; LUTSENKO, S. Copper transport in mammalian cells: special care for a metal with special needs. **J Biol Chem**, v. 284, n. 38, p. 25461-5, Sep 2009. ISSN 1083-351X. Available at: < <http://www.ncbi.nlm.nih.gov/pubmed/19602511> >.

KAWAJIRI, K.; FUJII-KURIYAMA, Y. The aryl hydrocarbon receptor: a multifunctional chemical sensor for host defense and homeostatic maintenance. **Exp Anim**, v. 66, n. 2, p. 75-89, May 2017. ISSN 1881-7122. Available at: < <https://www.ncbi.nlm.nih.gov/pubmed/27980293> >.

KAYED, R. et al. Permeabilization of lipid bilayers is a common conformation-dependent activity of soluble amyloid oligomers in protein misfolding diseases. **J Biol Chem**, v. 279, n. 45, p. 46363-6, Nov 2004. ISSN 0021-9258. Available at: < <http://www.ncbi.nlm.nih.gov/pubmed/15385542> >.

KELDER, J. et al. Polar molecular surface as a dominating determinant for oral absorption and brain penetration of drugs. **Pharm Res**, v. 16, n. 10, p. 1514-9, Oct 1999. ISSN 0724-8741. Available at: < <https://www.ncbi.nlm.nih.gov/pubmed/10554091> >.

KHANDAR, A. A. et al. Anion influence in the structural diversity of cadmium coordination polymers constructed from a pyridine based Schiff base ligand. **Inorganica Chimica Acta**, v. 427, p. 87-96, 2015.

KLEIN, W. L.; KRAFFT, G. A.; FINCH, C. E. Targeting small Abeta oligomers: the solution to an Alzheimer's disease conundrum? **Trends Neurosci**, v. 24, n. 4, p. 219-24, Apr 2001. ISSN 0166-2236. Available at: < <http://www.ncbi.nlm.nih.gov/pubmed/11250006> >.

KOPITO, R. R.; RON, D. Conformational disease. **Nat Cell Biol**, v. 2, n. 11, p. E207-9, Nov 2000. ISSN 1465-7392. Available at: < <https://www.ncbi.nlm.nih.gov/pubmed/11056553> >.

KOZŁOWSKI, H.; BROWN, D. R.; VALENSIN, G. **Metallochemistry of neurodegeneration : biological, chemical and genetic aspects**. Cambridge: Royal Society of Chemistry, 2006. ISBN 9780854043606 (hbk.) : No price 0854043608 (hbk.) : No price.

KOZŁOWSKI, H.; KOWALIK-JANKOWSKA, T.; JEŻOWSKA-BOJCZUK, M. Chemical and biological aspects of Cu²⁺ interactions with peptides and aminoglycosides. **Coordination Chemistry in Poland**, v. 249, n. 21, p. 2323-2334, 2005. Available at: < <http://www.sciencedirect.com/science/article/pii/S001085450500130X> >.

KWIATKOWSKI, J. S.; LESZCZYŃSKI, J.; TECA, I. Molecular structure and infrared spectra of furan, thiophene, selenophene and their 2,5-N and 3,4-N derivatives: density functional theory and conventional post-Hartree-Fock MP2 studies. **Structure, Properties and Dynamics of Molecular Systems**, v. 436-437, p. 451-480, 1997. Available at: < <http://www.sciencedirect.com/science/article/pii/S0022286097001257> >.

KYLE, R. A. Amyloidosis: a convoluted story. **Br J Haematol**, v. 114, n. 3, p. 529-38, Sep 2001. ISSN 0007-1048. Available at: < <https://www.ncbi.nlm.nih.gov/pubmed/11552976> >.

LAMBERT, M. P. et al. Diffusible, nonfibrillar ligands derived from Abeta1-42 are potent central nervous system neurotoxins. **Proc Natl Acad Sci U S A**, v. 95, n. 11, p. 6448-53, May 1998. ISSN 0027-8424. Available at: < <http://www.ncbi.nlm.nih.gov/pubmed/9600986> >.

LEE, H. J.; BAE, E. J.; LEE, S. J. Extracellular α -synuclein-a novel and crucial factor in Lewy body diseases. **Nat Rev Neurol**, v. 10, n. 2, p. 92-8, Feb 2014. ISSN 1759-4766. Available at: < <https://www.ncbi.nlm.nih.gov/pubmed/24468877> >.

LEE, J. et al. Biochemical characterization of the human copper transporter Ctr1. **J Biol Chem**, v. 277, n. 6, p. 4380-7, Feb 2002. ISSN 0021-9258. Available at: < <http://www.ncbi.nlm.nih.gov/pubmed/11734551> >.

LEE, V. M. Disruption of the cytoskeleton in Alzheimer's disease. **Curr Opin Neurobiol**, v. 5, n. 5, p. 663-8, Oct 1995. ISSN 0959-4388. Available at: < <http://www.ncbi.nlm.nih.gov/pubmed/8580719> >.

LEVINE, H. et al. Clioquinol and other hydroxyquinoline derivatives inhibit A β (1–42) oligomer assembly **Neuroscience Letters**, v. 465, n. 1, p. 99-103, 2009.

LI, L. et al. Synthesis and structural characterization of zinc(II) and cobalt(II) complexes based on multidentate hydrazone ligands. **Journal of Molecular Structure**, v. 1110, p. 180-184, 2016.

LIMA, P. C. et al. Synthesis and analgesic activity of novel N-acylarylhydrazones and isosters, derived from natural safrole. **Eur J Med Chem**, v. 35, n. 2, p. 187-203, Feb 2000. ISSN 0223-5234. Available at: < <https://www.ncbi.nlm.nih.gov/pubmed/10758281> >.

LINDEN, R. et al. Physiology of the prion protein. **Physiol Rev**, v. 88, n. 2, p. 673-728, Apr 2008. ISSN 0031-9333. Available at: < <https://www.ncbi.nlm.nih.gov/pubmed/18391177> >.

LIPINSKI, C. A. et al. Experimental and computational approaches to estimate solubility and permeability in drug discovery and development settings. **Adv Drug Deliv Rev**, v. 46, n. 1-3, p. 3-26, Mar 2001. ISSN 0169-409X. Available at: < <https://www.ncbi.nlm.nih.gov/pubmed/11259830> >.

LIU, B. et al. Vagotomy and Parkinson disease: A Swedish register-based matched-cohort study. **Neurology**, v. 88, n. 21, p. 1996-2002, May 2017. ISSN 1526-632X. Available at: < <https://www.ncbi.nlm.nih.gov/pubmed/28446653> >.

LLORET, A. et al. Amyloid- β toxicity and tau hyperphosphorylation are linked via RCAN1 in Alzheimer's disease. **J Alzheimers Dis**, v. 27, n. 4, p. 701-9, 2011. ISSN 1875-8908. Available at: < <http://www.ncbi.nlm.nih.gov/pubmed/21876249> >.

LOTHIAN, A. et al. Characterization of the metal status of natively purified alpha-synuclein from human blood, brain tissue, or recombinant sources using size exclusion ICP-MS reveals no significant binding of Cu, Fe or Zn. **Metallomics**, v. 11, n. 1, p. 128-140, 01 2019. ISSN 1756-591X. Available at: < <https://www.ncbi.nlm.nih.gov/pubmed/30465671> >.

LU, C. et al. Design, synthesis, and evaluation of multitarget-directed resveratrol derivatives for the treatment of Alzheimer's disease. **J Med Chem**, v. 56, n. 14, p. 5843-59, Jul 2013. ISSN 1520-4804. Available at: < <http://www.ncbi.nlm.nih.gov/pubmed/23799643> >.

LYKETSOS, C. G. et al. Mental and behavioral disturbances in dementia: findings from the Cache County Study on Memory in Aging. **Am J Psychiatry**, v. 157, n. 5, p. 708-14, May 2000. ISSN 0002-953X. Available at: < <http://www.ncbi.nlm.nih.gov/pubmed/10784462> >.

LÁZARO, D. F. et al. Systematic comparison of the effects of alpha-synuclein mutations on its oligomerization and aggregation. **PLoS Genet**, v. 10, n. 11, p. e1004741, Nov 2014. ISSN 1553-7404. Available at: < <https://www.ncbi.nlm.nih.gov/pubmed/25393002> >.

MACRAE, C. F. et al. Mercury CSD 2.0– new features for the visualization and investigation of crystal structures. **J Appl Crystallogr**, v. 41, n. 2, p. 466-470, 2020/03/18 2008. Available at: < <https://doi.org/10.1107/S0021889807067908> >.

MANCINO, A. M. et al. Effects of clioquinol on metal-triggered amyloid-beta aggregation revisited. **Inorg Chem**, v. 48, n. 20, p. 9596-8, Oct 2009. ISSN 1520-510X. Available at: < <http://www.ncbi.nlm.nih.gov/pubmed/19817493> >.

MANGIA, A. et al. Synthesis, characterization and HPLC behaviour of metal complexes of methyl pyruvate aroylhydrazones. v. 68, p. 137-140, 1983. Available at: < <http://www.sciencedirect.com/science/article/pii/S0020169300889513> >.

MARINO, T. et al. On the metal ion (Zn(2+), Cu(2+)) coordination with beta-amyloid peptide: DFT computational study. **Interdiscip Sci**, v. 2, n. 1, p. 57-69, Mar 2010. ISSN 1913-2751. Available at: < <http://www.ncbi.nlm.nih.gov/pubmed/20640797> >.

MARZBAN, L. et al. Impaired NH2-terminal processing of human proislet amyloid polypeptide by the prohormone convertase PC2 leads to amyloid formation and cell death. **Diabetes**, v. 55, n. 8, p. 2192-201, Aug 2006. ISSN 0012-1797. Available at: < <https://www.ncbi.nlm.nih.gov/pubmed/16873681> >.

MATTSON, M. P. Cellular actions of beta-amyloid precursor protein and its soluble and fibrillogenic derivatives. **Physiol Rev**, v. 77, n. 4, p. 1081-132, Oct 1997. ISSN 0031-9333. Available at: < <http://www.ncbi.nlm.nih.gov/pubmed/9354812> >.

MCEWEN, E. et al. Heme-regulated inhibitor kinase-mediated phosphorylation of eukaryotic translation initiation factor 2 inhibits translation, induces stress granule formation, and mediates survival upon arsenite exposure. **J Biol Chem**, v. 280, n. 17, p. 16925-33, Apr 2005. ISSN 0021-9258. Available at: < <https://www.ncbi.nlm.nih.gov/pubmed/15684421> >.

MELONI, G.; VAŠÁK, M. Redox activity of α -synuclein-Cu is silenced by Zn7-metallothionein-3. **Free Radic Biol Med**, v. 50, n. 11, p. 1471-9, Jun 2011. ISSN 1873-4596. Available at: < <https://www.ncbi.nlm.nih.gov/pubmed/21320589> >.

MELOV, S. ‘...and C is for Clioquinol’ – the A β Cs of Alzheimer's disease. **Trend in Neurosciences**, v. 25, n. 3, p. 121-123, 2002.

MERLINI, G.; BELLOTTI, V. Molecular mechanisms of amyloidosis. **N Engl J Med**, v. 349, n. 6, p. 583-96, Aug 2003. ISSN 1533-4406. Available at: < <https://www.ncbi.nlm.nih.gov/pubmed/12904524> >.

MIOTTO, M. C. et al. Copper binding to the N-terminally acetylated, naturally occurring form of alpha-synuclein induces local helical folding. **J Am Chem Soc**, v. 137, n. 20, p. 6444-7, May 2015. ISSN 1520-5126. Available at: < <http://www.ncbi.nlm.nih.gov/pubmed/25939020> >.

MIURA, T. et al. Metal binding modes of Alzheimer's amyloid beta-peptide in insoluble aggregates and soluble complexes. **Biochemistry**, v. 39, n. 23, p. 7024-31, Jun 2000. ISSN 0006-2960. Available at: < <http://www.ncbi.nlm.nih.gov/pubmed/10841784> >.

MOHAMMED, M. Synthesis and characterization of bis-acylhydrazone derivatives as tetradentate ligands and their dinuclear metal(II) complexes. **Periodica Polytechnica Chemical Engineering**, v. 56, p. 83, 01/01 2012.

MOLINO, I. et al. Efficacy of memantine, donepezil, or their association in moderate-severe Alzheimer's disease: a review of clinical trials. **ScientificWorldJournal**, v. 2013, p. 925702, 2013. ISSN 1537-744X. Available at: < <http://www.ncbi.nlm.nih.gov/pubmed/24288512> >.

MOONS, R. et al. Metal ions shape α -synuclein. v. 10, n. 1, p. 16293, 2020. Available at: < <https://doi.org/10.1038/s41598-020-73207-9> >.

MOORES, B. et al. Effect of surfaces on amyloid fibril formation. **PLoS One**, v. 6, n. 10, p. e25954, 2011. ISSN 1932-6203. Available at: < <http://www.ncbi.nlm.nih.gov/pubmed/22016789> >.

MORELL, M. et al. Inclusion bodies: specificity in their aggregation process and amyloid-like structure. **Biochim Biophys Acta**, v. 1783, n. 10, p. 1815-25, Oct 2008. ISSN 0006-3002. Available at: < <https://www.ncbi.nlm.nih.gov/pubmed/18619498> >.

MORGAN, M. T. et al. Glutathione limits aquacopper(I) to sub-femtomolar concentrations through cooperative assembly of a tetranuclear cluster. **J Biol Chem**, v. 292, n. 52, p. 21558-21567, 12 2017. ISSN 1083-351X. Available at: < <https://www.ncbi.nlm.nih.gov/pubmed/29101230> >.

MORIARTY, G. M. et al. A revised picture of the Cu(II)- α -synuclein complex: the role of N-terminal acetylation. **Biochemistry**, v. 53, n. 17, p. 2815-7, May 2014. ISSN 1520-4995. Available at: < <http://www.ncbi.nlm.nih.gov/pubmed/24739028> >.

NARASIMHAN, B.; SHARMA, D.; KUMAR, P. Biological importance of imidazole nucleus in the new millennium. **Medicinal Chemistry Research**, v. 20, n. 8, p. 1119-1140, November 01 2011. ISSN 1554-8120. Available at: < <https://doi.org/10.1007/s00044-010-9472-5> >.

NELSON, D. L. **Lehninger principles of biochemistry**. Fourth edition. New York : W.H. Freeman, 2005., 2005. Available at: < <https://search.library.wisc.edu/catalog/999964334502121> >.

NGUYEN, P. H. et al. Amyloid Oligomers: A Joint Experimental/Computational Perspective on Alzheimer's Disease, Parkinson's Disease, Type II Diabetes, and Amyotrophic Lateral Sclerosis. **Chemical Reviews**, v. 121, n. 4, p. 2545-2647, 2021. Available at: < <https://doi.org/10.1021/acs.chemrev.0c01122> >.

NIE, Q.; DU, X. G.; GENG, M. Y. Small molecule inhibitors of amyloid β peptide aggregation as a potential therapeutic strategy for Alzheimer's disease. **Acta Pharmacol Sin**, v. 32, n. 5, p. 545-51, May 2011. ISSN 1745-7254. Available at: < <http://www.ncbi.nlm.nih.gov/pubmed/21499284> >.

NIELSEN, L. et al. Effect of environmental factors on the kinetics of insulin fibril formation: elucidation of the molecular mechanism. **Biochemistry**, v. 40, n. 20, p. 6036-46, May 2001. ISSN 0006-2960. Available at: < <https://www.ncbi.nlm.nih.gov/pubmed/11352739> >.

NITSCH, R. M. et al. Release of amyloid beta-protein precursor derivatives by electrical depolarization of rat hippocampal slices. **Proc Natl Acad Sci U S A**, v. 90, n. 11, p. 5191-3, Jun 1993. ISSN 0027-8424. Available at: < <http://www.ncbi.nlm.nih.gov/pubmed/8506366> >.

NOGUEIRA, V. D. S. et al. Structural and spectroscopic investigation on a new potentially bioactive di-hydrazone containing thiophene heterocyclic rings. **J Mol Struct**, v. 1106, p. 121-129, 2016. Available at: < <http://www.sciencedirect.com/science/article/pii/S0022286015303811> >.

OLANOW, C. W.; TATTON, W. G. Etiology and pathogenesis of Parkinson's disease. **Annu Rev Neurosci**, v. 22, p. 123-44, 1999. ISSN 0147-006X. Available at: < <http://www.ncbi.nlm.nih.gov/pubmed/10202534> >.

OLIVEIRA, P. F. M. et al. Mechanochemical Synthesis and Biological Evaluation of Novel Isoniazid Derivatives with Potent Antitubercular Activity. **Molecules**, v. 22, n. 9, Sep 2017. ISSN 1420-3049. Available at: < <https://www.ncbi.nlm.nih.gov/pubmed/28862683> >.

OTTOLINI, D. et al. Alpha-synuclein at the intracellular and the extracellular side: functional and dysfunctional implications. **Biol Chem**, v. 398, n. 1, p. 77-100, 01 2017. ISSN 1437-4315. Available at: < <https://www.ncbi.nlm.nih.gov/pubmed/27508962> >.

PAIK, S. R. et al. Copper(II)-induced self-oligomerization of alpha-synuclein. **Biochem J**, v. 340 (Pt 3), p. 821-8, Jun 1999. ISSN 0264-6021. Available at: < <http://www.ncbi.nlm.nih.gov/pubmed/10359669> >.

PAJOUHESH, H.; LENZ, G. R. Medicinal chemical properties of successful central nervous system drugs. **NeuroRx**, v. 2, n. 4, p. 541-53, Oct 2005. ISSN 1545-5343. Available at: < <https://www.ncbi.nlm.nih.gov/pubmed/16489364> >.

PALL, H. S. et al. Raised cerebrospinal-fluid copper concentration in Parkinson's disease. **Lancet**, v. 2, n. 8553, p. 238-41, Aug 1987. ISSN 0140-6736. Available at: < <http://www.ncbi.nlm.nih.gov/pubmed/2886715> >.

PALLA, G. et al. Conformational behaviour and E/Z isomerization of N-acyl and N-aryloylhydrazones. v. 42, n. 13, p. 3649-3654, 1986. Available at: < <http://www.sciencedirect.com/science/article/pii/S0040402001873324> >.

PAN, K. M. et al. Conversion of alpha-helices into beta-sheets features in the formation of the scrapie prion proteins. **Proc Natl Acad Sci U S A**, v. 90, n. 23, p. 10962-6, Dec 1993. ISSN 0027-8424. Available at: < <https://www.ncbi.nlm.nih.gov/pubmed/7902575> >.

PARDRIDGE, W. M. Alzheimer's disease drug development and the problem of the blood-brain barrier. **Alzheimers Dement**, v. 5, n. 5, p. 427-32, Sep 2009. ISSN 1552-5279. Available at: < <http://www.ncbi.nlm.nih.gov/pubmed/19751922> >.

PARIENTE COHEN, N. et al. Aminomethylene-Phosphonate Analogue as a Cu(II) Chelator: Characterization and Application as an Inhibitor of Oxidation Induced by the Cu(II)-Prion Peptide Complex. **Inorganic Chemistry**, v. 58, n. 14, p. 8995-9003, 2019. Available at: < <https://doi.org/10.1021/acs.inorgchem.9b00287> >.

PARK, M. J. et al. Elevated levels of α -synuclein oligomer in the cerebrospinal fluid of drug-naïve patients with Parkinson's disease. **J Clin Neurol**, v. 7, n. 4, p. 215-22, Dec 2011. ISSN 2005-5013. Available at: < <https://www.ncbi.nlm.nih.gov/pubmed/22259618> >.

PARKINSON'S-DISEASE-FOUNDATION. Statistics on Parkinson's. 2016. Accessed on: June 23.

PATORSKI, P.; WYRZYKIEWICZ, E.; BARTKOWIAK, G. Synthesis and Conformational Assignment of N-(E)-Stilbenyloxymethylenecarbonyl-Substituted Hydrazones of Acetone and o-(m - and p -) Chloro- (nitro-) benzaldehydes by Means of ¹H and ¹³C NMR Spectroscopy. **Journal of Spectroscopy**, v. 2013, p. 197475, 2013. Available at: < <https://doi.org/10.1155/2013/197475> >.

PRASHANT, S. K. A. A. K. D. Metal Protein Attenuating Compounds (MPACs): An Emerging Approach for the Treatment of Neurodegenerative Disorders. v. 4, n. 2, p. 57-67, 2008. Available at: < <http://www.eurekaselect.com/node/67826/article> >.

PRUSINER, S. B. Novel proteinaceous infectious particles cause scrapie. **Science**, v. 216, n. 4542, p. 136-44, Apr 1982. ISSN 0036-8075. Available at: < <https://www.ncbi.nlm.nih.gov/pubmed/6801762> >.

_____. Prions. **Proc Natl Acad Sci U S A**, v. 95, n. 23, p. 13363-83, Nov 1998. ISSN 0027-8424. Available at: < <https://www.ncbi.nlm.nih.gov/pubmed/9811807> >.

PRZEDBORSKI, S.; VILA, M.; JACKSON-LEWIS, V. Neurodegeneration: what is it and where are we? **J Clin Invest**, v. 111, n. 1, p. 3-10, Jan 2003. ISSN 0021-9738. Available at: < <https://www.ncbi.nlm.nih.gov/pubmed/12511579> >.

RADA, J. P. et al. Binucleating Hydrazonic Ligands and Their μ -Hydroxodicopper(II) Complexes as Promising Structural Motifs for Enhanced Antitumor Activity. **Inorg Chem**, v. 58, n. 13, p. 8800-8819, Jul 2019. ISSN 1520-510X. Available at: < <https://www.ncbi.nlm.nih.gov/pubmed/31247881> >.

_____. Isoxazole-Derived Aroylhydrazones and Their Dinuclear Copper(II) Complexes Show Antiproliferative Activity on Breast Cancer Cells with a Potentially Alternative Mechanism Of Action. **ChemBioChem**, v. 21, n. 17, p. 2474-2486, 2020/10/23 2020. Available at: < <https://doi.org/10.1002/cbic.202000122> >.

RASIA, R. M. et al. Structural characterization of copper(II) binding to alpha-synuclein: Insights into the bioinorganic chemistry of Parkinson's disease. **Proc Natl Acad Sci U S A**, v. 102, n. 12, p. 4294-9, Mar 2005. ISSN 0027-8424. Available at: < <https://www.ncbi.nlm.nih.gov/pubmed/15767574> >.

REGLAND, B. et al. Treatment of Alzheimer's disease with clioquinol. **Dement Geriatr Cogn Disord**, v. 12, n. 6, p. 408-14, 2001 Nov-Dec 2001. ISSN 1420-8008. Available at: < <http://www.ncbi.nlm.nih.gov/pubmed/11598313> >.

REQUENA, J. R. et al. Copper-catalyzed oxidation of the recombinant SHa(29–231) prion protein. **Proceedings of the National Academy of Sciences**, v. 98, n. 13, p. 7170, 2001. Available at: < <http://www.pnas.org/content/98/13/7170.abstract> >.

REY, N. A.; CUKIERMAN, D. S. **Compostos N-acil-hidrazônicos, uso no tratamento de agregopatias degenerativas amiloides e não-amiloides, e composição farmacêutica**. Instituto Nacional da Propriedade Industrial 2020.

REY, N. A. et al. **Ligantes Binucleantes Fenólicos, Compostos Metálicos Binucleares, Composição Médico-Veterinária, Processos de Síntese de Ligantes Binucleantes, Processo de Síntese de Compostos Binucleares, Método de Tratamento de Neoplasias e Doenças Fúngicas e Uso**. INDUSTRIAL, I.-I. N. D. P. Brasil 2020.

RICE, M. E. Ascorbate regulation and its neuroprotective role in the brain. **Trends Neurosci**, v. 23, n. 5, p. 209-16, May 2000. ISSN 0166-2236. Available at: < <https://www.ncbi.nlm.nih.gov/pubmed/10782126> >.

RICHARDSON, D.; BERNHARDT, P. V.; BECKER, E. M. **Iron chelators and uses thereof**: US6989397 B1 2006.

RICHARDSON, D. R. Friedreich's ataxia: iron chelators that target the mitochondrion as a therapeutic strategy? **Expert Opin Investig Drugs**, v. 12, n. 2, p. 235-45, Feb 2003. ISSN 1354-3784. Available at: < <https://www.ncbi.nlm.nih.gov/pubmed/12556217> >.

RICHARDSON, D. R.; BECKER, E.; BERNHARDT, P. V. The biologically active iron chelators 2-pyridylcarboxaldehyde isonicotinoylhydrazone, 2-

pyridylcarboxaldehyde benzoylhydrazone monohydrate and 2-furaldehyde isonicotinoylhydrazone. **Acta Crystallogr C**, v. 55 (Pt 12), p. 2102-5, Dec 1999. ISSN 0108-2701. Available at: < <https://www.ncbi.nlm.nih.gov/pubmed/10641282> >.

RIEK, R. et al. NMR structure of the mouse prion protein domain PrP(121-231). **Nature**, v. 382, n. 6587, p. 180-2, Jul 1996. ISSN 0028-0836. Available at: < <https://www.ncbi.nlm.nih.gov/pubmed/8700211> >.

RIESNER, D. Biochemistry and structure of PrPC and PrPSc. **British Medical Bulletin**, v. 66, n. 1, p. 21-33, 5/11/2019 2003. Available at: < <https://doi.org/10.1093/bmb/66.1.21> >.

RIGAKU, O. CrysAlis PRO. Rigaku Oxford Diffraction. **Yarnton, England**, 2015.

RIVERA-MANCÍA, S. et al. The transition metals copper and iron in neurodegenerative diseases. **Chem Biol Interact**, v. 186, n. 2, p. 184-99, Jul 2010. ISSN 1872-7786. Available at: < <http://www.ncbi.nlm.nih.gov/pubmed/20399203> >.

RIVERO, R. et al. Synthesis, kinetics of photo-dimerization/photo-cleavage and physical properties of coumarin-containing branched polyurethanes based on polycaprolactones. v. 10, p. 84-95, 2015.

ROEPSTORFF, P.; FOHLMAN, J. Letter to the editors. **Biomedical Mass Spectrometry**, v. 11, n. 11, p. 601-601, 2019/05/19 1984. Available at: < <https://doi.org/10.1002/bms.1200111109> >.

ROTILIO, G. et al. Copper-dependent oxidative stress and neurodegeneration. **IUBMB Life**, v. 50, n. 4-5, p. 309-14, 2000 Oct-Nov 2000. ISSN 1521-6543. Available at: < <https://www.ncbi.nlm.nih.gov/pubmed/11327325> >.

SABATÉ, R.; GALLARDO, M.; ESTELRICH, J. An autocatalytic reaction as a model for the kinetics of the aggregation of beta-amyloid. **Biopolymers**, v. 71, n. 2, p. 190-5, 2003. ISSN 0006-3525. Available at: < <https://www.ncbi.nlm.nih.gov/pubmed/12767118> >.

SAIDO, T. C. et al. Dominant and differential deposition of distinct beta-amyloid peptide species, A beta N3(pE), in senile plaques. **Neuron**, v. 14, n. 2, p. 457-66, Feb 1995. ISSN 0896-6273. Available at: < <http://www.ncbi.nlm.nih.gov/pubmed/7857653> >.

SAMPSON, E. L.; JENAGARATNAM, L.; MCSHANE, R. Metal protein attenuating compounds for the treatment of Alzheimer's dementia. **Cochrane Database Syst Rev**, v. 5, p. CD005380, 2012. ISSN 1469-493X. Available at: < <http://www.ncbi.nlm.nih.gov/pubmed/22592705> >.

SANGUINETTI, M. C.; TRISTANI-FIROUZI, M. hERG potassium channels and cardiac arrhythmia. **Nature**, v. 440, n. 7083, p. 463-9, Mar 2006. ISSN 1476-4687. Available at: < <https://www.ncbi.nlm.nih.gov/pubmed/16554806> >.

SATYAJIT MONDAL, S. N., AYAN KUMAR DEYA, EKKEHARD SI^NNB, CARLA ERIBALB, STEVEN R. HER^RONC, SHYAMAL KUMAR CHATTOPADH^YAYA. Mononuclear and binuclear Cu(II) complexes of some tridentate aroyl hydrazones. X-ray crystal structures of a mononuclear and a binuclear complex. **Inorganica Chimica Acta**, v. 398, p. 98-105, 2013.

SAVINI, L. et al. New alpha-(N)-heterocyclichydrazones: evaluation of anticancer, anti-HIV and antimicrobial activity. **Eur J Med Chem**, v. 39, n. 2, p. 113-22, Feb 2004. ISSN 0223-5234. Available at: < <https://www.ncbi.nlm.nih.gov/pubmed/14987820> >.

SAYRE, L. M.; PERRY, G.; SMITH, M. A. Redox metals and neurodegenerative disease. **Curr Opin Chem Biol**, v. 3, n. 2, p. 220-5, Apr 1999. ISSN 1367-5931. Available at: < <https://www.ncbi.nlm.nih.gov/pubmed/10226049> >.

SCHWAB, S. et al. Sequence proximity between Cu(II) and Cu(I) binding sites of human copper transporter 1 model peptides defines reactivity with ascorbate and O₂. **J Inorg Biochem**, v. 158, p. 70-6, May 2016. ISSN 1873-3344. Available at: < <http://www.ncbi.nlm.nih.gov/pubmed/26778425> >.

SCHÖNEICH, C. Mechanisms of metal-catalyzed oxidation of histidine to 2-oxo-histidine in peptides and proteins. **J Pharm Biomed Anal**, v. 21, n. 6, p. 1093-7, Jan 2000. ISSN 0731-7085. Available at: < <https://www.ncbi.nlm.nih.gov/pubmed/10708394> >.

SCIOR, T.; GARCÉS-EISELE, S. J. Isoniazid is not a lead compound for its pyridyl ring derivatives, isonicotinoyl amides, hydrazides, and hydrazones: a critical review. **Curr Med Chem**, v. 13, n. 18, p. 2205-19, 2006. ISSN 0929-8673. Available at: < <https://www.ncbi.nlm.nih.gov/pubmed/16918349> >.

SCOTT, L. E.; ORVIG, C. Medicinal inorganic chemistry approaches to passivation and removal of aberrant metal ions in disease. **Chem Rev**, v. 109, n. 10, p. 4885-910, Oct 2009. ISSN 1520-6890. Available at: < <http://www.ncbi.nlm.nih.gov/pubmed/19637926> >.

SELKOE, D.; MANDELKOW, E.; HOLTZMAN, D. Deciphering Alzheimer disease. **Cold Spring Harb Perspect Med**, v. 2, n. 1, p. a011460, Jan 2012. ISSN 2157-1422. Available at: < <http://www.ncbi.nlm.nih.gov/pubmed/22315723> >.

SELKOE, D. J. Amyloid beta-protein and the genetics of Alzheimer's disease. **J Biol Chem**, v. 271, n. 31, p. 18295-8, Aug 1996. ISSN 0021-9258. Available at: < <http://www.ncbi.nlm.nih.gov/pubmed/8756120> >.

SERRANO-POZO, A. et al. Neuropathological Alterations in Alzheimer Disease. **Cold Spring Harbor Perspectives in Biology**, v. 3, n. 12, Dec 2011. ISSN 1943-0264. Available at: < <Go to ISI>://000298135700010 >.

SHELDRIK, G. M. Crystal structure refinement with SHELXL. **Acta Crystallogr C Struct Chem**, v. 71, n. Pt 1, p. 3-8, Jan 2015. ISSN 2053-2296. Available at: < <http://www.ncbi.nlm.nih.gov/pubmed/25567568> >.

SILVA, A. G. et al. Synthesis and vasodilatory activity of new N-acylhydrazone derivatives, designed as LASSBio-294 analogues. **Bioorg Med Chem**, v. 13, n. 10, p. 3431-7, May 2005. ISSN 0968-0896. Available at: < <https://www.ncbi.nlm.nih.gov/pubmed/15848755> >.

SMALL, G. W. et al. Diagnosis and treatment of Alzheimer disease and related disorders - Consensus statement of the American Association for Geriatric Psychiatry, the Alzheimer's Association, and the American Geriatrics Society. **Jama-Journal of the American Medical Association**, v. 278, n. 16, p. 1363-1371, Oct 22 1997. ISSN 0098-7484. Available at: < <Go to ISI>://A1997YA90500039 >.

SMITH, M. A. et al. Abnormal localization of iron regulatory protein in Alzheimer's disease. **Brain Res**, v. 788, n. 1-2, p. 232-6, Mar 1998. ISSN 0006-8993. Available at: < <http://www.ncbi.nlm.nih.gov/pubmed/9555030> >.

SMITH, M. A. C. Doença de Alzheimer. **Revista Brasileira de Psiquiatria**, v. 21, n. 2, p. 03-07, 1999.

SMOLIGA, J. M.; BAUR, J. A.; HAUSENBLAS, H. A. Resveratrol and health--a comprehensive review of human clinical trials. **Mol Nutr Food Res**, v. 55, n. 8, p. 1129-41, Aug 2011. ISSN 1613-4133. Available at: < <http://www.ncbi.nlm.nih.gov/pubmed/21688389> >.

SOREGHAN, B.; KOSMOSKI, J.; GLABE, C. Surfactant properties of Alzheimer's A beta peptides and the mechanism of amyloid aggregation. **J Biol Chem**, v. 269, n. 46, p. 28551-4, Nov 1994. ISSN 0021-9258. Available at: < <http://www.ncbi.nlm.nih.gov/pubmed/7961799> >.

SPILLANTINI, M. G. et al. Alpha-synuclein in Lewy bodies. **Nature**, v. 388, n. 6645, p. 839-40, Aug 1997. ISSN 0028-0836. Available at: < <https://www.ncbi.nlm.nih.gov/pubmed/9278044> >.

STANCU, I. C. et al. Models of β -amyloid induced Tau-pathology: the long and "folded" road to understand the mechanism. **Mol Neurodegener**, v. 9, p. 51, 2014. ISSN 1750-1326. Available at: < <http://www.ncbi.nlm.nih.gov/pubmed/25407337> >.

STEINER, T. The Hydrogen Bond in the Solid State. **Angewandte Chemie International Edition**, v. 41, n. 1, p. 48-76, 2002/03/24 2002. Available at: < [https://doi.org/10.1002/1521-3773\(20020104\)41:1<48::AID-ANIE48>3.0.CO](https://doi.org/10.1002/1521-3773(20020104)41:1<48::AID-ANIE48>3.0.CO) >.

SUVARAPU, L. N. et al. Spectral Characterization and Antibacterial Activities of Benzyloxybenzaldehydethiosemicarbazone, 3,4-Dihydroxybenzaldehydeisonicotinoylhydrazone and their Transitional Metal

Complexes. **E-Journal of Chemistry**, v. 8, p. 579892, 2011. Available at: < <https://doi.org/10.1155/2011/579892> >.

SWAIM, M. W.; PIZZO, S. V. Methionine sulfoxide and the oxidative regulation of plasma proteinase inhibitors. **J Leukoc Biol**, v. 43, n. 4, p. 365-79, Apr 1988. ISSN 0741-5400. Available at: < <https://www.ncbi.nlm.nih.gov/pubmed/2450941> >.

SYAKAEV, V. V. et al. NMR study of conformation and isomerization of aryl- and heteroarylaldehyde 4-tert-butylphenoxyacetylhydrazones. v. 788, n. 1, p. 55-62, 2006. Available at: < <http://www.sciencedirect.com/science/article/pii/S0022286005008112> >.

SÁNCHEZ-LÓPEZ, C. et al. Methionine 109 plays a key role in Cu(II) binding to His111 in the 92–115 fragment of the human prion protein. **Bioinorganic and bio-inspired chemistry of copper**, v. 481, p. 87-97, 2018. Available at: < <http://www.sciencedirect.com/science/article/pii/S0020169317310678> >.

TABATON, M. et al. Soluble Amyloid Beta-Protein Is a Marker of Alzheimer Amyloid in Brain but Not in Cerebrospinal-Fluid. **Biochemical and Biophysical Research Communications**, v. 200, n. 3, p. 1598-1603, May 16 1994. ISSN 0006-291X. Available at: < <Go to ISI>://A1994NL38800061 >.

TABNER, B. J. et al. Protein aggregation, metals and oxidative stress in neurodegenerative diseases. **Biochem Soc Trans**, v. 33, n. Pt 5, p. 1082-6, Nov 2005. ISSN 0300-5127. Available at: < <http://www.ncbi.nlm.nih.gov/pubmed/16246050> >.

THAIS, B. F.; MARIANA, C. F. S.; MICHELLE, C. P. A. R. P.-F. Analysis of the Applicability and Use of Lipinski's Rule for Central Nervous System Drugs. v. 13, n. 10, p. 999-1006, 2016. Available at: < <http://www.eurekaselect.com/node/143485/article> >.

THEILLET, F. X. et al. Structural disorder of monomeric α -synuclein persists in mammalian cells. **Nature**, v. 530, n. 7588, p. 45-50, Feb 2016. ISSN 1476-4687. Available at: < <https://www.ncbi.nlm.nih.gov/pubmed/26808899> >.

_____. Physicochemical properties of cells and their effects on intrinsically disordered proteins (IDPs). **Chem Rev**, v. 114, n. 13, p. 6661-714, Jul 2014. ISSN 1520-6890. Available at: < <https://www.ncbi.nlm.nih.gov/pubmed/24901537> >.

THOMPSON, D. J. A chemical hypothesis for arsenic methylation in mammals. **Chem Biol Interact**, v. 88, n. 2-3, p. 89-14, Sep 1993. ISSN 0009-2797. Available at: < <https://www.ncbi.nlm.nih.gov/pubmed/8403081> >.

THOTA, S. et al. N-Acylhydrazones as drugs. **Bioorg Med Chem Lett**, v. 28, n. 17, p. 2797-2806, 09 2018. ISSN 1464-3405. Available at: < <https://www.ncbi.nlm.nih.gov/pubmed/30006065> >.

TÕUGU, V.; KARAFIN, A.; PALUMAA, P. Binding of zinc(II) and copper(II) to the full-length Alzheimer's amyloid-beta peptide. **J Neurochem**, v. 104, n. 5, p. 1249-59, Mar 2008. ISSN 1471-4159. Available at: < <http://www.ncbi.nlm.nih.gov/pubmed/18289347> >.

UVERSKY, V. N.; MALOY, S.; HUGHES, K. Posttranslational Modification. In: (Ed.). San Diego: Academic Press, 2013. p.425-430.

VALIENTE-GABIOUD, A. A. et al. Structural basis behind the interaction of Zn²⁺ with the protein α -synuclein and the A β peptide: a comparative analysis. **J Inorg Biochem**, v. 117, p. 334-41, Dec 2012. ISSN 1873-3344. Available at: < <http://www.ncbi.nlm.nih.gov/pubmed/22832069> >.

VAN DE WATERBEEMD, H. et al. Estimation of blood-brain barrier crossing of drugs using molecular size and shape, and H-bonding descriptors. **J Drug Target**, v. 6, n. 2, p. 151-65, 1998. ISSN 1061-186X. Available at: < <https://www.ncbi.nlm.nih.gov/pubmed/9886238> >.

_____. Estimation of Blood-Brain Barrier Crossing of Drugs Using Molecular Size and Shape, and H-Bonding Descriptors. **Journal of Drug Targeting**, v. 6, n. 2, p. 151-165, 1998/01/01 1998. ISSN 1061-186X. Available at: < <https://doi.org/10.3109/10611869808997889> >.

VEDANI, A. et al. OpenVirtualToxLab--a platform for generating and exchanging in silico toxicity data. **Toxicol Lett**, v. 232, n. 2, p. 519-32, Jan 2015. ISSN 1879-3169. Available at: < <https://www.ncbi.nlm.nih.gov/pubmed/25240273> >.

VEDANI, A.; DOBLER, M.; SMIEŠKO, M. VirtualToxLab - a platform for estimating the toxic potential of drugs, chemicals and natural products. **Toxicol Appl Pharmacol**, v. 261, n. 2, p. 142-53, Jun 2012. ISSN 1096-0333. Available at: < <https://www.ncbi.nlm.nih.gov/pubmed/22521603> >.

VEDANI, A.; SMIESKO, M. In silico toxicology in drug discovery - concepts based on three-dimensional models. **Altern Lab Anim**, v. 37, n. 5, p. 477-96, Nov 2009. ISSN 0261-1929. Available at: < <https://www.ncbi.nlm.nih.gov/pubmed/20017578> >.

VEKRELLIS, K.; STEFANIS, L. Targeting intracellular and extracellular alpha-synuclein as a therapeutic strategy in Parkinson's disease and other synucleinopathies. **Expert Opin Ther Targets**, v. 16, n. 4, p. 421-32, Apr 2012. ISSN 1744-7631. Available at: < <https://www.ncbi.nlm.nih.gov/pubmed/22480256> >.

VICENTE MIRANDA, H. et al. Glycation potentiates α -synuclein-associated neurodegeneration in synucleinopathies. **Brain**, v. 140, n. 5, p. 1399-1419, May 2017. ISSN 1460-2156. Available at: < <https://www.ncbi.nlm.nih.gov/pubmed/28398476> >.

VICINI, P. et al. Synthesis and antiproliferative activity of benzo[d]isothiazole hydrazones. **Eur J Med Chem**, v. 41, n. 5, p. 624-32, May 2006. ISSN 0223-5234. Available at: < <https://www.ncbi.nlm.nih.gov/pubmed/16540208> >.

_____. Anti-HIV evaluation of benzo[d]isothiazole hydrazones. **Eur J Med Chem**, v. 44, n. 4, p. 1801-7, Apr 2009. ISSN 1768-3254. Available at: < <https://www.ncbi.nlm.nih.gov/pubmed/18614259> >.

VIEGAS, A. et al. Saturation-Transfer Difference (STD) NMR: A Simple and Fast Method for Ligand Screening and Characterization of Protein Binding. **Journal of Chemical Education**, v. 88, n. 7, p. 990-994, 2011. Available at: < <https://doi.org/10.1021/ed101169t> >.

VILES, J. H. et al. Copper binding to the prion protein: structural implications of four identical cooperative binding sites. **Proc Natl Acad Sci U S A**, v. 96, n. 5, p. 2042-7, Mar 1999. ISSN 0027-8424. Available at: < <https://www.ncbi.nlm.nih.gov/pubmed/10051591> >.

VISION, P. O.; LTD., R. P. **POV-Ray for Windows** 1991-2013.

WANG, Z. et al. Roles of methionine oxidation in E200K prion protein misfolding: Implications for the mechanism of pathogenesis in E200K linked familial Creutzfeldt–Jakob disease. v. 1864, n. 4, p. 346-358, 2016. Available at: < <http://www.sciencedirect.com/science/article/pii/S1570963916000157> >.

WESTERMARK, P.; ANDERSSON, A.; WESTERMARK, G. T. Islet amyloid polypeptide, islet amyloid, and diabetes mellitus. **Physiol Rev**, v. 91, n. 3, p. 795-826, Jul 2011. ISSN 1522-1210. Available at: < <https://www.ncbi.nlm.nih.gov/pubmed/21742788> >.

WHO, W. H. O. Zoonoses and veterinary public health: Prion diseases. https://www.who.int/zoonoses/diseases/prion_diseases/en/, 2004. Accessed on: March, 2021.

WILKANIEC, A. et al. Extracellular Alpha-Synuclein Oligomers Induce Parkin S-Nitrosylation: Relevance to Sporadic Parkinson's Disease Etiopathology. **Mol Neurobiol**, v. 56, n. 1, p. 125-140, Jan 2019. ISSN 1559-1182. Available at: < <https://www.ncbi.nlm.nih.gov/pubmed/29681024> >.

WINNER, B. et al. In vivo demonstration that alpha-synuclein oligomers are toxic. **Proc Natl Acad Sci U S A**, v. 108, n. 10, p. 4194-9, Mar 2011. ISSN 1091-6490. Available at: < <https://www.ncbi.nlm.nih.gov/pubmed/21325059> >.

WISHART, D. S. et al. ¹H, ¹³C and ¹⁵N chemical shift referencing in biomolecular NMR. v. 6, n. 2, p. 135-140, 1995. Available at: < <https://doi.org/10.1007/BF00211777> >.

WOLOZIN, B.; IVANOV, P. Stress granules and neurodegeneration. v. 20, n. 11, p. 649-666, 2019. Available at: < <https://doi.org/10.1038/s41583-019-0222-5> >.

WRIGHT, J. A.; WANG, X.; BROWN, D. R. Unique copper-induced oligomers mediate alpha-synuclein toxicity. **FASEB J**, v. 23, n. 8, p. 2384-93, Aug 2009. ISSN 1530-6860. Available at: < <http://www.ncbi.nlm.nih.gov/pubmed/19325037> >.

WULF, M. A.; SENATORE, A.; AGUZZI, A. The biological function of the cellular prion protein: an update. **BMC Biol**, v. 15, n. 1, p. 34, 05 2017. ISSN 1741-7007. Available at: < <https://www.ncbi.nlm.nih.gov/pubmed/28464931> >.

YANG, D. S. et al. Examining the zinc binding site of the amyloid-beta peptide. **Eur J Biochem**, v. 267, n. 22, p. 6692-8, Nov 2000. ISSN 0014-2956. Available at: < <http://www.ncbi.nlm.nih.gov/pubmed/11054124> >.

YUAN, Y.-X.; ZHENG, Y.-S. New Acylhydrazone Photoswitches with Quantitative Conversion and High Quantum Yield but without Hydrogen Bond Stabilizing (Z)-Isomer. **ACS Applied Materials & Interfaces**, v. 11, n. 7, p. 7303-7310, 2019. Available at: < <https://doi.org/10.1021/acsami.8b21719> >.

ZAMANI, H. A. et al. Synthesis of N'-(1-pyridin-2-ylmethylene)-2-furohydrazide and its application in construction of a highly selective PVC-based membrane sensor for La(III) ions. **Anal Sci**, v. 22, n. 7, p. 943-8, Jul 2006. ISSN 0910-6340. Available at: < <https://www.ncbi.nlm.nih.gov/pubmed/16837743> >.

ZECCA, L. et al. The role of iron and copper molecules in the neuronal vulnerability of locus coeruleus and substantia nigra during aging. **Proc Natl Acad Sci U S A**, v. 101, n. 26, p. 9843-8, Jun 2004. ISSN 0027-8424. Available at: < <https://www.ncbi.nlm.nih.gov/pubmed/15210960> >.

ZHAO, F. et al. Metal-catalyzed oxidation of histidine in human growth hormone. Mechanism, isotope effects, and inhibition by a mild denaturing alcohol. **J Biol Chem**, v. 272, n. 14, p. 9019-29, Apr 1997. ISSN 0021-9258. Available at: < <https://www.ncbi.nlm.nih.gov/pubmed/9083026> >.

ZHAO, J. et al. Substrate interaction inhibits γ -secretase production of amyloid- β peptides. **Chemical Communications**, v. 56, n. 17, p. 2578-2581, 2020. Available at: < <http://dx.doi.org/10.1039/C9CC09170J> >.

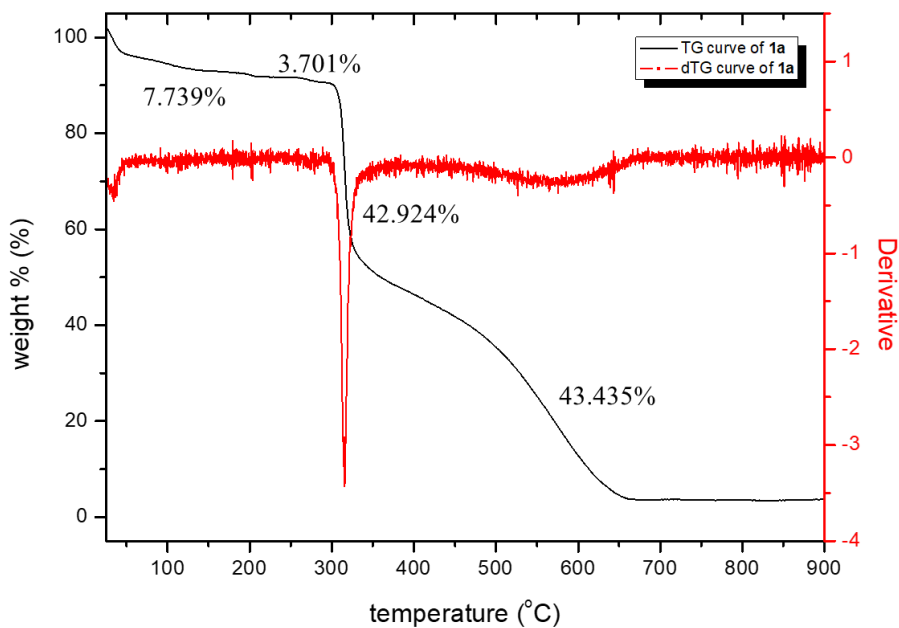
ZHENG, W. H. et al. Amyloid beta peptide induces tau phosphorylation and loss of cholinergic neurons in rat primary septal cultures. **Neuroscience**, v. 115, n. 1, p. 201-11, 2002. ISSN 0306-4522. Available at: < <http://www.ncbi.nlm.nih.gov/pubmed/12401334> >.



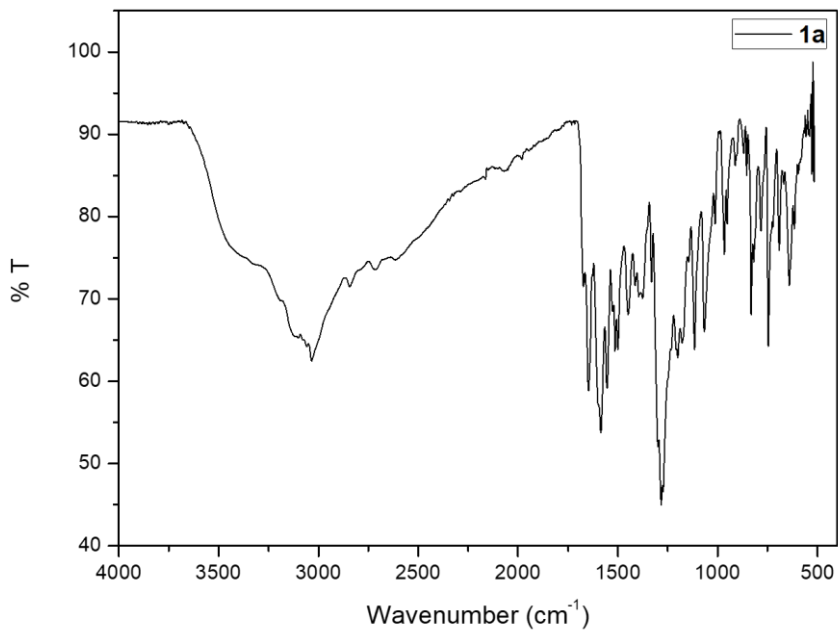
PUC-Rio - Certificação Digital Nº 1712623/CA

APPENDIX

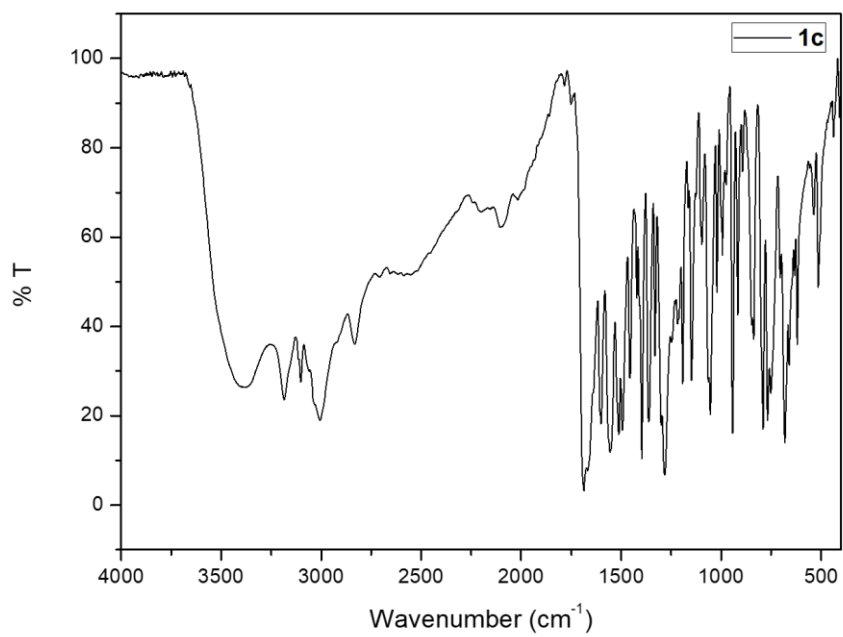
10. Appendix



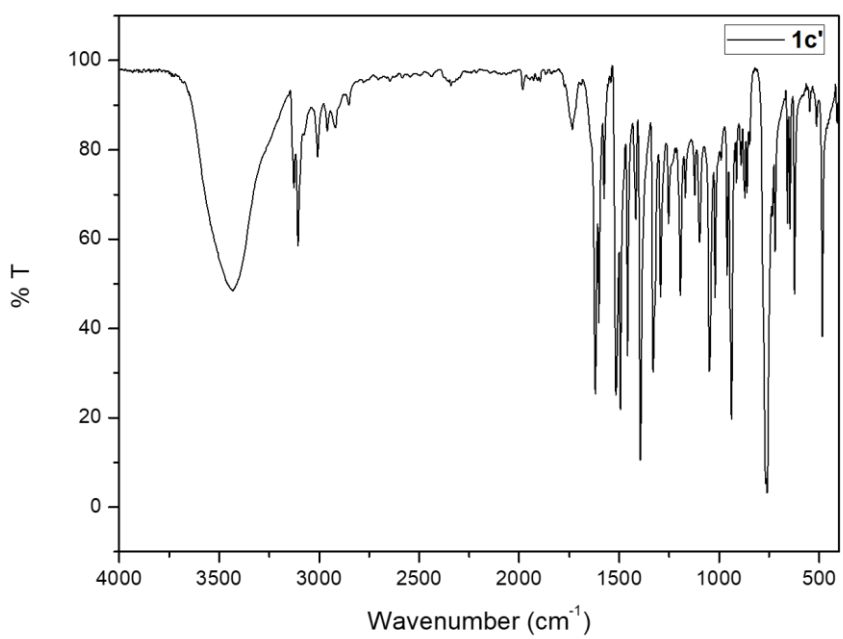
Appendix Figure 1. TG and dTG curves of polycrystalline solid **1a**.



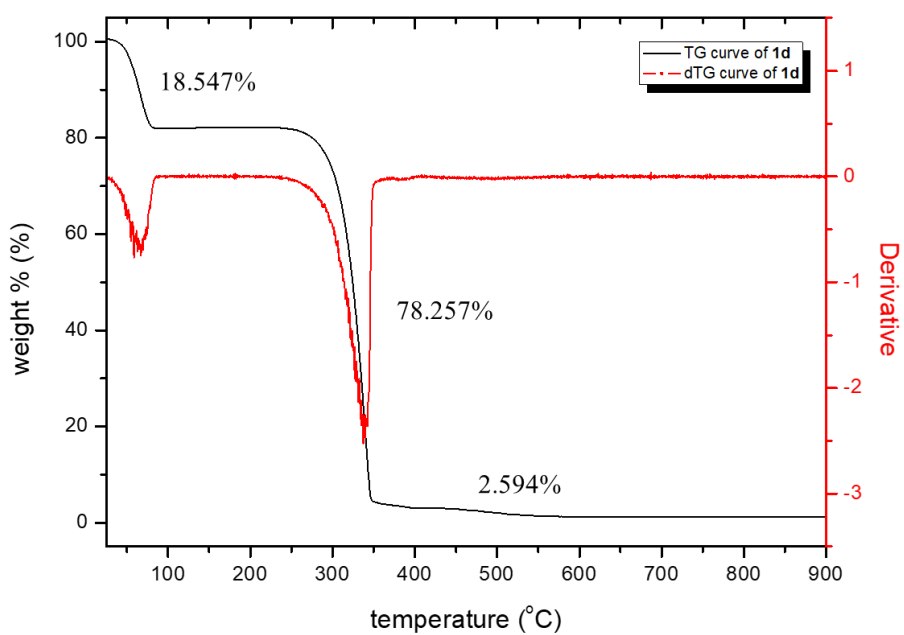
Appendix Figure 2. Mid-infrared spectrum of compound **1a**.



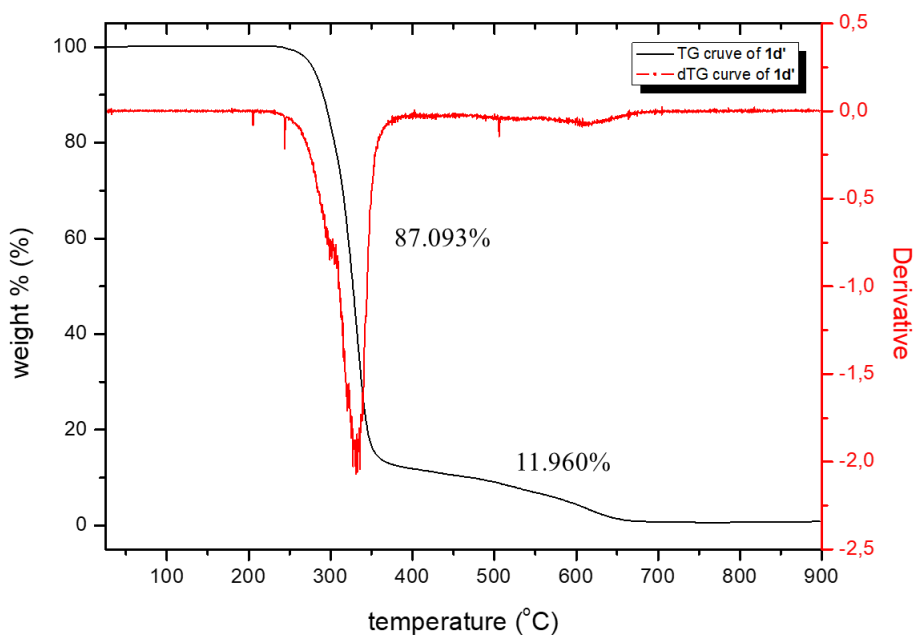
Appendix Figure 3. Mid-infrared spectrum of compound **1c**.



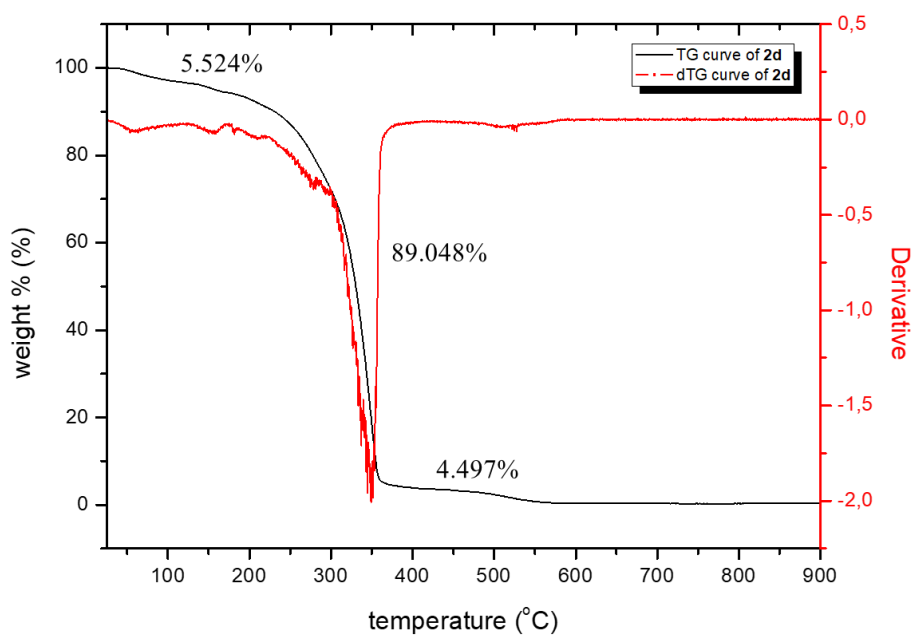
Appendix Figure 4. Mid-infrared spectrum of compound **1c'**.



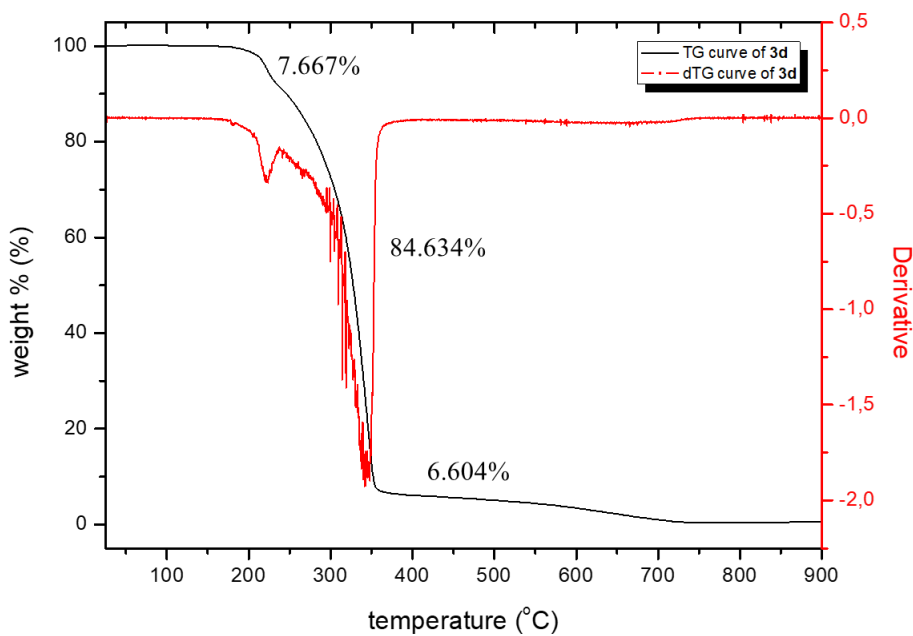
Appendix Figure 5. TG and dTG curves of polycrystalline solid **1d**.



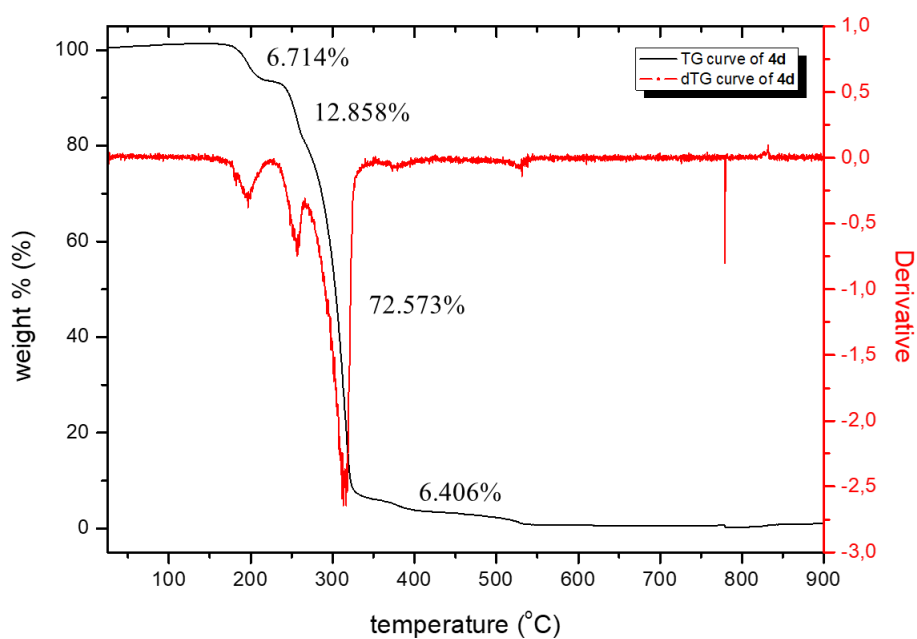
Appendix Figure 6. TG and dTG curves of single crystals of compound **1d'**.



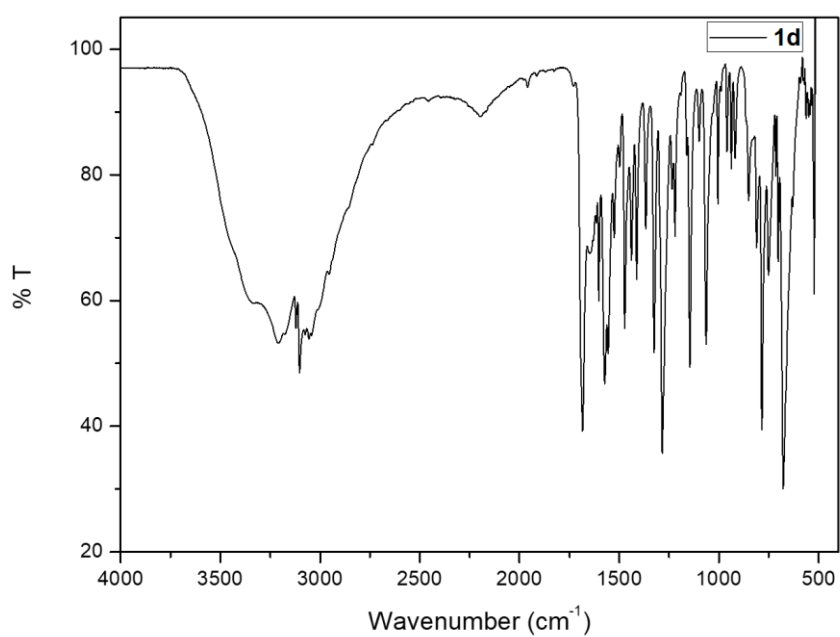
Appendix Figure 7. TG and dTG curves of single crystals of compound 2d.



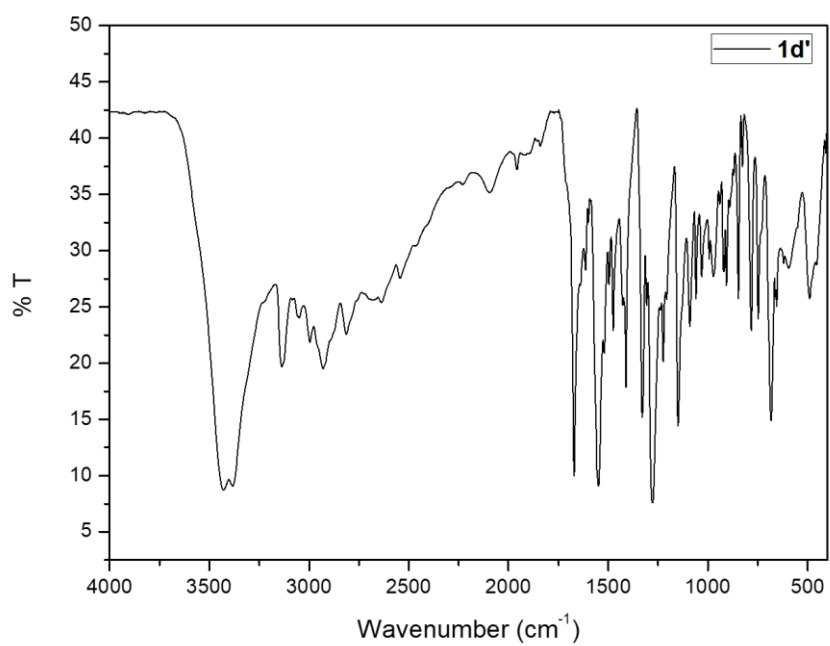
Appendix Figure 8. TG and dTG curves of single crystals of compound 3d.



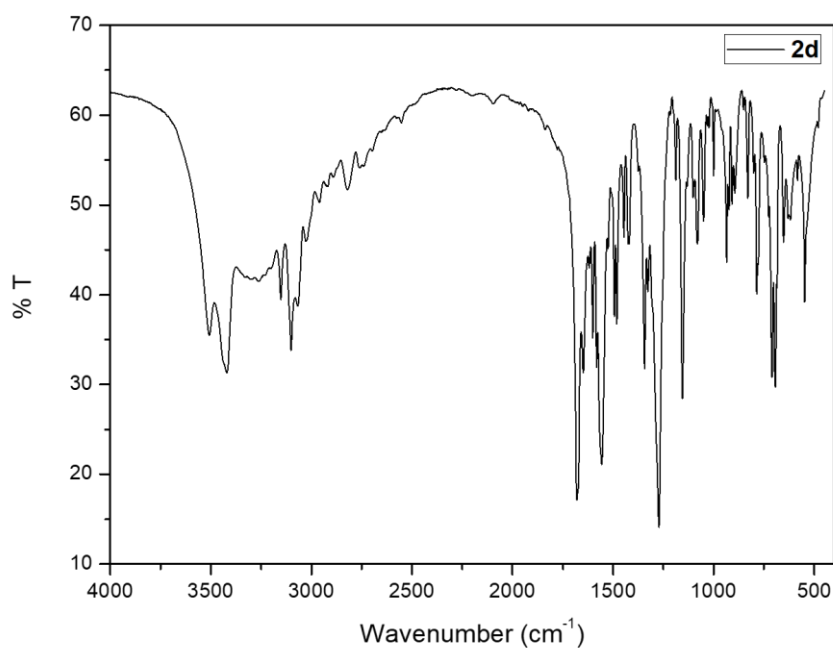
Appendix Figure 9. TG and dTG curves of single crystals of compound **4d**.



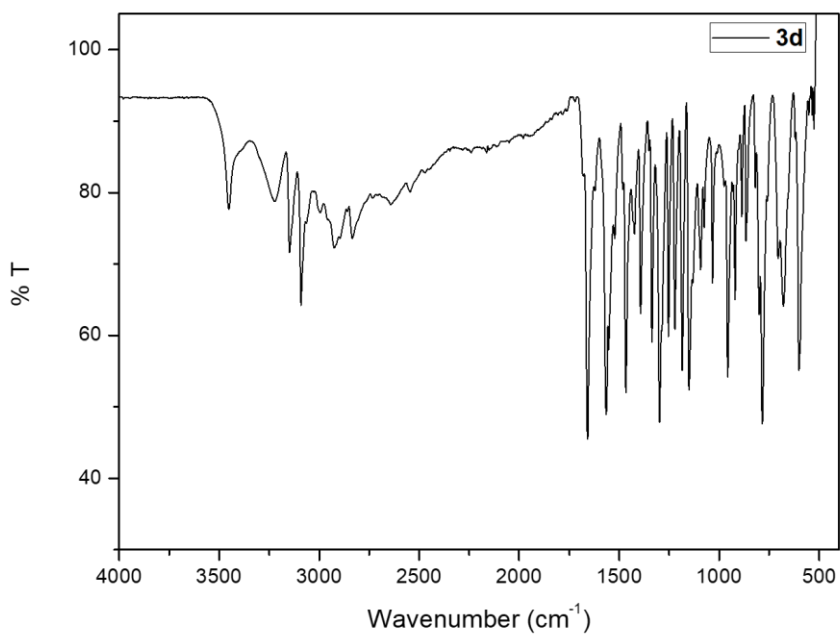
Appendix Figure 10. Mid-infrared spectrum of compound **1d**.



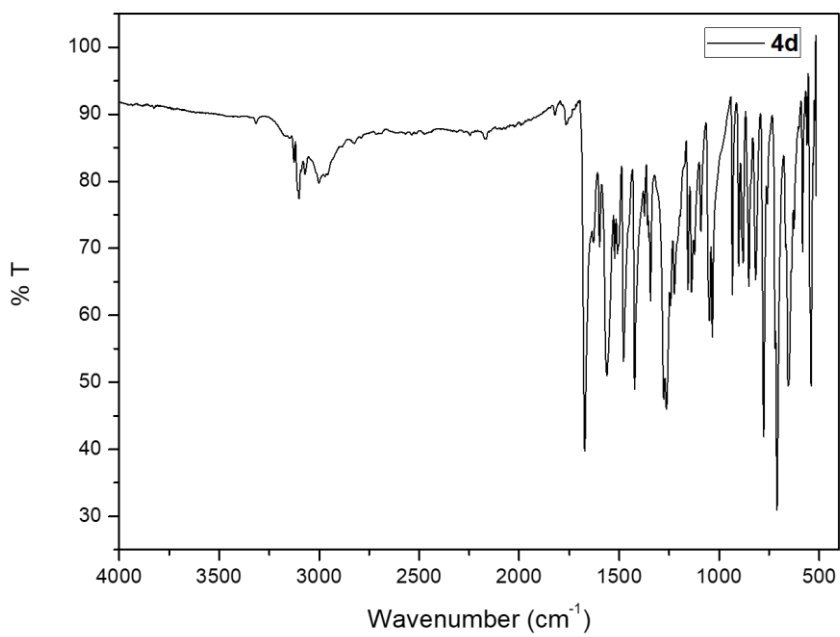
Appendix Figure 11. Mid-infrared spectrum of compound **1d'**.



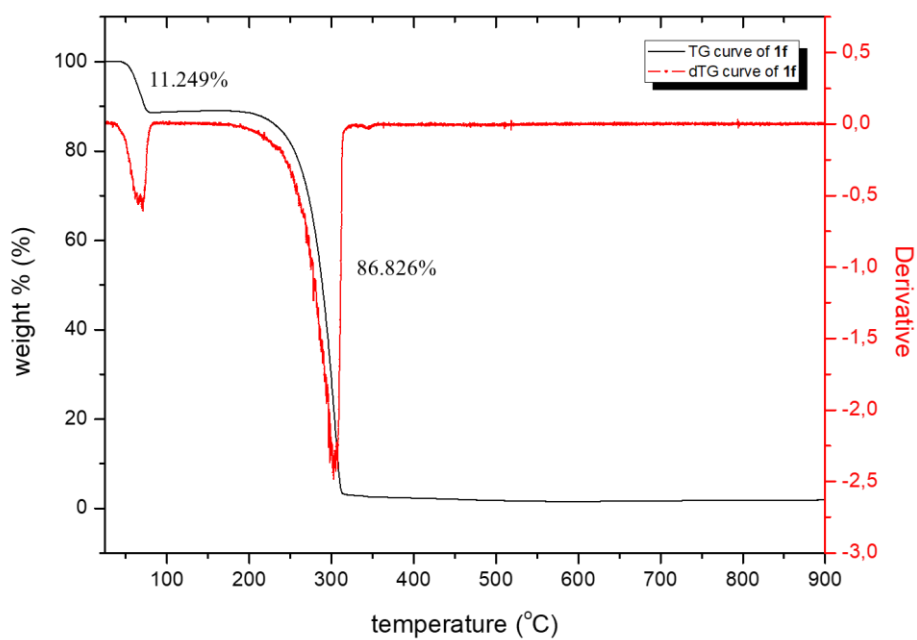
Appendix Figure 12. Mid-infrared spectrum of compound **2d**.



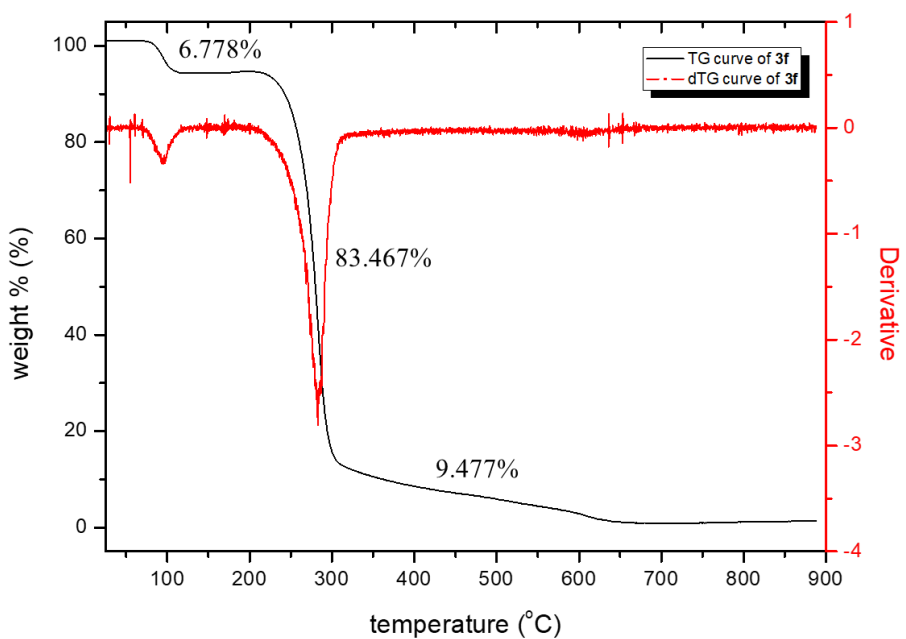
Appendix Figure 13. Mid-infrared spectrum of compound **3d**.



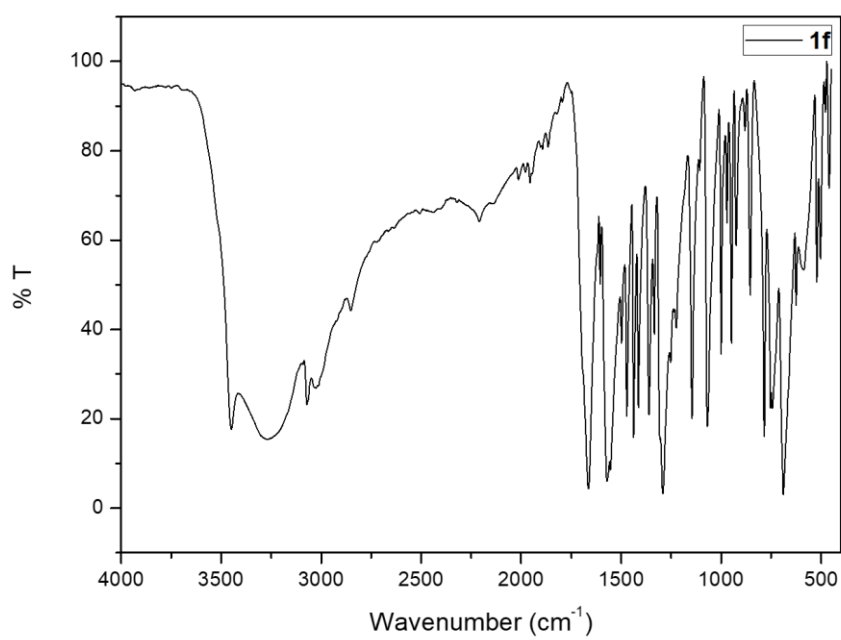
Appendix Figure 14. Mid-infrared spectrum of compound **4d**.



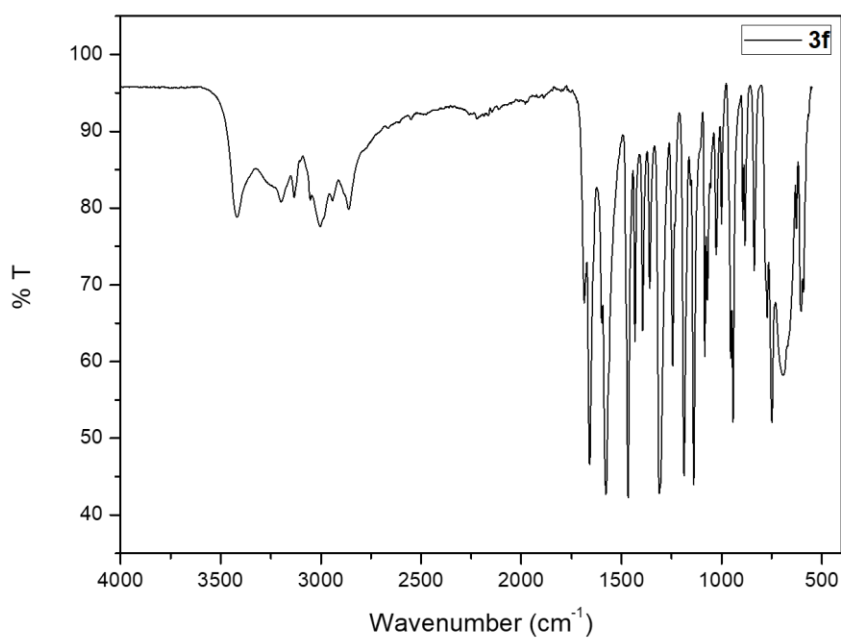
Appendix Figure 15. TG and dTG curves of compound **1f**.



Appendix Figure 16. TG and dTG curves of compound **3f**.



Appendix Figure 17. Mid-infrared spectrum of compound **1f**.



Appendix Figure 18. Mid-infrared spectrum of compound **3f**.



PUC-Rio - Certificação Digital Nº 1712623/CA

SCIENTIFIC PRODUCTION

11. Scientific Production

This work was developed during the 48 months of the Ph.D. Program from the Department of Chemistry of the Pontifical Catholic University of Rio de Janeiro (PUC-Rio). It is important to take into account that, due to the pandemic situation imposed by the emergence of COVID-19, the last 12 months of experimental work were greatly compromised. Nevertheless, mainly performed at the LABSO-Bio (*Laboratório de Síntese Orgânica e Química de Coordenação Aplicada a Sistemas Biológicos, PUC-Rio*), under the supervision of Prof. Dr. Nicolás A. Rey, and along with collaborators and 10 months spent at the University Medical Center Göttingen (Georg-August Universität, Germany), the present thesis work generated 4 full publications in indexed scientific journals, from which the student is the first author in all of them and even shared the correspondence with Prof. Rey in the latest published paper. The first page of each of these articles, in chronological order, are shown below. Full papers can be downloaded from the editors' websites.

Moreover, four novel 1-methyl-1H-imidazole-2-carboxaldehyde-derived *N*-acylhydrazones (compounds **1d**, **2d**, **3d** and **4d**), and, more generally, a Markush structure, were the subject of a recent patent application (BR1020200054236) in the Brazilian agency *Instituto Nacional da Propriedade Industrial* (INPI) (Rey and Cukierman, 2020). The first pages of the patent application are also shown below.

Parts of this work were also submitted to different regional and international conferences, which included oral and posters presentations, two of which selected for “best poster” awards. The first one, in 2017, was granted by the sponsor Inorganics at the 18th International Conference on Biological Inorganic Chemistry, while the second work was chosen as the best Inorganic Chemistry poster in the session, at the *XVII Encontro Regional da Sociedade Brasileira de Química do Rio de Janeiro*, in 2019.



Aroylhydrazones constitute a promising class of 'metal-protein attenuating compounds' for the treatment of Alzheimer's disease: a proof-of-concept based on the study of the interactions between zinc(II) and pyridine-2-carboxaldehyde isonicotinoyl hydrazone

Daphne S. Cukierman¹ · Elio Accardo¹ · Rosana Garrido Gomes¹ · Anna De Falco¹ · Marco C. Miotto² · Maria Clara Ramalho Freitas³ · Maurício Lanznaster⁴ · Claudio O. Fernández² · Nicolás A. Rey¹

Received: 18 June 2018 / Accepted: 22 August 2018 / Published online: 25 August 2018
© SBIC 2018

Abstract

With the increasing life expectancy of the world's population, neurodegenerative diseases, such as Alzheimer's disease (AD), will become a much more relevant public health issue. This fact, coupled with the lack of efficacy of the available treatments, has been driving research directed to the development of new drugs for this pathology. Metal-protein attenuating compounds (MPACs) constitute a promising class of agents with potential application on the treatment of neurodegenerative diseases, such as AD. Currently, most MPACs are based on 8-hydroxyquinoline. Recently, our research group has described the hybrid aroylhydrazone containing the 8-hydroxyquinoline group INHHQ as a promising MPAC. By studying the known structure-related ligand HPCIH, which does not contain the phenol moiety, as a simplified chemical model for INHHQ, we aimed to clarify the real impact of the aroylhydrazone group for the MPAC activity of a compound with potential anti-Alzheimer's activity. The present work describes a detailed solution and solid-state study of the coordination of HPCIH with Zn²⁺ ions, as well as its in vitro binding-ability towards this metal in the presence of the Aβ(1–40) peptide. Similar to INHHQ, HPCIH is able to efficiently compete with Aβ(1–40) for Zn²⁺ ions, performing as expected for an MPAC. The similarity between the behaviors of both ligands is remarkable. Taken together, the data presented herein point to aroylhydrazones, such as the compounds HPCIH and the previously published INHHQ, as encouraging MPACs for the treatment of AD.

Keywords Aroylhydrazones · MPAC · Alzheimer's disease · Zinc(II) · Aβ peptide

Electronic supplementary material The online version of this article (<https://doi.org/10.1007/s00775-018-1606-0>) contains supplementary material, which is available to authorized users.

✉ Nicolás A. Rey
nicoarey@puc-rio.br

¹ Departamento de Química, Pontifícia Universidade Católica do Rio de Janeiro, Rio de Janeiro, RJ 22451-900, Brazil

² Max Planck Laboratory for Structural Biology, Chemistry and Molecular Biophysics of Rosario (MPLbioR, UNR-MPIbpC) and Instituto de Investigaciones para el Descubrimiento de Fármacos de Rosario (IIDEFAR, UNR-CONICET), Universidad Nacional de Rosario, S2002LRK Rosario, Santa Fe, Argentina

³ Instituto de Química, Universidade Federal Rural do Rio de Janeiro, Seropédica, RJ 23890-000, Brazil

⁴ Instituto de Química, Universidade Federal Fluminense, Niterói, RJ 24020-141, Brazil

Abbreviations

Aβ	β-Amyloid peptide
HPCIH	Pyridine-2-carboxaldehyde isonicotinoyl hydrazone
INHHQ	8-Hydroxyquinoline-2-carboxaldehyde isonicotinoyl hydrazone
MPACs	Metal-protein attenuating compounds

Introduction

Alzheimer's disease (AD) is a neurodegenerative disorder that currently represents the most common form of dementia in the elderly. The Aβ peptide is usually considered essential in the development of AD and is at the center of the amyloid cascade hypothesis, which postulates that this peptide itself and/or the cleavage products of its precursor protein, the



Impact of pyridine-2-carboxaldehyde-derived aroylhydrazones on the copper-catalyzed oxidation of the M112A PrP_{103–112} mutant fragment

Daphne S. Cukierman¹ · Nikolett Bodnár² · Beatriz N. Evangelista¹ · Lajos Nagy³ · Csilla Kállay² · Nicolás A. Rey^{1,4}

Received: 21 May 2019 / Accepted: 23 July 2019 / Published online: 10 August 2019
© Society for Biological Inorganic Chemistry (SBIC) 2019

Abstract

Misfolded prion protein (PrP^{Sc}) is known for its role in fatal neurodegenerative conditions, such as Creutzfeldt–Jakob disease. PrP fragments and their mutants represent important tools in the investigation of the neurotoxic mechanisms and in the evaluation of new compounds that can interfere with the processes involved in neuronal death. Metal-catalyzed oxidation of PrP has been implicated as a trigger for the conformational changes in protein structure, which, in turn, lead to misfolding. Targeting redox-active biometals copper and iron is relevant in the context of protection against the oxidation of biomolecules and the generation of oxidative stress, observed in several conditions and considered an event that might promote sporadic prion diseases as well as other neurodegenerative disorders. In this context, *ortho*-pyridine aroylhydrazones are of interest, as they can act as moderate tridentate ligands towards divalent metal ions such as copper(II). In the present work, we explore the potentiality of this chemical class as peptide protecting agents against the deleterious metal-catalyzed oxidation in the M112A mutant fragment of human PrP, which mimics relevant structural features that may play an important role in the neurotoxicity observed in prion pathologies. The compounds inhere studied, especially HPCFur, showed an improved stability in aqueous solution compared to our patented lead hydrazone INHHQ, displaying a very interesting protective effect toward the oxidation of methionine and histidine, processes that are related to both physiological and pathological aging.

Keywords Aroylhydrazones · Human prion protein · Copper(II) · Methionine oxidation · Oxidative stress

Abbreviations

dMKHA	Ac-SKPKNMKHA-NH ₂	PrP ^C	Cellular prion protein
HPCIH	Pyridine-2-carboxaldehyde isonicotinoyl hydrazone	PrP ^{Sc}	Scrapie prion protein
HPCFur	Pyridine-2-carboxaldehyde 2-furoyl hydrazone	ROS	Reactive oxygen species
		RP-HPLC	Reverse-phase high performance liquid chromatography
		TFA	Trifluoroacetic acid

Electronic supplementary material The online version of this article (<https://doi.org/10.1007/s00775-019-01700-2>) contains supplementary material, which is available to authorized users.

✉ Nicolás A. Rey
nicoarey@puc-rio.br

¹ Departamento de Química, Pontifícia Universidade Católica do Rio de Janeiro, Rio de Janeiro 22451-900, Brazil

² Department of Inorganic and Analytical Chemistry, University of Debrecen, Debrecen 4032, Hungary

³ Department of Applied Chemistry, University of Debrecen, Debrecen 4032, Hungary

⁴ NMR-based Structural Biology, Max Planck Institute for Biophysical Chemistry, 37077 Göttingen, Germany

Introduction

The prion protein (PrP) is known for its role in fatal neurodegenerative conditions, such as the Creutzfeldt–Jakob disease, fatal familial insomnia, Gertsman–Straussler–Scheinker syndrome, and kuru [1, 2]. The physiological, cellular prion protein, usually denoted as PrP^C, is a cell surface glycoprotein highly expressed in the central and peripheral nervous system. PrP^C is composed of 209 amino acids, presenting the residues 23–231 from the original translation product that contains 253 amino acids. The peptide 1–22 is cleaved during trafficking and residues 232–253 are replaced by a saccharide moiety [3]. PrP^C is divided into two regions of

Cite this: *Dalton Trans.*, 2020, **49**,
16252

X1INH, an improved next-generation affinity-optimized hydrazonic ligand, attenuates abnormal copper(I)/copper(II)- α -Syn interactions and affects protein aggregation in a cellular model of synucleinopathy†

Daphne S. Cukierman,^{a,b} Diana F. Lázaro,^b Pamela Sacco,^c Patrícia R. Ferreira,^a Renata Diniz,^d Claudio O. Fernández,^c Tiago F. Outeiro^{b,e,f} and Nicolás A. Rey^{*,a}

Although normal aging presents an accumulation of copper and iron in the brain, this becomes more relevant in neurodegeneration. α -Synuclein (α -Syn) misfolding has long been linked with the development of Parkinson's disease (PD). Copper binding promotes aggregation of α -Syn, as well as generalized oxidative stress. In this sense, the use of therapies that target metal dyshomeostasis has been in focus in the past years. Metal-Protein Attenuating Compounds (MPACs) are moderate chelators that aim at disrupting specific, abnormal metal-protein interactions. Our research group has now established that *N*-acylhydrazones compose a set of truly encouraging MPACs for the bioinorganic management of metal-enhanced aggregopathies. In the present work, a novel ligand, namely 1-methyl-1*H*-imidazole-2-carboxaldehyde isonicotinoyl hydrazone (X1INH), is reported. We describe solution studies on the interaction and affinity of this compound for copper(II) ions showing that a fine tuning of metal-affinity was achieved. A series of *in vitro* biophysical NMR experiments were performed in order to assess the X1INH ability to compete with α -Syn monomers for the binding of both copper(I) and copper(II) ions, which are central in PD pathology. A preference for copper(I) has been observed. X1INH is less toxic to human neuroglioma (H4) cells in comparison to structure-related compounds. Finally, we show that treatment with X1INH results in a higher number of smaller, less compact inclusions in a well-established model of α -Syn aggregation. Thus, X1INH constitutes a promising MPAC for the treatment of Parkinson's disease.

Received 25th March 2020,
Accepted 5th May 2020

DOI: 10.1039/d0dt01138j

rsc.li/dalton

1. Introduction

Some transition metals exert fundamental roles in the brain, such as oxygen transport, neurotransmission and synaptic signaling, being also present in around one third of the enzymes in the human body.^{1,2} Although redox cycling is an important feature for the regular activity of some metalloenzymes, it is also involved in the generation of reactive oxygen species (ROS).³ Since metal ions are implicated both in the production and in the regulation of ROS, maintenance of their normal distribution is fundamental for healthy aging. In fact, many neurodegenerative diseases have been associated with poor metal homeostasis, being correlated with ROS-mediated oxidation, misfolding and aggregation of certain proteins.⁴⁻⁶ Although normal aging presents an accumulation of copper and iron in the brain, this becomes more relevant in neurodegeneration and in pathologies such as Alzheimer's (AD) and Parkinson's (PD) diseases.⁷

^aDepartamento de Química, Pontifícia Universidade Católica do Rio de Janeiro, 22451-045 Rio de Janeiro, RJ, Brazil. E-mail: nicoarey@puc-rio.br

^bDepartment of Experimental Neurodegeneration, Center for Biostructural Imaging of Neurodegeneration, University Medical Center Goettingen, 37073 Goettingen, Germany

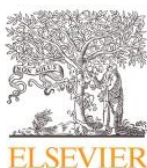
^cMax Planck Laboratory for Structural Biology, Chemistry and Molecular Biophysics of Rosario (MPLbioR, UNR-MPIbpC), and Instituto de Investigaciones para el Descubrimiento de Fármacos de Rosario (IIDEFAR, UNR-CONICET), Universidad Nacional de Rosario, Rosario, Argentina

^dDepartamento de Química, Universidade Federal de Minas Gerais, 31270-901 Belo Horizonte, MG, Brazil

^eMax Planck Institute for Experimental Medicine, 37075 Goettingen, Germany

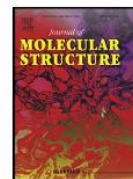
^fTranslational and Clinical Research Institute, Faculty of Medical Sciences, Newcastle University, Framlington Place, Newcastle Upon Tyne, NE2 4HH, UK

† Electronic supplementary information (ESI) available: Representative images, as well as quantification of the effects of HPClH and INHHQ on the aggregation of α -Syn are found in Fig. S1. Fig. S2 shows the effects of X1INH in the levels of α -Syn and its partition in Triton-X100 soluble/insoluble fractions. Crystallographic data for X1INH-HCl, CCDC 1968801. For ESI and crystallographic data in CIF or other electronic format see DOI: 10.1039/d0dt01138j



Contents lists available at ScienceDirect

Journal of Molecular Structure

journal homepage: www.elsevier.com/locate/molstr

Mildness in preparative conditions directly affects the otherwise straightforward syntheses outcome of Schiff-base isoniazid derivatives: Aroylhydrazones and their solvolysis-related dihydrazones

Daphne S. Cukierman^{a,*}, Beatriz N. Evangelista^a, Carlos Castanho Neto^b, Chris H.J. Franco^c, Luiz Antônio S. Costa^d, Renata Diniz^e, Jones Limberger^b, Nicolás A. Rey^{a,*}

^a Laboratório de Síntese Orgânica e Química de Coordenação Aplicada a Sistemas Biológicos (LABSO-Bio), Departamento de Química, Pontifícia Universidade Católica do Rio de Janeiro, Rio de Janeiro, 22451-900, Brazil

^b Laboratório de Síntese Orgânica e Química Fina (LaSOQF), Departamento de Química, Pontifícia Universidade Católica do Rio de Janeiro, Rio de Janeiro, 22451-900, Brazil

^c Departamento de Química, Campus Martelos, Universidade Federal de Juiz de Fora, Juiz de Fora, 36036-900, Brazil

^d Núcleo de Estudos em Química Computacional (NEQC), Departamento de Química, ICE, Universidade Federal de Juiz de Fora, Juiz de Fora, 36036-900, Brazil

^e Grupo de Cristalografia Química (GCQ), Departamento de Química, ICEx, Universidade Federal de Minas Gerais, Belo Horizonte, 31270-901, Brazil

ARTICLE INFO

Article history:

Received 28 June 2020

Revised 27 September 2020

Accepted 9 October 2020

Available online 10 October 2020

Keywords:

Aroylhydrazones

Dihydrazones

Isoniazid

Solvolysis

Hirshfeld surfaces

ABSTRACT

Aroylhydrazones are versatile compounds with a series of applications, from biological to technological spheres. The simplicity of their preparation allows for a great chemical variability and synthetic manageability. However, the process can be not as straightforward as one would imagine. Some parameters such as specific reactants, the amount of acid employed as catalyst and reaction temperature can have a direct impact on the obtained product. In the present work, we describe two series of novel isoniazid-derived compounds prepared from a pair of different aldehyde precursors, as well as the solvolysis, under harsh synthetic conditions, of the initially formed aroylhydrazones, leading to unexpected dihydrazones. All compounds were unequivocally characterized in solution using 1D and 2D NMR experiments in DMSO-*d*₆ and, in the solid-state, by other classic techniques. System I is composed by 2-(1H-pyrazol-1-yl)benzaldehyde and its hydrazone derivatives, while system II comprises 2-(4-methoxyphenoxy)benzaldehyde and its related Schiff-base products. The first aldehyde was obtained for the first time via the copper-catalyzed Ullmann C–N coupling between 2-bromobenzaldehyde and pyrazole. Single crystals of its aroylhydrazone and dihydrazone derivatives were isolated and thoroughly characterized, including Hirshfeld surfaces and energy frameworks studies. Finally, we describe an NMR and theoretically-based proposed reaction pathway for the unexpected formation of the dihydrazones involving the solvolysis of the initially formed isonicotinoyl hydrazone followed by attack to a second free aldehyde molecule.

© 2020 Elsevier B.V. All rights reserved.

1. Introduction

Aldehyde-derived hydrazones compose an organic class of compounds which present, in their structures, the functional group $R_1HC=N-NR_2R_3$. In hydrazones, the azomethine C=N double bond is conjugated with the electron pair of the neighboring nitrogen, which makes them more resistant to hydrolysis than common Schiff bases. Hydrazones, synthesized through the condensation reaction between hydrazides and carbonyl compounds, are

particularly interesting in medicinal chemistry and have been identified as important hits and lead compounds to act upon different molecular targets [1]. They have been employed in a wide spectrum of pharmacological applications [2], such as analgesics [3], anti-inflammatories [4], anti-tuberculosis [5], antitumor agents [6] and antimalarials [7]. Specifically, *N*-acylhydrazones have also been the subject of several studies in the inorganic chemistry field due to the presence of the $R_1R_2C=N-NH-CO-$ moiety, which allows them to perform as bidentate ligands, coordinating metal ions through the azomethine nitrogen and the carbonyl oxygen. For example, these compounds have been investigated as iron chelators for the control of neurodegenerative disorders such as Friedreich ataxia and other diseases related to the excess of this metal

* Corresponding authors.

E-mail addresses: daphcukierman@gmail.com (D.S. Cukierman), nicoarey@puc-rio.br (N.A. Rey).



**Pedido nacional de Invenção, Modelo de Utilidade, Certificado de
Adição de Invenção e entrada na fase nacional do PCT**

Número do Processo: BR 10 2020 005423 6

Dados do Depositante (71)

Depositante 1 de 1

Nome ou Razão Social: FACULDADES CATOLICAS

Tipo de Pessoa: Pessoa Jurídica

CPF/CNPJ: 33555921000170

Nacionalidade: Brasileira

Qualificação Jurídica: Instituição de Ensino e Pesquisa

Endereço: Rua Marquês de São Vicente, 225, Gávea

Cidade: Rio de Janeiro

Estado: RJ

CEP: 22451-900

País: Brasil

Telefone: (21) 3114-1303/4/5

Fax: (21) 3114-1309

Email: shirley@dctc.puc-rio.br

PUC-Rio - Certificação Digital N° 1712623/CA

**PETICIONAMENTO
ELETRÔNICO**

Esta solicitação foi enviada pelo sistema Petição Eletrônica em 18/03/2020 às
17:20, Petição 870200036250

Dados do Pedido

Natureza Patente: 10 - Patente de Invenção (PI)

Título da Invenção ou Modelo de Utilidade (54): COMPOSTOS N-ACIL-HIDRAZÔNICOS, USO NO TRATAMENTO DE AGREGOPATIAS DEGENERATIVAS AMILOIDES E NÃO-AMILOIDES, E COMPOSIÇÃO FARMACÊUTICA

Resumo: A presente invenção refere-se a uma família de compostos N-acil-hidrazônicos estruturalmente derivados do 1-metil-1H-imidazol-2-carboxaldeído, ou ainda sais farmacêuticamente aceitáveis dos mesmos, e uso dos referidos compostos para prevenir e/ou tratar agregopatias degenerativas amiloides (tais como as doenças de Alzheimer, Parkinson e diabetes do tipo 2) e não-amiloides (tais como a catarata). Estes compostos atuam como atenuadores da interação metalproteína, prevenindo e/ou diminuindo a oligomerização proteica através da competição com o peptídeo- ou proteína-alvo pela ligação a íons metálicos fisiológicos e, possivelmente, pela modulação da própria interação proteína-proteína. A invenção trata, ainda, de quatro compostos especificamente descritos como exemplos de N-acil-hidrazonas derivadas do 1-metil-1H-imidazol-2-carboxaldeído, a saber: 1-metil-1H-imidazol-2-carboxaldeído isonicotinoil hidrazona, 1-metil-1H-imidazol-2-carboxaldeído benzoil hidrazona, 1-metil-1H-imidazol-2-carboxaldeído 2-furoil hidrazona e 1-metil-1H-imidazol-2-carboxaldeído 2-tiofenil hidrazona. O atual pedido compreende também composições farmacêuticas.

Figura a publicar: 1

Dados do Procurador

Procurador:

Nome ou Razão Social: Francisco Carlos Rodrigues Silva

Numero OAB:

Numero API: 507

CPF/CNPJ: 51318601720

Endereço: Avenida Rio Branco, 01, Sala 2011, Centro

Cidade: Rio de Janeiro

Estado: RJ

CEP: 20090-003

Telefone: (21) 32128200

Fax:

Email: silva@atesa.com.br

**PETICIONAMENTO
ELETRÔNICO**

Esta solicitação foi enviada pelo sistema Peticionamento Eletrônico em 18/03/2020 às 17:20, Petição 870200036250



18thInternational Conference on
Biological Inorganic Chemistry
July 31st – August 4th
Florianópolis, Brazil

BEST POSTER AWARD CERTIFICATE

We certify that the abstract entitled “*Electronic Effects Modulate the Activity of Two Structure-Related MPACs: Being a Hydrazone Is Not Enough*” authored by **Daphne S. Cukierman**; Beatriz N. Evangelista; Carlos C. Neto; Anna De Falco; Chris H. de Jesus Franco; Marco C. Miotto; Renata Diniz; Jones Limberger; Claudio O. Fernández; Nicolás A. Rey presented during the 18th International Conference on Biological Inorganic Chemistry, from July 31st to August 4th, has been recognized by the sponsor **INORGANICS** as best poster

Certificado

PÔSTER PREMIADO - Química Inorgânica – INO

Certifico que o trabalho, apresentado por **DAPHNE S CUKIERMAN**, **Modulação das afinidades de ligantes N-acil-hidrazônicos por Cu²⁺ via variação do ângulo de mordida: otimização do potencial como MPACs** dos autores *DAPHNE S. CUKIERMAN, PATRÍCIA R. FERREIRA, NICOLÁS A. REY*, foi **premiado na categoria Química Inorgânica – INO**, no XVII Encontro Regional da SBQ-Rio, realizado no CCMN-UFRJ dos dias 2 a 5 de dezembro de 2019.

Rio de Janeiro, 05/12/2019.



Sabrina Baptista Ferreira

Profa. Dra. Sabrina Baptista Ferreira
Presidenta da Comissão Organizadora -
Secretária Regional da SBQ-Rio (IQ-UFRJ)